Single-sign CPL emitting Ln(III) complexes and their applications

DAVIDE FRANCESCO DE-ROSA

Department of Chemistry

Single-sign CPL emitting Ln(III) complexes and their applications

Davide F. De Rosa

A thesis submitted for the degree of Doctor of Philosophy

2024

Declaration

The work described herein was undertaken at the Department of Chemistry, Durham University between October 2020 and November 2023. All of the work is my own, except where specifically stated otherwise. No part has previously been submitted for a degree at this or any other university.

Statement of Copyright

Abstract

The present work concerns the synthesis and photophysical characterisation of novel europium(III) complexes that are versatile, robust, bright, linkable, and can display same-sign circularly polarised luminescence (CPL) spectra, *i.e.* all positive or negative transitions within a single emission manifold. Broad, intense, same-sign CPL emission manifolds are expected to aid spectroscopic detection using low-cost broad band pass filters or wider slit opening, increasing signal without opposite sign CPL bands cancelling out.

Highly conjugated arylalkynylpyridyl antennae attached to the 1,4,7-triazacyclononane macrocycle, and mixed donor moieties, *i.e.* both carboxylate and phosphinate donor groups to coordinate the central europium(III) ion, were incorporated in the complexes. Different peripheral linking groups, such as carboxylate anions and *para*-nitro groups, are embedded in the structure to allow facile late-stage conjugation of the complex. The effects of chemical modifications on CPL spectra were investigated.

A terbium(III) chiral complex was designed and tested as a green dopant for the fabrication of Circularly Polarised Organic Light Emitting Diodes (OLEDs). Despite some preliminary good results, the limited choice of available commercial host materials with an adequately broad bandgap is a problem that needs to be overcome to achieve efficient CP-OLEDs.

A europium(III) complex was found to display same-sign CPL transition for the $\Delta J = 1$ and $\Delta J = 2$ emission manifolds. Further investigation of the dependence of CPL properties (both shape and intensity) on solvent polarity highlighted that CPL emission tends to be brighter and mono-signate in low polarity solvents. Racemisation kinetics of enantiopure europium(III) complexes in different solvents was investigated. Kinetic stability is key to designing durable lanthanide(III) doped polymeric films with definite CPL properties.

Unlocking same-sign CPL emission allowed a further advancement in the field of CPL imaging. A handheld non-moving parts setup that can acquire a CPL image in a single shot, called Circularly Polarised Luminescence Photography (CPLP), was designed and validated using the europium(III) complex described above. This high-throughput instrument will integrate five layers of security readout comprising of multi-coloured, multi-spectral, opposing-helicity, combined with high spatial and temporal resolution in unclonable luminescent QR codes, which was prototyped in the present study.

List of Abbreviations

1PE	Single-Photon Excitation
2PE	Two-Photon Excitation
Alq3	*tris*(8-hydroxyquinolato)aluminium
AMP	Adenosine Monophosphate
APD	Avalanche Photodiode
B	Brightness
BET	Back Energy Transfer
Boc	*tert*-Butyloxycarbonyl
BOPP	Biaxially Oriented Polypropylene
BPF	Band Pass Filter
bpy	Bipyridine
BS	Beam Splitter
BSB	4,4'-di(triphenylsilyl)-biphenyl
CCD	Charge Coupled Device
CD	Circular Dichroism
CE	Current Efficiency
CMOS	Complementary Metal-Oxide Semiconductor
CP	Circularly Polarised
CPB	Circularly Polarised Brightness
CPL	Circularly Polarised Luminescence
CPLP	Circularly Polarised Luminescence Photography
CRI	Colour Rendering Index
CRR	Corrected Racemisation Rate
CSI	Chameleon Security Inks
CV	Cyclic Voltammetry
cyclen	1,4,7,10-Tetraazacyclododecane
DBSO	Dibenzylsulfoxyde

DCM	Dichloromethane
DFT	Density Functional Theory
DIEA	*N*,*N*-Diisopropylethylamine
DMF	Dimethylformamide
DMSO	Dimethylsulfoxide
DOTA	1,4,7,10-Tetraazacyclododecanetetraacetic Acid
dppf	1,1'-*bis*(diphenylphosphino)ferrocene
EQE	External Quantum Efficiency
eT	Electron Transfer
ET	Energy Transfer
ETL	Electron Transport Layer
EVA	Ethylene Vinyl Acetate
F8BT	poly(9,9-dioctylfluorene-co-benzothiadiazole)
FOV	Field of View
FWHM	Full Width at Half Maximum
hfbc	*tetrakis*(3-heptafluoro-butylryl-camphorato)
HOMO	Highest Occupied Molecular Orbital
HPLC	High Pressure Liquid Chromatography
HSA	Human Serum Albumin
HTL	Hole Transport Layer
IC	Internal Conversion
ICT	Internal Charge Transfer
L	Luminance
LDLS	Laser-Driven Light Source
LE	Local Excited State Emission
LED	Light-Emitting Diode
LIA	Lock-In Amplifier
LIA	Lock-In Amplifier
LSCM	Laser Scanning Confocal Microscope
LUMO	Lowest Unoccupied Molecular Orbital

LP	Linear Polariser
LPF	Long Pass Filter
LS	Light Source
mCPBA	*meta*-chloroperoxybenzoic Acid
MP	Multiphoton
MRI	Magnetic Resonance Imaging
NMP	*N*-Methyl-2-Pyrrolidone
NPB	*N*,*N'*-diphenyl-*N*,*N'*-bis(1-naphthyl)(1,1'-biphenyl)-4,4'-diamine
OLED	Organic Light-Emitting Diode
OXD-7	1,3-bis[2-(4-*tert*-butylphenyl)-1,3,4-oxadiazo-5-yl]benzene
PBS	Polarising Beam Splitter cube
PEDOT	Poly(3,4-ethylenedioxythiophene)
PEDOT:PSS	poly(3,4-ethylenedioxythiophene) polystyrene sulfonate
PES	Potential Energy Surface
PES	Potential Energy Surface
PET	Photo-Induced Electron Transfer
PhMoNa	Phase Modulation Nanoscopy
PL	Photoluminescence
PMMA	Poly(metyl methacrylate)
POC	Proof-of-Concept
PVK	Poly(*N*-vinylcarbazole)
PVP	Polyvinylpyrrolidone
Q	Quencher
QWP	Quarter Wave Plate
RAFT	Reversible Addition Fragmentation Chain Transfer
RGB	Red-Green-Blue
SM	Scanning Monochromator
SPF	Short Pass Filter
SS	Solid State
TACN	1,4,7-Triazacyclononane

TADF	Thermally Activated Delayed Fluorescence
TFA	Trifluoroacetic Acid
TFAA	Trifluoroacetic Anhydride
TFB	Poly(9,9-dioctylfluorene-alt-N-(4-*sec*-butylphenyl)-diphenylamine
tfc	3-(Trifluoroacetyl)camphor
THF	Tetrahydrofuran
TICT	Twisted Intramolecular Charge Transfer
TLC	Thin Layer Chromatography
tmpo	*tris*(2,6-dimethoxyphenyl)phosphine
TMS	Trimethylsilyl
TPBi	2,2',2''-(1,3,5-Benzinetriyl)-*tris*(1-phenyl-1-H-benzimidazole)
TR	Time-Resolved
TSPO1	diphenyl[4-(triphenylsilyl)phenyl]phosphine oxide
TTA	2-Thenoyltrifluoroacetate
UK	United Kingdom
UV	Ultraviolet
YAG	Yttrium Aluminium Garnet

Contents

CHAPTER ONE

Introduction

Chapter One: Introduction

1.1. Luminescence of Lanthanides

1.1.1. Introduction to Luminescence

Luminescence is the spontaneous emission of light by a substance. Being non-thermal, it is a non-equilibrium phenomenon. There are several types of luminescence, categorised according to the physical nature of the phenomenon that generates the excitation leading to light emission. The most commonly found forms of luminescence include: photoluminescence, where the excitation of the emitting species is achieved through the absorption of a photon; electroluminescence, where excitation is accomplished by recombination of charge carriers of opposite sign in the presence of an applied electric field; chemiluminescence, where a chemical reaction produces an excited species (known as bioluminescence if it takes place within a living being); triboluminescence, if the excitation is caused by mechanical actions on the material. The work presented in this thesis primarily concerns photoluminescence and electroluminescence. Here, the two phenomena are briefly contrasted.

The processes involved in photoluminescence are well represented using a Jabłoński diagram, (Figure 1.1), which shows the quantised energy levels within vibrational manifolds corresponding to the different electronic states of the relevant species.

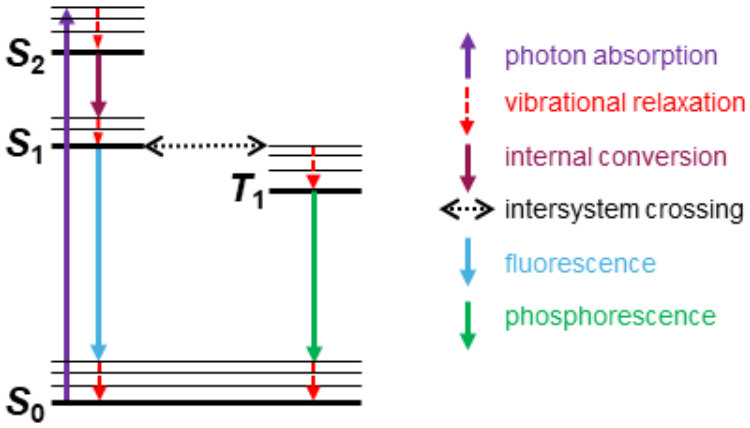

Figure 1.1. A representative Jabłoński diagram showing the major processes involved in photoluminescence.

In photoluminescence, the excitation is generated through the absorption of a photon of appropriate energy (or more than one photon with inversely proportional energies,

as will be discussed in Section 1.1.5). In general, photon absorption leads to electronic excitation of the photoluminescent species from the ground singlet state (S_0) to an excited vibrational level of a higher energy singlet state, the gap being equal to the energy of the absorbed photon. Absorption takes place on a 10^{-15} s timescale. Non-radiative vibrational relaxation dissipates part of the absorbed energy through molecular vibration and rotation (10^{-14} – 10^{-11} s). On a similar timescale, internal conversion (IC) brings the system to lower energy electronic singlet states. IC is a non-radiative relaxation process that does not alter the spin state, *i.e.* it is a fast, spin-allowed process. Eventually, the system reaches the lowest excited singlet state (S_1). Relaxation may happen either non-radiatively or result in the emission of a photon with a wavelength that is longer than the absorbed one due to non-radiative energy losses. This process is called *fluorescence* and occurs on a 10^{-9} – 10^{-7} s time scale. Through fluorescence, the system may reach any of the higher vibrational states of the S_0 manifold, so photons of different wavelength may be observed. It is observed that luminescence occurs only from the lowest excited state of a given multiplicity or, equivalently, that the emission wavelength is independent of the excitation wavelength. This empirical observation is known as Kasha's rule,[1] and is a consequence of the large overlap between vibrational wavefunctions that lay close in energy: non-radiative vibronic relaxation to the lowest excited state within the manifold is faster than the competing longer-lived fluorescence process. As an alternative, the excited species can undergo intersystem crossing (ISC) from the S_1 state to a triplet state of similar energy by flipping the spin of an electron. ISC is forbidden by electronic selection rules, accounting for its longer timescale (10^{-8} – 10^{-3} seconds). The system relaxes non-radiatively until it reaches the lowest excited triplet state (T_1). De-excitation from T_1 to S_0 may happen both non-radiatively and radiatively. The latter is termed *phosphorescence* and happens on a much slower timescale (10^{-4} – 10^{-1} seconds), reflecting the spin-forbidden nature of this phenomenon.

In the case of electroluminescence, excitation is accomplished by recombination of charge carriers of opposite sign (electrons and holes) in the presence of an applied electric field.[2,3] Electroluminescence from organic crystals was first observed by Sano and Pope from single crystals of anthracene in 1963.[4] The wavelength of the emitted photon depends on the energy gap of the semiconducting material hosting the exciton. Electrons and holes are spin ½ quasiparticles and produce 25% singlet and 75% triplet

excitons when they recombine, obeying the spin-statistic rule.[5] Since only singlet exciton relaxation can result in the emission of a photon, the efficiency of electroluminescent devices is inherently capped at 25%. Noteworthy examples of electroluminescent devices based on inorganic compounds are light-emitting diodes (LEDs). The active materials in LEDs are often based on compounds of elements from groups III and V of the periodic table, *e.g.* GaAs, Ga, AlGaAs, InGaP. The topic of electroluminescence and its applications, namely organic light emitting diodes (OLEDs)[6] is further expanded in Section 1.3.

1.1.2. Sensitised Lanthanide Emission

Lanthanide ions have unique optical properties, including sharp emission bands and long emission lifetimes, of the order of milliseconds for Tb(III) and Eu(III). These features are unusual for metal ion emitters in the condensed phase, especially when comparing their behaviour to transition metal ions: emission spectra of transition metal ions are very broad, spanning hundreds of nm, and have relatively short-lived excited states (order of 10^{-6} s). Overlayed lanthanide emission spectra are shown in Figure 1.2.

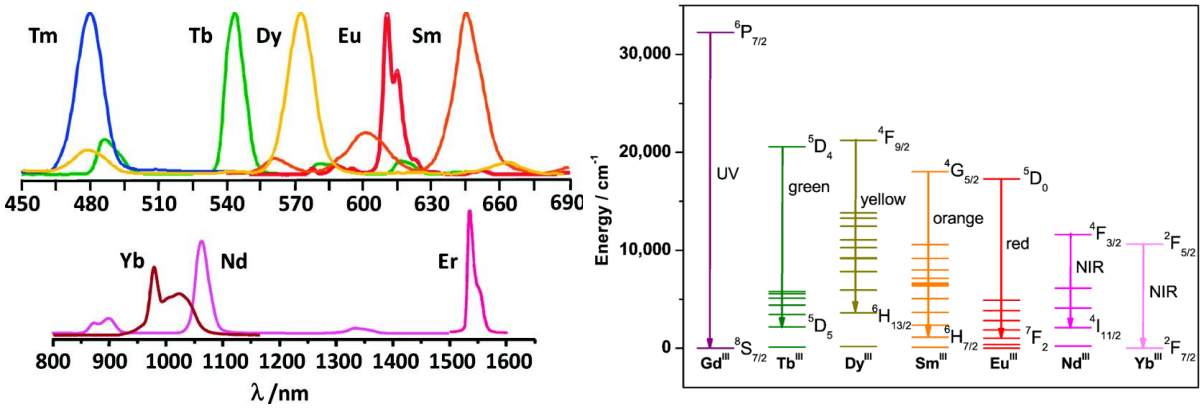

Figure 1.2. Selected low resolution emission spectra of lanthanides (*left*) and the electronic transitions they arise from (*right*). Adapted from [7,8].

The optical properties of lanthanides arise from their partially filled 4f orbitals. The 5s and 5p orbitals are filled and their average radial distances are such that $\langle r_{5s}\rangle, \langle r_{5p}\rangle > \langle r_{4f}\rangle$, so outer electrons shield the inner 4f orbitals. For this reason, external perturbations have a relatively minor effect on the intensity and the energy of the emission bands.

Lanthanide optical bands arise from 4f → 4f transitions. The matrix element of the electric dipole operator **d**, *i.e.* $\langle 4f|\boldsymbol{d}|4f\rangle$, vanishes for parity. This selection rule is known as the Laporte selection rule and means that electric dipole transitions are forbidden for lanthanides. This selection rule accounts for the intrinsically low molar extinction coefficients (typically in the range 0.5 – 3 M^{-1} cm^{-1}) of the free ions.[9] However, in the presence of an external perturbation, electronic states with different parity are mixed into the 4*f* orbitals of the free ion. This results in very small but non-vanishing transition amplitudes, giving rise to the so-called induced electric dipole transitions.[10] These small radiative rates account for the strikingly long emission lifetimes that are observed. Moreover, bilinear processes, such as energy transfer, up-conversion, and cross-relaxation, which are also characterised by slow rates, have sufficient time to occur, unlike in analogous transition metal ion systems. These intrinsic, unique spectroscopic properties allow for a vast number of applications, such as in the laser industry[11], scintillators used to detect charged particles[12], optical fibres[13], and time-gated sensing[14–16].

Direct excitation of the lanthanide ion is inefficient due to their low molar extinction coefficients. This issue can be overcome by excitation through an indirect pathway, usually termed *sensitisation*. By placing a carefully designed coordinating organic ligand close to the ion and exciting the ligand at its own absorption wavelength, its excitation energy can be transferred to the lanthanide ion via an efficient intramolecular energy transfer (ET) process. This indirect excitation pathway of the Ln(III) ion is termed the *antenna effect*, and results in a substantial improvement in brightness when compared to direct excitation of the lanthanide, (Figure 1.3).

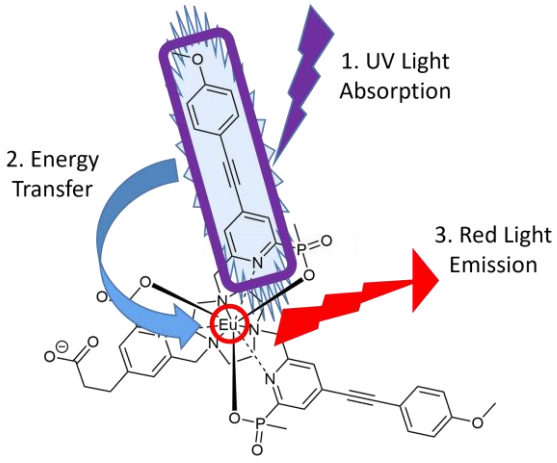

Figure 1.3. Schematic representation of the steps involved in the antenna effect. UV light is absorbed by the organic fluorophore (1); energy transfer to the Eu(III) occurs (2); Eu(III) emits visible light (3).

The lanthanide ion may relax from its excited state by emitting light. As a consequence of the shielding of the 4f orbitals, the energies of *f-f* transitions are generally insensitive to changes in the ligand field, *i.e.* the local electromagnetic field due to the surrounding chemical species. However, the overall spectral form is sensitive to changes in local symmetry, coordination geometry, and ligand polarisability, especially for Eu(III) and Yb(III).[17] The ligand is commonly referred to as either the *donor*, *antenna,* or *sensitiser*, while the emitting ion is the *acceptor*. Single photon excitation of the ligand usually occurs in the UV region, whereas the lanthanide emission is observed in the visible or near-IR (450 – 1600 nm, Figure 1.2). The wavelength difference between the photon absorbed by the antenna and the one emitted by the lanthanide is called the *pseudo-Stokes' shift* and usually spans a few hundred nm, (Figure 1.4).[10] Despite the inherent energy losses associated with pseudo-Stokes' shift, this phenomenon simplifies the detection of emitted light since the wavelength range of the emitted light is far from the optimal excitation wavelength (λ_{exc}), preventing the detection of stray excitation light.

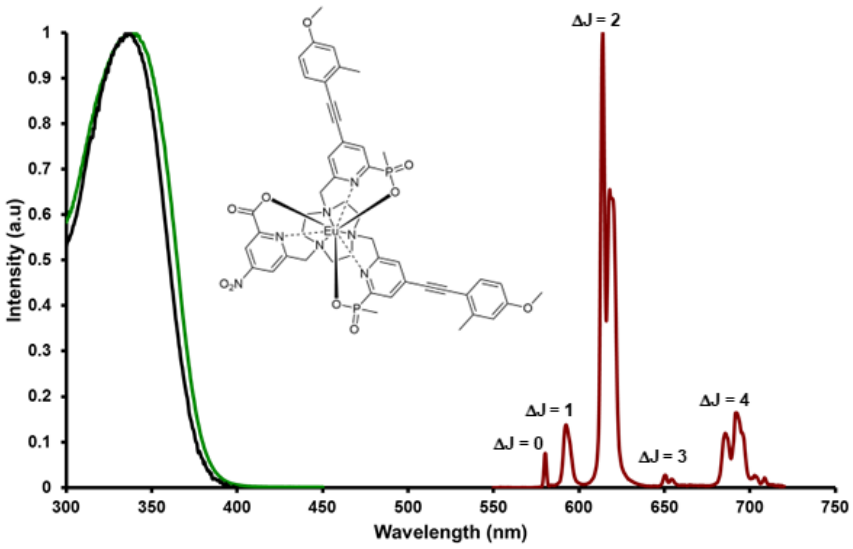

Figure 1.4. Pseudo-Stokes' shift between absorption (by the organic ligand) and emission (from the lanthanide centre) spectra of a nine-coordinate Eu(III) complex. Total angular momentum variations Δ*J* are used to label the emission manifolds. Adapted from [18].

The energy gap between the ligand donor state and the lanthanide accepting state must satisfy constraints to achieve efficient sensitisation of the lanthanide centre. These conditions are most easily seen by representing energy levels using Jabłoński diagrams, (Figure 1.5) First, the ideal antenna should have a high molar extinction coefficient at the excitation wavelength to ensure efficient energy harvesting. Second,

the energy gap between the S_1 and T_1 states of the ligand should be small to encourage ISC over competing deactivation pathways, such as antenna fluorescence and non-radiative decay of the excited state, which reduce the efficiency of the overall lanthanide sensitisation process. Third, intramolecular ET from the excited electronic state of the antenna to the acceptor excited level of the lanthanide needs to be optimised. This ET process is described using either the Förster or Dexter mechanisms.[19,20] The Dexter mechanism involves a short-range electron transfer from a donor to an acceptor; the Förster mechanism consists of a non-radiative ET mediated by a long-range dipole-dipole interaction. The latter mechanism is characterised by an r^{-6} dependence. For the ET process to happen efficiently, the T_1 state of the antenna should match closely the energy gap of the accepting excited state of the lanthanide. However, there is a trade-off: while the energy mismatch should be as small as possible not to hinder direct ET, an excessive reduction of the energy difference would favour the disadvantageous back energy transfer process (BET). For instance, the trade-off energy difference is around 9 k_BT, *i.e.* about 1800 cm^{-1} at room temperature for Eu^{3+} and Tb^{3+}.

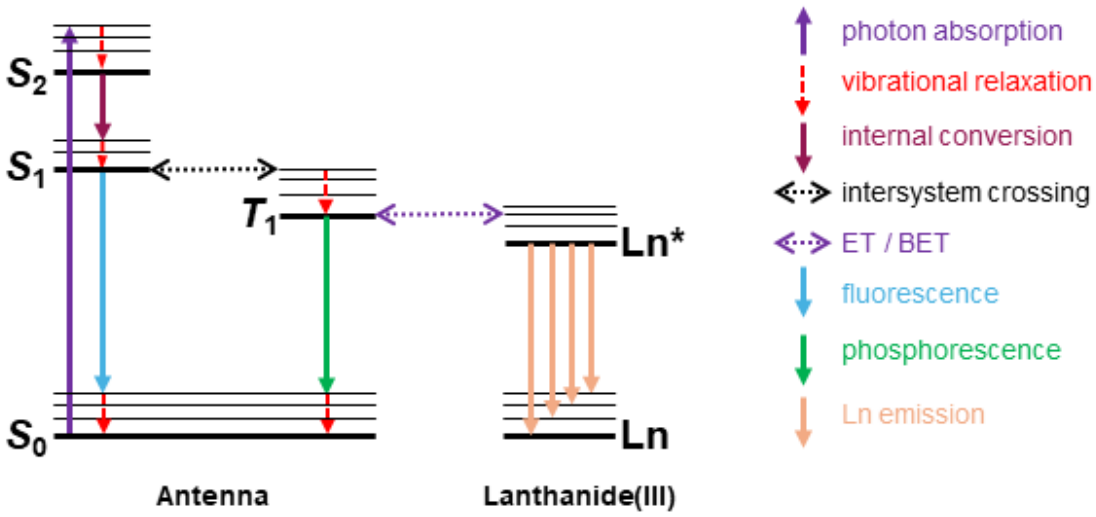

Figure 1.5. An expanded Jabłoński diagram showing the major processes involved in sensitised lanthanide emission.

An alternative sensitisation pathway involves an internal charge transfer (ICT) excited state. In this case, the excited triplet state is not required for the ET step from the ligand to the lanthanide. The precise mechanism is still unclear, and it is thought that in some cases both ICT and ET are to be considered to explain sensitisation. ICT Is typically observed in antennae consisting of spatially separated electron-rich and

electron-deficient moieties which are strongly π conjugated, (Figure 1.6).[21] The antenna is characterised by the simultaneous presence of an electron-rich terminal aryl system, functionalised with electron donating groups, and an electron poor pyridyl ring, made even more electrophilic by the proximity of the Eu(III) ion acting as a charge sink. The ground state electron density is therefore mainly localised on the peripheral aryl group, whereas the ICT excited state is localised on the pyridyl ring. From a spectrophotometric point of view, ICT manifests itself in absorption spectra as broad, intense, structureless bands, whose energy and intensity show a strong dependence on medium polarity.

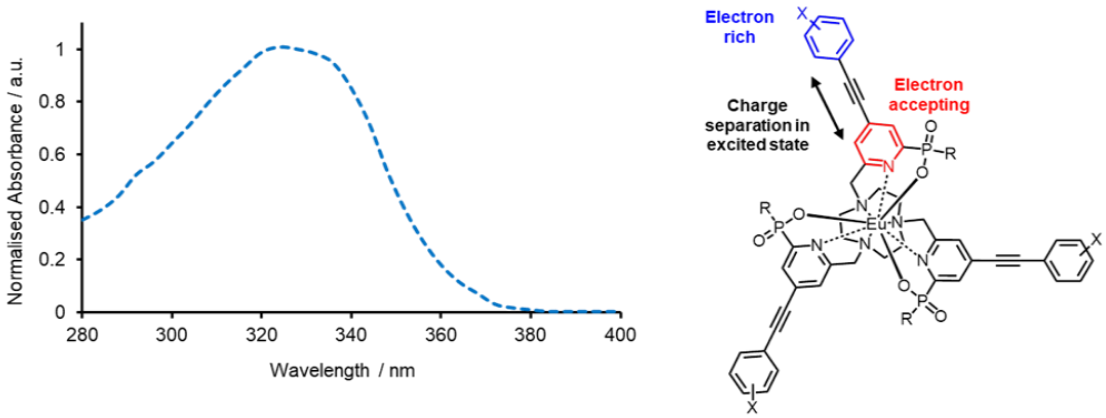

Figure 1.6. An example of a broad absorption spectrum due to an ICT transition (*left*) and a generalised Eu(III) complex structure with three pyridylalkynylaryl sensitisers (*right*), which shows ICT transitions. R = Me or Ph, X = electron donating groups. Adapted from [22].

The efficiency of the sensitisation of lanthanides is highly dependent on the nature of the ligand, especially in terms of the energy levels of the involved species. The local symmetry and strength of the ligand field around the lanthanide ion also plays a role in the overall emission profile. This sensitivity towards the chemical environment of the lanthanide can be exploited to devise highly sensitive analytical luminescent switches and probes: the interaction of the analyte with the ligand alters the geometry of the structure and its energy levels, affecting both the symmetry of the ligand field, the ET rate equations and, ultimately, the emission spectrum. The modulation of properties such as emission intensity, lanthanide paramagnetic shift, lifetimes, circularly polarised luminescence (CPL, *vide infra* - Section 1.2) in response to variation in properties such as pH and temperature or upon binding to analytes such as human serum albumin (HSA), urate, glyphosate, ADP/ATP, and Mg^{2+} has been extensively exploited by Parker *et al.* to devise lanthanide molecular sensors.[14–17]

To maximise the efficiency of the antenna effect, the lanthanide ion must be securely attached to the antenna. To achieve this, the lanthanide ion is typically bound to a chelating moiety onto which are grafted chromophore moieties. The energy levels of the antennae should be carefully chosen to match those of the lanthanide ion to sensitise and preferably match common excitation sources such as 365 nm UV LEDs or laser sources such as the Nd:YAG (Yttrium Aluminium Garnet) 355 nm 3rd harmonic. The energy levels of Tb(III) and Eu(III) ions are shown in Figure 1.7. The ground state of Tb(III) is a $^7F_6$ spectroscopic term. All spins in the six half-filled 4*f* orbitals are parallel to maximise the exchange interaction, stabilising the system.[23] According to Kasha's rule, only the lowest excited state is emissive.[1] For Tb(III), the emissive state corresponds to the excited $^5D_4$ state. The most intense emission band of Tb(III) is the $^5D_4 \rightarrow {}^7F_5$, which lies at around 544 nm, in the green region. The ground state of Eu(III) is a $^7F_0$ term and the emissive excited state is the $^5D_0$ state.

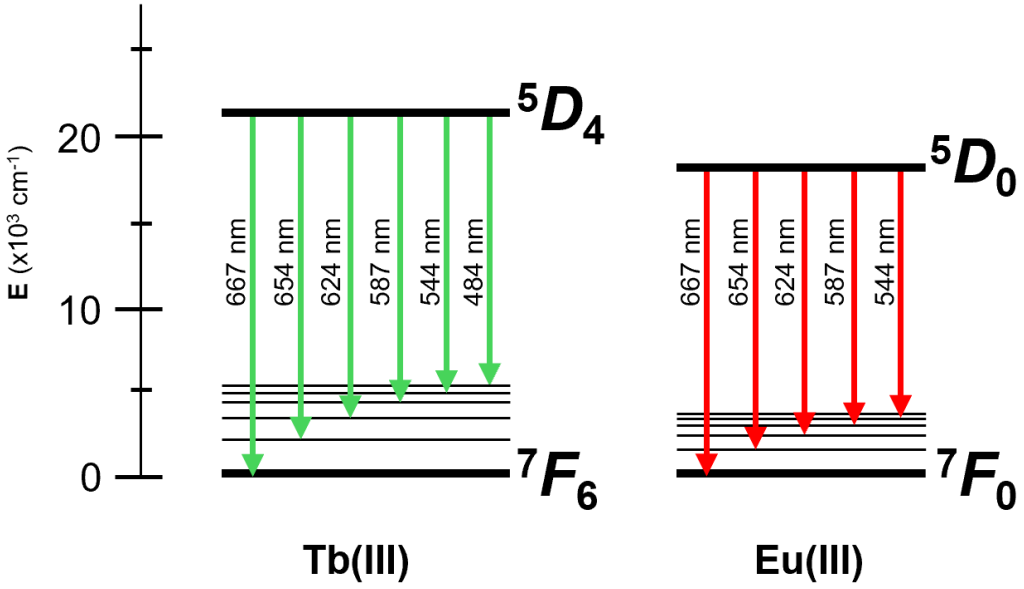

Figure 1.7. Partial Jabłoński diagram of Tb(III) (*left*) and Eu(III) (*right*) and the observed transitions in the visible from the $^5D_4$ and $^5D_0$ excited states respectively.

For Eu(III) complexes, the character of the various Δ*J* transitions varies according to their electric or magnetic dipole nature. Table 1.1 provides information about the intensity and the sensitivity to environment properties of the transitions.[24] In particular,

the brightest transition is the $^5D_0 \rightarrow {}^7F_2$, which lies at around 614 nm, in the red region, corresponding to the $\Delta J = 2$ manifold in the emission spectrum.

Selection rules predict when vanishing intensity is to be expected for an optical transition in terms of changes in the values of quantum numbers *L* and *S* and *J* describing the states that are involved. For instance, considerations about the parity of the quantum mechanical operator governing a certain transition, *e.g.* electric or magnetic dipole, quadrupole, etc., restrict the parity properties of the initial and final states that may have non-vanishing transition matrix elements. In particular, all electric dipole *f-f* transitions are formally forbidden for centrosymmetric systems by the orbital selection rule, known as Laporte rule. Selection rules hold true when these quantum numbers are exactly conserved. This is not the case for lanthanides due to the impact of spin-orbit coupling. Moreover, if the ion is in a chemical environment having a lower degree of symmetry, the Laporte rule may be relaxed by mixing between orbitals of different parity. This can be due to a mixing between the orbitals of the metal centre and the ligands, known as ligand field, or through asymmetric molecular vibrations that transiently lower the symmetry, known as vibronic coupling. In this case, transition dictated by electric interaction are called induced electric dipole transitions. Magnetic dipole transitions are normally inherently weaker than electric dipole transitions. In the case of lanthanides, induced electric dipole transitions due to a relaxation of Laporte rule are of similar intensity when compared to the inherently weak, but Laporte-allowed magnetic dipole transitions.[25] Considerations about the electric or magnetic character of transitions seen for Eu(III) ions and their intensity are reported in Table 1.1.

Table 1.1. Different $^5D_0$ to ^7F_J transitions seen for Eu(III), with wavelengths, intensities, and main character of the transition indicated. Table extracted from ref[26].

ΔJ	**Character**	**Region (nm)**	**Intensity**	**Comments**
0	ED	577-581	V. weak	Absent in high symmetry
1	MD	585-600	Strong	Environment dependent
2	ED	610-625	V. weak to v. strong	Absent if centrosymmetric
3	ED	640-655	V. weak	'Forbidden'
4	ED	680-710	Medium to strong	Environment dependent

1.1.3. Ligands for Lanthanide Sensitisation

As a consequence of the 4*f* orbitals contraction, interactions between Ln(III) ions and the surrounding ligands are dominated by electrostatic effects. The preferred coordination number of lanthanide ions in solution is eight or nine. The number of coordinated donors deeply affects properties such as radiative lifetimes, quenching, and differential responses upon binding to analytes. For this reason, the choice of the coordination number must correspond to the intended purpose of the synthetic target. Careful selection of the chemical nature of the ligands allows for fine control over thermodynamic and kinetic stability, solubility, photophysical properties, and response to environmental properties, such as solvent and/or the presence of target analytes.

In most applications, stability towards lanthanide ion dissociation is a key requirement. Chelating ligands show improved binding stability due to the chelate effect: the dissociation of the complex would involve the liberation of the chelating agent at the expense of coordinating multiple solvent molecules, effectively removing them from the bulk. This is a more ordered configuration; hence the dissociation is entropically disfavoured. Podate complexes exploit the chelate effect and strongly bind Ln(III) ions, saturating their coordination sphere and shielding them from other coordinating molecules, such as water, which may lead to non-radiative quenching of the lanthanide excitation. An example of a podate complex was reported by Raymond, (Figure 1.8), in which four 2-hydroxyisophtalamide pendant arms are bound to ethylendiamine.[27,28] This ligand efficiently sensitises Sm(III), Eu(III), Tb(III), and Dy(III) and shows CPL activity. Unfortunately, the detailed geometry of these coordination complexes remains unknown.

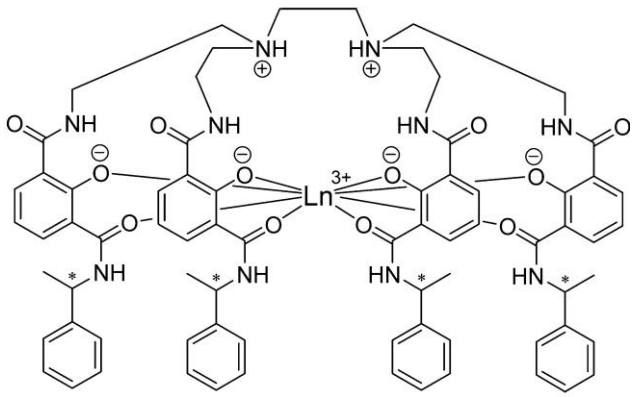

Figure 1.8. Conjectural structure for the podate lanthanide complexes reporter by Raymond, where Ln = Sm, Eu, Tb, Dy. Adapted from [28].

The macrocyclic effect makes complexes even less prone to metal dissociation: in addition to the entropic advantage due to the presence of multiple coordinating atoms, there is an additional entropically favourable contribution due to the preorganised nature of the coordinating species within the macrocycle. Moreover, the geometric constraint provided by the macrocycle limits the speciation of the complex and makes it easier to determine its structure and coordination modes. An example of a macrocyclic ligand that provides both chelating coordination and sensitisation is the *tris*-bipyridine cryptand shown in Figure 1.9. The ligand has a cage shape and provides eight donor nitrogen atoms. However, such compounds suffer from low aqueous solubility and low quantum yields due to luminescence quenching operated by solvent molecules in the first coordination shell of the lanthanide ion, (*vide infra* - Sections 1.1.3 and 1.1.6).[29]

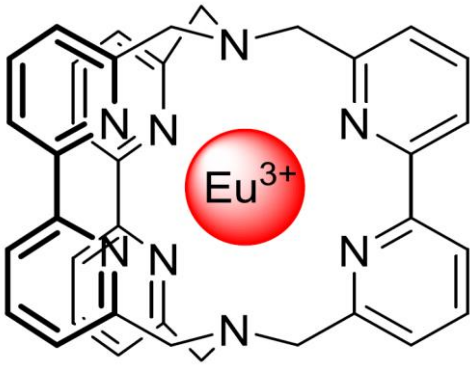

Figure 1.9. The Eu(III) complex of the *tris*-bipyridine cryptand ligand. Adapted from [29].

A complex may be chiral even in the absence of a stereogenic centre in its ligands. This is the case when propeller chirality arises from the twisted arrangement of ligands around the metal centre, (Figure 1.10). According to the helicity of the ligands, the two enantiomers of the complex are labelled *Δ* or *Λ*. More precisely, these complexes can only exist in the (*SSS*)-*Δ*(*λλλ*) and (*RRR*)-*Λ*(*δδδ*) conformers due to steric effects limiting the number of accessible combinations of conformation with the three instances of chirality within the complex. For this reason, the configuration of enantiomer will be specified by indicating the propeller chirality *Δ* or *Λ* for the sake of simplicity.

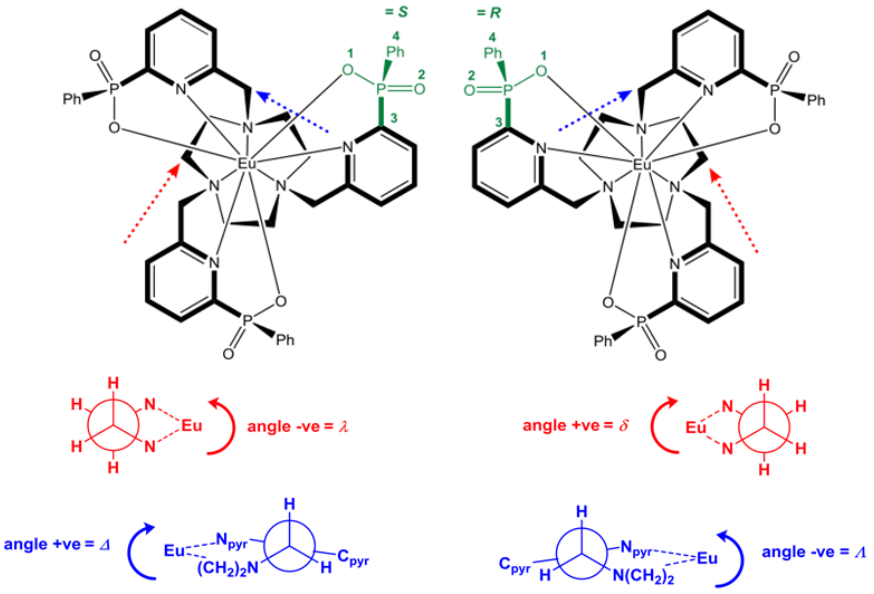

Figure 1.10. Stereochemistry of (*SSS*)-*Δ(λλλ)* (*left*) and (*RRR*)-*Λ(δδδ)* (*right*) enantiomers characteristic of TACN-based Eu(III) complexes. Stereochemistry at P (*green*) and Newman projections of the C-C bond of ring NCCN (*red*) and $NCCN_{py}$ (*blue*) chelates are shown.[30]

Such complexes are known as *dynamically racemic* complexes. Being racemic, they show no chiroptical properties such as Circular Dichroism (CD) and Circularly Polarised Luminescence (CPL). In the presence of a chiral additive, the equilibrium between the *Δ* and *Λ* enantiomers shifts in favour of the enantiomer most stabilised by diastereomeric interactions with the chiral additive. This induced chirality phenomenon is known as the *Pfeiffer effect.*[31–33]. Responsivity towards chiral species, such as amino acids[34,35] and sugars[36] make dynamically racemic complexes interesting to probe living systems[37]. It is worth noting that the Pfeiffer effect does not arise from displacement of one of the achiral ligands with the chiral additive. The chemical structure of the complex does not change: the effect originates from the interaction of the complex with the outer-sphere hydrogen bonding network of the chiral additive.[35]

β-Diketonates are bidentate ligands widely used to sensitise lanthanides. *β*-Diketonates bind lanthanide ions tightly due to their high oxophilicity. They can be used to prepare anionic eight-coordinate *tetrakis* or neutral *tris* complexes. The latter require at least a molecule of solvent or other donors, frequently bipyridines or phenanthrolines, to complete the coordination sphere. In the case of Eu(III), the distance between the ion and the donor oxygen atoms is commonly only 2.3 – 2.4 Å, favouring the ET mechanism; and the diketonate-centred $\pi \rightarrow \pi^*$ transition is strong and falls in the near UV. Functionalisation of the 1 and 3 carbon atoms allows modulation of the energy of the excited state and permits the introduction of chirality, which is essential to obtain CPL activity. The remarkable *β*-diketonate complex $Eu(TTA)_3 \cdot 2(DBSO)$ (TTA = 2-thenoyltrifluoroacetate, DBSO = dibenzylsulfoxyde) displays the highest quantum yield, (*vide infra* - Section 1.1.4), reported for a Eu(III) complex (85%) in the solid state thanks to the rigidity of the fused ring system and the presence of the fluorine atoms.[38,39] $CsEu(hfbc)_4$ shows the highest reported absolute value of the dissymmetry factor (|1.38|) for lanthanide-based small molecule emitters.[40,41] With a structure similar to $CsEu(hfbc)_4$, $Eu(facam)_3$ in dimethylsulfoxide shows a dissymmetry factor, (*vide infra* - Section 1.2.2), of |0.78| and is used as a standard for the calibration of CPL instruments, (Figure 1.11).[42]

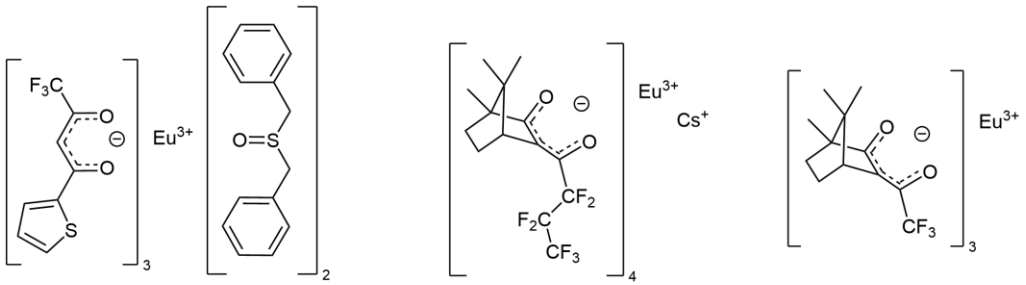

Figure 1.11. Examples of notable *β*-diketonate Eu(III) complexes: $Eu(TTA)_3.2(DBSO)$ (*left*); $CsEu(hfbc)_4$ (*centre*); $Eu(facam)_3$ (*right*). Adapted from [43].

The macrocycle effect has been extensively exploited in the literature to afford highly stable lanthanide complexes. One of the earliest examples of this, for a non-luminescence application, is the Gd(III)-DOTA (DOTA = 1,4,7,10-tetraazacyclododecanetetraacetic acid), used as contrast agent for magnetic resonance imaging (MRI) (Figure 1.12).[44] The high binding constant of $[Gd(DOTA)]^-$ ($\log K = 24.9$)[44] and its slow rate of acid-catalysed dissociation ensure the stability against dissociation required for *in vivo* applications.

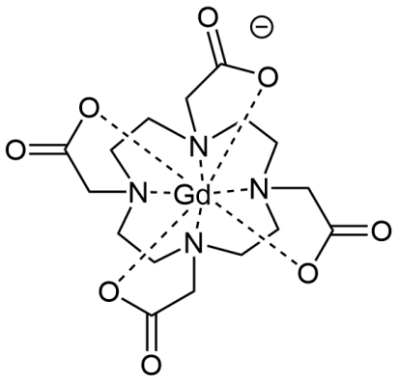

Figure 1.12. Typical structure of Gd(III)-DOTA MRI contrast agent. DOTA = 1,4,7,10-tetraazacyclododecanetetraacetic acid. Adapted from [44].

The 12-membered macrocyclic core shown in Figure 1.12 is known as cyclen (1,4,7,10-tetraazacyclododecane, 12-N_4). Its smaller analogue, TACN (1,4,7-triazacyclononane, 9-N_3), has extensively been used to coordinate lanthanide ions and plays the central role in the present work. Both cyclen and TACN do not provide enough donor atoms to complete the coordination sphere of the lanthanide. Extra donor atoms must be introduced through appropriate functionalisation of the macrocycle. Typical ligand designs include anionic donors such as carboxylates, phosphinates, and sensitising antennae endowed with donor atoms (Figure 1.13). Direct evidence of the antennae providing coordination sites to the lanthanide ion is gathered by absorbance shift upon complexation or using IR spectroscopy to monitor the frequency of aromatic ring or carbonyl vibrations. The choice of the antenna is highly dependent on the specific lanthanide ion to sensitise, as the donor antenna excited state energy should match the lanthanide acceptor excited state energy, *e.g.* $^5D_4$ for Tb(III) (20,500 cm^{-1}); $^5D_1$ and $^5D_0$ for Eu(III) (19,000 and 17,400 cm^{-1}, respectively)[45]. In the case of Eu(III), good sensitisation is provided by antennae based on phenanthroline[46] and 8-benzyloxyquinoline[47] moieties, (Figure 1.13). The favourable ET mechanism can be rationalised in terms of the triplet energy of 1,10-phenanthroline, which is reported to be ~22,100 cm^{-1}, which is ~4,500 cm^{-1} above the Eu(III) $^5D_0$ state. The triplet energy of 8-benzyloxyquinoline is found to be ~17,700 cm^{-1}, above that of the Eu(III) $^5D_0$ but below $^5D_1$.

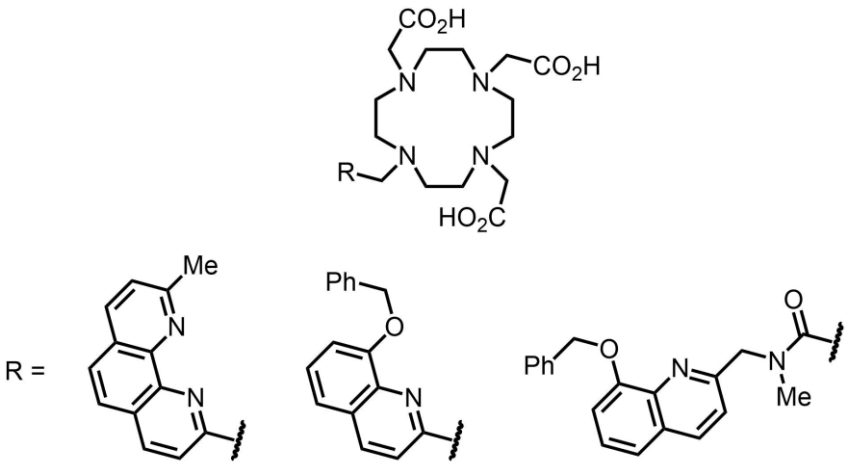

Figure 1.13. Examples of ligands used to functionalise cyclen and sensitise Eu(III): phenanthroline *(centre left)*, 8-benzyloxyquinoline (*centre and right*).

Other chromophores used in cyclen-based Eu(III) complexes include tetraazatriphenylene, acridone, and azaxanthone or azathioxanthones. Azaxanthone and azathioxanthones have been used to make *in cellulo* probes for bicarbonate and citrate.[48] Functionalised azaxanthone have triplet energies in the range ~ 21,200 – 25,400 cm^{-1}. Competitive ligand fluorescence is typically observed for azaxanthone derivatives.[49]

A recent development in cyclen-based Eu(III) molecular sensors was made by Butler *et al*. and concerns the selective recognition of adenosine monophosphate (AMP) in the presence of ADP and ATP,[50] as these species are often simultaneously present *in vivo*. Discrimination among those species poses a particular challenge due to their structural similarity and to the smaller negative charge of AMP compared to ADP and ATP, which in turn disfavours interaction with cationic binders. The goal was achieved by careful toggling of steric hindrance to exclude larger interfering anions such as ATP and with the installation of a phenylboronic acid moiety to reversibly bind the ribose ring of AMP, (Figure 1.14).

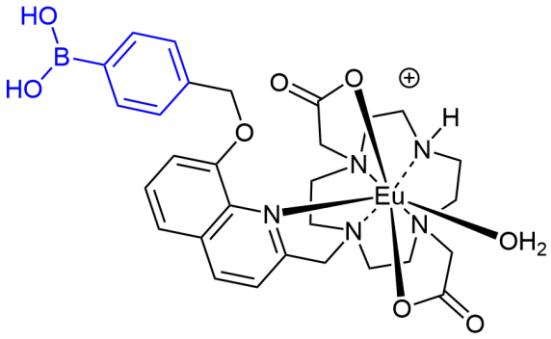

Figure 1.14. Structure of **[Eu·*p*BOH$_2$]$^+$** showing preferential binding to AMP over ATP. Image adapted from [50].

The macrocyclic ligands described so far are based on a cyclen scaffold. TACN-based ligands will be discussed below. The TACN analogue of DOTA, known as NOTA (Figure 1.15, *left*), only provides six donor atoms. However, it forms a very stable C_3 symmetric complex of Ga(III) (log K = 31) which is used in positron emission tomography.[51] Analogues of NOTA where the carboxylate donor arms have been replaced with phosphinate groups have also been made, (Figure 1.15, *centre*). Phosphinate donors have various advantages over carboxylates. Firstly, they have lower pK_a values (1.4 vs. 3.1 for the carboxylates), rendering the resulting ligand more stable to metal dissociation under acidic conditions.[51] Secondly, the pentavalency at P enables further functionalisation of the ligand, *e.g.* to introduce extra donor atoms to complete the lanthanide coordination sphere or to control properties such as solubility. Thirdly, the phosphinate moiety is bulkier than the carboxylate, contributing to better shielding of the metal ion from the solvent.[52]

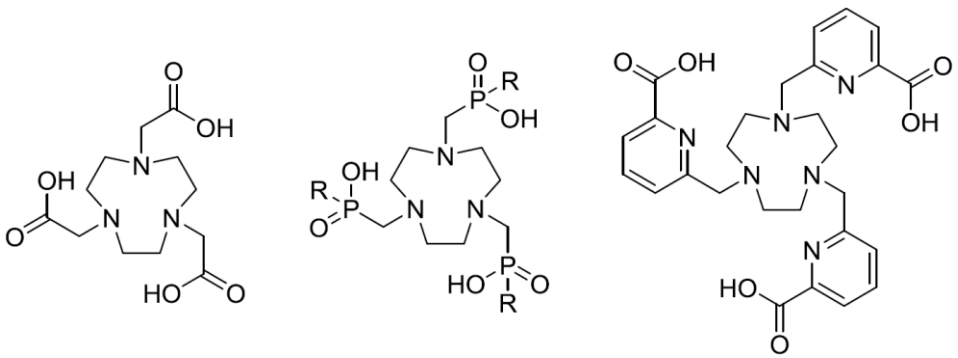

Figure 1.15. TACN-based ligand for lanthanide ions: TACN-N,N',N''-triacetic acid (NOTA) (*left*), the triphosphinic acid derivative of TACN (*centre*), and the tris-picolinic acid derivative of TACN (*right*). Adapted from [52].

The use of sensitising moieties with donor atoms, such as pyridine rings, allows the antennae to also function as coordinating moieties, (Figure 1.15, *right*). Single pyridine chromophore arms, such as the one shown in Figure 1.15, do not have the right energy gap to excite lanthanides. More conjugated systems have energy levels which are more suited for the excitation of lanthanides. Common extended chromophores include pyridylalkynylaryl and bi-aryl antennae, predominantly used to sensitise Eu(III) and Tb(III), respectively.

Early examples of the use of pyridylalkynylaryl chromophores to sensitise Eu(III) are shown in Figure 1.16. Pyridylalkynylaryl chromophores were first used in the context of lanthanide sensitisation in the early 1990s, incorporated into chelating aminopolycarboxylate ligands.[53] The excitation mechanism of pyridylalkynylaryl chromophores differs from that of all the previously discussed antennae, which exploit either $n \rightarrow \pi^*$ or $\pi \rightarrow \pi^*$ transitions to sensitise lanthanide luminescence. Pyridylalkynylaryl chromophores utilise an ICT excited state, which corresponds to higher values of the molar extinction coefficient, leading to improved overall complex brightness. The presence of an ICT excited state arises from the peculiar electronic structure of pyridylalkynylaryl chromophores: electron rich aryl groups and electron deficient pyridine groups are linked by a conjugated alkyne. This creates a large charge separation along the chromophore, resulting in a broad, intense ICT absorption band. The charge separation is increased upon binding to the Ln(III) ion: the Lewis acidic metal centre makes the pyridyl moiety more electron deficient and acts as a charge sink, stabilising the ICT state with its electron withdrawing properties. For instance, the Eu(III) complex of the ligand shown in Figure 1.16 (*right*) has a molar extinction coefficient of 48 400 $M^{-1}\,cm^{-1}$ and a luminescence quantum yield of 22% in water.[54] For comparison, rhodamine B, a widely employed organic fluorophore, has a molar extinction coefficient of 100 000 $M^{-1}\,cm^{-1.}$ Ligands used for Eu(III) usually do not sensitise Tb(III) effectively, since its excited state is too low-lying, favouring BET from the Tb(III) ion.

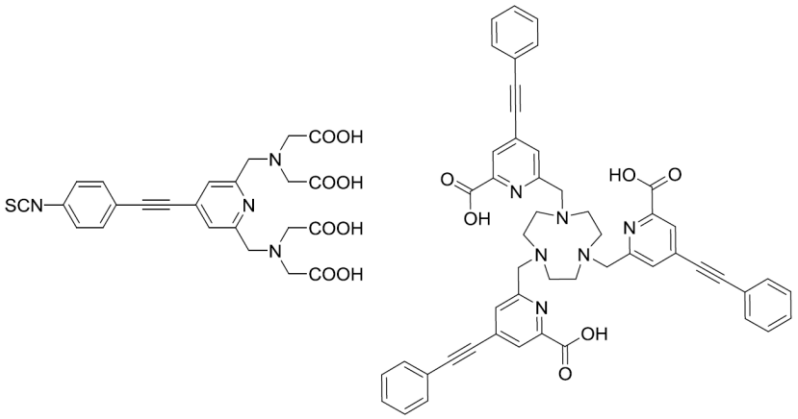

Figure 1.16. Early examples of pyridylalkynylaryl chromophores for Eu(III) sensitisation. Adapted from [53,54].

The absorption maximum of unfunctionalised pyridylalkynylaryl chromophores such as the ones shown in Figure 1.16 lies around 315 nm, which is unsuitable for biological applications where prolonged irradiation at short wavelengths damages cells. Functionalisation of the aryl group (constituting the top half of the antenna) with an electron donating group exacerbates the charge disparity along the chromophore, reducing the energy gap between the HOMO and the ICT excited state. This results in the red shifting of the absorption maximum of the chromophore. Typical functionalisation of the aryl group exploits methyl or methoxy groups, (Figure 1.17). Absorption maxima up to 355 - 360 nm can be achieved,[22,55] allowing for the excitation with a low-cost 365 nm LEDs as well as safer use for biological applications. This bathochromic shift is not accompanied by a reduction in the molar extinction coefficient, which remains consistently in the range of 45 000 – 60 000 $M^{-1}cm^{-1}$ for the trisubstituted ligand.[22]

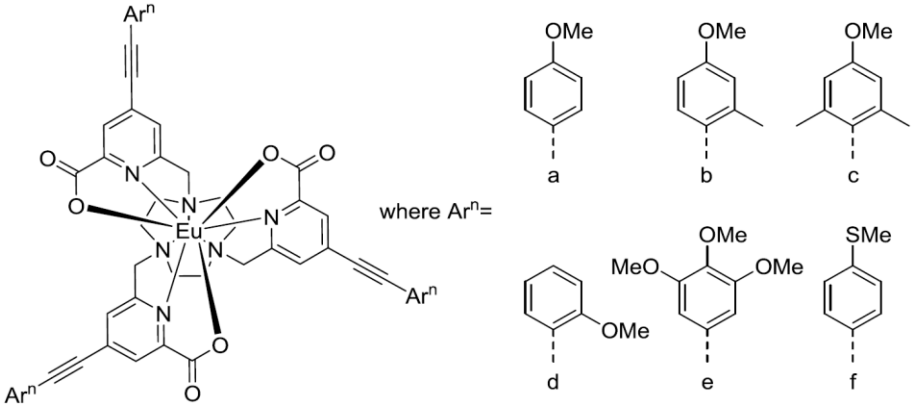

Figure 1.17. Examples of pyridylalkynylaryl-based Eu(III) complexes, containing differently functionalised aryl groups. Adapted from [22].

The geometry of analogous phosphinate complexes has been investigated by means of DFT (Density Functional Theory) computational analyses[22] and X-ray crystallography[56], revealing that the crystal structure involves a distorted tri-capped trigonal prismatic coordination polyhedron with *pseudo*-C_3 symmetry. This behaviour is paralleled in solution: complexes exhibit only one ^{31}P NMR resonance and the ^{1}H NMR spectrum is consistent with time averaged C_3 symmetry. The replacement of carboxylate donors with phosphinate groups also slightly affects the absorption wavelength, resulting in a small additional redshift,[22] which can be interpreted in terms of the geometry of the complex. The tetrahedral geometry at the P atoms produces a more constrained chelate than the carboxylate analogue. Moreover, the P-O bond is longer than C-O, which in turn makes the N_{py}-Ln bond slightly longer in the phosphinates than in the carboxylates. As a result, there is a stronger coordination in the carboxylate complex with the Lewis acidic metal centre, which acts as a charge sink, making the pyridine more electron deficient. For this reason, the chromophore has a larger charge separation leading to a slightly more red-shifted absorption band.

The ICT excited state of pyridylalkynylaryl chromophores is not sufficiently high in energy to sensitise Tb(III). For this reason, ligands that sensitise Eu(III) well are usually ineffective for Tb(III). Tb(III)-Specific sensitisers that exploit ICT transitions similarly to pyridylalkynylaryl chromophores include bi-aryl chromophores, (Figure 1.18).[45] It is interesting to note that functionalisation of the top aryl moiety results in twisting around the aryl-aryl bond and the resulting disruption of the conjugation causes a significant decrease in the molar extinction factor. Surprisingly, the overall effect of the functionalisation of the top aryl moiety is an overall increase in brightness: the substituents sterically hinder non-radiative relaxation through the rotation about the aryl-aryl bond. For this reason, the decrease in the molar extinction factor is balanced by the increase in quantum yield.

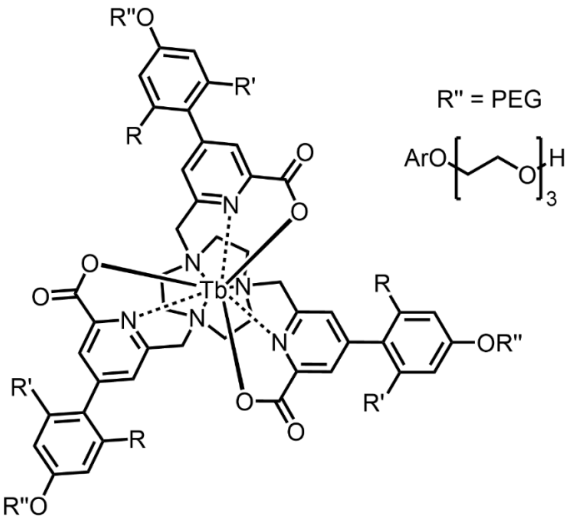

Figure 1.18. Example of a Tb(III) complex with bi-aryl antennae (PEG = polyethylene glycol). Adapted from [45].

The modulation of spectroscopic properties of lanthanide complexes upon changes in the environment or binding to analytes led to their use as analytical probes.[57] Notable examples include human serum albumin,[58] urate,[59] glyphosate,[60] ADP/ATP,[61] Mg^{2+},[62] and to devise pH probes (Figure 1.19)[55]. In the Eu(III) complex shown in Figure 1.20, protonation of a tertiary amine group grafted onto the aryl ring of pyridylalkynylaryl antennae results in a dramatic improvement in the emission intensity and lifetime.

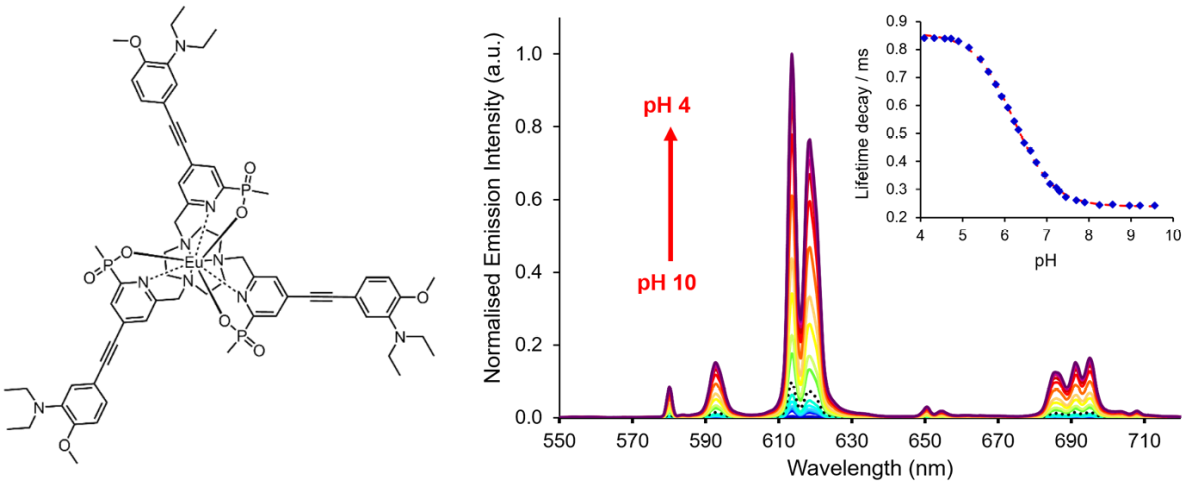

Figure 1.19. Variation of Eu(III) emission spectrum and lifetime with pH (*right*) for an Eu(III) complex (*left*). Adapted from [55].

If endowed with suitable chemical functionalities, *e.g.* carboxylate, amino, nitro, thiol, lanthanide complexes may be coupled *a posteriori* to different substrates, such as

targeting vectors or proteins (*bioconjugation*). Ideally, the presence of the extra chemical functionality used for the coupling should not disrupt the photophysical properties of the unfunctionalised complex. Moreover, the introduction of linking functionalities should not complicate the synthesis excessively: late-stage functionalisation is hence preferred, allowing for a modular, easier synthetic route.

Extra functional groups, typically alkyl chains bearing a suitable functionality at one end, may be grafted onto different positions on the ligand. The various possibilities include alkylation of the carbon atoms of the TACN scaffold, incorporation of the alkyl chain on the substituents of the aryl ring of pyridylalkynylaryl antennae, and replacement of one of the antennae with an appropriately functionalised single arm, (Figure 1.20). The first possibility involves the preparation of functionalised derivatives of the macrocycle, disadvantageously making it compulsory to insert the extra functionality already at the earliest stages of the synthetic route.[63] The second possibility offers a more versatile synthetic approach, since the appropriately functionalised extended chromophore can be prepared separately and grafted onto the TACN scaffold at a later stage of the synthetic route. However, functionalisation of the antennae may alter their finely gauged photophysical properties either by changing their electronic properties or geometrical distortion operated by the interactions with the linker itself. The third possibility presents the advantage of introducing the extra functionality at the latest stages of the synthesis, but also requires the addition of the two types of pendant arms to be carried out in two separate stages. Precise control over the number of added arms can be achieved by exploiting protective group chemistry on the TACN scaffold. The complex loses its C_3 symmetry due to the three substituents not being identical. However, using functionalised pyridyl rings as single arms, which have a structure that resembles the one of the 'bottom' components of the pyridylalkynylaryl chromophores, makes the ligand field experienced by the central Ln(III) ion *quasi*-C_3 symmetric. Indeed, inequalities in the peripheral region of the complex do not heavily affect the symmetry of the ligand field at the core of the complex. Evidence supporting this hypothesis is provided by the symmetry properties of ^{31}P and ^{1}H NMR spectra.[15] The use of a linker arm with two chromophores constitutes the main strategy throughout the present work, allowing for late-stage

insertion of the extra functionality in the complexes and minimal perturbation of their original photophysical properties.

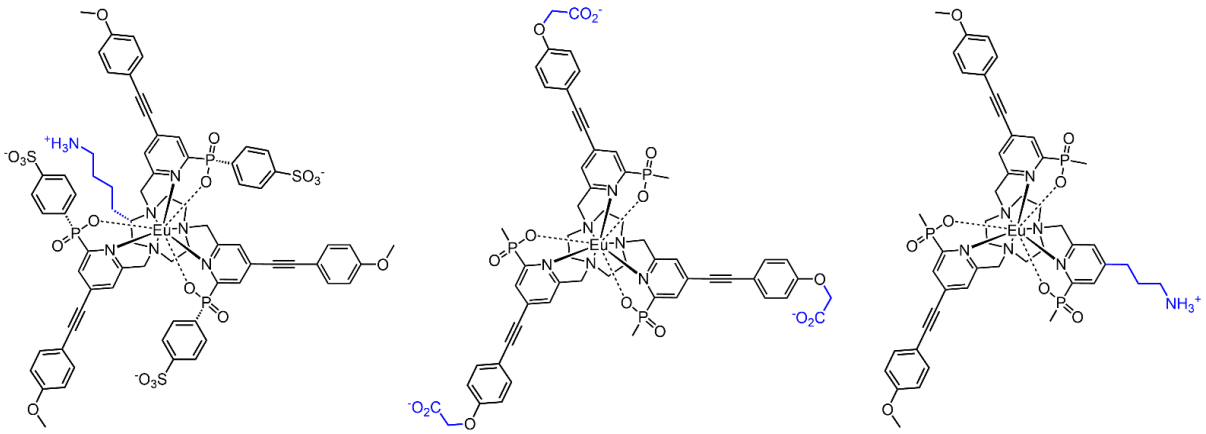

Figure 1.20. Example of possible sites for functionalisation of Eu(III) complexes (*blue*): carbon atoms of the TACN scaffold (*left*); aryl rings of pyridylalkynylaryl antennae (*centre*); single pyridyl arm (*right*). Adapted from [64].

Thoughtful choice of the specific chemical functionality used allows for facile successive conjugation of the complex. For example, the use of an alkyl chain bearing an amine functionality (Figure 1.20, *right*) allows for conjugation to thiol-bearing species via the introduction of a maleimide linker, (Figure 1.21).[15] The reaction conditions required for these steps are gentle and do not damage the complex, even when present as the enantiomerically pure species that are often prone to racemisation upon exposure to heat.[65]

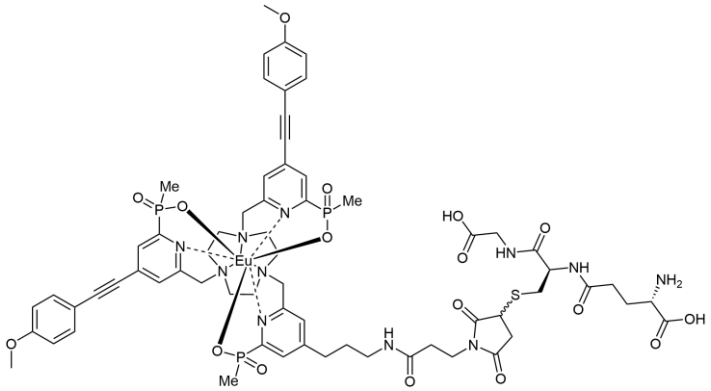

Figure 1.21. Example of a Eu(III) complex whose single pyridyl arm was used for bioconjugation to glutathione by means of a maleimide linker. Adapted from [18].

Bioconjugation of Ln(III) complexes to species such as targeting vectors and proteins opens the door to applications involving *in vivo* cell studies and selective biological

targeting. For example, Eu(III) complexes functionalised with ER-Targeting Vector AcCFFKDEL (ER = endoplasmic reticulum) showed good localisation in the endoplasmic reticulum after 23 hours of incubation in mouse embryonic fibroblast cells.[15] Localisation of the Eu(III) complexes has been verified by comparison with the ER-Tracker Green dye. Multiple Eu(III) complexes were found to be non-toxic for cells.[18,55,66] Non-toxicity, combined with the possibility of targeting specific cellular districts, fuels future studies of Eu(III) complexes as targeted biological probes.

Cell uptake studies have been trialled also using unfunctionalised complexes. Remarkably, it was observed that the two enantiomers making the racemic mixture localise in different cellular districts upon uptake. In particular, the racemic mixture of a C_3-symmetric unfunctionalised Eu(III) complex was used to incubate cells. Upon uptake, the selective mitochondrial localisation of the *Λ* enantiomer and the lysosomal localisation of the *Δ* enantiomer was observed, (Figure 1.22).[67] These observations suggest that chiral Eu(III) probes have great potential as chiral probes to investigate chiral environments, such as living organisms.

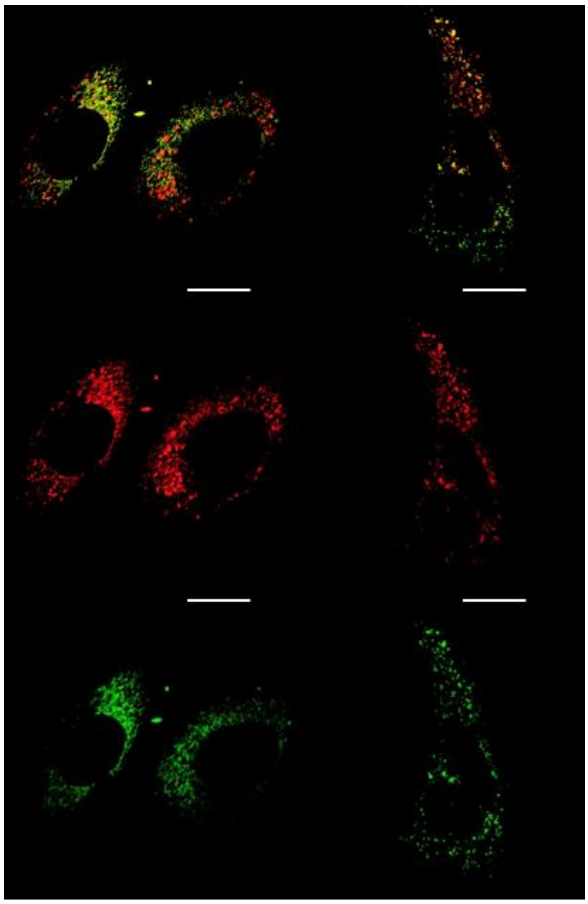

Figure 1.22. Confocal microscopy images of cells show the predominant mitochondrial and lysosomal localisation profiles respectively (red for Eu(III) emission, green for Mitotracker Green and LysoTracker Green). Scale bars in white refer to 10 µm, adapted from [66].

Prolonged UV irradiation, especially of short wavelength, damages cells. Moreover, UV light is scattered and absorbed by the cellular medium. For these reasons, it is desired to devise complexes capable of two-photon excitation, *i.e.* the simultaneous absorption of two photons of half energy, in order to circumvent the use of UV light. An example of a chelate Eu(III) complex with a significant two-photon absorption cross-section is shown in Figure 1.23.[68] The exploitation of two-photon absorption for Eu(III) complexes is part of the aims of the present work and is discussed in more detail later, (*vide infra* – Section 1.1.5).

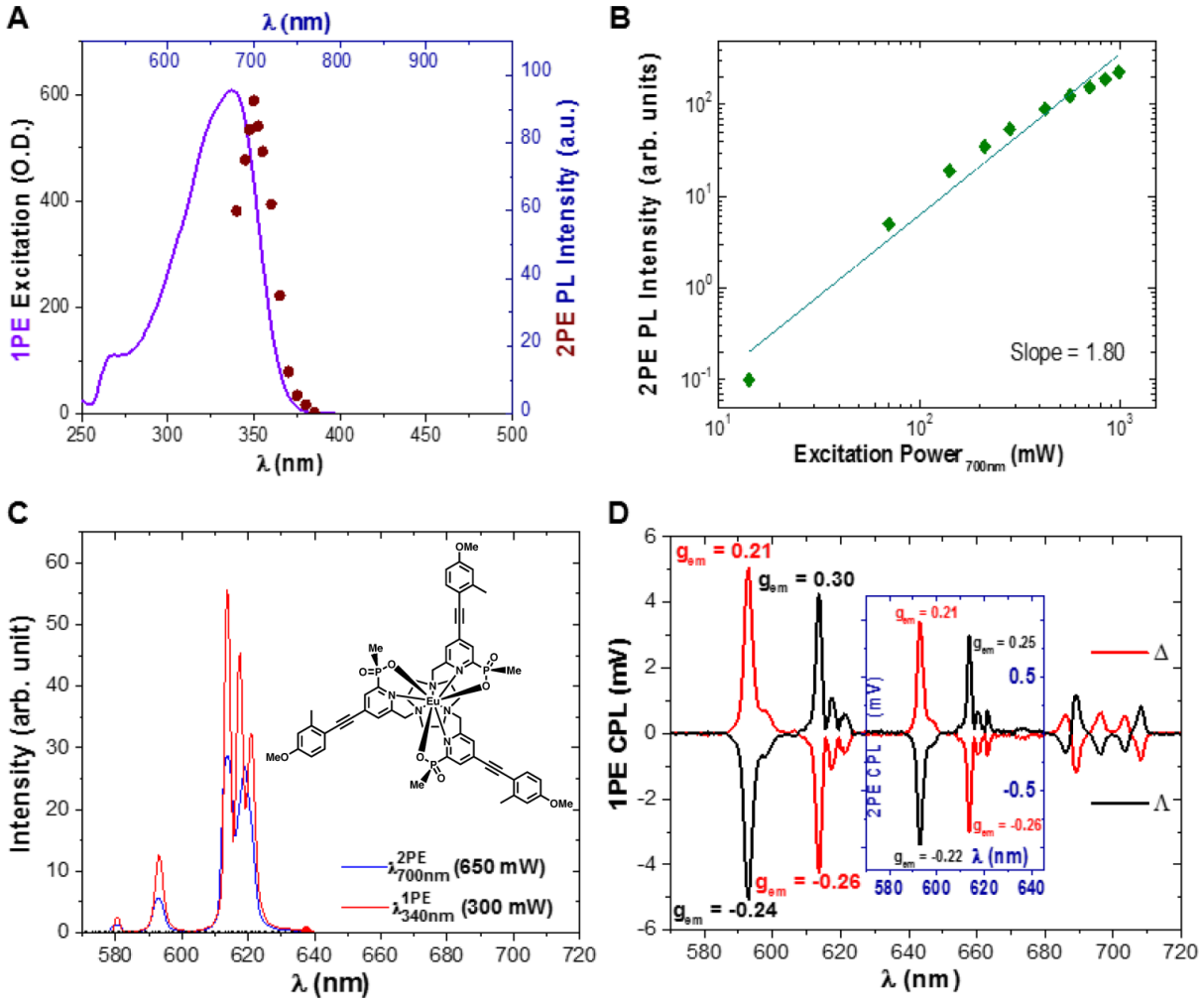

Figure 1.23. (*A*) One photon excitation (*solid purple line*) and two-photon excitation (*maroon dots*) spectra (λ_{em} = 615 nm) of a chelate Eu(III) complex. (*B*) Excitation power dependency (*green diamonds*) of the 2PE induced photo luminescence (PL) intensity. (*C*) One (λ_{ex} = 365 nm, *solid red line*) and two-photon (λ_{ex} = 720 nm, *solid blue line*) induced emission spectra of the depicted complex **[Eu.L^{10}]**. (*D*) One photon and (*insert*) two-photon CPL spectra of Λ- and Δ-Eu:**[Eu.L^{10}]** (solid black and red line respectively). Spectra recorded in MeOH and cross section found σ^2 = 73 ± 3 GM (10^{-50} cm^{4}s/photon). Adapted from [69].

1.1.4. Observables and Parameters in Luminescence Spectroscopy

The excited state of the lanthanide ion, sensitised by the antenna, is long lived (order of milliseconds in systems where deactivation pathways are suppressed) due to the forbidden nature of the *f-f* transitions involved. Neglecting other de-excitation pathways, the luminescence signal decays over time according to a first order rate equation, *i.e.* a mono-exponential decay, where I_t and I_0 are the emission intensities at times *t* and zero respectively and τ is the *lifetime* of emission.

$$I_t = I_0 e^{-\frac{t}{\tau}} \quad (1.1)$$

The lifetime can be obtained experimentally by monitoring the emission intensity at several time points after excitation. The plot of $\ln(I_t)$ as a function of time has a slope equal to $-1/\tau$. The *radiative rate constant* for the decay of the lanthanide excited state *k* is defined as the inverse of its lifetime, *i.e.* $k = 1/\tau$.

The emission of radiation is the desired outcome for the lanthanide excited state relaxation, but it is not the only possible one. Several phenomena compete with it, such as vibrational quenching and BET. The interplay between the various processes can be rationalised in terms of appropriate rate constants. Unlike lifetimes, rate constants are additive, meaning that the global rate of deactivation of a state is the sum of all the constant rates of the deactivation processes that act upon said state. The total relaxation rate (k_{tot}) can be expressed as the sum of radiative and non-radiative contributions (k_{rad} and k_{nonrad} respectively).

$$k_{tot} = k_{rad} + \sum k_{nonrad} \quad (1.2)$$

From a more general point of view, it is possible to consider all the mechanisms in which energy is transferred that take place along the process of lanthanide sensitisation, starting from ligand excitation to lanthanide relaxation. This is summarised in Figure 1.24, where an appropriate rate constant is attributed to each mechanism involved. The relative magnitude of the rate constants for a given excited state determines the population of the various intermediate states, and the overall efficiency of photon emission. To achieve optimal lanthanide luminescence, it is important to devise the system in a way such that k_{ISC}, k_{ET}, and k_{Ln^*} are maximised and, at the same time, all the other deactivation processes are inhibited. Quenching of the antenna excited singlet state may happen via electron transfer (eT) or through

collision with a quencher (Q). Molecular oxygen, having a triplet ground state, may quench the excited triplet state of the antenna. The excited lanthanide state can be quenched by several processes, such as ET to a different species, eT, or BET. Remarkably, energy is easily transferred from the lanthanide to neighbouring X-H vibrational oscillators (X = C, N, O). The N-H and O-H oscillators are most efficient at quenching the europium $^5D_0$ excited state at 17,200 cm^{-1} as it closely matches the higher vibrational levels of such oscillators.[70] For this reason, the presence of water molecules in the first coordination sphere of lanthanides reduces emission intensity and lifetime. Conversely, deuterated water does not present this issue, as the oscillators levels are spaced differently due to the higher mass of the deuterium isotope.

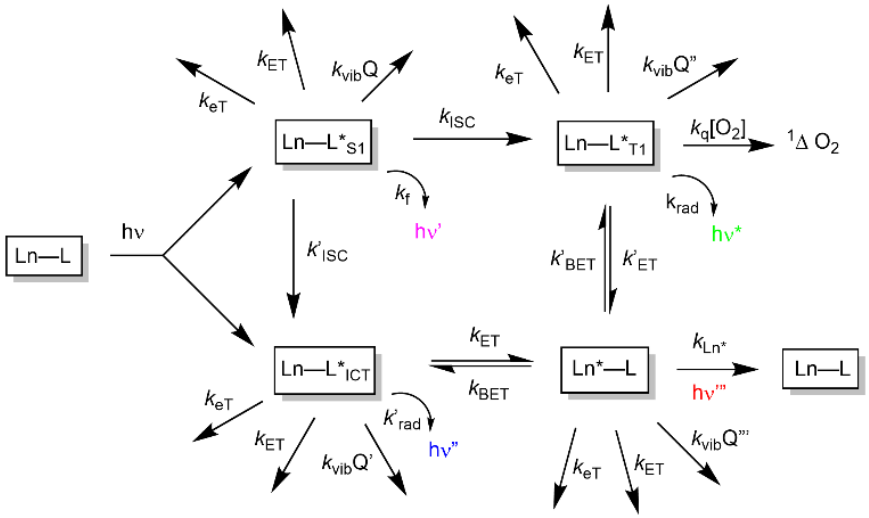

Figure 1.24. Schematic representation of the ET pathways between the various ligand and lanthanide excited states. Adapted from [17].

The overall efficiency of the system is best described by the photoluminescence *quantum yield,* ϕ. Operationally, this is defined as the ratio between the number of emitted and absorbed photons:

$$\phi = \frac{\text{number of emitted photons}}{\text{number of absorbed photons}} \qquad (1.3)$$

An intrinsic quantum yield ϕ^{Ln} can be defined for an isolated lanthanide centre as the quantum yield of the luminescence that arises from *f-f* transitions upon direct

excitation. ϕ^{Ln} Is linked to rate constants: it can be expressed as the ratio between the radiative rate constant (k_{rad}) and the total relaxation rate (k_{tot}):

$$\phi^{\mathrm{Ln}} = \frac{k_{\mathrm{rad}}}{k_{\mathrm{rad}} + \sum k_{\mathrm{nonrad}}} = \frac{\tau_{\mathrm{obs}}}{\tau_{\mathrm{rad}}} \quad (1.4)$$

In the presence of a suitable sensitising antenna, the overall quantum yield ϕ of the system is greatly improved. Defining η_{ISC} as the efficiency of the ISC process from the antenna excited singlet state to the excited triplet state and η_{ET} as the efficiency of the ET process from the antenna excited triplet state to the excited lanthanide state, ϕ can be expressed as:

$$\phi = \eta_{\mathrm{ISC}}\eta_{\mathrm{ET}}\phi^{\mathrm{Ln}} \quad (1.5)$$

Whilst the overall quantum yield ϕ represents the probability of the lanthanide centre to emit a photon once the antenna is excited, the *brightness* (*B*) of the system is defined as the product between the quantum yield and the molar extinction coefficient (ε); it accounts for the likelihood of the antenna being excited after irradiation at a given wavelength, λ.

$$B(\lambda) = \varepsilon(\lambda)\,\phi \quad (1.6)$$

1.1.5. Multiphoton Excitation

Multiphoton absorption is a non-linear optical phenomenon consisting of the simultaneous absorption of two or more photons simultaneously (within 10^{-15} – 10^{-16} s).[8] This is particularly useful to improve the signal-to-noise ratio since other fluorescent species potentially present in the system do not usually exhibit multiphoton fluorescence. Increasing the excitation wavelength moves the absorption out of the biological window, a region in which photons interact strongly with cells and tissues, causing detrimental loss of signal.

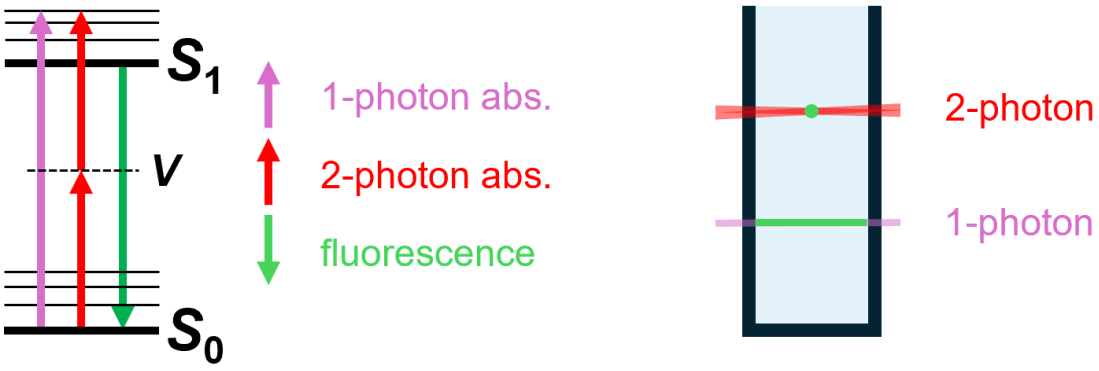

Figure 1.25. A Jabłoński diagram depicting multiphoton excitation where $h\nu_1 = 2h\nu_2$, and V is a virtual transition state (*left*). Schematisation of the effect of fluorescence arising in a cuvette from 2-photon and 1-photon excitation (1PE): excitation volume of 2-photon excitation (2PE) is a small volume (*right*).

In particular, two-photon excitation (2PE) involves two photons with energy $h\nu_2$ being absorbed to overcome the excitation energy $h\nu_1$, where $\nu_1 = 2\nu_2$, (Figure 1.25). This non-linear process proceeds through a virtual transition state *V*. The requirement for simultaneous absorption means that laser light sources are needed to produce high intensities such that two photons can be present at the site of the absorption within $10^{-15} – 10^{-16}$ s. For applications in cell imaging, detection with longer wavelength excitation also reduces the risk to healthy cells, which are damaged by higher energy UV light.

For a single-photon excitation (1PE) process, the number of photons absorbed NA_1 displays a linear dependence on excitation laser power *I*, related by an effective cross-section σ_1.[71]

$$NA_1 = \sigma_1 I \tag{1.7}$$

For 2PE, the number of photons absorbed NA_2 now displays a quadratic dependence on excitation laser power *I*, related by an effective cross-section σ_2.

$$NA_2 = \sigma_2 I^2 \tag{1.8}$$

The number of absorbed photons and the number of emitted photons are related through the quantum yield, (*vide supra* - Section 1.1.4). Hence, plotting the logarithm of the emission intensity for a luminescent compound *vs* the logarithm of laser excitation power results in a linear plot with a gradient of two, corresponding to two photons absorbed. The cross-section is usually obtained more conveniently by

comparison with a reference with a known cross-section such as rhodamine B in methanol. The cross-section of a sample S against a reference R is obtained by equation 1.9, where σ is the cross section, F is the fluorescence intensity, C is the sample concentration, and ϕ is the quantum yield.[72]

$$\sigma_s^2 = \frac{F_s}{\phi_s C_s} \times \frac{\phi_R C_R \, \sigma_{2R}^2}{F_R} \qquad (1.9)$$

The requirement for simultaneous absorption of two photons means 2PE can put very small volumes under investigation; only points where the intensity of excitation light is high enough will have enough photons present for 2PE, which has added benefits in biological applications. 2PE has further scope for development; in one example, the CPL behaviour of a Eu(III) complex was maintained upon 2PE.[69] The complex had previously been used in 1PE chiroptical imaging of chiral environments in live cells, meaning 2PE could be used in similar studies in the future for this complex.

1.1.6. Effects of Medium Polarity on Emission

The reversible change in spectral properties induced by variation of the energy difference between the ground and excited states, as a result of the local solvent, is referred to as *solvatochromism*. Ligand fields in complexes that lie close to trigonal symmetry are often very small, so they are among the most susceptible to variation in the size and sign of the ligand field splitting.[65] The optical properties of such complexes are sensitive to solvent polarity, even when the solvent is not present in the first coordination sphere. This is the case with nine-coordinate systems based on 1,4,7-triazacyclononane (TACN).

The main factors that determine the ligand field at a lanthanide centre are the symmetry and constitution of the coordination complex.[73] Additional factors include local symmetry and geometry distortions, the presence of metal and ligand solvent dipolar interactions, as well as hydrogen bonding, the polarisability of the ligand and of its donor atoms.[74] Variations in the ligand field affect the energies, intensities, and spectral form of emission. Different solvents may also affect the balance between the rate of radiative and non-radiative deactivation pathways, *e.g.* solvents containing O-H oscillators are good quenchers of Eu(III) excited states. Solvent polarity affects the

molar absorption coefficient of the ligand, as it alters its oscillator strength, but also the dissymmetry factor of CPL, changing the rotatory strength of the system.

Some C_3 symmetric Eu(III) complexes show remarkable solvent dependence: increasing solvent polarity results in a hypsochromic shift in λ_{max} of 30 nm.[65] The most intense variations are observed in the energy splitting and relative intensity ratios of the transitions within the hypersensitive $\Delta J = 2$ and $\Delta J = 4$ manifolds. For instance, the relative energies of the sublevels in the $^7F_2$ manifold increased as the solvent polarity is decreased. This variation can be rationalised by considering the Stark splitting of the $^7F_2$ manifold in water and chloroform, (Figure 1.26).[65]

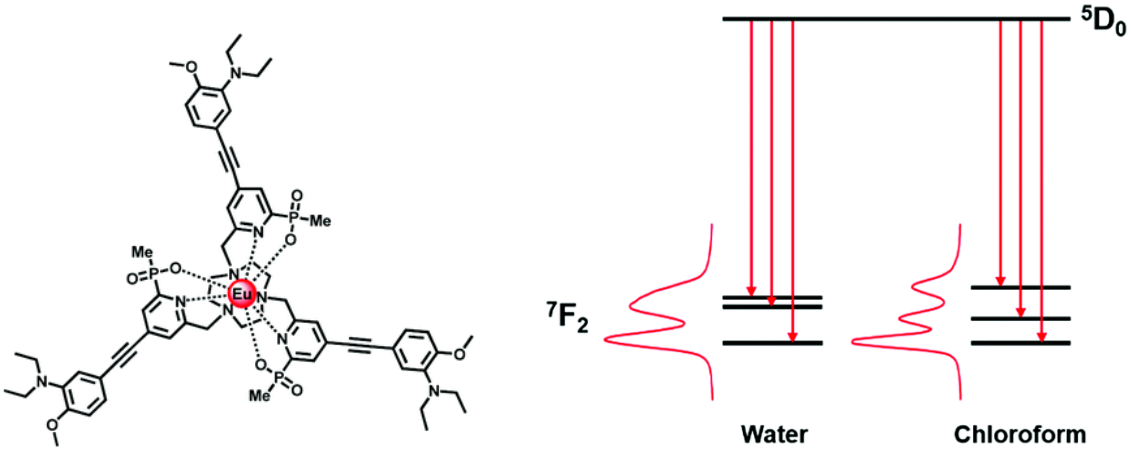

Figure 1.26. Representation of the change in the Stark splitting of the $^7F_2$ manifold in water and chloroform (*right*) for a C_3 symmetric Eu(III) complex (*left*). Adapted from [65].

Concerning total emission spectral changes, the overall integrated emission intensity ratio for the $\Delta J = 2$ vs $\Delta J = 1$ manifolds exhibits a modest increase with increasing solvent polarity, consistent with enhanced ligand polarisability in more polar media.[65] There are reasons to believe that the effect of solvent polarity could be attributed to perturbations in the donor ability and/or polarisability of the pyridyl and phosphinate groups, and not simply to effects associated with dipolar coupling involving the extended chromophore dipole.[65] For Ln(III) complexes where ICT state transitions play a major role, the energy of the ground and the excited state of the sensitising chromophore is dependent on solvent polarity. This has been exploited to devise 'switch on' lanthanide probes, as the energy increase of the ICT excited state in less polar media allows for more efficient downhill energy transfer to the lanthanide centre.[75]

These observations about the importance of solvent show that polarity of the medium in which the lanthanide-based system is embedded must be taken into serious consideration when designing applications. A similar dependence of emission on the polarity of the medium can be expected under different experimental settings, such as in solid state. Clarifying this point is one of the aims of the present work, (*vide infra* – Chapter Three).

1.2. Circularly Polarised Luminescence (CPL)

1.2.1. Theory of CPL

Circularly polarised luminescence (CPL) involves the emission of left and right circularly polarised light of differing intensity from a chiral non-racemic luminescent species. The first observation of CPL by Samojlov in 1948 was made while studying the light emission of sodium uranyl acetate single crystals. The theoretical interpretation of CPL was developed by Riehl and Richardson during the 1970's and 1980's,[42] according to which CPL should be understood as the emission counterpart of circular dichroism (CD), a phenomenon that concerns the differential absorption of left and right circularly polarised light.

The classical description of light consists of a propagating electromagnetic wave, constituted by oscillating electric and magnetic fields perpendicular to each other. The *polarisation* of the wave is defined as the direction of the electric field vector. If the electric field vector oscillates in a single plane, the light is said to be *linearly polarised.* More generally, the electric field vector can be decomposed into two perpendicular components with equal oscillation frequency on the plane perpendicular to the direction of propagation of the wave. When these two perpendicular components have identical amplitude, but a quarter wavelength phase shifted from one another, the wave is said to be *circularly polarised*. In this case, the total electric (and magnetic) electric field vector describes a helical wave about the propagation axis, (Figure 1.27). Circularly polarised light is chiral: two possible helical configurations exist, *i.e.* left- and right-handed, which are non-superimposable mirror images.

From a quantum mechanics standpoint, each photon has intrinsic helicity, which is related to its spin state. Photons are massless particles that can be in two spin states,

namely ±1, which correspond to an angular momentum value of $\pm\hbar$, describing left- and right-handed photons respectively. In this model, linearly polarised light is constituted by a superposition of equal amounts of left and right-handed photons.

Conversion between linearly and circularly polarised light is possible using a quarter-wave plate at 45° with respect to the plane of linear polarisation. Due to the birefringence of the quarter-wave plate, one of the two components of the incident linearly polarised light is retarded by a quarter of a wavelength, resulting in circularly polarised light.

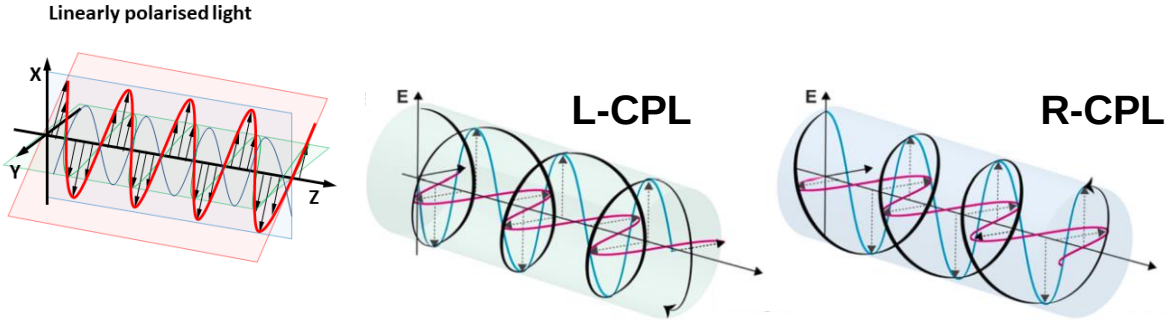

Figure 1.27. Representation of linearly polarised light (*left*), left circularly polarised light (*centre*), and right circularly polarised light (*right*).

Since circularly polarised light is chiral, CD and CPL are used to investigate chiral properties of materials. The two techniques are complementary to each other: CD spectroscopy measures the difference in absorption of circularly polarised light, hence providing information about the ground state of the absorptive species; CPL spectroscopy measures the difference in emission intensity of circularly polarised light, allowing to investigate chirality in the emissive excited states.

1.2.2. Observables and Parameters in CPL Spectroscopy

CPL Spectroscopy quantifies the differential emission of circularly polarised light from a sample after excitation with unpolarised light. To do so, the instrument measures two independent quantities: the *emission circular intensity differential*, $\Delta I(\lambda)$, and the *total luminescence intensity*, $I(\lambda)$, which are equal to the difference and sum of the intensities of left and right circularly polarised light respectively. To factor out variations in recorded intensities due to the specific instrument used, the entity of the differential

emission of circularly polarised light is quantified by a ratio called the *dissymmetry factor*, $g_{em}(\lambda)$ (also denoted as $g_{lum}(\lambda)$ in the literature), defined as:

$$\Delta I(\lambda) = I_{\mathrm{L}}(\lambda) - I_{\mathrm{R}}(\lambda) \qquad I(\lambda) = I_{\mathrm{L}}(\lambda) + I_{\mathrm{R}}(\lambda) \tag{1.10}$$

$$g_{\mathrm{em}}(\lambda) = \frac{2\Delta I(\lambda)}{I(\lambda)} \tag{1.11}$$

The minimum absolute value of g_{em}, zero, corresponds to no circular polarisation, *i.e.* $I_{\mathrm{L}}(\lambda) = I_{\mathrm{R}}(\lambda)$. The theoretical maximum value is ±2, corresponding to the emission of light which is purely left or right circularly polarised.

This experimental definition of the dissymmetry factor can be linked to the physical properties of the emitting species. For a transition $i \rightarrow j$, g_{em} can be expressed in terms of the rotational strength, R_{ij}, related to the magnitude of CPL of the transition, and the dipole strength, D_{ij}, related to the total emission intensity. These two quantities are functions of the transition electric and magnetic dipole vectors, **μ** and **m** respectively.[76]

$$R_{\mathrm{ij}} = \left|\boldsymbol{\mu}_{ij}\right| \cdot \left|\mathbf{m}_{ij}\right| cos\theta_{\boldsymbol{\mu},\mathbf{m}} \qquad D_{ij} = \left|\boldsymbol{\mu}_{ij}\right|^2 + \left|\mathbf{m}_{ij}\right|^2 \tag{1.12}$$

$$g_{\mathrm{em}}(\lambda) = \frac{4R_{\mathrm{ij}}}{D_{\mathrm{ij}}} \tag{1.13}$$

where $\theta_{\boldsymbol{\mu},\mathbf{m}}$ represents the angle between the electric and magnetic transition dipole vectors. Since the magnetic dipole transition moment is usually significantly smaller in magnitude than its electric counterpart, the expression for g_{em} simplifies to:

$$g_{\mathrm{em}}(\lambda) = 4\frac{\left|\mathbf{m}_{ij}\right|}{\left|\boldsymbol{\mu}_{ij}\right|}\cos\theta_{\boldsymbol{\mu},\mathbf{m}} \tag{1.14}$$

From this expression it follows that the most dissymmetric bands are to be sought among transitions that are magnetic dipole allowed but electric dipole forbidden. At the same time, the factors controlling CPL emission are different from those regulating total emission. Whilst the oscillator strength of a given transition is proportional to the square of the transition dipole moment, the dissymmetry factor is inversely proportional to it. For this reason, emission bands that are simultaneously highly dissymmetric and bright are rarely observed.

On average, chiral lanthanide complexes have the highest values of dissymmetry factors, (Table 1.2). In particular, enantiopure chiral Eu(III) and Tb(III) complexes have g_{em} values which fall typically in the range ±(0.1 – 0.5).[77] At the time of writing, the highest g_{em} value for a small molecule emitter (+1.38) was reported for the Δ*J* = 1 band of (+)-CsEu(hfbc)$_4$ in ethanol, thanks to the rigidity of the fused ring system and the fluorine atoms.[41]

By analogy to the definition of the fluorescence brightness, *B*, (*vide supra* – Section 1.1.4), the brightness of CPL-active systems is calculated as:[78]

$$B_{\mathrm{CPL}}(\lambda) = \varepsilon(\lambda)\,\phi\,\frac{|g_{\mathrm{em}}(\lambda)|}{2} = B(\lambda)\,\frac{|g_{\mathrm{em}}(\lambda)|}{2} \qquad (1.15)$$

This quantity expresses the total amount of circularly polarised photons emitted and allows for a direct comparison among emitting systems belonging to different classes, (Table 1.2). In the case of two-photon excitation of a CPL emitter, an analogous brightness to Circularly Polarised Brightness (CPB) can be defined as shown in eq. 1.16.[69]

$$CPB_{2\mathrm{PE}} = \sigma^2 \times \phi_{\mathrm{em}} \times \frac{g_{\mathrm{lum}}}{2} \qquad (1.16)$$

The spectral changes due to polarity, (*vide supra* – Section 1.1.6), are also seen in CPL. Whilst the magnetic transition dipole is expected to be unaffected by a change in the local solvent, the magnitude and direction of the electric transition dipole change. Since the value of g_{em} also depends on the angle $\theta_{\boldsymbol{\mu},\mathbf{m}}$, variations in the direction of the electric transition dipole moment strongly affect the dissymmetry factor, even to the point of reversing its sign. This has been observed in a C_3 symmetric Eu(III) system: the g_{em} of the Δ*J* = 2 transition decreased by more than a factor of 10 on changing from chloroform to ethanol. The same transition has the opposite sign in the case of methanol.[65] Paralleling the behaviour observed in total emission, the ratio of CPL intensity in Δ*J* = 2 and Δ*J* = 4 manifolds can also change dramatically with solvent polarity. The change in g_{lum} due to a variation in the rotatory strength is not the only factor to affect the CPL brightness, B_{CPL}: both $\varepsilon(\lambda)$ and ϕ vary due to the effect of medium polarity on the ligands and to the solvent effect on the ET rate equations that determine the overall ET efficiency respectively. It follows that accurate *a priori*

prediction of the CPL brightness is not currently approachable, due to the high number of factors affecting it, although significant progress is being made, particularly in the case of organic emitters.[31,79]

Table 1.2. Maximum representative values of g_{lum} and average B_{CPL} of the relevant transition for CPL-active systems; N.D., not determined. Adapted from [80].

CPL-active system	**Maximum representative g_{em}**	**Average B_{CPL} ($M^{-1}cm^{-1}$)**
Ln complexes	~0.1–1.4 (10^0)	Eu (ΔJ = 1): 286 Eu (ΔJ = 2): 69 Tb: 146 Yb: 4
Cr complexes	~10^{-1}	174
Chiral nanotubes from CPL-active chiral subunits	~10^{-1}	N.D.
Helicenes	~10^{-2}	5
Ketones	~10^{-2}	1.1
Helical polymers	~10^{-2}	N.D.
Cyclophanes	~10^{-2}	68
Chiral nanotubes with achiral dopants	~10^{-3}	N.D.
BODIPY derivatives	~10^{-3}	47
Self-assembled chiral nanoparticles	~10^{-3}	N.D.
Quantum dots	~10^{-3}	N.D.
Proteins	~10^{-4}	N.D.
Nanographene	~10^{-4}	N.D.
Organoboranes	~10^{-5}	N.D.

1.2.3. CPL Instrumentation

The availability of commercial CPL spectrometers is a recent development. This, combined with the high cost of such commercial apparatus (over £100,000 at the time of writing), explains the common use of custom-built CPL spectrometers for most CPL studies present in the literature. The vast majority of these custom-built CPL

spectrometers share a similar underlying set-up. The schematics of the instrument present at Durham University and used to record the spectra in the present work is represented in Figure 1.28.

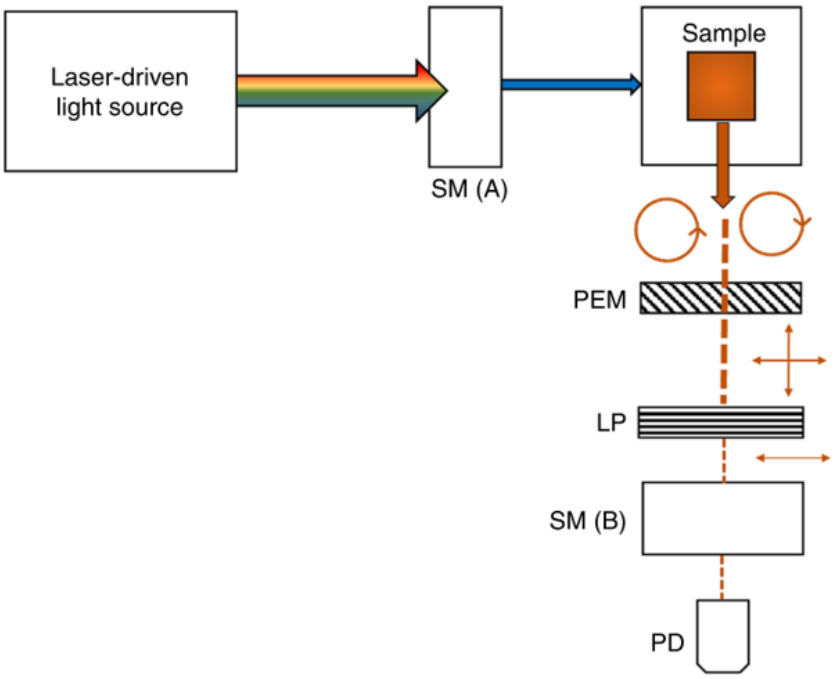

Figure 1.28. Simplified scheme of the set-up of the home-built CPL spectrometer used at Durham University. SM = scanning monochromator, PEM = photoelastic modulator, LP = linear polariser, PD = photodiode, PMT = photomultiplier tube. Circles with arrows represent circularly polarised light; vertical and horizontal arrows represent linearly polarised light. Adapted from reference [81].

Unpolarised light coming from a laser source and monochromated by a scanning monochromator (SM) is shone on the sample. This allows for the selection of light with wavelength corresponding to the absorption maximum of the luminescent sample under analysis. The emitted light is collected through a slit at an angle of 90° relative to the direction of the incoming radiation to minimise collection of any undesired scattered excitation light. The emitted light then passes through a circular analyser module which consists of a photo-elastic modulator (PEM) and a linear polariser (LP). The PEM works as an oscillating quarter-wave: periodic physical stress is applied to a clear isotropic material, such as quartz, making it anisotropic. Under operating conditions, the left and right circularly polarised components that make up the incident light beam are alternatively converted into linearly polarised light, which is subsequently selected by the LP. An emission SM is used to select the wavelength to detect using a photomultiplier tube (PMT). To measure the intensity of light that

corresponds to the left- and right-handed components of the emitted beam, detection must be synchronous with respect to the PEM oscillations. To do so, a lock-in amplifier latched on the PEM oscillation frequency is used. The instrument records the difference signal (AC) and the total signal (DC), which are then converted into the CPL and total emission signals.[82] Since lower energy photons have a lower probability of producing an electric current in the light detector, a red correction is applied when scanning higher wavelengths.

This setup (from here on referred to as PEM-CPL) presents a few drawbacks despite being predominant in the sector, one of which is the cost of constructing such instruments being still considerably high (~ £50,000 at the time of writing). Moreover, the time required to record a CPL spectrum with an adequate signal-to-noise ratio is long, *e.g.* tens of minutes for a single CPL scan and approximately 45 minutes for a typical scan protocol for a chiral lanthanide system. Such a protocol typically involves 5 accumulated scans over a 150 nm range with 0.5 nm integration steps and a 500 µs integration time per step. Such a long exposure of the sample to intense light is detrimental for species that are prone to photobleaching, hence the need for imaging instrumentation with high throughput.

Recent work by Mackenzie *et al.* led to the development of a new design for CPL spectrometers based on the parallel acquisition of two emission spectra, one for each component of circularly polarised light, (Figure 1.29).[81] This allows for the simultaneous acquisition of the whole spectrum, as well as for a substantial cost reduction (~ £12,000 at the time of writing).

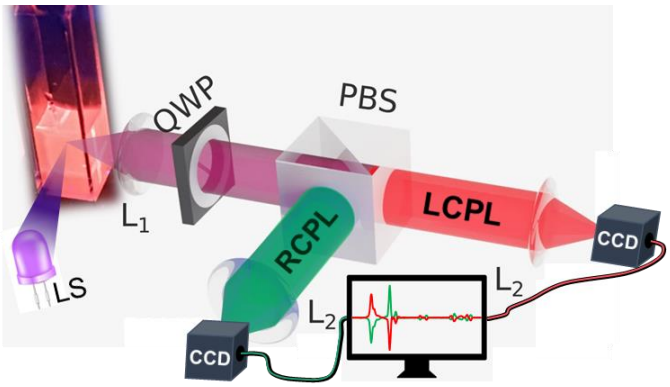

Figure 1.29. A new CPL spectrometer set-up designed at Durham University. LS = light source, L = lens, QWP = quarter wave plate, 50/50 PBS = 50/50 polarising beam splitter, SS spectrometer = solid state CCD spectrometer. Adapted from reference [81].

In this setup, the sample is excited using the light produced by a 365 nm LED and passed through a short pass filter (SPF, < 400 nm). The emitted light is again collected at an angle of 90° relative to the direction of the incoming radiation. When contrasted with the former design, the PEM is replaced with a static achromatic quarter wave plate (QWP) and a 50/50 non-polarising beam splitter (50/50 BS). The QWP converts the left- and right-handed components of the emitted light into two orthogonal linearly polarised components. The 50/50 BS splits the linearly polarised light into two physically distinct detection channels, each of which is independently capable of analysing both components of the beam through the automated rotation of LP placed immediately after the BS. A schematic representation of the functioning of the QWP and LP is shown in Figure 1.30. A long pass filter (LPF, > 450 nm) used to cut out any light coming from the LED precedes the detection module. The scanning monochromator of the traditional design is replaced with two solid state (SS) charge coupled device (CCD) spectrometers, one for each channel. Within this module, the incoming light beam is diffracted, and each wavelength is recorded at the same time on a SS CCD array. The simultaneous operation of spectrometers in both channels allows for the real-time and time-gated acquisition of CPL spectra. Since the SS CCD does not contain moving parts, the scan times drop from several minutes to 10 milliseconds. This drastic improvement opens up many applications, including real-time CPL spectra acquisition, time-dependent CPL measurements, experiments involving photosensitive emissive species, and the possibility of routinely averaging several acquisitions in a short time window to significantly improve the signal-to-noise ratio.

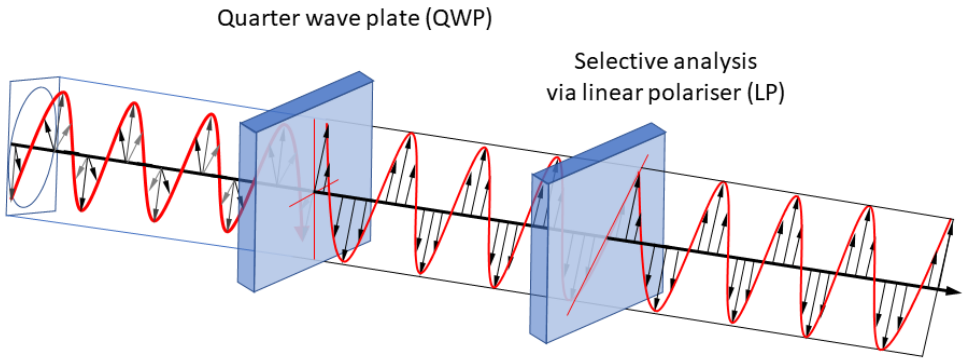

Figure 1.30. Schematic representation of the functioning of the quarter wave plate (QWP) and linear polariser (LP). The QWP converts circularly polarised light into linearly polarised light; the LP selects one of the two orthogonal linear polarisation states to selectively analyse each one alternately.

1.2.4. The Necessity for Improved Calibration Standards

The advancement in instrumentation due to the introduction of solid-state dual-channel parallel detection is a significant step forwards in the field of CPL spectroscopy. However, the potential and limitations of this new device have not been fully explored at the time of writing.[81] Instrumentation progress requires an accompanying improvement in the available CPL active emitting species used to validate and calibrate the spectrometers.

$Eu(facam)_3$ in dimethylsulfoxide shows a dissymmetry factor of |0.78| and is used as a standard for the calibration of CPL instruments, (Figure 1.31, *left*).[42] Its widespread use, first promoted in 1986 by Riehl and Richardson, can be justified in terms of its availability (the (-) enantiomer is available at ~ £110/g at the time of writing) in high purity due to its widespread use as an NMR shift reagent; it can easily be excited using lamps at 350 nm or a 466 nm laser; the magnitude of g_{em} for different transitions spans over an order of magnitude. However, the use of $Eu(facam)_3$ as a calibration standard for CPL spectroscopy has been criticised.[83] The (+) enantiomer is not as readily available. In 1999, Maupin showed that the CPL spectrum of $Eu(facam)_3$ in dimethylsulfoxide is sensitive to the presence of small amounts of water.[84]

In 2007, Muller proposed a new Eu(III) complex as a CPL calibration reference, *i.e.* $Eu(BPEPC)_3^{3+}$ in MeCN (BPEPC = *N,N′*-bis(1-phenylethyl)-2,6-pyridinedicarboxamide), (Figure 1.31, *centre*).[85,86] This chelate complex is cheaper and comes in both enantiomers; it is stable in solution over several months and under continuous UV irradiation for three days; the g_{em} values of its transitions span the 0.24 – 0.001 range, making it suitable to calibrate CPL spectrometers over a two orders of magnitude range. However, the use of $Eu(BPEPC)_3^{3+}$ as a CPL calibration standard requires the use of dangerous short wavelength excitation (290 nm, 308 nm) and high concentration solutions (~ 6.6 mM).

A more highly conjugated analogue of BPEPC was developed by Starck *et al.* in 2019, (Figure 1.31, *right*).[86] Functionalisation of BPEPC in the *para* position of the dipicolinate ring with terminal arylalkynes extends the conjugation of the antenna, allowing excitation with cheap 365 nm LEDs. The good photophysical properties of the original BPEPC chelate are preserved: the g_{em} values of its transitions span the 0.26

– 0.05 range and the complex has been reported to be stable in solution for 4 months. However, it was reported that emission in MeCN abruptly diminishes at concentrations below ~1.2×10^{-5} M due to ligand dissociation.

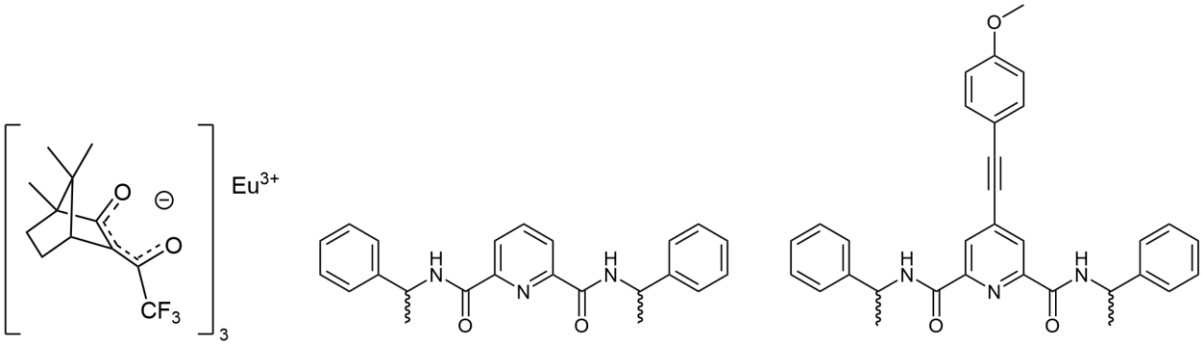

Figure 1.31. Commonly used CPL calibration standards: $Eu(facam)_3$ (*left*), BPEPC ligand (*centre*), and *para*-arylalkynyl functionalised BPEPC ligand (*right*), (BPEPC = N,N′-bis(1-phenylethyl)-2,6-pyridinedicarboxamide). Adapted from [83,86].

The ideal CPL calibration standard should be chemically stable, not prone to ligand exchange and metal ion dissociation, not racemise, and insensitive to photobleaching. Chelate complexes, such as BPEPC derivatives, suffer from these issues. Macrocyclic Eu(III) complexes, such as the ones based on the tightly binding TACN scaffold, (*vide supra* – Section 1.1.3), are much more resilient to metal ion dissociation, even at very low concentrations. Such complexes are more stable towards racemisation because of the cumulative effect of several stabilising effects, including the geometric constraints introduced by the macrocycle and steric hindrance among the extended chromophores and the functionalised phosphinate moieties. Due to these reasons, interconversion between the *Δ* and *Λ* enantiomers is highly hindered. Examples of such complexes were reported to have racemisation half-lives on the scale of hundreds of hours or greater with heating at 60 °C. The rate of interconversion was observed to be highly solvent dependent.[64,68] Further investigations on these topics were performed in the present work, (See Chapters Three and Four). These kinds of complexes overcome the limitations of state-of-the-art CPL reference standards. The design of macrocyclic Eu(III) complexes for CPL calibration is one of the aims of the present work.

1.3. Circularly Polarised Organic LEDs (CP-OLEDs)

1.3.1. Introduction to OLEDs

Organic light emitting diodes (OLEDs) are coloured light sources used in modern displays for smartphones, computers, and televisions. Unlike their older competitor liquid crystal displays (LCDs), OLEDs do not require backlighting,[87] allowing for a 'true black', higher energy efficiency, and thinner profiles.[88] OLED devices can also be prepared as flexible displays.[89]

OLED technology had a fast development, as it only traces back to 1987, when it was firstly introduced at Eastman Kodak.[90] Early prototypes suffered from several issues, most of which have been addressed in the last four decades. There are two main issues with OLEDs: short operational lifetimes compared to LCDs, due to the higher instability of organic emitters,[91] particularly in the blue;[92] large energy requirements compared to LCDs.

Light emission in OLEDs is the result of electroluminescence occurring upon radiative recombination of excitons formed within the emissive layer, (Figure 1.32). Electrons and holes pair up to form excitons. Excitons in organic semiconductors are usually Frenkel excitons, *i.e.* strong interacting small radius excitons, where the distance between the bound electron and hole is of the order of one or a few unit cells. The theoretical efficiency of fluorescent OLEDs is capped at 25% due to spin-statistics reasons: only 25% of the excitons arising from the combination of two spin ½ particles are in a singlet state, and therefore able to emit light. New phosphorescent and TADF materials[93] are able to harvest the energy of both singlet and triplet excitons[94] through different mechanisms.

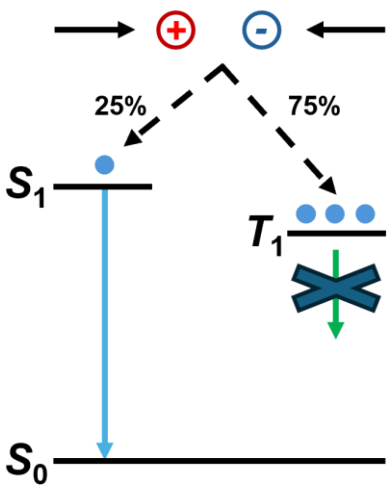

Figure 1.32. Formation of singlet and triplet excitons upon electron-hole recombination. Traditional fluorescent semiconducting materials only exploit singlet exciton energy, as light emission from the more populated triplet T_1 is spin forbidden.

1.3.2. Structure of OLEDs

OLEDs typically consist of thin multilayer assemblies of organic semiconductors, (Figure 1.33).[91] The unique structure of OLEDs plays a pivotal role in their functionality, enabling the efficient generation of light through electroluminescence.

Techniques used to deposit the various layers include vacuum deposition, sputtering, and solution processing. In vacuum deposition organic or inorganic materials are heated in a high-vacuum chamber, causing them to sublime and deposit onto the substrate in thin layers, allowing for nanometric control over the thickness of the film. Sputtering involves the use of lasers or electron beams to dislodge molecules of the material, which then deposit onto the desired substrate. Solution processing involves the use of organic solutions that are deposited on the substrate, followed by evaporation of the solvent. This methodology is compatible with flexible OLED display fabrication.[95]

The main layers in an OLED are the cathode, the anode, and the active (or emissive) layer. Electrons and holes are injected from the cathode and anode, respectively, and move towards the opposite electrode. Charge carrier recombination occurs in the emissive layer after formation of an exciton, which may decay radiatively resulting in the emission of a photon. Optionally, more layers can be inserted between the electrodes and the active layer to modulate and optimise charge carrier transport properties (transport and blocking layers). The sequence and thickness of the layers, the choice of organic materials, and the position of the recombination zone significantly influence the device's performance.

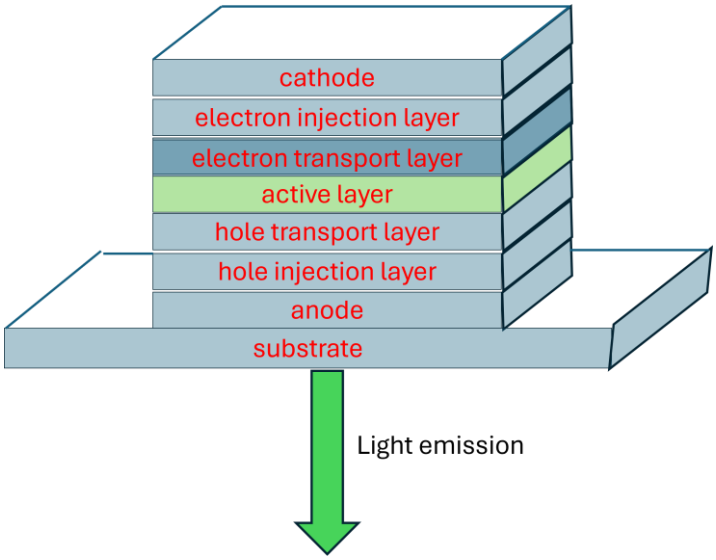

Figure 1.33. Layered structure of a common OLED. Image adapted from [91].

Charge transport in amorphous organic solid is not band-like, meaning it does not follow a linear relationship between current and voltage. Instead, it is often rationalised using Marcus' charge hopping model.[96] According to this model, charges hop between localised states within the disordered organic material, influenced by the energy landscape and the reorganisation energy associated with the charge transfer process, (Figure 1.34). Electrons and holes are injected from the cathode and anode, respectively (*I*), transported through the organic materials (*II*), and recombine in the active layer (*III*), where radiative de-excitation may occur. Charge hopping is affected by the presence of defects, impurities, and the morphology of the organic layers, ultimately shaping the electrical characteristics of the OLED.

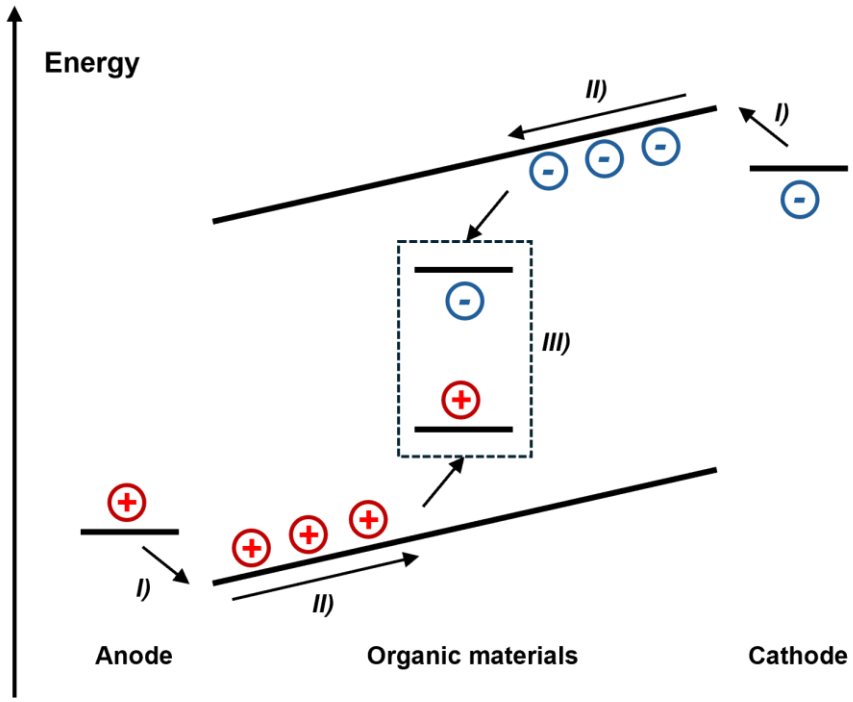

Figure 1.34. Schematic description of the steps involved in the charge hopping transport of charge carriers from electrode injection to charge recombination in the active layer. Electrons (*blue circles*) and holes (*red circles*) are injected from the cathode and anode, respectively (*I*), transported through the organic materials (*II*), and recombine in the active layer (*III*).

Due to the localised nature of the states involved in the charge hopping mechanism, the interaction between contiguous layers is usually described in terms of a plot of the work function associated with each layer. Careful matching of the energy differences between the various bands leads to optimal charge transport and efficiency properties in OLEDs. Interlayers such as charge injection and transport layers add an intermediate energy level to reduce the gap between two adjacent layers and therefore facilitate the charge injection process. Conversely, blocking layers may be added for the opposite reason of preventing leakage of charges to adjacent layers to ensure that the recombination zone be strictly contained in the active layer only.

The structure of the active layer is highly varied. The two main categories of active layers are emissive polymers or small molecules, and host-guest systems. In the case of emissive polymers or small molecules, the same chemical entity hosts the exciton and its radiative de-excitation process. In the case of host-guest systems, the exciton is formed on the host (usually a semiconductive polymer) and then energy is transferred to the luminescent guest (usually a small organic molecule or a metal complex).

1.3.3. Materials for OLEDs

Because of the strong dependency of electric properties on the energy bands of each layer, the functionality and efficiency of OLEDs crucially depend on the materials employed in their construction. A brief overview of the most used materials for different layers include:

- **Substrate**: A transparent glass or quartz substrate.
- **Anode**: Indium Tin Oxide (ITO) is commonly used as the anode material due to its high transparency and conductivity, allowing efficient hole injection into the organic layers.
- **Hole Injection Layer**: A high work-function material like PEDOT:PSS (poly(3,4-ethylenedioxythiophene) polystyrene sulfonate) improves the brightness and performance of OLEDs by a factor of up to 10 times by aiding holes to reach the active layer and by reducing damaging charge accumulation at interfaces.[97]
- **Hole Transport Layer (HTL)**: Organic materials like N,N'-diphenyl-N,N'-bis(1-naphthyl)(1,1'-biphenyl)-4,4'-diamine (NPB) are often used as HTL, facilitating the transport of holes from the anode to the emissive layer. Nitrogen-rich materials are usually selected as the hole transport properties arise from available lone pairs.
- **Active Layer**: Small molecules and polymer emitters in active layers include *tris*(2-phenylpyridine)iridium ($Ir(ppy)_3$), *tris*(8-hydroxyquinolinato)aluminum (Alq3), polyfluorenes, Poly(*N*-vinylcarbazole) (PVK), and poly(9,9-dioctylfluorene-co-benzothiadiazole) (F8BT).
- **Electron Injection/Transport Layer (ETL)**: Organic materials like 2,2',2''-(1,3,5-Benzinetriyl)-*tris*(1-phenyl-1-H-benzimidazole) (TPBi) aid the electron transport from the cathode to the emissive layer. Injecting electrons is easier than injecting holes due to their larger mobility.
- **Cathode**: Metals with a low work function such as aluminium and calcium are commonly used to inject electrons into the organic layers. They can be reflective (around 100 nm thickness) or semi-transparent (30 nm or below).

Transition metal ion complexes are commonly used as a dopant in polymeric blends that constitute the active layers in OLEDs.[98] These complexes themselves support all three processes of charge injection, charge transport, and emissive recombination. These properties arise from their excellent stability in multiple redox states.[99] The

emission bands of transition metals usually have full width at half maximum (FWHM) values of the order of 100 nm. State-of-the-art emitters in OLEDs have FWHM in the 20-40 nm range.[100] For this reason, the saturation of colours on displays built using transition metal ion complexes is not optimal. Conversely, the energy of the emission band can be tuned by careful engineering of the ligands.[99]

In the last 30 years, great attention has been paid to the development of lanthanide-based OLEDs. Lanthanides' unique optical properties (*vide infra* – 1.1.2) such as emission bands with FWHM less than 10 nm can be exploited in OLEDs to achieve high colour purity and fixed emission wavelength. Lanthanide ions unlock 100% of the theoretical efficiency in OLEDs: the energy of both singlet and triplet excitons is harvested by the lanthanide ion and can result in radiative de-excitation,(Figure 1.36).[94]

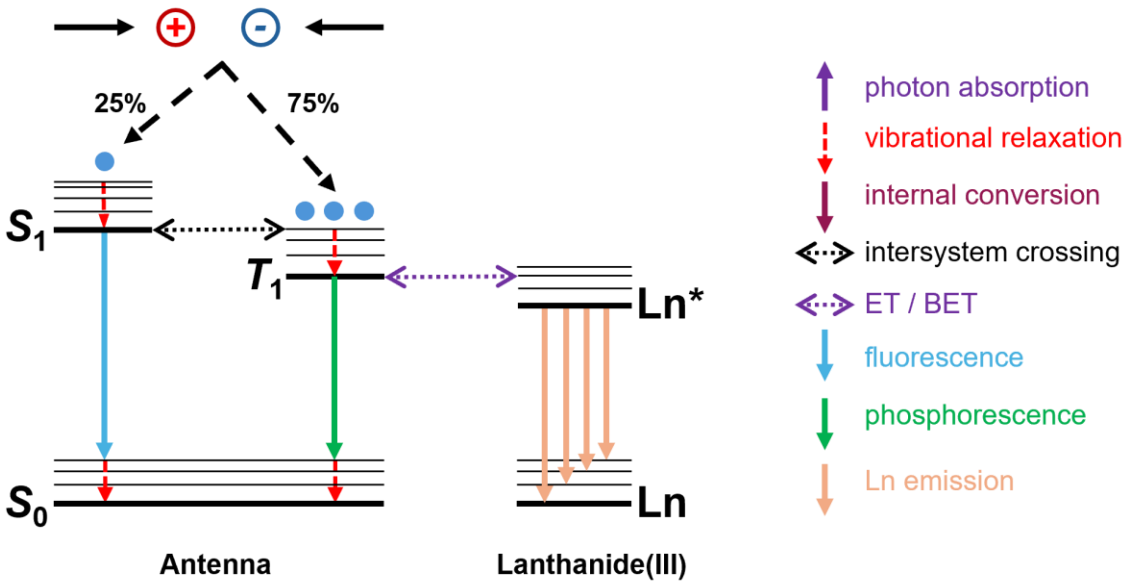

Figure 1.36. Typical Jabłoński diagram of doped emitting layer in lanthanide complex-based OLEDs. Electrical excitation populates the singlet and triplet excited states of the host. Energy is transferred from the singlet to the triplet excited states of the ligand.ISC and intramolecular ET allow for the excitation of the lanthanide ion. Adapted from [94].

Eu(III)-based OLEDs constitute an established technology for standard electroluminescent devices.[101,102] Typical examples of eight-coordinate electroluminescent Eu(III) complexes exploit *β*-diketonate ligands: the volatility of such complexes favours thermal deposition processes used to manufacture OLEDs on the industrial scale.[94] Very diverse ligands have been studied in association to lanthanides

for electroluminescence purposes, including carboxylates, terphenyls, and porphyrins as either dopant complexes or integrated into polymeric structures.

1.3.4. Circularly Polarised OLEDs

A future, ambitious technological improvement is the implementation of chiroptically active OLEDs, which would overcome some intrinsic limitations of state-of-the-art OLEDs. Circularly Polarised OLEDs (CP-OLEDs) represent a specialised category of OLEDs that emit light with circular polarisation, unlike conventional OLEDs that emit unpolarised light. This unique characteristic has sparked significant interest in both the scientific and industrial communities due to its potential applications in advanced display technologies, 3D imaging, emerging optical communication systems, and improving energy consumption of displays.

All common displays have an anti-glare filter which exploits the inversion of CP light upon reflection to absorb all incident light, (see Figure 1.37). This allows displays to be used even in broad daylight. The downside is that anti-glare filters also cut out 50% of the radiation arising from an unpolarised light emitter. Ideally, a CPL emitter would not suffer such loss, effectively doubling up the display's energy efficiency.

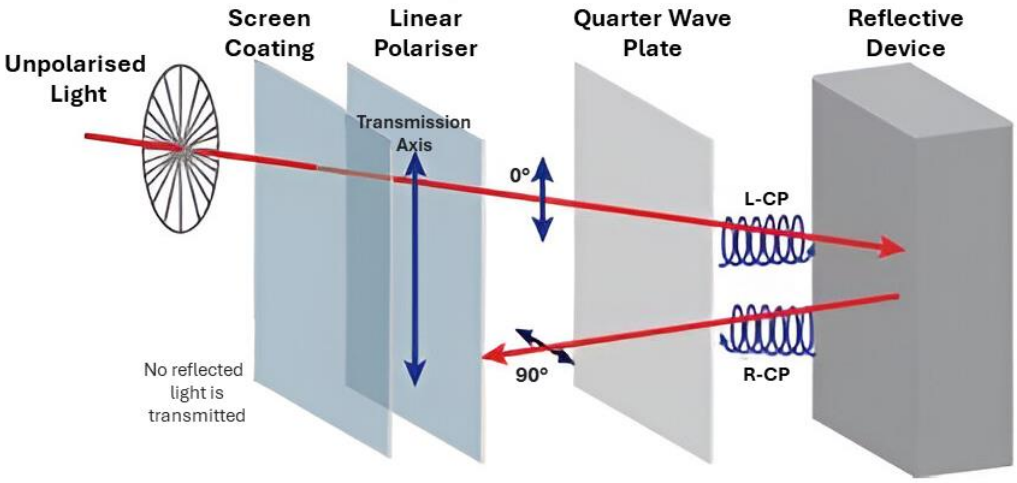

Figure 1.37. Schematic structure of an anti-glare filter.

The circular polarisation in CP-OLEDs is achieved by incorporating chiral organic molecules within the device structure. They can either be emissive chiral polymers, achiral emissive polymers with chiral additives, or achiral hosts with chiral emissive

guests. Non-racemic lanthanide complexes have high dissymmetry factors in circularly polarised luminescence (*vide infra* – Section 1.2.2). This property makes electroluminescent lanthanide complexes interesting in the pursuit of chiral OLEDs. A first step in this direction was taken by Zinna *et al.*, who employed the lanthanide salt caesium *tetrakis*(3-heptafluoro-butylryl-camphorato) Eu(III) complex ($CsEu(hfbc)_4$), displaying the highest available circularly polarised photoluminescence, as a chiral dopant in OLEDs, (see Figure 1.10).[103] Several difficulties in terms of efficiency, stability, chiral materials, and fabrication techniques need to be overcome before CP-OLEDs can find applications in the broad electronics market.

1.3.5. OLED Parameters

The key measurements used to characterise the performance and efficiency of OLEDs in the present work include:

- **Luminance (L)**: Luminance measures the intensity of light emitted by an OLED device in units of candela per square meter (cd/m^2). Typical commercial OLEDs used in computers and smartphones have a luminance of 100 – 1000 cd/m^2.
- **External Quantum Efficiency (EQE)**: EQE quantifies the number of photons emitted per injected electron-hole pair and is expressed as a percentage. A higher EQE indicates a more efficient conversion of electrical energy into light, signifying superior device efficiency.
- **Lifetime**: OLED lifetime measures the duration an OLED device can maintain a specified level of luminance before reaching a defined degradation threshold. Different lifetimes between different coloured pixels implies a loss of colour fidelity over time.
- **Electroluminescence Spectra**: The electroluminescence emission spectra of OLEDs describe the specific wavelengths of light emitted by the device. Precise control of emission spectra is crucial for achieving desired colours in displays and lighting applications, as narrow electroluminescence spectra provide high colour purity light, improving the CRI.
- ***J-V-L* Curves**: The *J-V-L* curves provide a comprehensive understanding of an OLED's behaviour concerning current density (*J*), voltage (*V*), and luminance

(*L*). These curves reveal the device's operational characteristics, highlighting their semiconduction properties and the typical diode opening profile in current density, as well as the turn-on voltage above which light is emitted.

1.4. Aims and Objectives

The present work concerns devising TACN-based Ln(III) complexes that are versatile, bright, linkable, chemically robust, and that display desirable CPL behaviour.

1) The first aim is to synthesise complexes that display same-sign CPL transitions within a single emission manifold and provide synthetic design rules for Eu(III) complexes with such properties. This is important because having a broad, intense, unique sign CPL emission manifold will greatly aid spectroscopic detection using low-cost broad band pass filters. Same-sign CPL bands do not suffer from sign cancellation effects that would lead to a smaller apparent dissymmetry factor. This will be achieved by investigating the effects of the nature of the coordinating moieties employed, which are either carboxylate or phosphinate groups. The nature of the coordinating groups is expected to affect the stability towards racemisation and spectral properties.

2) The second aim is to design TACN-based Eu(III) complexes having different substituents, to test their late-stage conjugation properties. Having a stable, bright tag that can be easily attached to different species makes these complexes interesting for applications such as CPL imaging in cell uptake studies. One of the Eu(III) complexes will bear a single pyridyl pendant arm, enabling linkage of the complex to various molecules via a *para*-nitro group to allow for facile late-stage functionalisation with a broad set of substituents in a previous study. Pursuit of a larger scale preparation via simplification of the synthetic route opens the possibility of testing novel conjugation reactions, such as thiol-bearing polymer end-group modification to obtain Eu(III)-tagged CPL emissive polymers. This is possible since conjugation reactions are mild and are expected to preserve the enantiopurity of the complex.

3) The third aim is to devise a novel Tb(III) chiral complex to be used as a green dopant for the fabrication of Circularly Polarised OLEDs. TACN-based complexes have ideal robustness and racemisation stability to perform well in electrochemical environments. State-of-the-art lanthanide-based OLEDs only feature Eu(III) complexes, due to their smaller band gap. The larger band gap of Tb(III) complexes is likely to pose a problem due to the limited choice of available commercial host materials having an adequately broad band gap.

4) The fourth aim is to clarify the effect of the nature of the solvent on racemisation kinetics and CPL spectral properties. The driving force is the idea to use Eu(III) complexes as local environment molecular probes and as dopants in polymer-based films with appropriate polarity to achieve desired spectral specifications. This is particularly relevant when envisioning applications where lanthanide-based films producing bright monosignate CPL can be used for calibration of CPL instrumentation. In particular, the effects of solvent on enhancing CPL emission will be thoroughly investigated.

5) The fifth aim is to investigate the temperature dependence of emission intensity, CPL, and lifetime of Eu(III) complexes that also display known pH responsivity. The remarkable sensitivity of such complexes to temperature makes them ideal candidates for applications as small molecule thermometers. The first proposed interpretation to account for the temperature dependence in terms of relying on the same quenching mechanism that has been used to account for pH responsivity is challenged by new experimental evidence. Mechanistic insight is sought to account for the temperature sensitivity of Eu(III) complexes that are not pH responsive.

6) The sixth aim is to exploit the superior CPL properties of lanthanide complexes, namely their high dissymmetry and brightness, as an additional extra layer of security in advanced security inks. This is largely attributed to the limitations posed by current CPL instrumentation, where high throughput detection of L-CPL and R-CPL is not available. The difficulty with lanthanide complexes is that their emission manifolds are narrow and comprise of multiple transitions that often have discordant signs in CPL spectra. Unfortunately, any high throughput instrument cannot at the same time have a resolution sufficient to differentiate between the individual opposing-sign transitions and this polarisation cancellation effect manifests as a loss of signal even for emitters with a high dissymmetry factor and brightness. Another aspect that needs to be addressed is the necessity of complexes to be stable towards racemisation at the high temperatures used in industrial lamination processes.

7) The previous aim calls for a further innovation in the field of CPL instrumentation. A novel handheld non-moving parts setup that can acquire a CPL image in a single shot, called Circularly Polarised Luminescence Photography (CPLP) will be constructed. The core idea is to adapt a commercially available polarisation sensitive camera having a built-in polariser array and lens array and coupling it with a quarter-wave plate to convert circular polarisation into linear polarisation before it reaches the camera module. The instrumental setup will be validated using the complexes presented in this work. Such a tight-bound system of instruments and emitters will be able to integrate five layers of security readout comprising of multi-coloured, multi-spectral, opposing-helicity, combined with high spatial and temporal resolution. This innovation will likely ignite new research avenues especially in the field of lanthanide chemistry and luminescent security ink development for enhanced security applications. CPLP will play a vital role in the new era of layered information photography enabling the development of physically unclonable stochastically micro-patterned CPL-active security inks.

CHAPTER TWO

Synthesis and Photophysical Study of Lanthanide Complexes

Chapter Two: Synthesis and Photophysical Study of Lanthanide Complexes

The main objectives of the work presented in this Chapter are:

1) Synthesis of a Eu(III) complex that displays mono-signate CPL transitions within a single emission manifold;
2) Design of a Eu(III) complex with linkers that enable late-stage functionalisation;
3) Synthesis of a Tb(III) complex with the potential to be used as the CPL-active green emitter to fabricate circularly polarised OLEDs;

2.1. A series of Eu(III) mixed donor complexes

The aim of the present work is to devise TACN-based Eu(III) complexes that are versatile, bright, linkable, and display desirable CPL behaviour. The ideal target should be chemically robust, display same sign CPL transitions within a single emission manifold, bear a functionalised alkyl chain to be exploited for late-stage conjugation of the complex with different species, and be suitable for cell uptake studies. Having a broad, intense, unique sign CPL emission manifold should greatly aid spectroscopic detection, as it would be possible to use low-cost broad band pass filters, allowing a large number of photons to reach the detector without opposite sign CPL bands cancelling each other out within the wavelength interval of interest. One of the aims of the present work is checking the effect of replacing one or more phosphinate donors with carboxylates on the coherence of the sign of CPL emission within one or more manifolds, (Figure 2.1).[52] However, the presence of the phosphinate donors is beneficial as it enhances the stability of the complex against enantiomer interconversion due to its stronger binding to the central lanthanide ion, and facilitates chiral HPLC resolution, (*vide supra* – Section 1.1.3). For these reasons, the synthetic targets are mixed donor complexes, *i.e.* possess carboxylate and phosphinate donor groups.

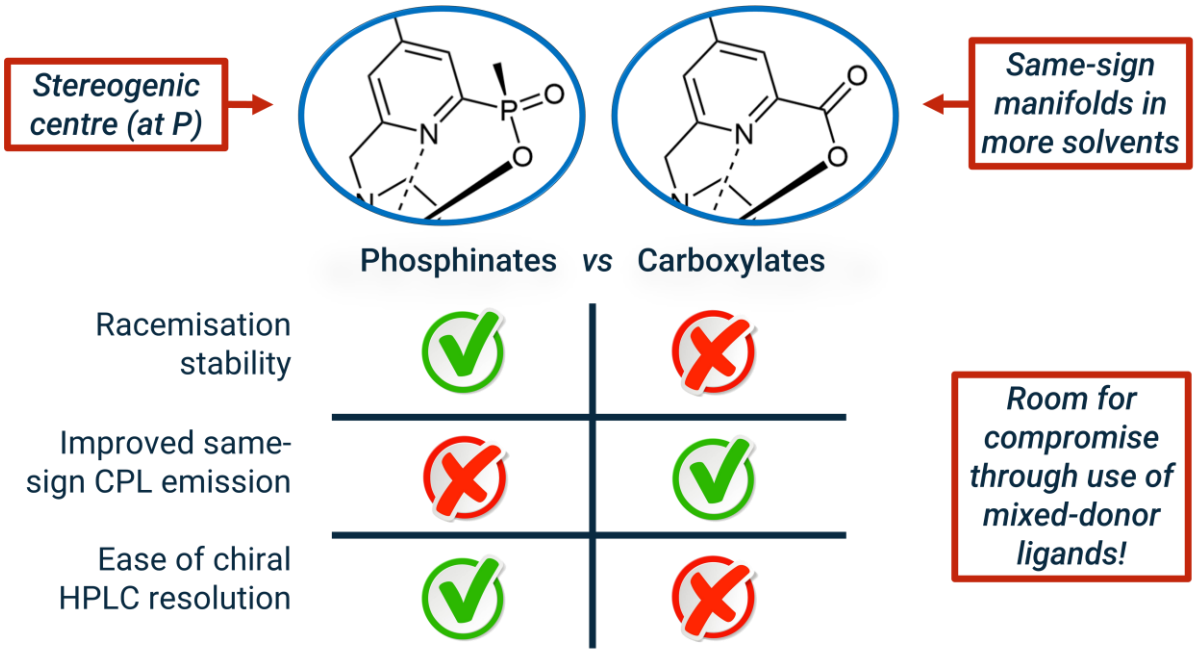

Figure 2.1. Comparison of phosphinate and carboxylate donors in Ln(III) complexes.

The synthetic target should be easily functionalised in order to use the complex as a CPL tag for imaging. The need for a functionalised alkyl chain that allows for late-stage conjugation of the complex can be fulfilled by designing a different type of pendant arm: two pyridylalkynylaryl arms provide effective sensitisation of the Eu(III) ion, whereas a single arm bears the desired functionalised alkyl chain, (Figure 2.2).

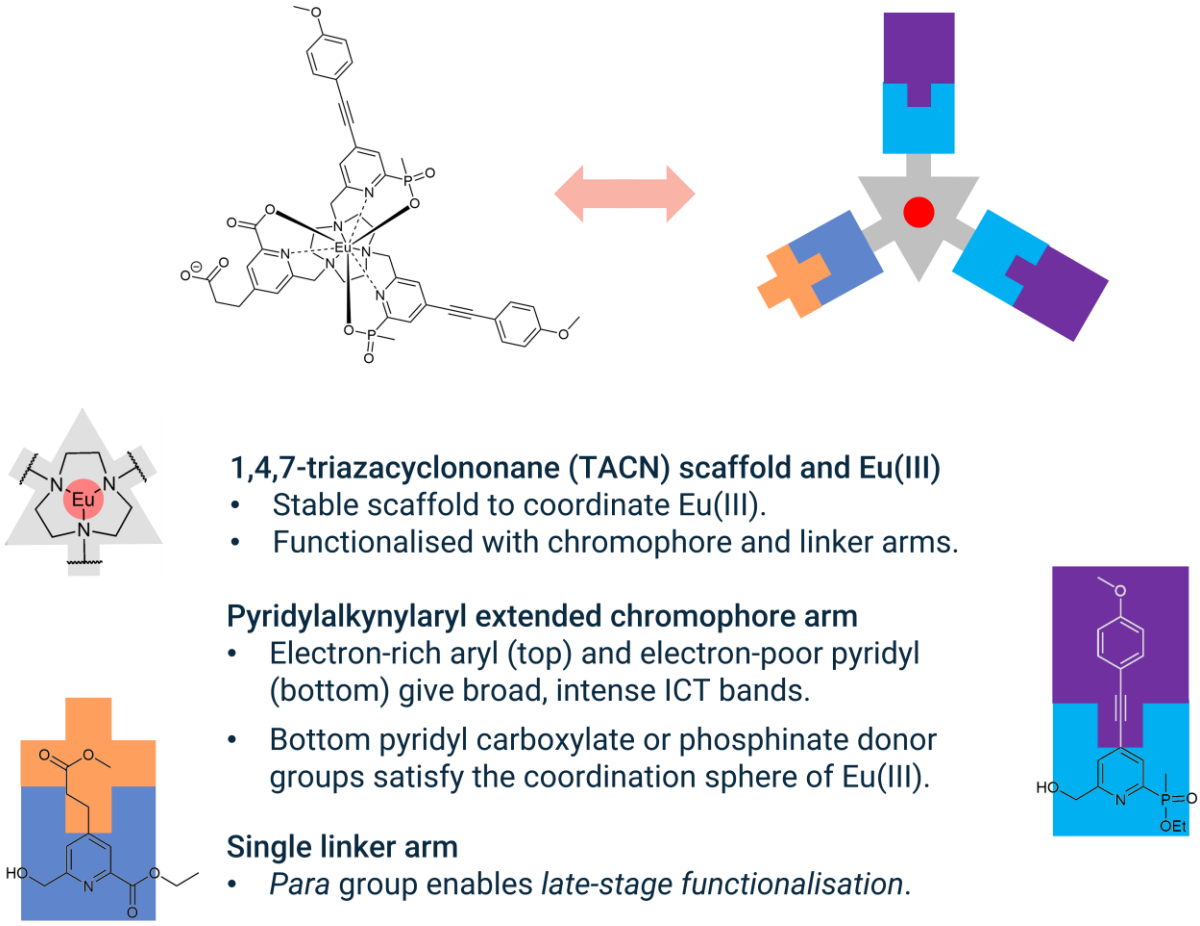

Figure 2.2. Pictorial representation of the structure of Eu(III) complexes and their components.

The single arm was chosen to be a pyridine derivative mimicking the 'bottom' component of the extended chromophore arm to afford a high degree of local symmetry about the Eu(III) centre. For the same reason, the functionalised alkyl chain should be grafted onto the peripheral end of the single arm, *i.e.* at the *para* position. The single arm will also bear the desired carboxylate donor for metal complexation, whereas the two extended arms are endowed with phosphinate donors. A selection of eight possible target complexes is shown in Figure 2.3.

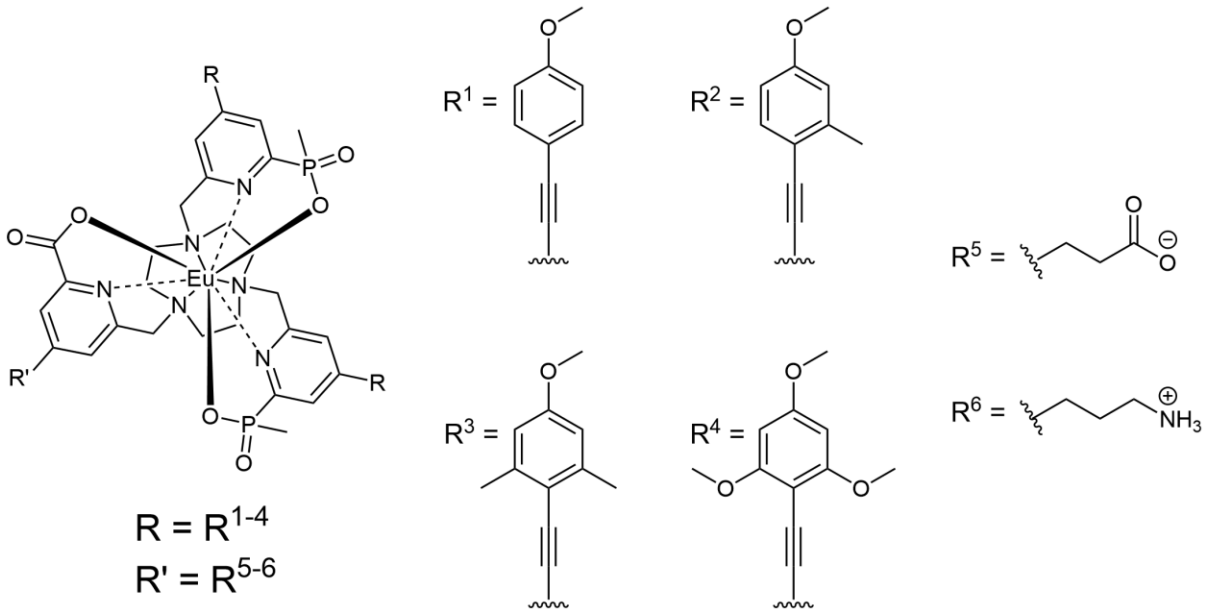

Figure 2.3. Selection of possible synthetic target complexes **[Eu.L$^{1-4}$]** and **[Eu.L$^{1'-4'}$]**.

These complexes differ in the functionalised alkyl arm, which can be either a carboxylate anion or a protonated amine, and in the functionalisation of the peripheral phenyl ring in the extended chromophore. Having chemically different single arms (amine or carboxy groups) permits the conjugation with a wide variety of chemical species, whereas the functionalisation of the extended chromophore with electron donating methyl or methoxy groups shifts the absorption maximum to more suitable longer wavelengths, (*vide supra* - Section 1.1.3).

The eight possible target complexes that can be synthesised by combining the R = R$^{1-4}$ antennae with the R' = R$^{5-6}$ are termed **[Eu.L$^{1-4}$]** for the series where R' = R^5 and R = R$^{1-4}$, and **[Eu.L$^{1'-4'}$]** for the series where R' = R^6 and R = R$^{1-4}$ to improve variety and versatility of the linking moiety for bioconjugation. The focus of this work will be to seek to prepare complexes **[Eu.L$^{1-4}$]** and to explore their photophysical behaviour. The amino series **[Eu.L$^{1'-4'}$]** is only presented as a future investigation that is not part of this work, except for the investigation of the synthesis of the amino linking pyridyl arm (*vide infra* – compound **6**) from a common precursor shared with the carboxylate linking pyridyl arm (*vide infra* - compound **4**).

2.2. Synthesis of the Complexes

The retrosynthetic analysis emphasises the similarities between the targets and how these similarities exemplify the modularity of the synthetic route. The synthetic work has been broken down into three subsections: the synthesis of the precursor arms, the preparation of ligand intermediates containing two antennae and an extra available slot for the single arm, and the addition of the single arm to the dialkylated TACN and the subsequent hydrolysis and metal complexation step to afford the desired complex.

2.1.1. Retrosynthetic Analysis

The synthesis of the complexes **[Eu.L$^{1\text{-}4}$]** was envisaged to exploit the advantages of common intermediates. For the sake of clarity, a partial retrosynthetic analysis of **[Eu.L^{1}]** is shown, (Figure 2.4). The disconnection of the ligand to appropriate synthetic precursors is shown, *i.e.* the extended chromophore precursor arm, the single precursor arm, and the commercially available macrocycle 1,4,7-triazacyclononane (TACN). The complexes **[Eu.L$^{1\text{-}4}$]** and **[Eu.L$^{1'\text{-}4'}$]** may be obtained by changing the single pyridyl precursor arm and/or the top component of the extended chromophore arm. This analysis highlights the ease of introducing synthetic variety to such complexes. The synthesis of **L^{1}** consists of the stepwise alkylation of two different kinds of pendant arm: two extended pyridylalkynylaryl chromophores and one single pyridyl arm bearing an appropriately functionalised alkyl chain. Fine control over the number of alkylated arms of each type is achieved by exploiting Boc protecting group chemistry on the TACN macrocycle.

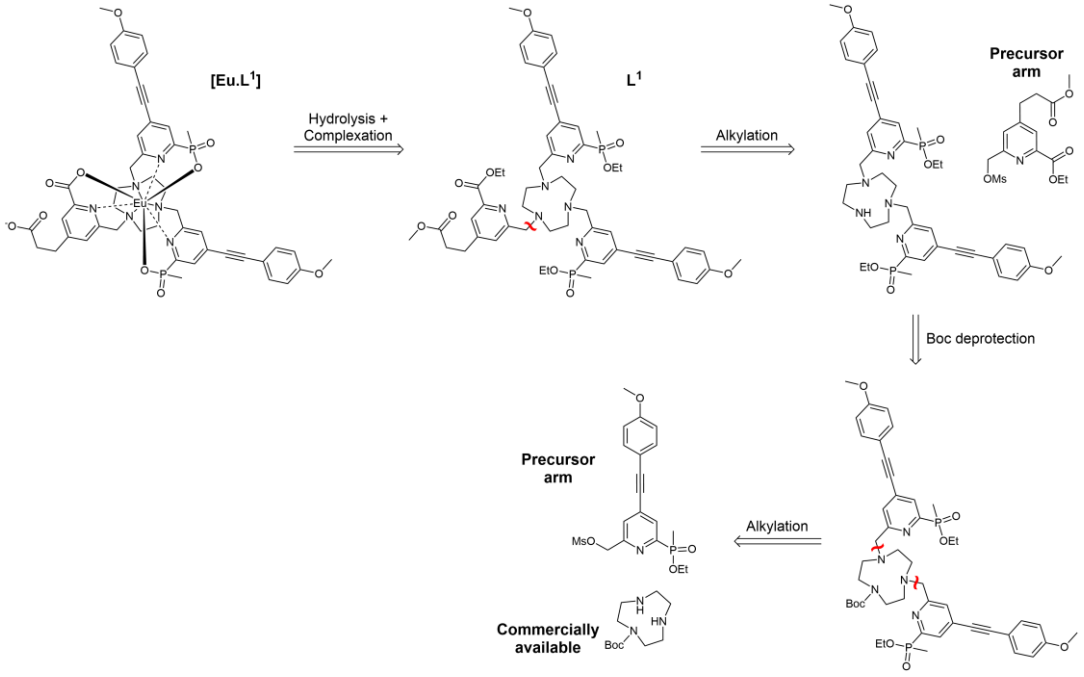

Figure 2.4. Disconnection of **[Eu.L^1]** to its precursor compounds (Boc = *tert*-butyloxycarbonyl).

Similarly, a retrosynthetic analysis was performed for the extended pyridylalkynylaryl chromophore arm, (Figure 2.5). The target antenna was disconnected into two compounds, *i.e.* the 'top' and 'bottom' components of the antenna. The synthesis of the 'bottom' component, *i.e.* the 4-bromopyridine derivative, has been reported[104] and the 'top' component can be disconnected to appropriate commercially available precursors.

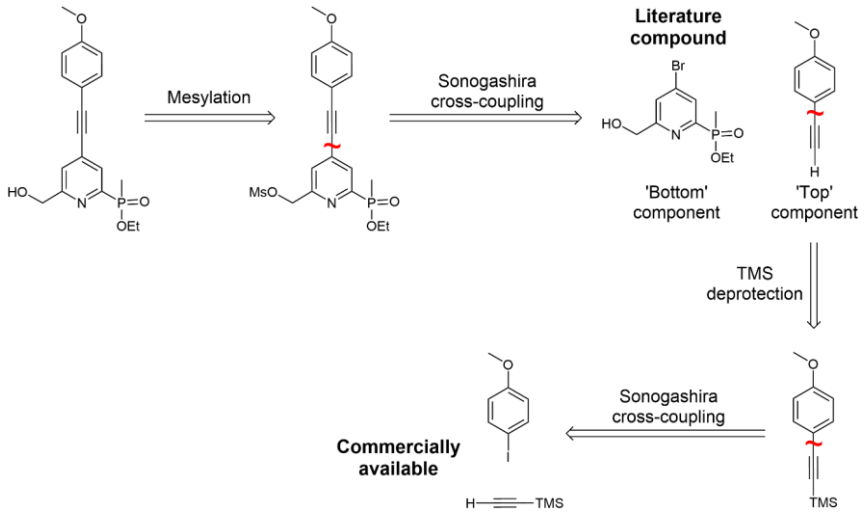

Figure 2.5. Retrosynthetic analysis of the pyridylalkynylaryl chromophore precursor (TMS = trimethylsilyl).

2.1.2. Single Arm Precursor Synthesis

The single pyridine precursor arm **2** was synthesised in two steps, (Figure 2.6).

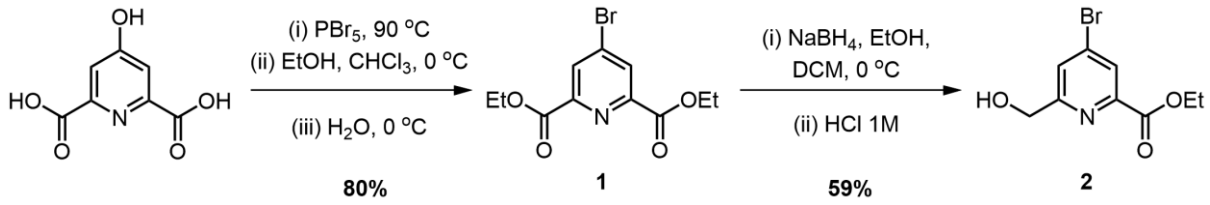

Figure 2.6. Synthesis of the common intermediate **2** through bromination, esterification, and reduction of the commercially available chelidamic acid.

Compound **1** was prepared form the commercially available chelidamic acid as previously described.[105] Bromination of chelidamic acid using PBr_5 resulted in bromination at three positions, *i.e.* the alcohol and the two carboxylic acids, with the corresponding liberation of three equivalents of gaseous HBr. Subsequent same-pot esterification of the acyl bromide groups with EtOH in chloroform at 0 °C afforded the ethyl diester. Following quenching of the reaction with cold water, the pure product was obtained by recrystallisation from hexane (80% yield).

Whilst the synthesis of the methyl ester analogue of compound, **2**, has also been reported[106], the ethyl analogue was pursued here owing to concerns about displacement of the Me group in subsequent S_N2 reactions and its lower hydrolytic stability. The synthesis of **2** was achieved analogously. The reduction of compound **1** with sodium borohydride in EtOH and DCM was performed at 0 °C. The controlled, slow reduction of the relatively unreactive ester functionalities by sodium borohydrate on compound **1** was monitored by TLC (3% MeOH in DCM) and was observed to proceed very slowly. The two carboxylic acid moieties within compound **1** are identical, eliminating the possibility of pursuing a regioselective approach and chemically distinguishing between the two groups. Hence, a method using kinetic control, exploiting the slow rate of reduction described, was envisaged to obtain the desired product, avoiding complete reduction and formation of the undesired diol. The reaction was closely monitored via TLC with the slow, gradual addition of fresh sodium borohydride to drive the reaction to completion, whilst minimising the formation of the unwanted diol. The reaction was quenched with 1 M HCl prior to the complete consumption of the starting material to prevent the unwanted reduction of the target product, and the product was purified by silica column chromatography (59% yield).

The *para*-brominated picolinate **2** can be functionalised in a Pd(0)-catalysed Heck coupling at the *para* position with a terminal alkene species. Methyl acrylate and *tert*-butyl *N*-allylcarbamate were used as the terminal alkene species to give the carboxylate and amine single arm precursor in two steps each (protected as the methyl ester and Boc derivative respectively). The Heck reaction favours the formation of the *E* stereoisomer. Analysis of the ^{1}H NMR spectra confirmed that compounds **3** and **5** were obtained as the *E* stereoisomers: the two alkene hydrogen atoms show large values of the $^{3}J_{H\text{-}H}$ coupling (~16 Hz), indicating that they are *trans* with respect to the double bond.

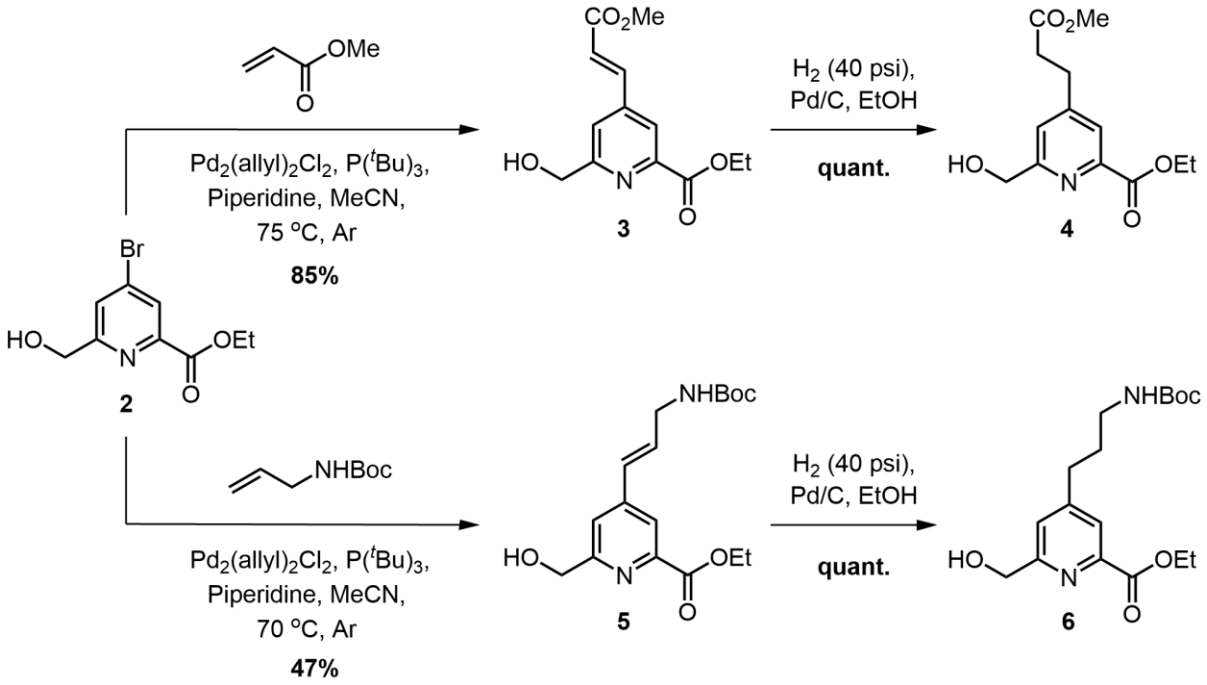

Figure 2.7. The common intermediate **2** can be functionalised in the *para* position to an appropriate terminal alkene via a Pd(0)-catalysed Heck coupling reaction, yielding compounds **3** and **5**. Hydrogenation is performed to obtain the two single arm precursors **4** and **6**, bearing an ester functionality and a Boc-protected amine, respectively.

In the synthetic route to obtain compound **4**, the methyl ester functionality was introduced using a Heck coupling reaction between **2** and methyl acrylate. The robust nature of this metal cross-coupling methodology allows for flexibility in the choice of solvent, base, and catalyst. The target compound is a common intermediate that may be used as the single arm for the synthesis of several complexes. As it is likely to be required in sizeable quantities, it is crucial to identify the optimal conditions for its

preparation. Therefore, a series of conditions was trialled, the results of which are detailed in Table 2.1.

Table 2.1. Summary of the various conditions trialled in the Heck coupling of compound **2** with methyl acrylate (not shown in the reagents for clarity).

Reagents	Conditions	Yield
$Pd(OAc)_2$, PPh_3, Et_3N, Toluene	Ar, 75 °C, 5 d[(a)]	58%[(b)]
$Pd_2(allyl)_2Cl_2$, $P(^tBu)_3$, Piperidine, MeCN	Ar, 75 °C, 18 h	68%[(c)]
$Pd(dppf)Cl_2$.DCM, Pyrrolidine, THF	Ar, 60 °C, 18 h	N.D.[(d)]

(*a*) Multiple additions of fresh reagents were required to push the reaction forward; (*b*) Starting material **2** still detected by LC/MS after stated reaction time; (*c*) Complete starting material consumption observed; (*d*) Traces of product detected after stated reaction time.

Palladium acetate is known to be a commonly used catalyst for reactions involving aryl bromides and terminal alkenes and was trialled in the first instance.[107] Monitoring of the reaction by LC/MS suggested the presence of significant starting material after a reaction time of five days. Given the lack of complete reaction, the reaction mixture was extracted using an aqueous wash before purification by reverse-phase HPLC (water/MeCN) to estimate the yield. Despite obtaining a reasonable yield of compound **3** (58%), the reaction time required for this catalyst was found to be excessively long.

Accordingly, a different palladium catalyst was examined. Given the success of the palladium(II) allyl chloride dimer, $Pd_2(allyl)_2Cl_2$, in reported Sonogashira cross-coupling reactions,[55,108] similar reaction conditions were trialled. In this instance, the palladium(II) allyl chloride dimer was found to afford the product in high yield (68%) following reaction overnight and purification via aqueous wash and reverse-phase HPLC (water/MeCN). Notably, TLC and LC/MS analysis confirmed the complete consumption of the starting material, in contrast to the palladium acetate catalysed reaction.

Concurrently, the performance of a bulkier catalyst, $Pd(dppf)Cl_2$.DCM, was investigated. After 18 hours, LCMS analysis indicated the minor formation of some product as well as the presence of conspicuous amounts of leftover starting material. Given the previous dimer catalyst was found to achieve a superior result (reaction completion in good yield) within this time frame, the reaction was abandoned, and the

yield was not determined. From these preliminary the dimer catalyst was identified as the most suitable for the Heck cross-coupling reaction to yield compound **3**.

In the synthetic route to obtain compound **5**, the Boc-protected primary amine functionality was introduced using a Heck coupling reaction between **2** and *tert*-butyl *N*-allylcarbamate. In a similar fashion to the trials performed for the synthesis of compound **3**, a series of reaction conditions was investigated, the results of which are detailed in Table 2.2.

Palladium acetate was trialled in two different solvents, *i.e.* MeCN and toluene. In the first case, the reaction did not proceed to completion and required the further addition of reagents to yield the desired product in moderate yield (42%). After 48 hours, LC/MS suggests the absence of starting material. Notably, the reaction mixture turned black immediately even before the addition of the base. This observation may be attributed to the coordinating capability of the MeCN solvent. For this reason, the reaction was tested under the same conditions, replacing MeCN with non-coordinating toluene. In this case, the reaction mixture did not turn black and proceeded to completion in 18 hours, giving an amber-coloured crude product. LC/MS indicates the presence of unreacted starting material. Purification of the amber-coloured crude product by reverse-phase HPLC (water/MeCN) following an aqueous wash afforded the pure product (47%).

Allylpalladium(II) chloride dimer proved to be the best catalyst for the synthesis of the methyl ester analogue compound **3**. For this reason, the same reaction conditions were tested for the synthesis of compound **5**. After 18 hours, LC/MS suggests that the reaction is complete. The amber crude product was purified via aqueous wash and reverse-phase HPLC (water/MeCN) to give the pure product (47%).

The use of palladium acetate in toluene and allylpalladium(II) chloride dimer in MeCN were equivalent in terms of yield. However, the purification of the latter reaction mixture by reverse-phase HPLC proved easier due to the lack of formation of other undesired absorbent species, evidenced by a cleaner chromatogram. Moreover, compound **2** is completely used in the reaction carried out using allylpalladium(II) chloride dimer as the catalyst. Overall, the Heck reaction to synthesise compound **5** is not as straightforward as the one to make compound **2**. Not only was the yield considerably lower, but the presence of starting material in the reaction mixture was

confirmed via LC/MS. The lack of complete reaction here may be attributed to a difference in reactivity of the substrates. The greater reactivity of methyl acrylate with respect to *tert*-butyl *N*-allylcarbamate is due to the presence of the electron withdrawing carbonyl group conjugated to the alkene.

Table 2.2. Summary of the various conditions trialled in the Heck coupling of compound **5** with *tert*-butyl *N*-allylcarbamate (not shown in the reagents for clarity).

Reagents	Conditions	Yield
$Pd(OAc)_2$, PPh_3, Et_3N, MeCN	Ar, 50 °C, 2 d[(a)]	42%[(c)]
$Pd(OAc)_2$, PPh_3, Et_3N, Toluene	Ar, 75 °C, 18 h	47%[(b)]
$Pd_2(allyl)_2Cl_2$, $P(^tBu)_3$, Piperidine, MeCN	Ar, 70 °C, 18 h	47%[(c)]

(*a*) Further additions of fresh reagents required to push the reaction forward; (*b*) Starting material **2** still detected by LC/MS; (*c*) Complete starting material consumption observed.

The alkene functionality in compounds **3** and **5** was converted to the alkane via palladium-catalysed hydrogenation. The reaction was performed using a Parr hydrogenator set-up at 40 psi H_2 in EtOH and quantitative conversion to compounds **4** and **6** was achieved, respectively. The primary alcohol functionality in these compounds will be converted to the mesylate immediately prior to use in the following steps to facilitate S_N2 alkylation.

2.1.3. Extended Chromophore Precursor Synthesis

The synthesis of the single phosphinate pyridine precursor arm, *i.e.* ethyl (6-(hydroxymethyl)-4-(bromopyridin-2-yl)(methyl)phosphinate, **11**, corresponding to the 'bottom' component of pyridylalkynylaryl antennae, was previously described in the literature, (Figure 2.8).[104] The compound was prepared in five steps from 2-bromo-6-methyl-4-nitropyridine with only minor deviations to the reported procedure.

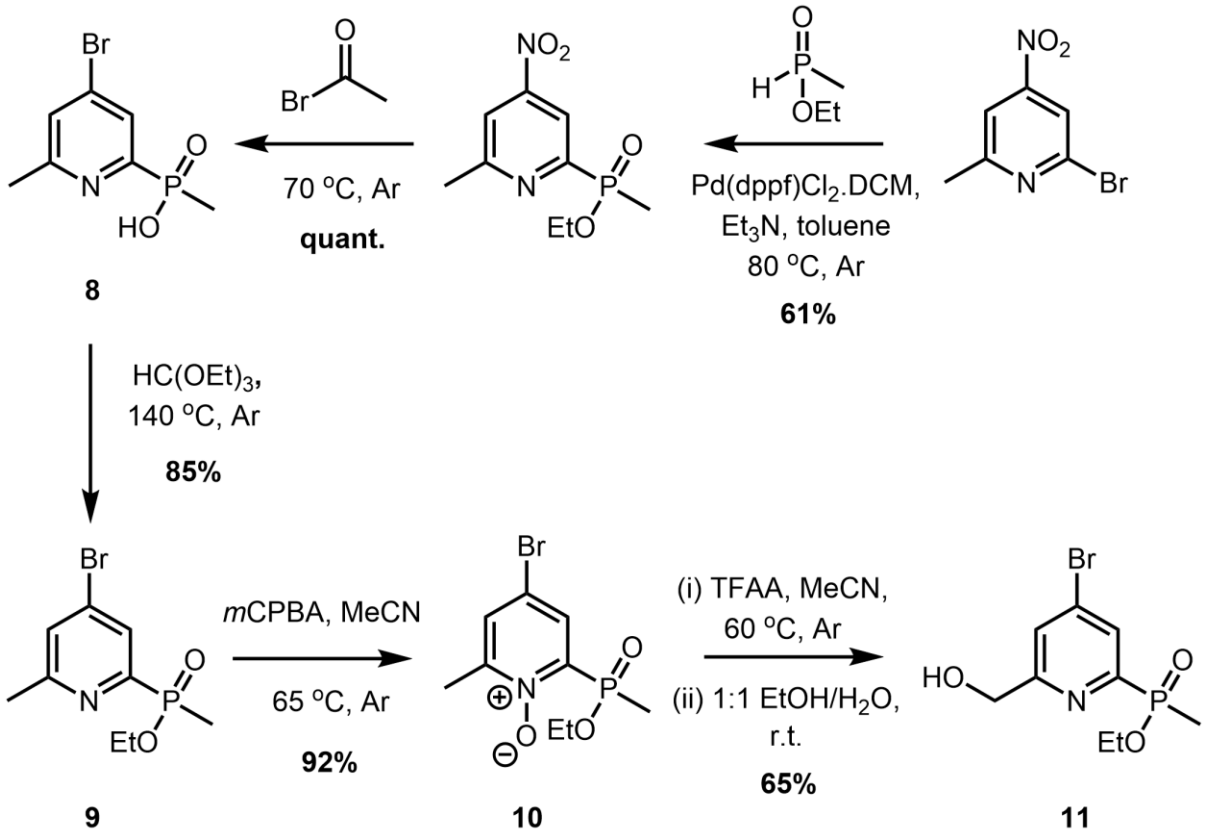

Figure 2.8. Synthesis of the common precursor for the bottom half of pyridylalkynylaryl antennae, compound **11**, ethyl (6-(hydroxymethyl)-4-(bromopyridin-2-yl)(methyl)phosphinate (dppf = 1,1'-bis(diphenylphosphino)ferrocene, *m*CPBA = *meta*-chloroperoxybenzoic acid, TFAA = trifluoroacetic anhydride).

The phosphinous ester MePO(OEt)H was prepared by hydrolysis of methyldiethoxyphosphine, liberating one equivalent of EtOH. This phosphinous ester was grafted onto the 2-position of the pyridine ring using a palladium-catalysed coupling reaction with 2-bromo-6-methyl-4-nitropyridine (61% yield). Conversion of the nitro group to a bromine atom was performed quantitatively using acetyl bromide. This reaction involves nucleophilic aromatic substitution, facilitated by intermediate formation of an *N*-acetyl pyridinium cation. Collaterally, these reaction conditions result in the undesired hydrolysis of the ethyl phosphinate ester, which can be restored to the phosphinate ethyl ester functionality by refluxing in triethylorthoformate (85% yield).

The pyridine nitrogen atom was converted to the *N*-oxide using *meta*-chloroperbenzoic acid (*m*CPBA) with a 92% yield followed by a [3,3]-sigmatropic Boekelheide rearrangement with trifluoroacetic anhydride (TFAA).[109] The rearrangement results in

the trifluoroacetic ester of the pyridine ring. Room temperature hydrolysis results in the final pyridine precursor **11** as the primary alcohol (65% yield).

*2.1.4. Synthesis of the Antennae Precursor for **L**$^{3-4}$*

The *para*-methoxy-*ortho*-dimethyl alkynylaryl chromophore precursor, compound **14**, was prepared in three steps from the commercially available 3,5-dimethyl-4-iodophenol, (Figure 2.9).

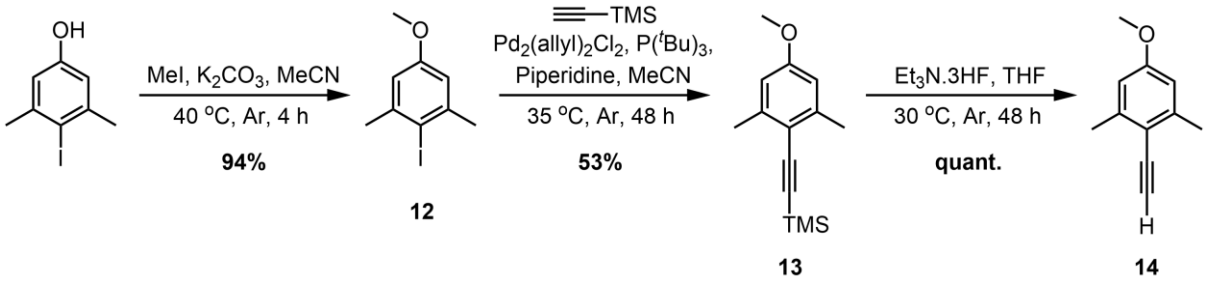

Figure 2.9. Synthesis of the *para*-methoxy-*ortho*-dimethyl alkynylaryl chromophore precursor, compound **14**.

Firstly, the phenol was methylated by an S_N2 alkylation reaction with iodomethane, using potassium carbonate as the base to give compound **12** in high yield (94%) and without the need for further purification, as confirmed by ^{1}H NMR spectrum analysis. Secondly, the alkyne functionality protected by a trimethylsilyl (TMS) group was introduced through a Pd(0)-catalysed Sonogashira cross-coupling reaction between **12** and trimethylsilylacetylene. Usually, a Cu(I) co-catalyst is used to facilitate the reaction.[110] However, the presence of copper leads to the formation of undesired homo-coupled alkyne side products and the need for strict exclusion of oxygen from the reaction.[111] A copper-free protocol circumvents these issues and its use will be particularly beneficial in later stages of the synthetic route, where the Sonogashira coupling reaction will centre on more 'valuable' late-stage synthetic intermediates. Purification of the crude material by column chromatography (silica, 0 to 10% EtOAc in hexane in 2% increments) afforded the pure product in moderate yield (53%). Thirdly, the TMS protecting group was removed to expose the terminal alkyne **14**. The deprotection step was carried out using a nucleophilic fluoride source, *i.e.*

triethylamine trihydrofluoride to give **14** in high yield (93%) following an aqueous wash to remove excess hydrofluoride reagent and resulting salts.

The alkynylaryl chromophore precursor, **14**, was reacted with the bottom part of the chromophore, **11**, in a copper(I) co-catalysed Sonogashira cross-coupling reaction to afford the pyridylalkynylaryl extended chromophore **15** as the primary alcohol, (Figure 2.10). The Sonogashira coupling reaction was performed using $Pd(dppf)Cl_2$.DCM as the catalyst, CuI as the co-catalyst, triethylamine as the base, and THF as the solvent, paralleling the conditions reported for the synthesis of the phosphinate analogue of compound **14**.[22] The alkyne **14** was used in a small excess (1.1 eq.) with respect to the bottom pyridyl **11**: it was reported previously that compound **11** and pyridylalkynylaryl primary alcohols possess similar retention times in reverse-phase HPLC, rendering purification hard if the crude product contains any leftover **11**.[64] To make sure that oxygen is excluded from the reaction, anhydrous reagents were used and the reaction mixture was degassed by multiple freeze-pump-thaw cycles. The reaction was heated at 65 °C for 18 hours and the crude material was purified via reverse-phase HPLC (MeOH/water) after an aqueous wash to yield the pure product **15** (63%).

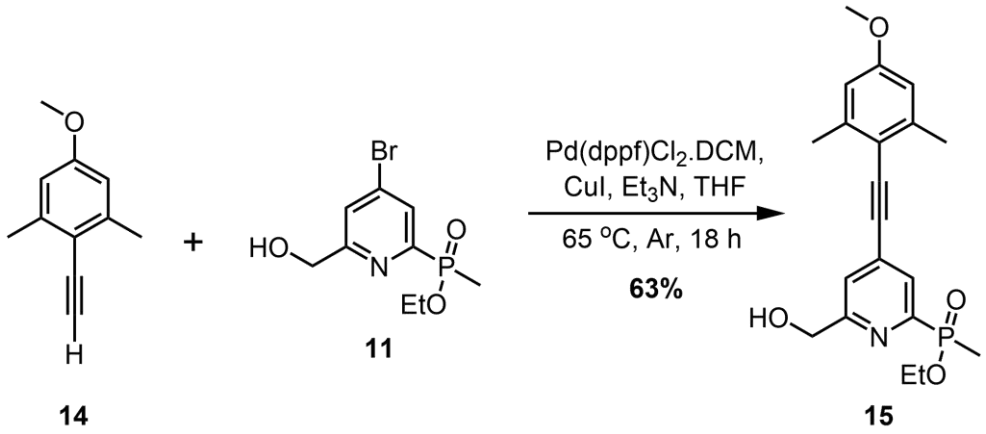

Figure 2.10. Copper(I) co-catalysed Sonogashira cross-coupling reaction between compounds **14** and **11** to afford the pyridylalkynylaryl antenna precursor **15** for the synthesis of $\mathbf{L^3}$.

A similar synthetic route to prepare the trimethoxy analogue of the pyridylalkynylaryl antenna for the ligand $\mathbf{L^4}$ was tested without success, (Figure 2.11).

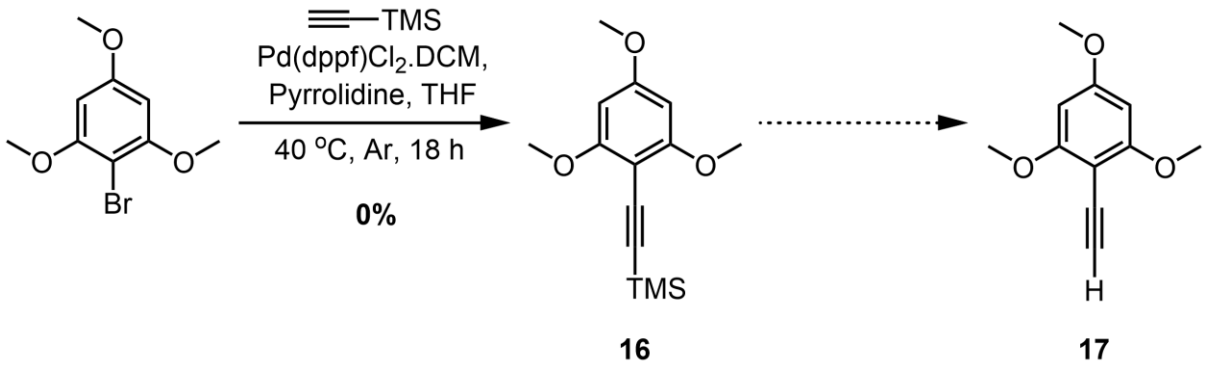

Figure 2.11. Analogue synthetic route failed to afford the alkynylaryl antenna precursor **17** for the synthesis of the ligand **L**[4].

Three different reaction conditions were trialled, (Table 2.3). First, a copper-free Sonogashira coupling reaction was tested using Pd(dppf)Cl_2.DCM and pyrrolidine in THF. After 18 hours, LC/MS suggested the presence of traces of the product **16**. Second, a different copper-free Sonogashira coupling reaction was tried using allylpalladium(II) chloride dimer, P(^{t}Bu)$_3$, and piperidine in MeCN. The failure of this second attempt led to the trial of a Cu(I) co-catalysed Sonogashira coupling reaction, performed using Pd(dppf)Cl_2.DCM, CuI, and Et_3N in THF. No undesired homo-coupling side products were detected, as well as no product **16**. In all three runs, LC/MS suggested the presence of large amounts of unreacted starting material, implying that 1-bromo-2,4,6-trimethoxybenzene, unlike its less sterically hindered analogues, is a poor substrate for Sonogashira coupling reactions. For this reason, this synthetic route has been discarded.

Table 2.3. Summary of the various conditions trialled in Sonogashira coupling reaction between trimethylsilylacetylene and 1-bromo-2,4,6-trimethoxybenzene (not shown in the reagents for clarity).

Reagents	Conditions	Yield
Pd(dppf)Cl_2.DCM, Pyrrolidine, THF	Ar, 40 °C, 18 h[(a,b)]	0%
$Pd_2(allyl)_2Cl_2$, P(^{t}Bu)$_3$, Piperidine, MeCN	Ar, 35 °C, 18 h[(a)]	0%
Pd(dppf)Cl_2.DCM, CuI, Et_3N, THF	Ar, 40 °C, 18 h[(a,c)]	0%

(*a*) Starting material still detected by LC/MS; (*b*) Traces of product **16** were detected by LC/MS ; (*c*) The reaction mixture was degassed by freeze-pump-thaw (4 cycles).

A different procedure to make compound **17** was reported to be successful, (Figure 2.12).[52] This two-step Corey-Fuchs reaction starts from a different starting material, *i.e.* 2,4,6-trimethoxybenzaldehyde.[112]

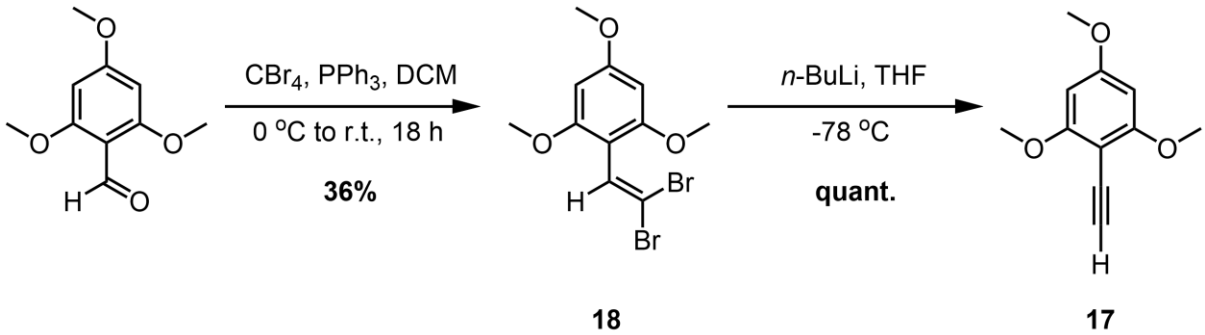

Figure 2.12. Successful synthetic route for **17** consisting in a two-step Corey-Fuchs reaction.

In the first step, 2,4,6-trimethoxybenzaldehyde was reacted with carbon tetrabromide and triphenylphosphine to afford the dibromoalkene **18** after an aqueous wash and silica column chromatography in isocratic DCM (36%). Quantitative conversion of the dibromoalkene **18** to the terminal alkyne **17** was performed using *n*-butyllithium as a base: the dibromoalkene undergoes an elimination reaction to give a bromoalkyne that, upon a lithium-halogen exchange, affords the terminal alkyne after an aqueous work up.

The alkynylaryl chromophore precursor, **17**, was reacted with the bottom part of the chromophore, **11**, in a copper-free Sonogashira cross-coupling reaction to afford the pyridylalkynylaryl extended chromophore **19** as the primary alcohol, (Figure 2.13). In this copper-free Sonogashira reaction, allylpalladium(II) dimer chloride was used as the catalyst, P(^{t}Bu)$_3$ and piperidine as the base, and MeCN as the solvent with heating at 40 °C, to give the product in moderate yield (43%) after purification by aqueous wash and reverse-phase HPLC (water/MeCN).

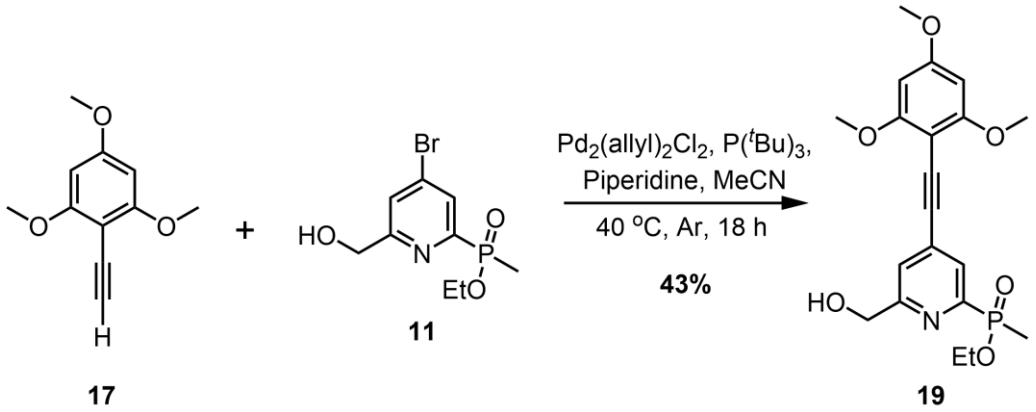

Figure 2.13. A copper-free Sonogashira cross-coupling reaction between compounds **17** and **11** to afford the pyridylalkynylaryl antenna precursor **19** for the synthesis of $\mathbf{L^4}$.

2.1.5. Synthesis of $\boldsymbol{L^{2\text{-}4}}$

The pyridylalkynylaryl antenna used as the precursor for the ligand $\mathbf{L^2}$, *i.e.* compound **20**, had already been made by Dr M. Starck as the primary alcohol following a reported procedure.[22] The preparation of the antenna precursors for ligands $\mathbf{L^3}$ and $\mathbf{L^4}$, *i.e.* compounds **15** and **19**, has been described in Section 2.2.5. The subsequent steps, *i.e.* selective dialkylation of each antenna on the TACN macrocycle and alkylation of the third ring nitrogen atom with the single arm picolinate, do not depend on the substituents present on the top half of the pyridylalkynylaryl antenna. For this reason, the following steps in the synthesis of ligands $\mathbf{L^{2\text{-}4}}$ are described in detail only for the $\mathbf{L^2}$ precursor.

With the required precursor compounds prepared, the ligands $\mathbf{L^{2\text{-}4}}$ were synthesised from a TACN scaffold. For this purpose, a TACN macrocycle bearing a single Boc protecting group was chosen to facilitate controlled stepwise alkylation of the two pyridylalkynylaryl arms onto the scaffold. The Boc-protected TACN was prepared in three steps following a reported procedure.[113] The macrocycle was used as the hydrochloride salt for convenience, without prior conversion to the free amine. The single arm **20** was converted to the mesylate ester **21** immediately prior to its use in the following S_N2 alkylation step. Conversion of the primary alcohol to the mesylate was performed using methanesulfonic anhydride in THF. LC/MS analysis indicated that quantitative conversion to the mesylate had occurred within 1 hour. The product was used in the next step after a water wash to remove methanesulfonic acid.

Introduction of the two pyridylalkynylaryl antennae onto the TACN scaffold was performed through an S_N2 alkylation reaction between the Boc protected macrocycle and the mesylate **21** in MeCN, in the presence of potassium carbonate, (Figure 2.14). The reaction was carried out under argon to prevent water from hydrolysing the mesylate. A small excess of the mesylate **21** was used (2.4 eq.) and the reaction was left overnight to ensure completion of the double alkylation reaction and was confirmed by LC/MS analysis. Filtration and purification by reverse-phase HPLC (water/MeCN) afforded the dialkylated TACN **22** as the Boc protected compound in high yield (80%). ^1H and ^{13}C NMR spectra show that restricted rotation about the carbamate NCO bond of the Boc group makes the pyridylalkynylaryl arms non-equivalent on the NMR timescale at room temperature.

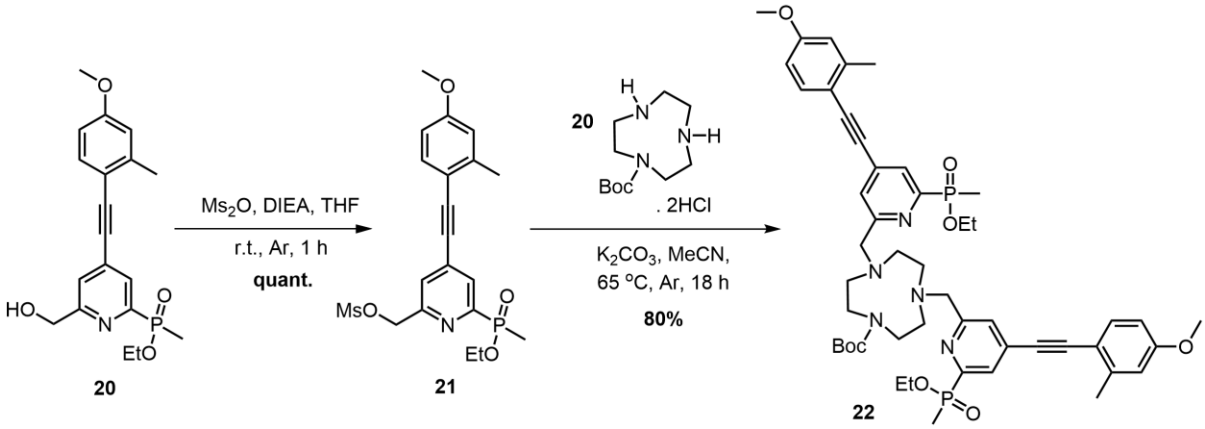

Figure 2.14. Synthesis of the dialkylated TACN derivative **22**, the precursor of ligand **L²**.

The syntheses of the dialkylated TACN derivatives **24** and **26**, the precursors of ligands **L³⁻⁴** respectively, were carried out analogously. Conversion of the primary alcohol pyridylalkynylaryl antennae **15** and **19** to the mesylates **23** and **25** each proceeded in quantitative yield. The following S_N2 alkylation steps afforded compounds **24** and **26** in good yields (78% and 59% respectively) after filtration and reverse-phase HPLC purification (water/MeCN).

Boc deprotection of compounds **22**, **24**, and **26**, the precursors of ligands **L²⁻⁴** respectively, proved unsuccessful using trifluoroacetic acid (TFA) in DCM (10% v/v). Mass spectrometry showed a mass increase equal to the molecular weight of a water molecule. NMR spectrometry showed evidence of loss of replacement of the triple

bond with a double bond. This evidence can be rationalised in terms of the formation of a hydrated side product where the triple bond of the pyridylalkynylaryl antenna turns into a double bond, irreversibly disrupting its photophysical properties. This aspect will be investigated in further detail in Section 2.2.6.

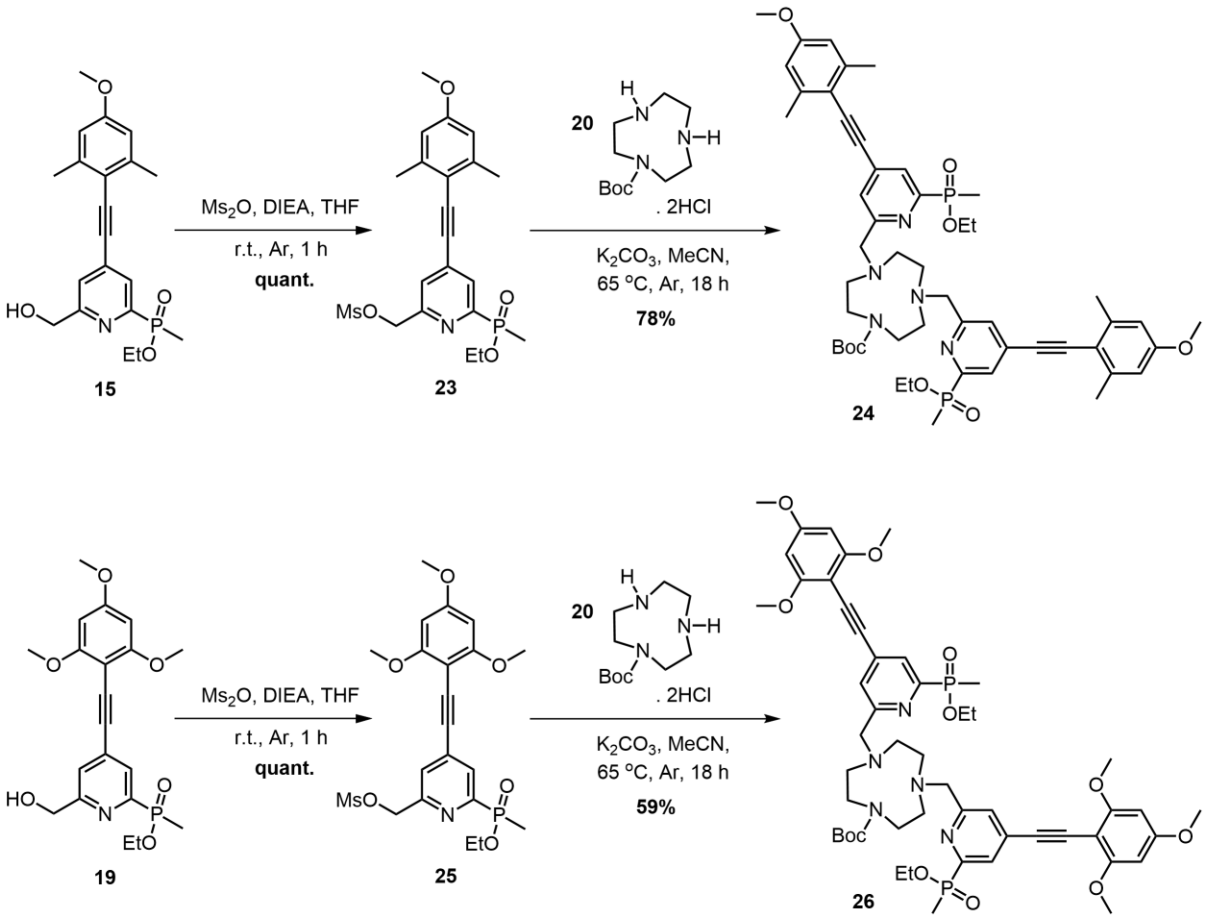

Figure 2.15. Synthesis of the dialkylated TACN derivatives **24** and **26**, the precursors of ligands $\mathbf{L^{3\text{-}4}}$ respectively.

*2.1.6. Synthesis of **[Eu.L^1]***

The dialkylated TACN intermediate **27**, used as a precursor for the synthesis of the ligand $\mathbf{L^1}$, was already made by Dr J.D. Fradgley as the Boc protected amine following a reported procedure.[18] The preparation of the single picolinate arm **4** bearing an ester functionality that will constitute the third pendant arm of $\mathbf{L^1}$ has been discussed in Section 2.1.2. Compound **27** was de-protected using trifluoroacetic acid (TFA) in DCM

(10% v/v) to quantitatively afford the dialkylated TACN as the trifluoroacetate salt of the secondary amine, **28**, (Figure 2.16).

The single arm **4** was converted to the mesylate **29** immediately prior to its use in the following S_N2 alkylation step. The deprotected dialkylated compound, **28** was used as its trifluoroacetate salt in an S_N2 alkylation with an excess (2.5 eq.) of the mesylate ester, **29**. Reaction monitoring by LC/MS after 18 hours indicated complete consumption of compound **17** and the presence of remaining hydrolysed mesylate, *i.e.* the primary alcohol **4**. Purification by reverse-phase HPLC (0.1% formic acid in water/0.1% formic acid in MeCN) afforded the ligand $\mathbf{L^1}$ (57%).

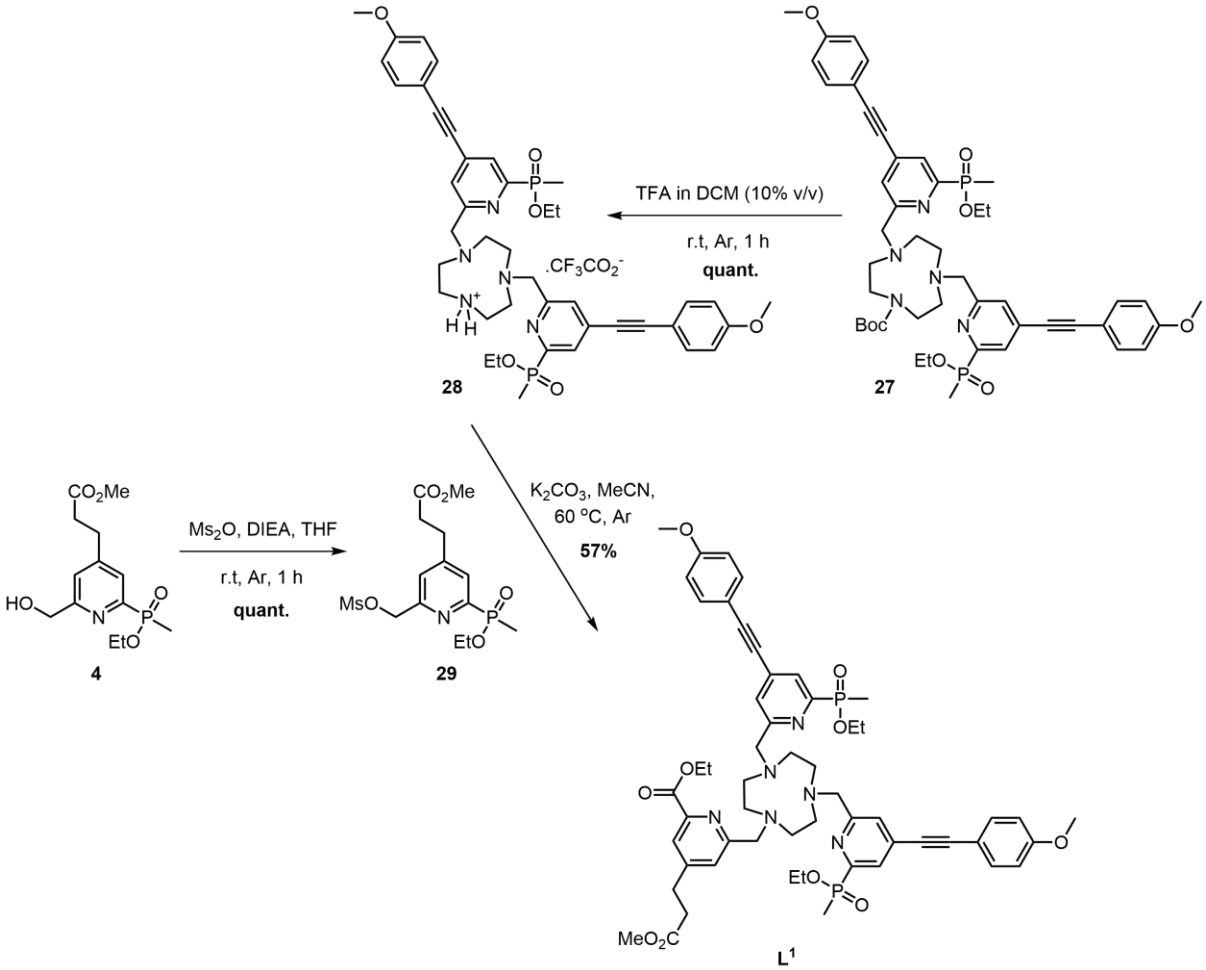

Figure 2.16. Synthesis of the ligand, $\mathbf{L^1}$. TFA = trifluoroacetic acid, DIEA = N,N-diisopropylethylamine.

The target complex **[Eu.L^1]** was obtained through a well-established complexation protocol, (Figure 2.17).[18,55] The ligand $\mathbf{L^1}$ was dissolved in MeOH/water and the pH

adjusted at 12 through dropwise addition of $NaOH_{(aq)}$. The solution was stirred at 60 °C for 18 hours to hydrolyse the two phosphinate ester groups and the methyl and ethyl esters of the single picolinate arm to give the salt, **30**. Evidence of reaction completion was obtained by LC/MS analysis. In the following step, the pH of the reaction mixture was adjusted to 6 using $HCl_{(aq)}$. $EuCl_3.6H_2O$ was added (1.1 eq.) and the reaction stirred at 60 °C for 18 hours. Metal complexation of **30** to give the target complex **[Eu.L^1]** was monitored via LC/MS. Purification by reverse-phase HPLC (water/MeCN) afforded the complex **[Eu.L^1]** with a 29% yield over the two steps.

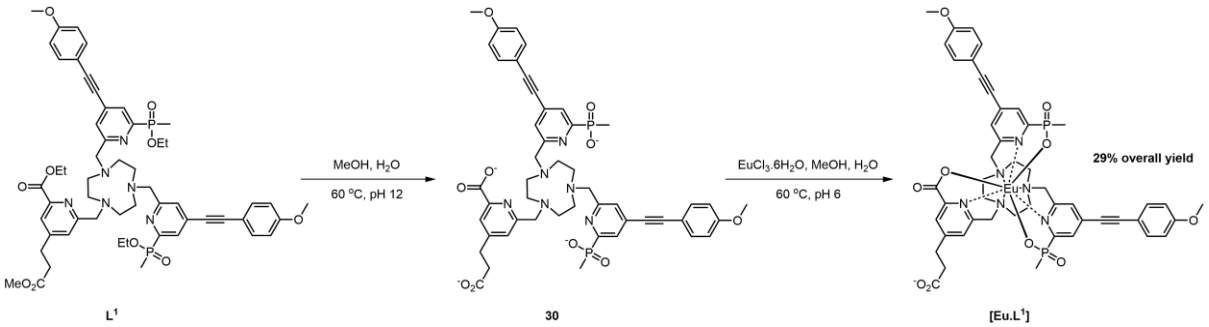

Figure 2.17. Hydrolysis and metal complexation of the ligand **L^1** with Eu(III) to afford the complex **[Eu.L^1]**.

*2.1.7. Analysis of Racemic **[Eu.L¹]***

The absorption, excitation, and emission spectra of **[Eu.L¹]** in MeOH are shown in Figure 2.18 and a summary of its photophysical properties in different solvents is given in Table 2.4. The excitation spectrum closely parallels the absorption of the antennae, confirming that the sensitisation is due to energy transfer occurring from the antennae to the central Eu(III) ion. The shape of the observed broad absorption transition is typical of an internal charge transfer state, (*vide supra* – Section 1.1.2). The symmetry about the metal ion in mixed-donor complexes is lower than in same-donor complexes, (*vide supra* – Section 1.1.3). A greater number of transitions are allowed in a less symmetrical environment. In particular, it is possible to identify three bands within the Δ*J* = 2 manifold of **[Eu.L¹]** instead of the two bands that are typically visible in C_3 symmetric Eu(III) complexes.[114]

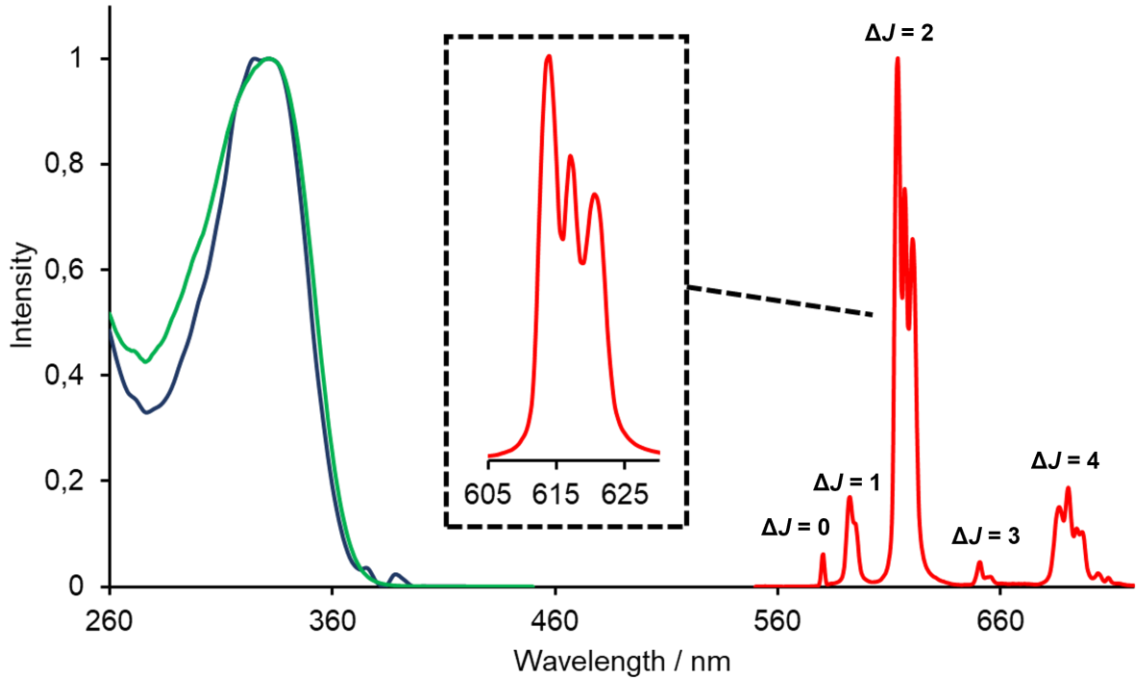

Figure 2.18. Absorption (*blue*), excitation (*green*, recorded at λ_{em} = 614 nm), and emission spectra (*red*, excited at λ_{exc} = 332 nm) of **[Eu.L¹]** in MeOH. Compared to C_3-symmetrical Eu(III) complexes, a greater number of transitions are allowed due to the lower symmetry about the metal centre. A detail of the Δ*J* = 2 manifold is shown in the central insert.

Table 2.4. Summary of photophysical properties of **[Eu.L^1]** in various solvents (295 K).

Solvent	λ_{exc} / nm	τ / *ms*	$\phi^{(a)}$ / %
H_2O	324	1.00	N.D.
D_2O	328	1.24	21
MeOH	332	1.20	34

(*a*) Parameter calculated at the stated excitation wavelength. Experimental errors of lifetime and quantum yields are ±5 and 15% respectively. N.D. = not determined.

Quantum yields are usually measured indirectly against a literature reference standard having a known quantum yield or, more recently, using an integrating sphere. The reference standard used within this work is $[Ru(bpy)_3]Cl_2$ in water.[115] The ratio between the quantum yield to determine and that of the reference is related to more conventionally accessible spectrophotometric properties via the following equation:

$$\frac{\phi}{\phi_{\mathrm{ref}}} = \frac{n^2}{n_{\mathrm{ref}}^2} \times \frac{S}{S_{\mathrm{ref}}} \times \frac{A_{\mathrm{ref}}}{A} \times \frac{I_{\mathrm{lamp}}^{\lambda}}{I_{\mathrm{lamp}}^{\lambda_{\mathrm{ref}}}} \qquad (2.1)$$

Where *n* is the refractive index of the solvent in which the measurements are carried out, *S* is the integral of the emission spectrum between appropriate limits, *A* is the absorbance of the species at the chosen wavelength, and I_{lamp} is the intensity of the lamp at the wavelength of excitation.

*2.1.8. Chiral resolution of **[Eu.L^1]***

The complex **[Eu.L^1]** exists as a racemic mixture of the *SS-Δ(δδδ)* and *RR-Λ(λλλ)* isomers, analogously to other similar Eu(III) complexes based on TACN scaffolds with phosphinate pyridylalkynylaryl pendant arms.[116] *S* and *R* refer to the absolute configurations at the stereogenic phosphinate centres assigned using the Cahn-Ingold-Prelog priority rules; *Δ* and *Λ* to the sign of the torsion angle defined by the $N_{py}CCN_{TACN}$ atoms, which define the chiral conformation arising from the twist of the three pendant arms around the metal centre; and *δ* and *λ* to the torsion angle defined by the $N_{TACN}CCN_{TACN}$ atoms, which define the chelate ring conformation on the TACN macrocycle. Despite multiple sources of chirality being present in such complexes,

only the *SS-Δ(δδδ)* and *RR-Λ(λλλ)* isomers are observed due to steric hindrance reasons which inhibit formation of any other isomers, as confirmed by X-ray crystallography studies of structurally related complexes.[117] For the sake of brevity, the *SS-Δ(δδδ)* and *RR-Λ(λλλ)* isomers will be referred to as the *Δ* and *Λ* isomers respectively.

In order to investigate the CPL behaviour of **[Eu.L^1]**, it is necessary to separate the two enantiomers. Previously, resolution of racemic Eu(III) complexes was achieved by chiral HPLC. In particular, the enantiomers of Eu(III) complexes featuring methoxy-substituents on the aryl rings have been separated using a Daicel CHIRALPAK-ID column, (Figure 2.19).[66,118] However, the previously separated Eu(III) complexes contained three phosphinate donors, whereas **[Eu.L^1]** contains two phosphinate and one carboxylate donor groups. For this reason, elution of **[Eu.L^1]** was trialled on two different chiral columns, *i.e.* Daicel CHIRALPAK-IC and ID, to investigate which one would provide the best separation.

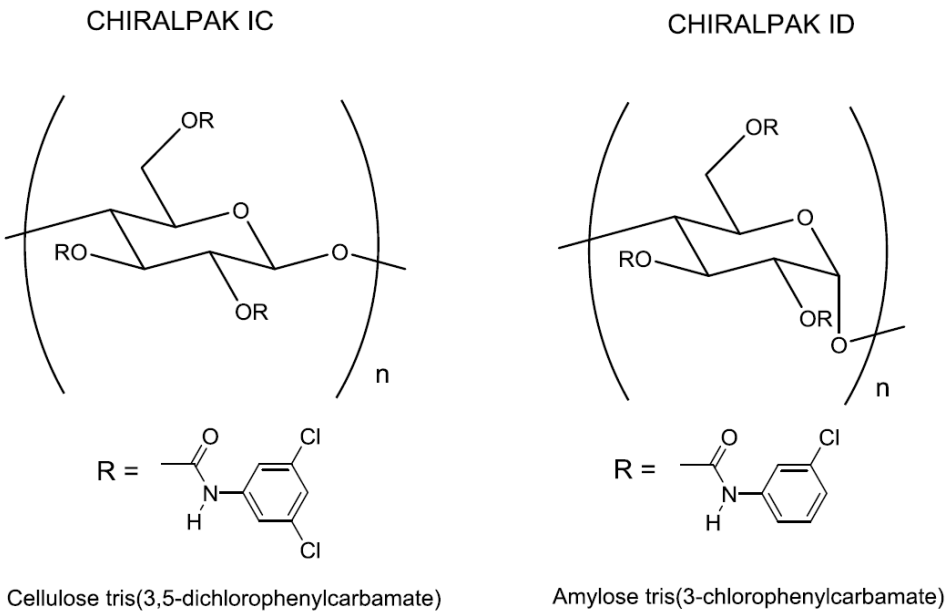

Figure 2.19. The chiral stationary phases used in Daicel CHIRALPAK-IC and ID columns.

The complex **[Eu.L^1]**, bearing a negatively charged carboxylate anion arm, failed to be retained on both the IC and ID chiral columns. The negative charge of **[Eu.L^1]** was removed by conversion into the methyl ester **[Eu.L^1]^a**, (Figure 2.20, *left*). This was achieved by stirring **[Eu.L^1]** in MeOH containing a drop of acetyl chloride at room

temperature under argon for 48 hours (34%). Chiral resolution of the racemic mixture of **[Eu.L^1]^a** failed on both the IC and ID chiral columns.

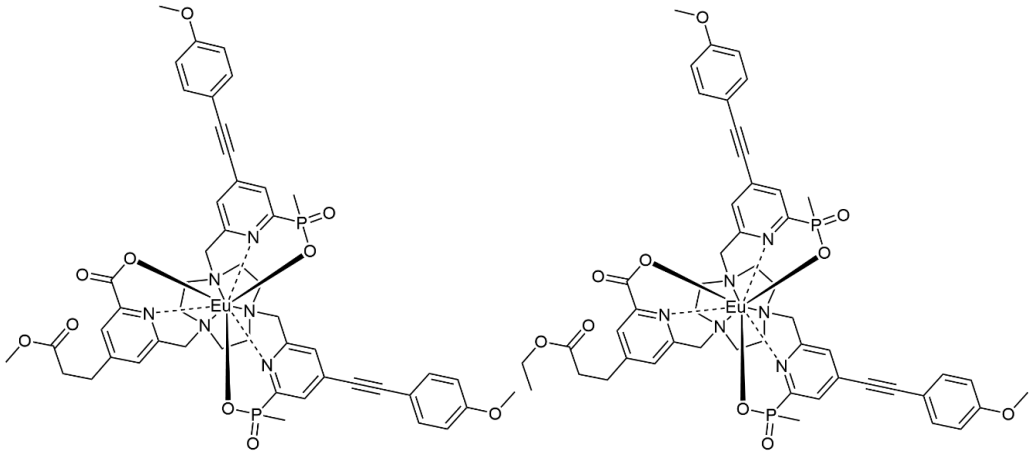

Figure 2.20. Structure of the methyl (*left*) and ethyl ester (*right*) of **[Eu.L^1]**, compounds **[Eu.L^1]^a** and **[Eu.L^1]^b** respectively.

To make the ester arm more apolar, **[Eu.L^1]** was converted to its ethyl ester **[Eu.L^1]^b** (58%), (Figure 2.20, *right*). The reaction conditions used for the esterification reaction were the same used for the synthesis of **[Eu.L^1]^a**, with the difference that EtOH was used as the solvent instead of MeOH. The ethyl ester successfully **[Eu.L^1]^b** separated into the *Δ* and *Λ* isomers on the analytical and semi-preparative CHIRALPAK-IC columns with an isocratic methanol eluent on a 3.5 milligram scale, (Figure 2.21).

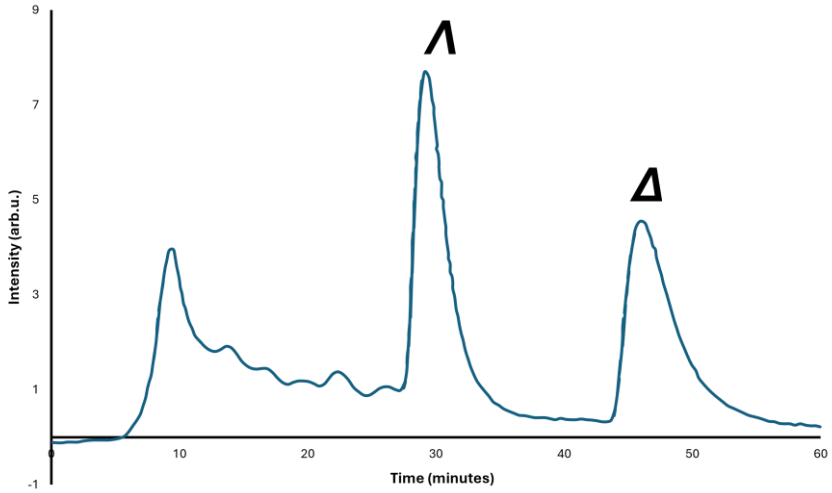

Figure 2.21. Chiral HPLC trace showing the resolution of the enantiomers of **[Eu.L^1]^b** using a CHIRALPAK-IC column (semi-preparative, 295 K, MeOH, 4 mL min^{-1}, UV detector λ = 335 nm). The absolute configuration of the enantiomers was determined by CPL analysis, (*vide infra* – Section 2.2.2).

*2.1.9. CPL characterisation of **[Eu.L^{1b}]***

CPL spectra were recorded for each enantiomer of the complex **[Eu.L^{1b}]** in various solvents, *i.e.* MeOH, EtOAc, *N*-methyl-2-pyrrolidone (NMP), and water, (Figure 2.22). In every case, mirror imaged CPL spectra were observed for the two enantiomers. The signs of the lines within the Δ*J* = 4 manifold (680 - 710 nm) are stable across all solvents and directly correlate with the absolute configuration of the complex, previously determined from X-ray crystal structure analysis.[116,117] Notably, the sign sequence of the five observed transitions in the Δ*J* = 4 manifold are - / + / - / - / + for the *Λ* enantiomer, (orange lines in Figure 2.22). This allows for the spectroscopic assignment of the configuration of the enantiomers without having to resort to X-ray diffraction.

The Δ*J* = 1 and Δ*J* = 2 manifolds, *i.e.* the brightest two, display emission bands having the same CPL sign in NMP and EtOAc, successfully achieving the same-sign CPL emission within a single manifold presented earlier. It is interesting to note that the CPL spectra show more sign variations in the case of water. The signs of CPL emission bands vary also in the case of MeOH. However, the bands within the Δ*J* = 1 and Δ*J* = 2 manifolds have the same sign, effectively keeping opposite CPL sign cancellation low. Since one of the aims of this work is fabricating polymer-based films containing CPL-active Eu(III) complexes, EtOAc was chosen as it is a solvent that mimics the monomeric units constituting polymethylmethacrylate (PMMA). The bright, same sign emission observed in EtOAc suggests that similar favourable CPL emission may be achieved in PMMA films, (*vide infra* – Section 3.2).

CPL spectra have also been recorded for a different Eu(III) complex, **[Eu.L$^{1''}$]**, (Figure 2.23). This complex had already been made and chirally resolved by Dr J.D. Fradgley following a reported procedure,[18] but its CPL properties had not been investigated. **[Eu.L$^{1''}$]** differs from the proposed target compound **[Eu.L$^{1'}$]** only in the absence of mixed donors and is therefore a good predictor of the expected CPL properties of the **[Eu.L$^{1'\text{-}4'}$]** amino series.

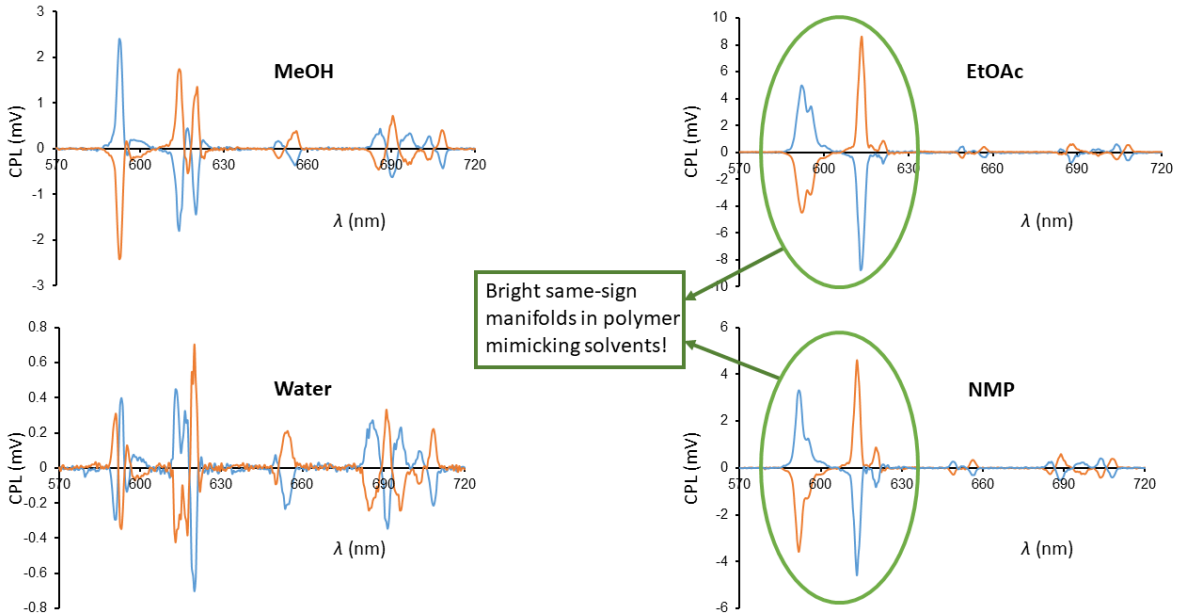

Figure 2.22. CPL spectra of the *Δ* (*blue*) and *Λ* (*orange*) enantiomers of **[Eu.L^{1b}]** in different solvents. Clockwise from top left: MeOH, EtOAc, NMP, and water. Excitation at λ_{exc} = 328 nm.

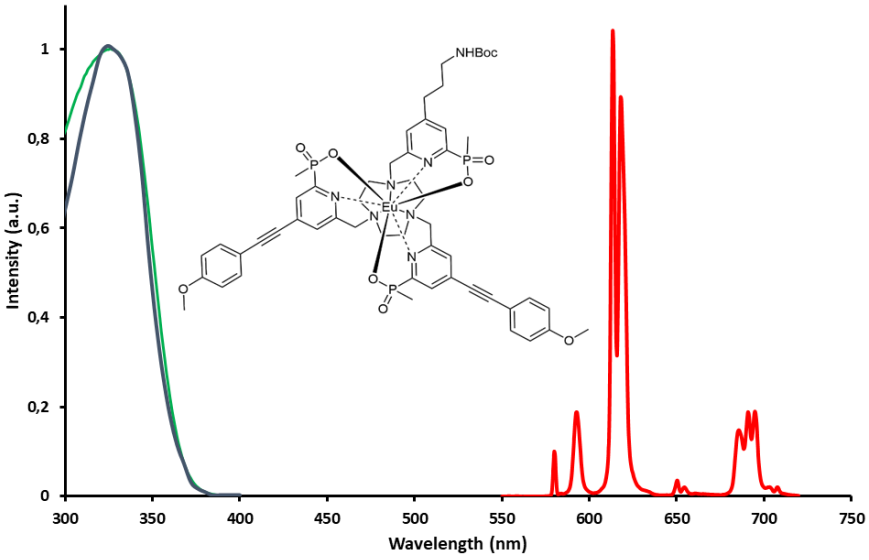

Figure 2.23. Absorption (*blue*), excitation (*green*, recorded at λ_{em} = 614 nm), and emission spectra (*red*, excited at λ_{exc} = 328 nm) of complex **[Eu.L$^{1''}$]** in water, an analogue of the proposed target complex **[Eu.L$^{1'}$]** bearing three phosphinate donors. Adapted from [18].

The CPL spectra of **[Eu.L$^{1''}$]** show that same sign emission in the Δ*J* = 1 and Δ*J* = 2 manifolds in NMP and EtOAc, (Figure 2.24). As expected, the spectral properties of

the carboxylate linker and the amino linker are similar to each other, with the advantage of different possibilities for late-stage conjugation of the complexes.

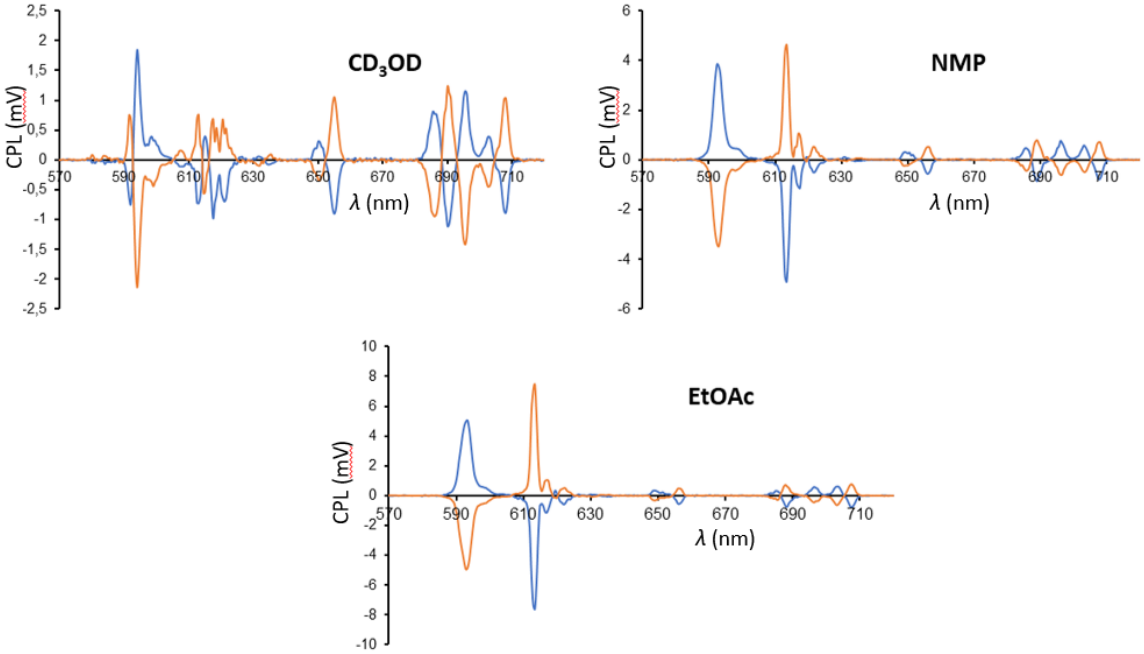

Figure 2.24. CPL spectra of the *Δ* (*blue*) and *Λ* (*orange*) enantiomers of **[Eu.L$^{1"}$]** in different solvents. Clockwise from top left: CD_3OD, NMP, and EtOAc. Excitation at λ_{exc} = 325 nm.

2.1.10. Multiphoton studies of ***[Eu.L^{1b}]***

As previously discussed, the excitation of Eu(III) complexes in the UV region of the spectrum may pose issues for cell studies and for the use in LED-based spectrophotometers, (*vide supra* – Section 1.2.3). One way of overcoming this issue is to exploit *multiphoton* absorption. Multiphoton absorption involves the simultaneous absorption of two or more photons to excite a chromophore. Multiphoton processes are non-linear phenomena, hence the quadratic dependence on the intensity of the excitation light. For this reason, the observation of multiphoton processes requires the use of powerful light sources. The multiphoton instrument at Durham University exploits a 5 W tunable femtosecond pulsed laser in the 680 – 1300 nm region. Previous studies have proven that Eu(III) complexes display two-photon absorption, effectively shifting the excitation wavelength from the UV to the near IR region (710 to 850 nm).[119,120]

Multiphoton excitation spectra of the *Λ* enantiomer of **[Eu.L^{1b}]** were recorded in NMP, (Figure 2.25). First, the integrated two-photon emission intensity was plotted as a function of excitation energy on a logarithmic scale, (Figure 2.25, *right*). The slope of the fitting line is close to 2, confirming that the emission arises from a two-photon process. The red circles in Figure 2.25-*left* represent the emission intensity of the two-photon process (*red axes*), superimposed to the one-photon excitation spectrum (*black axes*). Saturation of the molecules available in the small excitation volumes accounts for the non-linearity at large power in Figure 2.25-*left*.

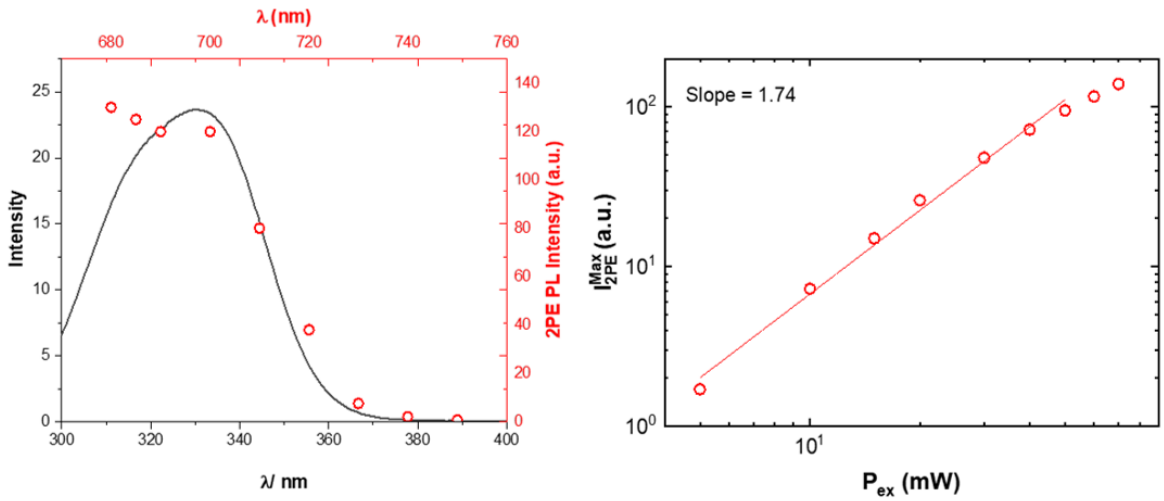

Figure 2.25. Multiphoton excitation spectrum of **[Eu.L^{1b}]** in NMP (*red circles, left*) compared with single photon excitation (*black line, left*); excitation power dependency on the integrated multiphoton luminescence intensity (*right*).

The NIR laser was used to excite the *Λ* enantiomer of **[Eu.L^{1b}]** in NMP and record a CPL spectrum, (Figure 2.26). The recorded CPL spectrum only spans the 570-650 nm region since a 650 nm short-pass filter was used to protect the detector from scattered laser radiation. It is possible to distinguish two distinct CPL bands arising from the Δ*J* = 1 and Δ*J* = 2 manifolds.

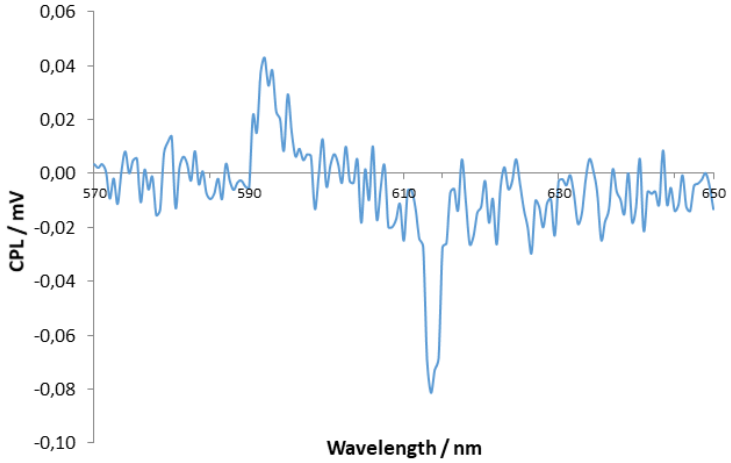

Figure 2.26. CPL spectrum of **[Eu.L^{1b}]** in NMP obtained upon two-photon absorption at 680 nm, 70% power at 680 nm, 980 mW.

The total emission intensity and CPL intensity arising from the excitation of the *Λ* enantiomer of **[Eu.L^{1b}]** in NMP at different excitation wavelengths were compared, (Figure 2.27). The absolute CPL intensity is lower with the two-photon excitation at 680 nm than the one-photon excitation due to the large difference in the total number of excited molecules between the multiphoton laser's focal volume compared to the lamp's light beam. When factoring out this effect due to an imbalance in the number of emitting molecules involved, the total emission intensity arising from the two-photon excitation is much higher than the one-photon excitation happening at 365 nm, *i.e.* the operating wavelength of the LED excitation source of the novel solid-state CPL spectrophotometer, (*vide supra* – Section 1.2.3). It is therefore plausible that it will be possible to achieve higher CPL brightness for the two-photon process rather than the one-photon process. This topic will be the subject of further investigation in the future, along with the evaluation of the two-photon absorption cross section.

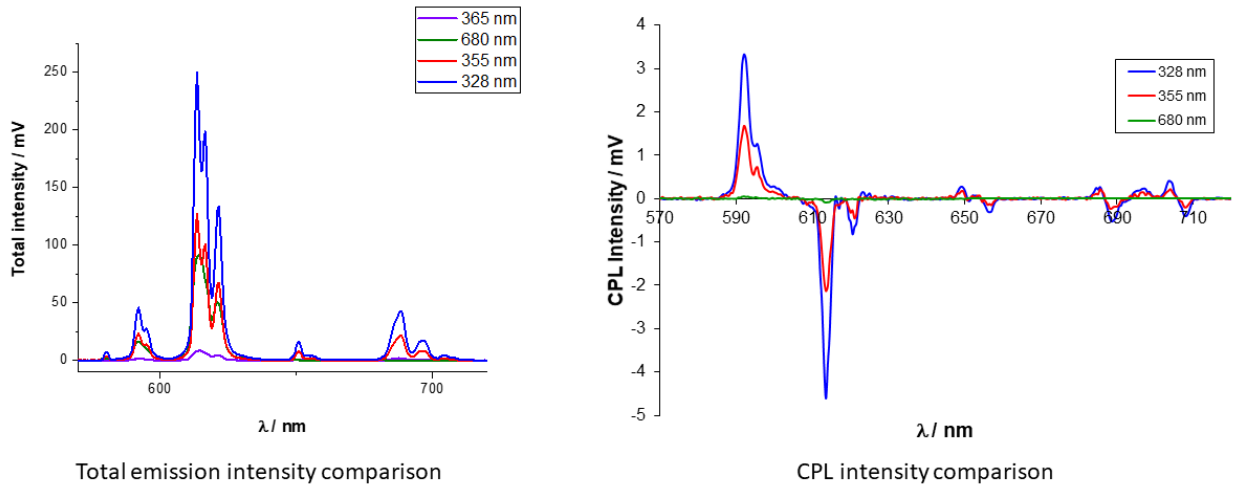

Figure 2.27. Comparison between total emission (*left*) and CPL spectra (*right*) of the *Λ* enantiomer of **[Eu.L^{1b}]** in NMP at various excitation wavelengths.

2.2. p-NO_2 Eu(III) complex [Eu.L^5]

2.2.1. Introduction

A novel Eu(III) complex, **[Eu.L^5]**, was synthesised, comprising a functionalised macrocycle based on 1,4,7-triazacyclononane (TACN) with three pyridyl-based carboxylate donor groups which saturate the coordination sphere of Eu(III). Two pyridylalkynylaryl antennae were grafted onto the macrocycle to enable efficient sensitisation of Eu(III) emission both in the UV region with single-photon excitation and in the near-infrared (NIR) with two-photon excitation (2PE). A third macrocycle site was functionalised with a single pyridyl pendant arm, enabling linkage of the complex to various molecules via a *para*-nitro group, which has previously been shown to allow for facile late-stage functionalisation with a broad set of substituents. The work in the present section was performed in collaboration with a Master's student in the Pal group, Samuel Parr.

The main aim of this work was to study how the total emission and CPL spectral profile of all-carboxylate complexes differ from those of all-phosphinate complexes, which have been thoroughly characterised previously by the Parker group and the Pal group. An additional advantage is the shorter synthetic route: phosphinate-based complexes require a synthetic precursor to the chromophore that is prepared in five steps, whereas the analogous precursor to carboxylate donors is prepared in only two steps.

For this reason, the feasibility of scaling up the synthesis from the usual milligram scale to tens of milligrams was significantly increased. A more conspicuous amount of complex would also enable the possibility of thin film and polymer conjugation studies via RAFT (Reversible Addition Fragmentation Chain Transfer) thiol end-group modifications. The reactivity of thiols towards the *p*-NO_2 group of the complex can be exploited for conjugation to thiol-bearing biological vectors for *in vivo* cell internalisation studies and CPL imaging.

*2.2.2. Retrosynthetic analysis of **[Eu.L^5]***

Retrosynthetic analysis was conducted on the target compound **[Eu.L^5]** and is presented in Figure 2.28, establishing the requirement of two precursor intermediates and commercially available 1,4,7-triazacyclononane (TACN).

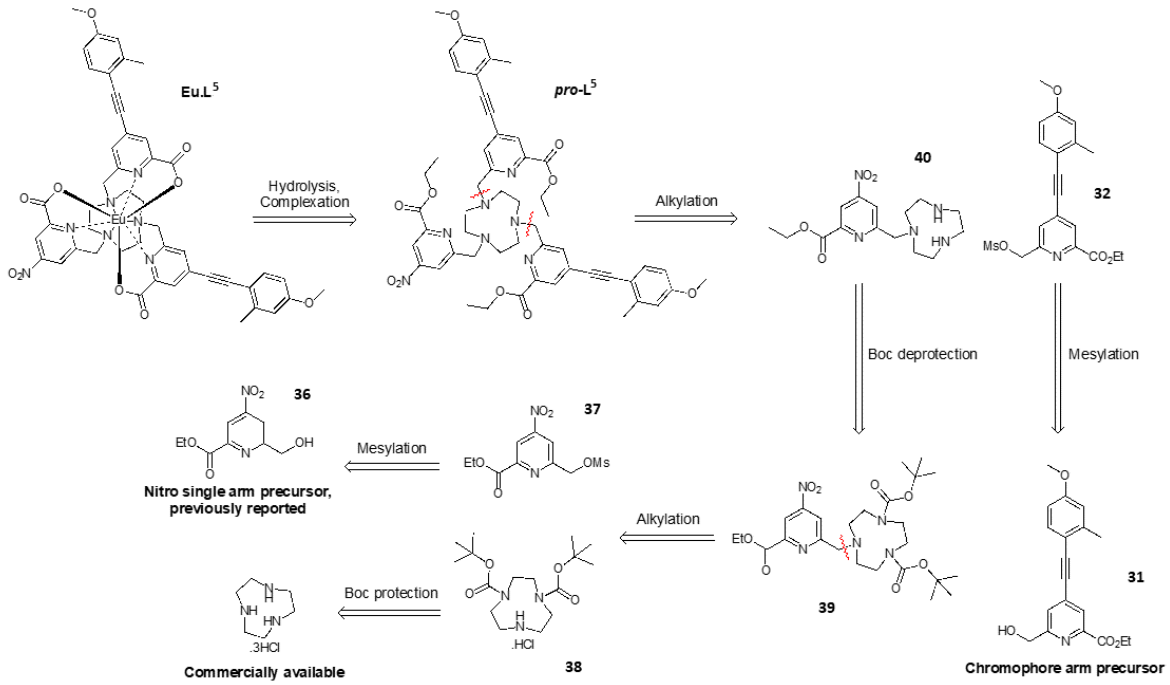

Figure 2.28. Retrosynthetic analysis of **[Eu.L^5]**.

2.2.3. Chromophore Arm Precursor Synthesis

Compound **31**, the precursor to the chromophore arm, was synthesised using a Sonogashira cross-coupling, (Figure 2.29) between commercially available 1-ethynyl-4-methoxy-2-methylbenzene and the previously reported bottom component compound **2**, (*vide supra* - Section 2.1.2). Sonogashira cross-couplings form a new

C–C bond between an aryl halide and terminal alkyne over a Pd(0) catalyst and a Cu(I) co-catalyst. The methyl ester analogue of compound **31** has been reported using the 4-iodo analogue of compound **2** in the reaction.[22] The analogous procedure was followed here to afford compound **37** with a 37% yield.

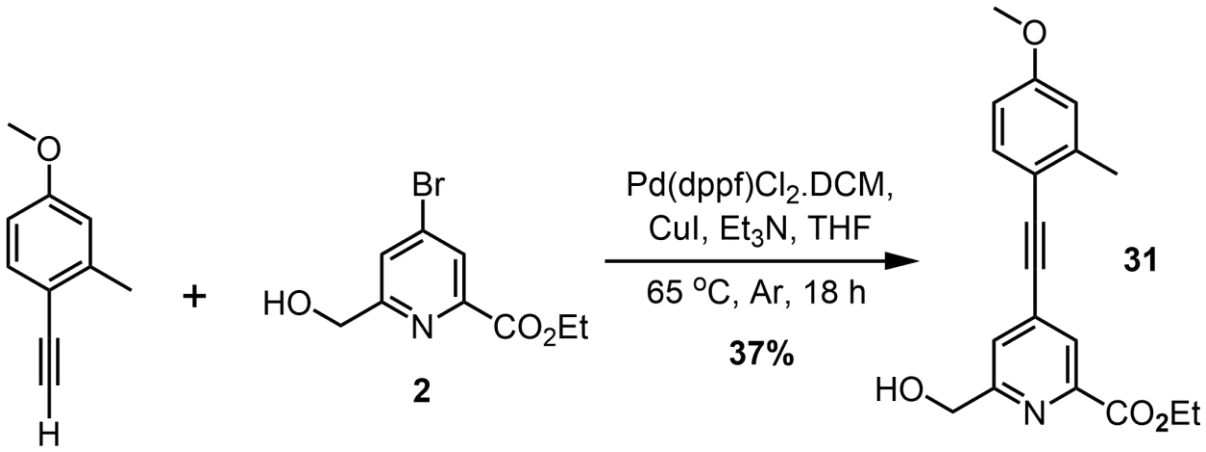

Figure 2.29. Synthesis of the precursor to the chromophore arm compound **31**, prepared using a Sonogashira cross-coupling reaction.

2.2.4. Photophysical Characterisation of the Chromophore Arm

Absorption, excitation, and emission spectra were recorded for the chromophore arm precursor, compound **31** in DCM, MeOH, H_2O, and MeCN, (Figure 2.29-30, Table 2.5).

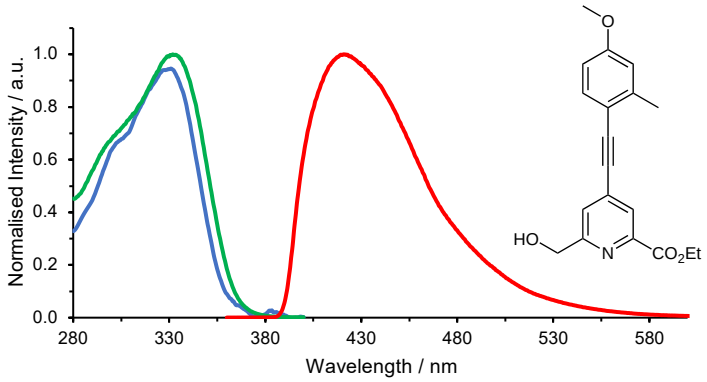

Figure 2.30. Absorption (*blue*), excitation (*green*, λ_{em} = 421 nm), and emission spectra (*red*, λ_{exc} = 334 nm) of the chromophore arm in DCM.

The values in Table 2.5 are maximum emission wavelengths (λ_{em}) of the chromophore arm in each of the four solvents stated above. The absorption, excitation, and emission spectra of the chromophore arm are presented in Figure 2.31 and Table 2.5. The absorption profile is broad, intense, and structureless, characteristic of ICT states. In

each solvent, the absorption and emission spectra also appear to be mirror images of each other, a consequence of Franck-Condon factors that is characteristic of an organic fluorophore.

Table 2.5. Maximum emission wavelength (λ_{em}) of the chromophore arm in various solvents with the normalised Reichardt solvent polarity parameters E_T^N of each solvent.

Solvent	λ_{em} / nm	E_T^N [29]
H_2O	414	1.000
MeOH	452	0.762
MeCN	449	0.460
DCM	421	0.309

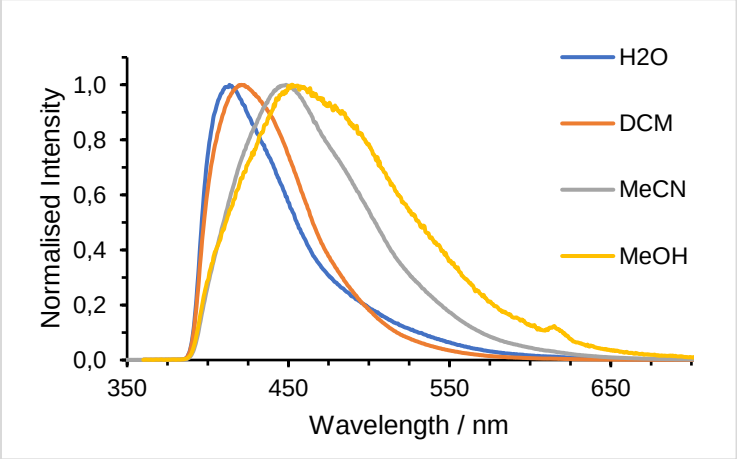

Figure 2.31. Emission spectra of the chromophore arm in various solvents.

Stokes shifts of a minimum of 84 nm in H_2O and a maximum of 122 nm in MeOH were observed across the four solvents studied. For the chromophore arm precursor in the four solvents studied, no correlation between the emission wavelength and the normalised Reichardt solvent polarity parameter E_T^N was observed and the absorption maximum remained constant at 330 nm. A lack of correlation points to the existence of specific solvent interactions with the fluorophore which are not included in the usual model where the fluorophore is treated as being spherical and the solvent treated as a dielectric medium, not accounting for specific solvent effects. The assumption of a spherical chromophore does not describe well the elongated pyridylalkynylaryl chromophore but will be a better approximation for the resulting complex due to its globular shape.

2.2.5. Single Arm Precursor Synthesis

The *para*-nitro single arm precursor compound **36** was synthesised in four steps from the commercially available starting material 6-methylpyridine-2-carboxylic acid, (Figure 2.32).

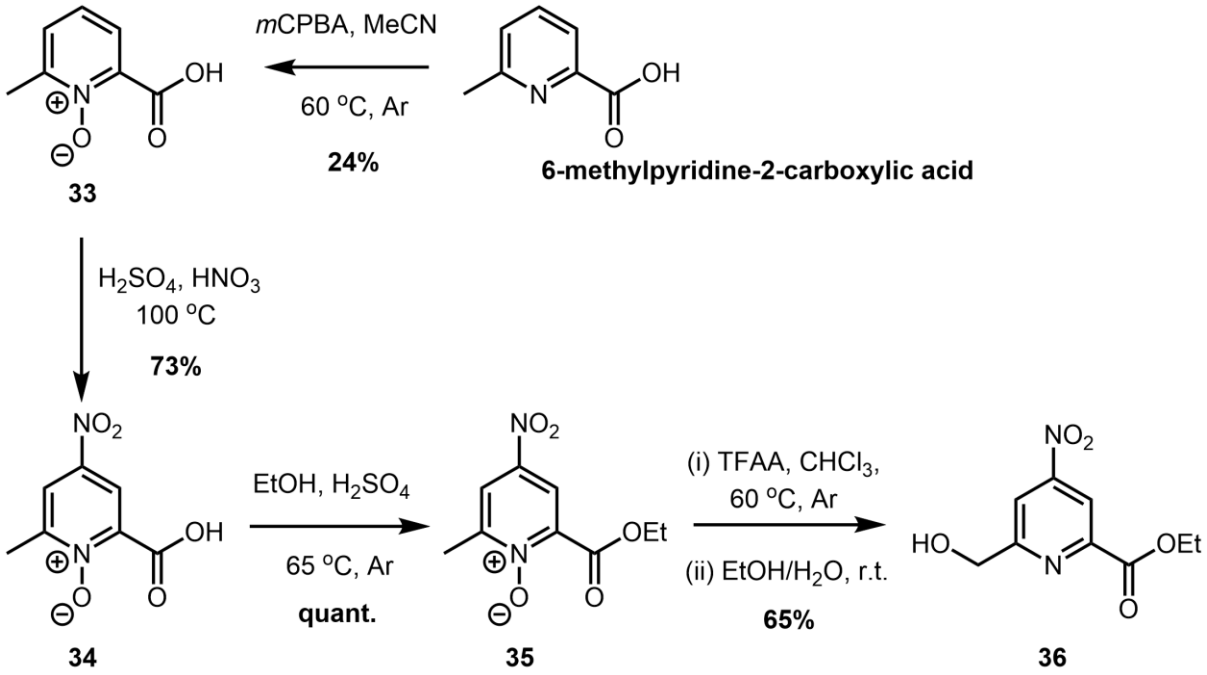

Figure 2.32. Synthesis of the previously reported intermediate compound **36** from commercially available 6-methylpyridine-2-carboxylic acid via *N*-oxide formation, nitration of the activated pyridyl, esterification, and a Boekelheide rearrangement.

Compound **33** has been previously reported in the literature[121] and was synthesised here using the following adapted procedure. Commercially available 6-methylpyridine-2-carboxylic acid was dissolved in dry acetonitrile (MeCN). To the solution, two equivalents of *m*CPBA were added and the reaction mixture was stirred at 60 °C overnight. Oxidation of pyridine occurs in the presence of *m*CPBA to generate the *N*-oxide. The ring activation imparted by the *N*-oxide allows the nitration performed in the following step. The crude product was purified by column chromatography to yield compound **33** (24% yield, silica, 50:50 EtOAc:hexane, increasing to 100% EtOAc in 10% increments, then 1% acetic acid in EtOAc).

Compound **34** was synthesised as reported previously in the literature.[121] Use of the *N*-oxide **33** activates the pyridyl ring making it more nucleophilic while preventing reaction at the nitrogen atom; the *N*-oxide has a higher HOMO and so is more reactive to electrophiles while the oxygen blocks reaction at the nitrogen.[122] Under nitrating

conditions, compound **33** is selectively nitrated at the *para*-position to the *N*-oxide. Inspection of the resonance structures of compound **33** demonstrates that the most nucleophilic sites are at the *ortho* and *para*-positions to the *N*-oxide, (Figure 2.33). Since both *ortho*-positions are already substituted in compound **33**, selective nitration occurs at the *para*-position. Subsequent proton loss to regain aromaticity forms compound **34**. The reaction was monitored by LCMS and upon completion the mixture was quenched by ice and used in the next step without further purification (73% yield).

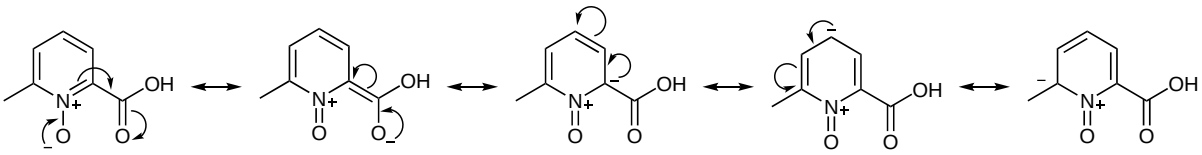

Figure 2.33. Resonance structures of compound **33**.

Compound **35** was synthesised exploiting an acid catalysed esterification reaction.[121] Compound **34** was stirred at 70 °C under argon in excess EtOH and in the presence of sulfuric acid. Sulfuric acid protonates the carbonyl oxygen, which promotes nucleophilic attack at the carbon by EtOH. The adduct tautomerises and water is eliminated to form the ester compound **35**, which was used in the next step without further purification (quantitative conversion).

Compound **36** was obtained through a Boekelheide rearrangement. The mechanism for a Boekelheide rearrangement is shown in Figure 2.34. Upon addition of trifluoroacetic anhydride to a solution of compound **35** in $CHCl_3$, the *N*-oxide O^- performs a nucleophilic attack on the trifluoroacetic anhydride. Trifluoroacetate is liberated leaving the intermediate with a positive charge on the nitrogen atom. The acidic *α*-methyl group is deprotonated by trifluoroacetate to form an alkene. A subsequent [3,3]-sigmatropic shift affords the trifluoroacetylated methyl pyridine derivative of compound **35**. Hydrolysis of the trifluoroacetic ester derivative in 1:1 water/EtOH liberates compound **36** (65% yield).

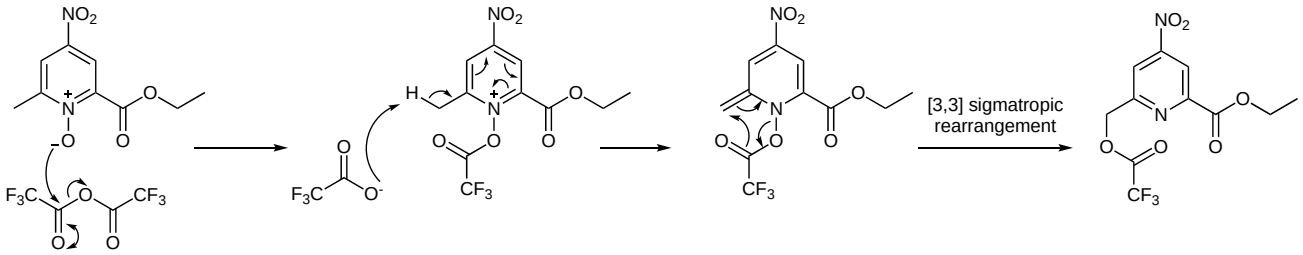

Figure 2.34. Boekelheide rearrangement of compound **35** to form compound **36** in the presence of TFAA.

*2.2.6. Synthesis of pro-L[5] and **[Eu.L[5]]***

Once the precursors to the pendant arms and diBoc TACN required to synthesise the ligand precursor *pro*-L[5] were obtained, a study was conducted to determine the optimal order of alkylation of the chromophore arm precursor and nitro single arm precursor, compounds **31** and **36** respectively, onto a TACN scaffold. Control over the number of TACN sites alkylated is achieved *via* Boc protection chemistry. *A priori*, one could either alkylate by adding both chromophore arms first followed by the single arm or the opposite way round.

Both the chromophore arm precursor and nitro single arm precursor were quantitatively converted to their mesylate analogues, compounds **32** and **37** respectively, prior to alkylation. Formation of the mesylates was confirmed by the appearance of an additional resonance in their ^{1}H NMR spectra corresponding to the mesylate methyl group. An S_N2 alkylation reaction to graft the chromophore arms onto the TACN scaffold was performed in the presence of potassium carbonate in acetonitrile under an argon atmosphere at 60 °C (72% yield). Subsequent removal of the Boc protection group required use of trifluoroacetic acid and was carried out in DCM (20% v/v TFA in DCM). Under alkylation or deprotection conditions two possible side reactions were identified that would form undesired by-products: under alkylation conditions, the *p*-NO_2 group may be susceptible to nucleophilic aromatic substitution; under deprotection conditions, the alkynyl group of the chromophore precursor in trifluoroacetic acid is susceptible to hydration to give the corresponding enol, (Figure 2.35).[52] For this reason, a preliminary study of the optimal alkylation order was performed.

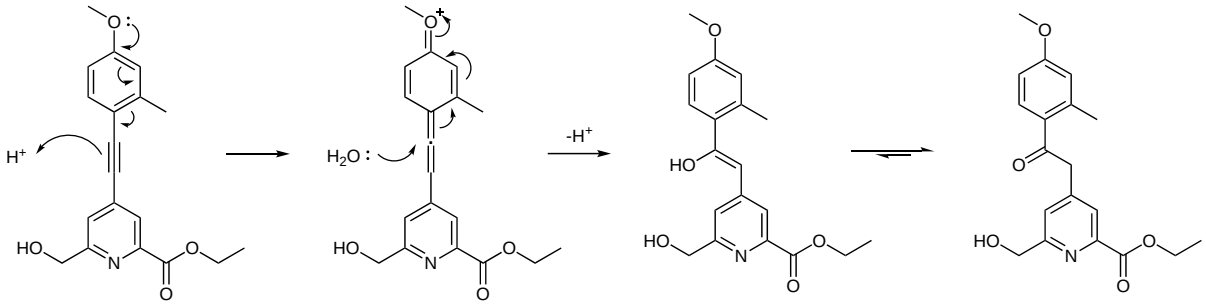

Figure 2.35. Proposed mechanism for hydration of the chromophore arm. Adapted from [52].

The *para*-nitro substituent in the single arm precursor was designed to be easily substituted by nucleophiles such as thiols for late-stage functionalisation. Previously reported *para*-nitro complexes have demonstrated nucleophilic substitution in relatively mild conditions.[123] Hence, the basic conditions employed in the alkylation steps present a potential obstacle to the formation of the synthetic target **[Eu.L^5]**. Two alternative synthetic routes were proposed, (Figure 2.36), differing in the order of grafting, and corresponding deprotection of the various compounds involved.

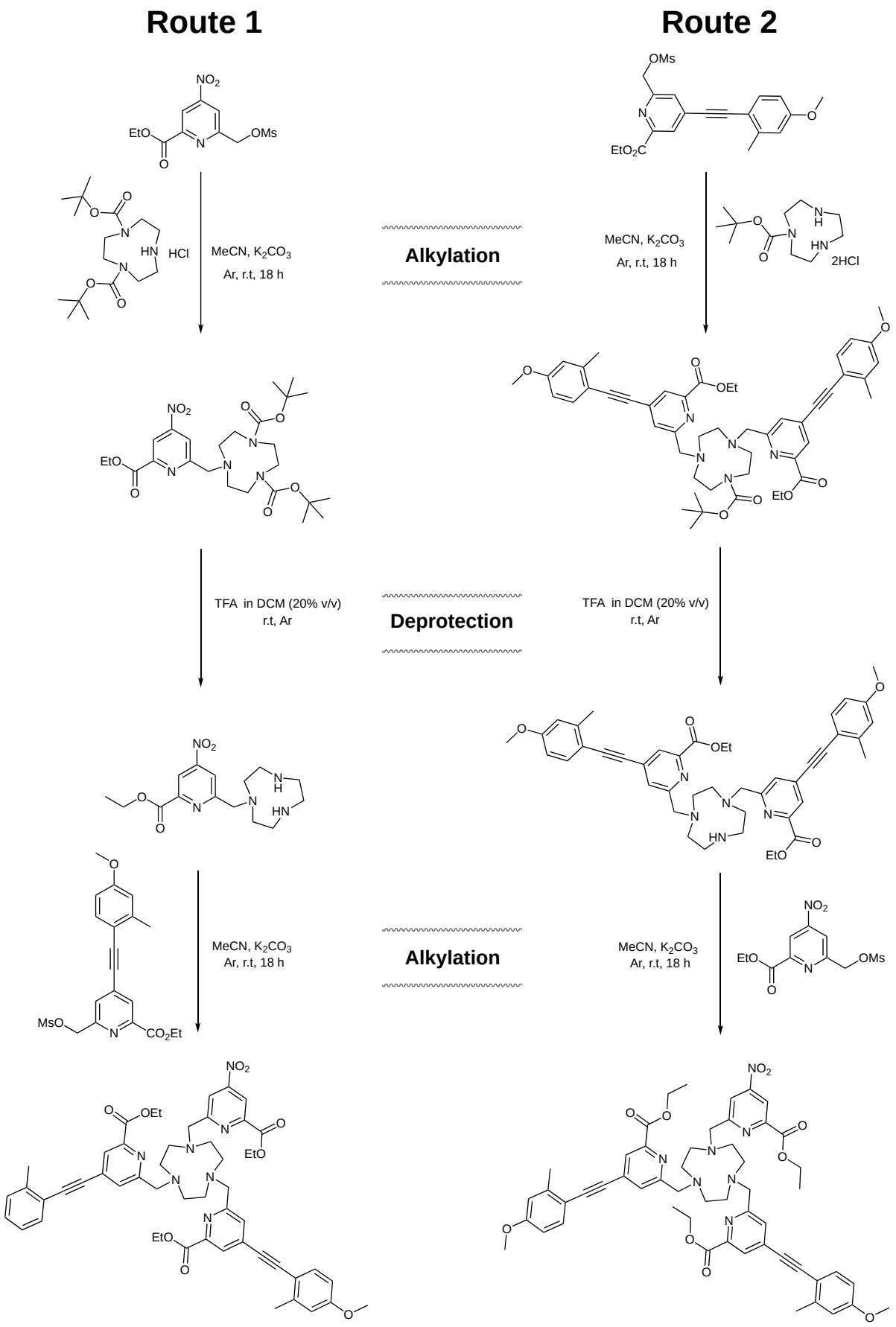

Figure 2.36. Proposed synthetic route options for the synthesis of **[Eu.L^5]**, differing in the order of addition of the chromophore arms and the nitro single arm.

In route 1, the mesylate of the single arm precursor is first grafted onto diBoc TACN. DiBoc TACN has only one nitrogen atom available for alkylation, hence ensuring precise control over the number of substituents installed on the macrocycle. The resulting compound is deprotected using trifluoroacetic acid prior to installation of the chromophore arms. Route 1 avoids exposure of the chromophore arm to trifluoroacetic acid. Route 2 follows the alternative order: the mesylate of the chromophore precursor is first grafted onto a TACN scaffold this time with only one protecting Boc group (monoBoc-TACN). The resulting compound is deprotected using trifluoroacetic acid prior to installation of the single arm, limiting exposure of the nitro group on the single arm to basic conditions to one reaction rather than two.

A study was conducted to determine which of the two previously described routes was the most viable. The aim of the study was to test the stability of the chromophore precursor in trifluoroacetic acid and compare this to the stability of the nitro group of the nitro single arm precursor in 4 equivalents K_2CO_3. A solution of the nitro single arm precursor **36** (14 mg, 0.061 mmol) in MeCN was stirred with K_2CO_3 (34 mg, 0.25 mmol) for 72 h under argon at room temperature. The single arm precursor was observed to be completely stable, with LC/MS monitoring demonstrating no substitution of the starting material. At the same time, a solution of the chromophore arm precursor (12 mg, 0.037 mmol) in trifluoroacetic acid in DCM (20% v/v) was monitored over time when it was stirred at room temperature under argon for 72 h. Significant hydration of the chromophore arm precursor was observed. Figure 2.37 demonstrates the amount of the hydrated product, reported as a percentage of the total amount of chromophore and hydrated product as a function of time, obtained from the relative integrals of the total ion count peaks in the LC/MS.

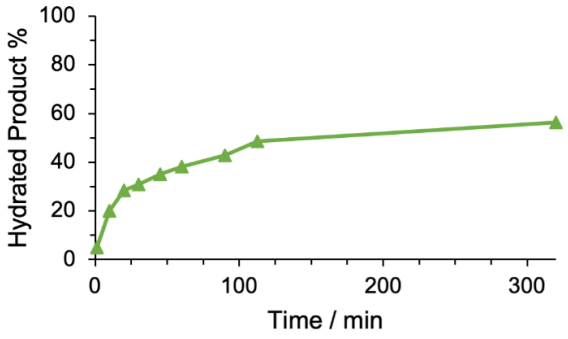

Figure 2.37. Amount of hydrated product formed over time (*green triangles*), reported as a percentage of the total amount of chromophore and hydrated product when the chromophore precursor was stirred in TFA in DCM (20% V/V) solution.

The results from the study demonstrate the vulnerability of the alkynyl group in the chromophore precursor and its subsequent derivatives to hydration in acidic conditions. Based on these results and the apparent stability of the nitro group on the single arm to potassium carbonate, it was decided to proceed using route 1, avoiding exposure of the alkynyl group to trifluoroacetic acid, as shown in Figure 2.36. In the alkylation steps the inorganic salts formed were removed by centrifugation. Di-*tert*-butyl 7-((6-(ethoxycarbonyl)-4-nitropyridin-2-yl)methyl)-1,4,7-triazacyclononane-1,4-dicarboxylate, compound **39**, was formed in 67% yield and deprotected without further purification. The deprotection step proceeded with a quantitative yield and subsequent alkylation afforded *pro*-L^5 in 72% yield.

Once the precursor to the ligand *pro*-L^5 had been isolated, the complex **[Eu.L^5]** was synthesised using the established procedures of hydrolysis and complexation (Figure 2.38) as previously reported.[18]

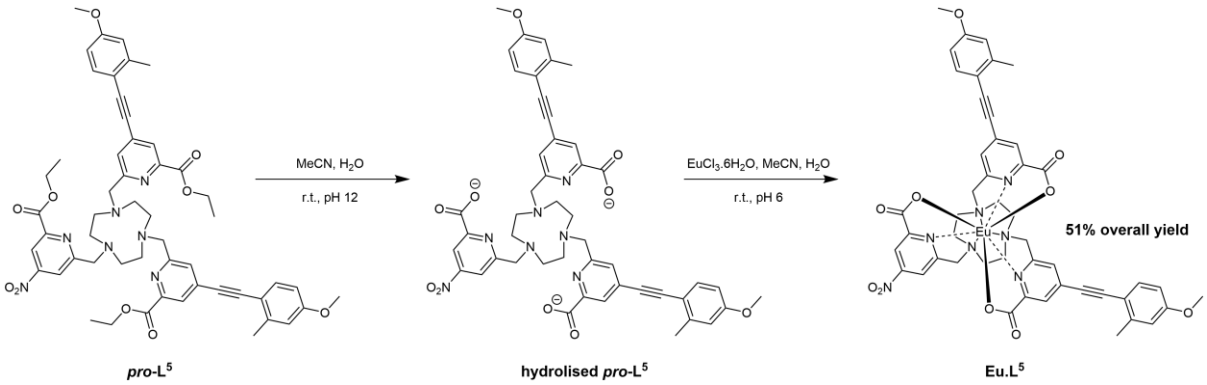

Figure 2.38. Hydrolysis and complexation of *pro*-L^5 to form **[Eu.L^5]**.

First, the three ethyl ester groups on *pro*-L^5 are hydrolysed. 1 M NaOH solution was used to adjust a 50/50 v/v solution of *pro*-L^5 in MeCN and H_2O to pH 12. The hydrolysis was monitored by LCMS and once complete, 1M HCl was added to adjust the solution to pH 6.5, prior to the addition of Eu(III) chloride hexahydrate. The presence of the nine donor atoms on the now hydrolysed ligand provides a stable coordination site for Eu(III), and complexation occurs to form **[Eu.L^5] (**51% yield over two steps). The complex was obtained in large amounts (50 mg) compared to the usual scale of phosphinate-based complexes (order of milligrams), allowing for the exploration of bulk applications such as thin films and polymer conjugation studies.

*2.2.7. Stability of **[Eu.L^5]** in Nucleophilic Solvents*

[Eu.L^5] is formed as a racemic mixture of the *Δ*(*λλλ*) and *Λ*(*δδδ)* enantiomers. To enable potential future use as a chiral CPL emitter, the complex **[Eu.L^5]** must be resolved into the two enantiomers using chiral HPLC. Prior to attempting chiral resolution, the stability of **[Eu.L^5]** in MeOH and H_2O was investigated at room temperature and at 60 °C to determine if the complex would be robust for attempted chiral HPLC using these solvents and for future applications. The stability tests were carried out due to concerns that the nitro group on the single arm could undergo nucleophilic substitution, preventing the use of MeOH, the solvent of choice for chiral resolution on the available chiral columns (Daicel ChiralPak IC & ID). The complex was observed to be completely stable under the conditions at room temperature and at 60 °C, as confirmed *via* LCMS.

The stability of **[Eu.L^5]** in MeOH allowed for the testing of chiral HPLC resolution conditions in isocratic methanol, isocratic ethanol, and isocratic acetonitrile. However, no chiral separation was achieved. A more thorough investigation needs to be performed to resolve the two enantiomers of **[Eu.L^5]** on chiral HPLC.

*2.2.8. Thiol Substitution of **[Eu.L^5]** as a Proof-of-concept for Bioconjugation*

Previous studies have reported the synthesis of a diphosphinate analogue of **[Eu.L^5]** that was shown to undergo nucleophilic aromatic substitution of the nitro group, allowing for late-stage functionalisation of the complex for biological targeting and imaging, (*vide supra* - Section 1.4.1).[18] To demonstrate the potential of **[Eu.L^5]** in analogous applications, a proof-of-concept investigation was undertaken in which the racemate **[Eu.L^5]** was stirred with reduced L-glutathione under various conditions.

A preliminary test was carried out mimicking the conditions used in the reported study, where ammonium bicarbonate buffer solution (25 mM) was used.[18] MeOH was required to assist dissolution of the complex due to its poor solubility in aqueous media. **[Eu.L^5]** (1 mg) was dissolved in MeOH (1 mL). Ammonium bicarbonate solution (3 mL, 25 mM) was added to ensure the reaction was carried out at physiological pH, as being able to perform conjugation under these mild conditions is important for devising biological sensing applications in the future. Two equivalents of reduced L-glutathione

were added and the solution was stirred at 293 K, with monitoring by LCMS. After 6 h, conversion of the complex to **[Eu.L^{5B}]**, the L-glutathione substituted derivative of **[Eu.L^{5}]**, (Figure 2.39) was observed but the starting complex was still present. The reaction was confirmed to have occurred, so a brief optimisation was attempted varying the ratio of ammonium bicarbonate buffer and methanol used as the reaction solvent. To each test solution, varying stoichiometries of reduced L-glutathione were added relative to the amount of **[Eu.L^{5}]**. Full conversion was observed with 25 equivalents of reduced L-glutathione in pure methanol. Future work will aim to optimise the process further, attempting to lower the equivalents of reduced L-glutathione while still obtaining a satisfactory yield. Importantly, **[Eu.L^{5B}]**, was able to be formed under extremely mild conditions: room temperature, exposed to the atmosphere, at physiological pH, and without using harsh conditions or catalysts. The mild conditions mean that the proof-of-concept study has demonstrated that **[Eu.L^{5}]** can be further investigated for its uses in biological applications. A brief photophysical characterisation of **[Eu.L^{5B}]** was obtained, (Table 2.6).

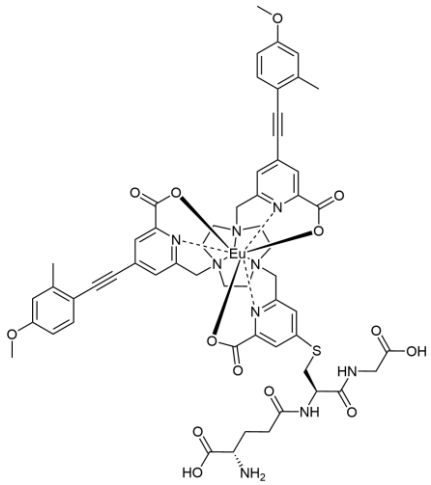

Figure 2.39. Structure of the L-glutathione substituted complex **[Eu.L^{5B}]**.

Table 2.6. Absorption maximum λ_{abs}, quantum yield ϕ, and emission lifetime τ of **[Eu.L^{5B}]** in methanol.

Complex	λ_{abs} / nm	ϕ / %	τ (± 0.03) / ms
[Eu.L^{5B}]	344	7	0.94

*2.2.9. Photophysical Studies and Solvatochromism of **[Eu.L^{5}]***

The racemic complex **[Eu.L^{5}]** was fully characterised by obtaining UV-Vis absorption, excitation, and emission spectra in different solvents. The molar extinction coefficient

$\varepsilon(\lambda)$ was measured in DCM to be (46 ± 6) x 10^3 M^{-1} cm^{-1} at 348 nm. The quantum yield ϕ, brightness $B(\lambda)$, and emission lifetime τ of the complex in various solvents were also measured, (Table 2.7).

Table 2.7: Absorption maximum λ_{abs}, quantum yield ϕ, brightness $B(\lambda)$, and emission lifetime τ of **[Eu.L^5]** in various solvents, with normalised Reichardt polarity parameters E_T^N of the solvents. [a] It is assumed here that quantum yields are constant across the absorption band for [**Eu.L^5**]. [b] The complex was dissolved in minimal MeOH prior to dissolution in H_2O, due to low solubility in H_2O (final solution 10% v/v MeOH in H_2O). N.D. = not determined.

Solvent	λ_{exc} / nm	E_T^N [29]	ϕ / %	$B(\lambda)$ at 348 nm[a] / mM^{-1} cm^{-1}	τ (± 0.03) / ms
H_2O[b]	352	1.000	<1	0.2	0.52
MeOH	348	0.762	14	6.4	0.97
EtOH	346	0.654	13	6.1	0.95
Isopropanol	344	0.546	21	9.5	1.01
MeCN	340	0.460	12	5.7	1.13
DMSO	340	0.444	13	5.8	0.96
DMF	338	0.404	10	4.5	1.02
Acetone	338	0.355	15	6.9	1.12
NMP[124]	332	0.355	ND	ND	0.99
DCM	348	0.309	11	5.2	1.01

A plot of the absorption, emission, and excitation spectra of **[Eu.L^5]** in MeOH is shown in Figure 2.40, displaying a large pseudo-Stokes shift of over 250 nm, that is the difference between the absorption maximum of the sensitising ligand and the characteristic Eu(III) emission at approximately 615 nm.

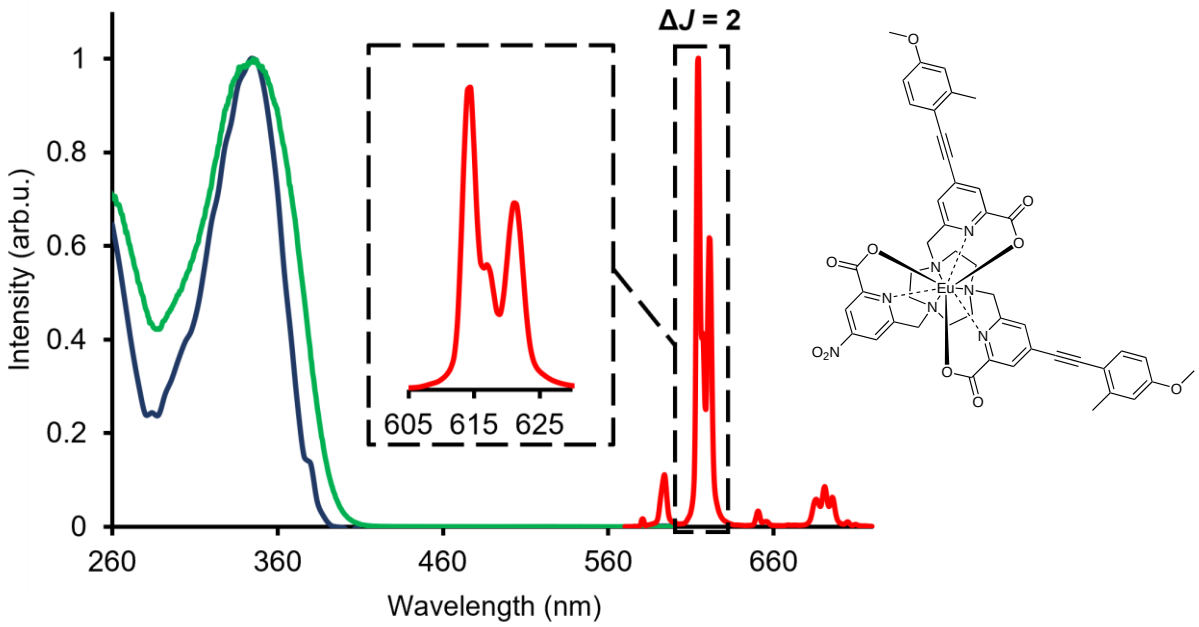

Figure 2.40. Absorption (*blue*), excitation (*green*, λ_{em} = 615 nm), and emission spectra (*red*, λ_{exc} = 348 nm) of **[Eu.L^5]** in methanol. The central insert shows three clear bands in the Δ*J* = 2 manifold.

The excitation spectrum closely follows the curve of the absorption spectrum, confirming that Eu(III) centred emission is occurring in **[Eu.L^5]** as a result of the antenna effect. In the free chromophore arm, the energy absorbed during excitation is re-emitted as short-lived fluorescence. When the chromophore is bound in the complex, the energy transfer rate is larger than the rate of radiative emission from the chromophore. As a consequence, it is the long-lived emission from Eu(III) that is observed while fluorescence from the ligand is completely suppressed.[121]

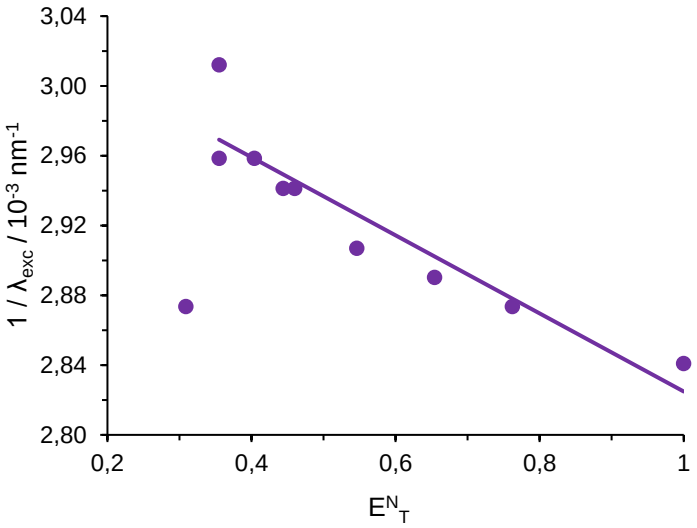

Figure 2.41: Maximum absorption frequency as a function of normalised Reichardt solvent polarity parameter E^N_T (purple) for **[Eu.L^5]** in various solvents, exhibiting positive solvatochromism.

With the exception of DCM, **[Eu.L^5]** displays an increase in λ_{abs} as the relative polarity of the solvent increases (Table 2.7, Figure 2.41). The increase in λ_{exc} with increasing solvent polarity results from the relative stabilisation of the ground and excited charge transfer states of the complex. The excited charge transfer state is preferentially stabilised compared to the ground state, with a larger relative stabilisation in more polar solvents, (discussed in Section 1.2.5). In more polar solvents, the absorptive transition has lower energy, resulting in the so-called positive solvatochromism observed here. The inverse dependence of the absorption maximum with increasing solvent polarity is consistent with an increased stabilisation of the internal charge transfer state in more polar solvents, previously discussed in Section 1.2.5. An analogous complex previously reported, bearing three chromophore arms of identical nature to **[Eu.L^5]** but with all phosphinate donors instead of carboxylate donors, also demonstrated positive solvatochromism.[65] The point in Figure 2.41 resulting from **[Eu.L^5]** in DCM is an outlier and suspected to be due to the presence of specific solvent effects in DCM, such as H bonding.

No correlation between the solvent polarity and the quantum yield and lifetime of **[Eu.L^5]** in solution was observed. Notably, **[Eu.L^5]** in water had an exceptionally low quantum yield, which can be rationalised considering the effective quenching of the europium excited states by O–H oscillators (*vide supra* – Section 1.1.4), which can

interact more with the central lanthanide ion due to their weaker binding affinity compared to phosphinate-based ligands.

The spectral form of the total emission spectrum of **[Eu.L^5]** was found to be solvent dependent, (Figure 2.42.A). Previous studies have shown that the Δ*J* = 2 and Δ*J* = 4 manifolds in Eu(III) complexes are sensitive to solvent effects[65] so these were investigated in more detail for **[Eu.L^5]**, (Figure 2.42.B-C). The most intense transition A, in the Δ*J* = 2 manifold centred around 614 nm, showed a very minor change in the maximum; with increasing solvent polarity a small bathochromic shift was observed. The shoulder of the main transition results from another transition that has been resolved previously for complexes with all phosphinate donors[65] but cannot be resolved for the complex **[Eu.L^5]** which has all carboxylate donors. **[Eu.L^5]** displays two main bands in the Δ*J* = 2 manifold, consistent with previously reported all carboxylate donor analogues[106] and with the *quasi-C*$_3$ symmetry of the ligand field. A longer wavelength transition ***B*** centred around 622 nm is also visible and with increasing solvent polarity a hypsochromic shift of the maximum was observed.

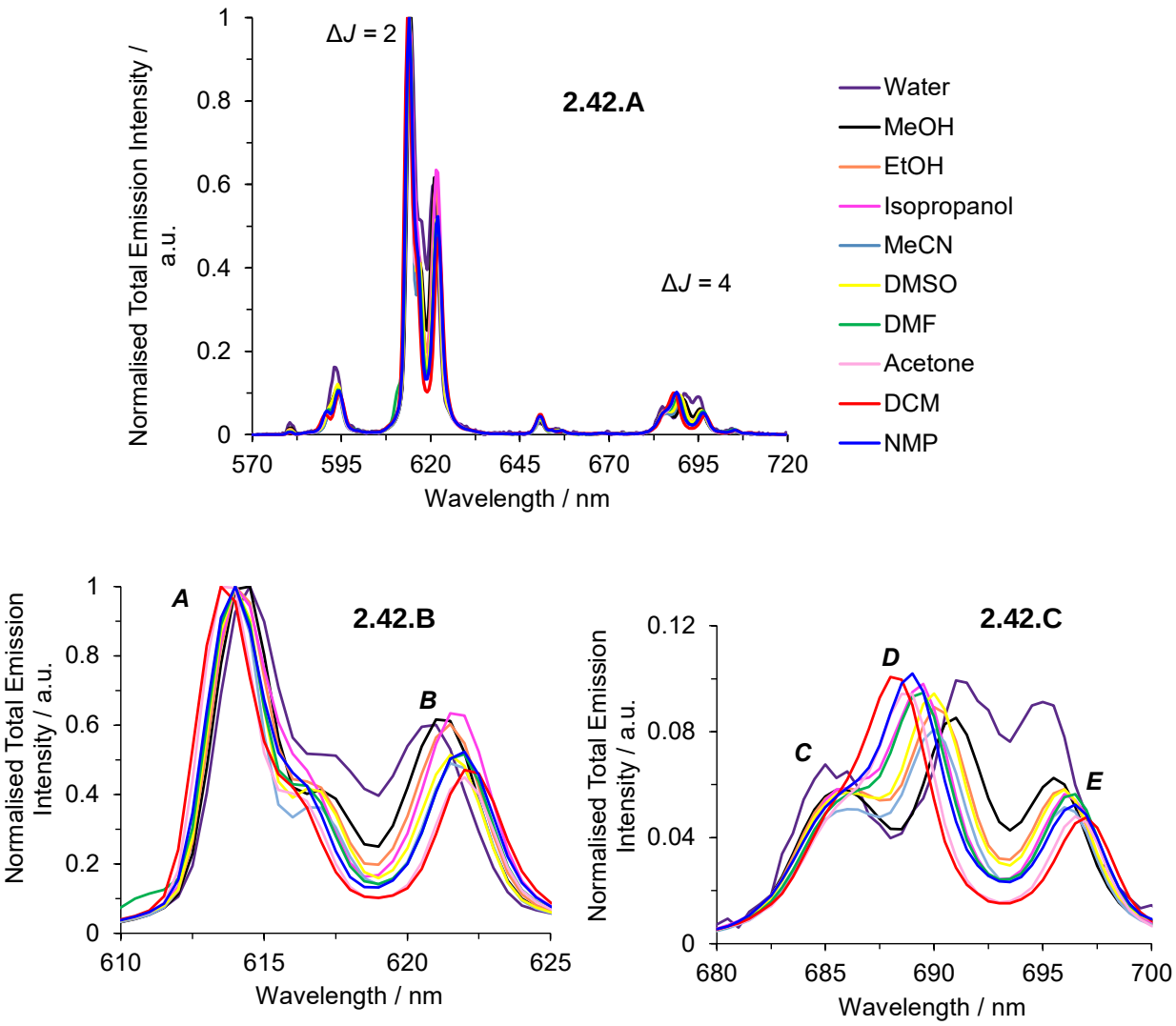

Figure 2.42: (**2.42.A**) Total emission spectra of **[Eu.L^5]** in various solvents (excitation at λ_{exc} for each solvent). Expanded emission spectra of **[Eu.L^5]** in various solvents to show the ΔJ = 2 (**2.42.B**) and ΔJ = 4 (**2.42.C**) manifolds. Legend for all three figures shown in top right.

In the Δ*J* = 4 manifold, the most intense transition ***D*** was observed around 689 nm with a transition ***C*** not clearly resolved around 685 nm and a third transition ***E*** around 696 nm. The transition ***C*** appears to display little variation in intensity or position with solvent polarity. With increasing solvent polarity, the most intense transition ***D*** was observed to undergo a bathochromic shift. In contrast, transition **C** appears to undergo a hypsochromic shift as solvent polarity increases.

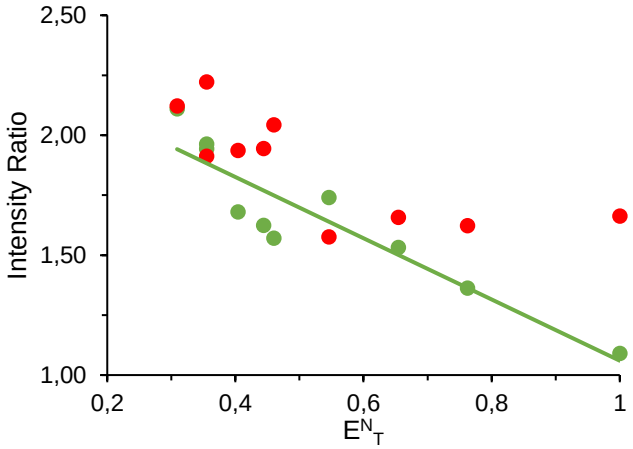

Figure 2.43: Ratios of the intensity of emissive transitions ***A*** *vs.* ***B*** (red) and ***D*** *vs.* ***E*** (green) in **[Eu.L^5]** as a function of solvent polarity. Transitions are labelled as described in Figure 2.42.

The intensity ratios of emissive transitions ***A*** *vs.* ***B*** (*red*, 614 – 621 nm) and ***D*** *vs*. ***E*** (*green*, 688 – 697 nm) in the Δ*J* = 2 and Δ*J* = 4 manifolds respectively were compared to determine if there was any correlation with solvent polarity, (Figure 2.43). For the intensity ratio of ***D*** *vs.* ***E***, a negative correlation was observed with increasing solvent polarity.

In the total emission spectra of **[Eu.L^5]**, the Δ*J* = 2 manifold and the Δ*J* = 4 manifold were found to be highly solvent dependent as seen in previous studies.[52,65] As will be demonstrated in the following pages, **[Eu.L^5]** was shown to have no water molecules present in its primary coordination sphere, (*vide supra* - Section 2.1.11). It is reasonable to suggest that solvent polarity effects on the ligand field are not due to first-shell interaction but rather to the influence the hypersensitive transitions and that the coupling of the solvent dipole to the chromophore arm dipole, especially in the internal charge transfer state, affect its polarisability and therefore the emission spectra of the complex.

*2.2.10. Effect of Deuterated Solvents on the Photophysical Properties of **[Eu.L^5]***

The photophysical properties of **[Eu.L^5]** in deuterated ethanol (EtOD) and deuterium oxide (D_2O) were also measured. A comparison between the photophysical properties of **[Eu.L^5]** in the deuterated solvents and their hydrogenated analogues is presented in Table 2.8.

Table 2.8: Absorption maximum λ_{exc}, quantum yield ϕ, brightness $B(\lambda)$, and emission lifetime τ of **[Eu.L^5]** in H_2O and EtOH and their deuterated analogues.
[a] It is assumed here that quantum yields are constant across the absorption band for **[Eu.L^5]**.
[b] The complex was dissolved in minimal MeOH prior to dissolution in H_2O, due to low solubility in H_2O (final solution 10% V/V MeOH in H_2O).

Solvent	λ_{exc} / nm	ϕ / %	B(348 nm)[a] / mM^{-1} cm^{-1}	τ (± 0.03) / ms
H_2O[b]	348	0.50	0.2	0.52
EtOH	348	13	6.1	0.95
D_2O	350	0.78	0.4	0.60
EtOD	352	21	9.8	1.07

A 56% increase in quantum yield was observed going from H_2O to D_2O, along with a 15% increment in emission lifetime. Analogously, a 62% increase in quantum yield and a 12% increase in emission lifetime were observed going from EtOH to EtOD. These increases can be attributed to a reduced amount of vibrational quenching of the Eu(III) excited state in the deuterated solvents. As seen in Section 1.1.4, quenching of the $^5D_0$ state by five vibrational quanta of the O–D bond is less efficient than quenching by three vibrational quanta of the O–H bond.[125]

Using equation 2.2,[126] the number of solvent molecules in the first coordination sphere of **[Eu.L^5]** was calculated to be 0.27 ± 0.13, *i.e.* no water molecules are present in the first coordination sphere of **[Eu.L^5]**. This result provides direct evidence for the complete saturation of the primary coordination sphere of **[Eu.L^5]** by the TACN-based ligand.

$$q = 1.11\ [\tau_{H2O}^{-1} - \tau_{D2O}^{-1} - 0.31] \qquad (2.2)$$

*2.2.11. Multiphoton Excitation of **[Eu.L^5]***

The requirement for simultaneous absorption of two photons means 2PE can put small voxels under investigation; only points where the intensity of excitation light is high enough will have enough photons present for 2PE.[69] 2PE was attempted for **[Eu.L^5]** in ethanol as a proof-of-concept study, assessing the viability for **[Eu.L^5]** to be excited in this way. The excitation maximum of **[Eu.L^5]** in ethanol had been determined previously as 346 nm, so the emission spectrum of **[Eu.L^5]** was recorded at excitation wavelengths from 680 – 710 nm. The two-photon emission intensities were superimposed on the single-photon absorption spectrum, (Figure 2.44.A). The form of the emission spectrum of **[Eu.L^5]** in ethanol being unchanged when excited at 355 nm or 710 nm (a detail of the $\Delta J = 2$ manifold is shown in Figure 2.44.B) confirms that the emission does not depend on the pathway used to populate the emissive excited state. The dependence of the emission intensity on the laser power was measured, (Figure 2.44.C), and the slope was found to be 1.75 ± 0.15, confirming that excitation does indeed occur *via* a 2PE process. Finally, using equation 11, with comparison to rhodamine B in methanol,[72] the 2PE cross-section of **[Eu.L^5]** in ethanol was calculated to be 460 GM, where 1 GM = 10^{-50} cm^4 photon^{-1}.

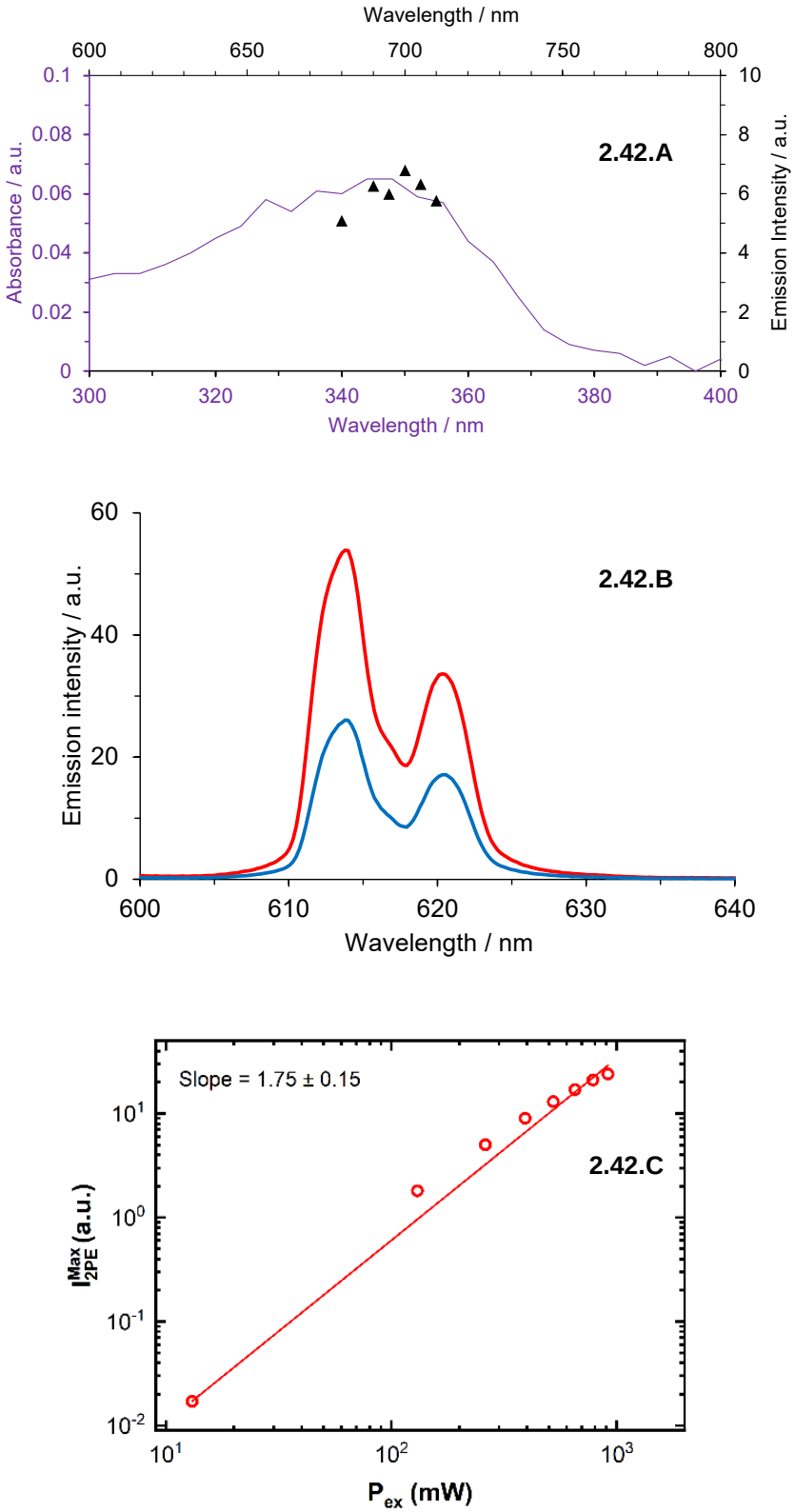

Figure 2.44: (2.44.A) Single-photon absorption spectrum (*solid purple line*) and 2PE emission intensity (*black triangles*) for **[Eu.L^5]** in EtOH. **(2.44.B)** Emission spectra of **[Eu.L^5]** from 1PE (λ_{exc} = 355 nm, *red*) and 2PE (λ_{exc} = 710 nm, *blue*) in ethanol. **(2.44.C)** Power dependency of the emission intensity (*red circles*) of the 2PE at λ_{exc} = 700 nm.

*2.2.12. Late-stage substitution of the para-nitro group of **[Eu.L^5]***

Failure of chiral resolution of **[Eu.L^5]** is attributed to its poor solubility in MeOH, *i.e.* the solvent of choice for chiral HPLC using the DAICEL ChiralPak-IC and -ID columns, as well as to the strong electron withdrawing effect of the nitro group, effectively reducing the intensity of the *π*-stacking interactions with the aromatic moieties in the chiral stationary phase. Other solvents that provide better solubility were trialled as the mobile phase for chiral resolution, such as EtOH, MeCN, EtOAc, but without success. For this reason, late-stage substitution of the electron withdrawing *para*-nitro group of **[Eu.L^5]** for an electron donating *para*-methoxy group was attempted, (Figure 2.45).

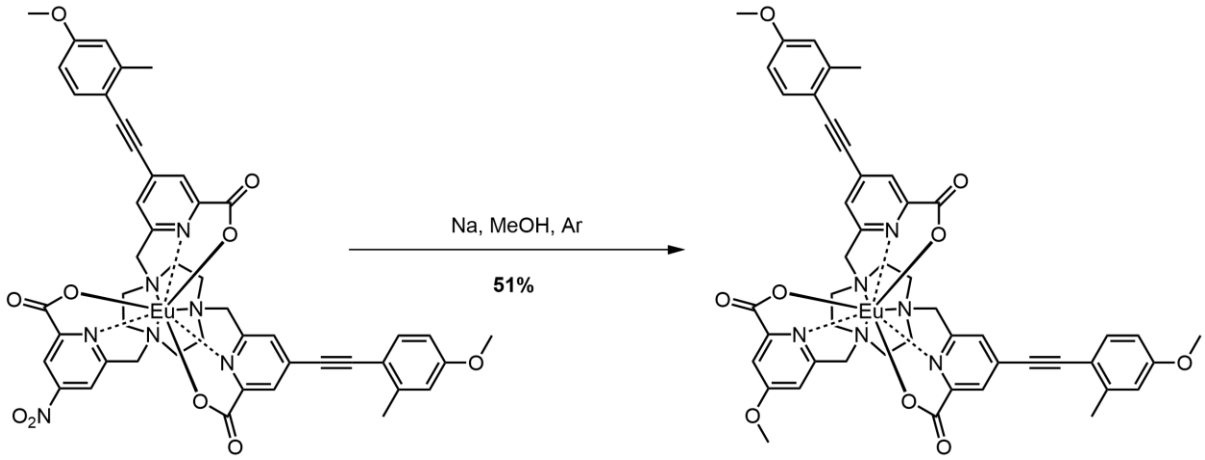

Figure 2.45: Late-stage substitution of the *para*-nitro group with a *para*-methoxy group.

Sodium methoxide formed *in situ* by oxidising metallic sodium with methanol was used as the nucleophile to readily displace the *para*-nitro group via nucleophilic aromatic substitution, exploiting a late-stage functionalisation concept previously described in the literature.[123] The reaction proceeded to completion as soon as the sodium methoxide solution was added to the **[Eu.L^5]** complex. This was evident due to the low solubility of the *para*-nitro complex in MeOH, as opposed to the *para*-methoxy product, resulting in the immediate disappearance of the white suspension to afford a clear light-yellow solution. Chiral HPLC failed in this case too: the next step consists of the exploration of different chiral stationary phases with which the complex interacts more strongly. A screening approach is necessary since it is not possible to predict how the complex will interact with different chiral stationary phases.

2.3. Tb(III) Complexes for OLEDs

2.3.1. Definition of the target

The structures of three possible synthetic targets, hereinafter collectively referred to as **[Tb.L^{A-C}]**, are shown in Figure 2.46. These complexes are based on a 1,4,7-triazacyclononane (TACN) scaffold possessing C_3 symmetry about the central metal ion. The TACN macrocycle is grafted with three identical pendant biaryl arms. Biaryl chromophores are efficient sensitisers for Tb(III) emission due to their excited state at around 22,000 cm^{-1} (the emissive level of Tb(III) $^5D_4$ is 22,450 cm^{-1}).[17,127] The large steric hindrance afforded by the phenyl phosphinate donor arms make these complexes good candidates for chiral resolution via chiral HPLC.

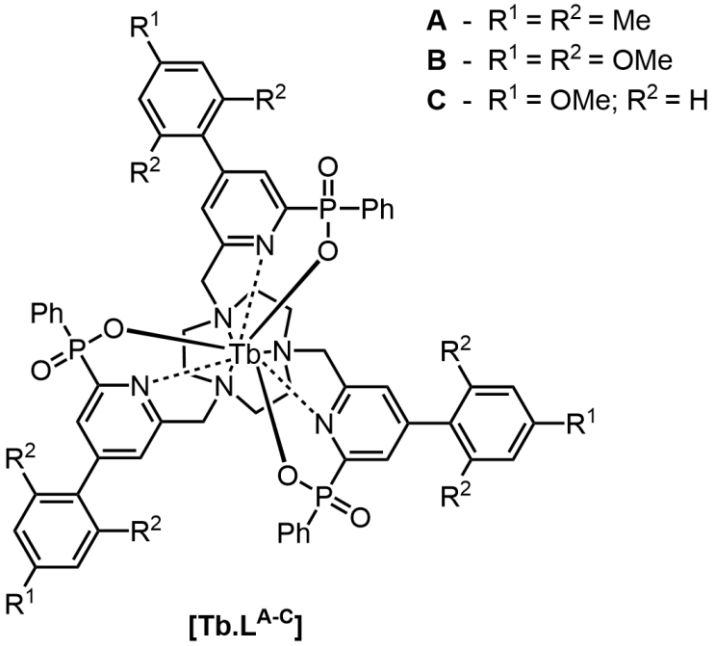

Figure 2.46. Structure of the three proposed synthetic targets **[Tb.L^{A-C}]**.

Diversity is easily included using different commercially available top aryl rings with varying substituents, for example compounds **A-C**. The substituents are expected to affect the solubility of the complex while only marginally affecting the sensitisation efficiency of the antenna, therefore allowing tailoring of solubility in chlorinated solvent usually preferred to make OLEDs *via* solution-based processing. High brightness due to efficient biaryl antenna sensitisation and highly dissymmetric CPL arising from Tb(III), coupled with high thermal and racemisation stability due to the high steric bulk of the phenyl phosphinate donors are expected to afford good CP-OLEDs with a long lifespan.

The photophysical characterisation of racemic and enantiopure complexes was carried out in Durham, whereas electrochemical characterisation and OLED trialling were performed at Imperial College by Dr Francesco Furlan. Identification of the HOMO – LUMO of the complex was performed by cyclic voltammetry following a procedure previously reported at University of Pisa.[128]

*2.3.2. Synthesis of **[Tb.L^{A-C}]***

A schematic description of the synthetic route to afford **[Tb.L^{A-C}]** is presented in Figure 2.47.

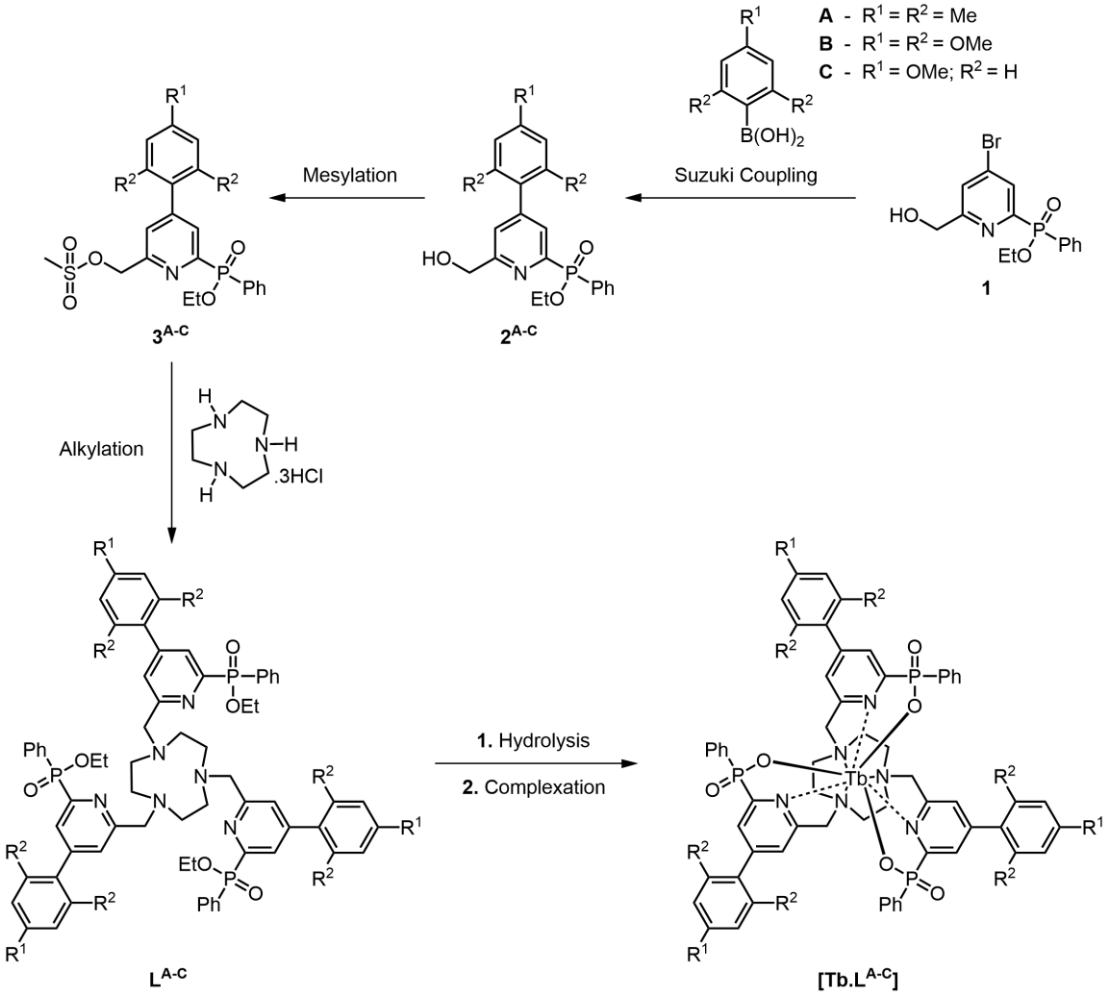

Figure 2.47. Schematic synthetic route to make **[Tb.L^{A-C}]** from a common intermediate prepared in 5 steps, compound **1**, and three commercial arylboronic acids, compounds **A-C**.

The common precursor **1** can be reacted with three different arylboronic acids, compounds **A-C**, in palladium(0)-catalysed Suzuki-Miyaura cross-couplings to afford

the chromophores as alcohols (compounds **2^{A-C}**). Similar coupling reactions on analogous substrates have been reported in detail.[45] To probe the feasibility of this synthetic step, a small scale proof-of-concept test were carried out successfully. Mesylation of the antenna to facilitate the subsequent trialkylation of TACN, followed by hydrolysis of the phosphinate esters and complexation with a suitable Tb(III) salt will afford the targets **[Tb.L^{A-C}]** as a racemic mixture.[55,123] **[Tb.L^{A}]** was selected as the representative of the **[Tb.L^{A-C}]** series and synthesised to perform the preliminary work described in the present section.

Suzuki coupling reaction conditions were optimised using a different, easier to prepare precursor compared to the phenyl phosphinate pyridyl shown in Figure 2.47, *i.e.* the previously synthesised dicarboxylate ester, compound **1**. This was done under the assumption that the specific nature of the ester groups does not affect the reactivity of the *para*-bromo group towards the arylboronic acid. Three reaction conditions were trialled based on previous examples in the literature, all using caesium carbonate as the base, in different solvents and with different palladium catalysts, (Figure 2.48).[45,123,129] Reactions were performed at 90 °C after degassing the solution for 15 minutes prior to the addition of the catalyst. LC/MS was performed after 48 hours revealing that all conditions resulted in yields around 60%. However, condition number 2 was picked due to the absence of side products for the sake of an easier purification.

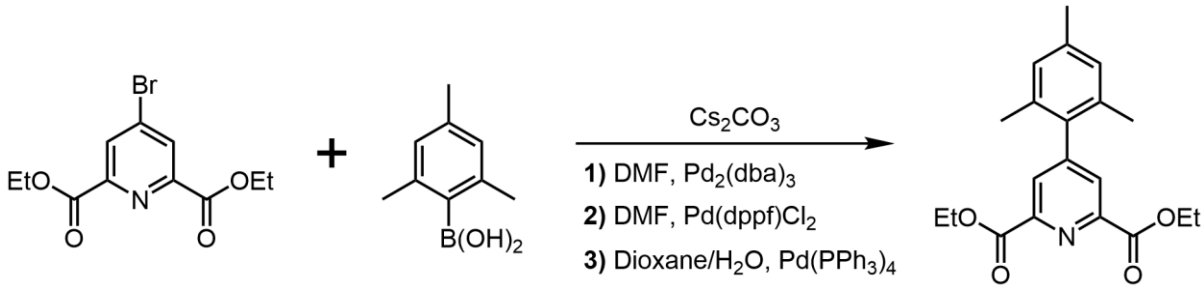

Figure 2.48. Three conditions to test solvent and palladium catalyst for Suzuki coupling.

Reaction conditions 2 were used to prepare compound **2^{A}** as shown in Figure 2.48. The crude product showed no starting material in LC/MS after 48 hours. The product was extracted in EtOAc/10% LiCl w/w in water to remove DMF. The black residue obtained by evaporating the organic layer was further purified on reverse phase HPLC in MeCN/water to afford the product with a 58% yield. Analogous reaction conditions were used to prepare compound **2^{B}** from the corresponding top aryl **B**. However, the

reaction proceeded at a slower rate due to the larger steric hindrance at the boronic acid reaction site. Compound **2^{A}** was selected over its counterpart **2^{B}** to explore the rest of the synthetic route due to its easier preparation.

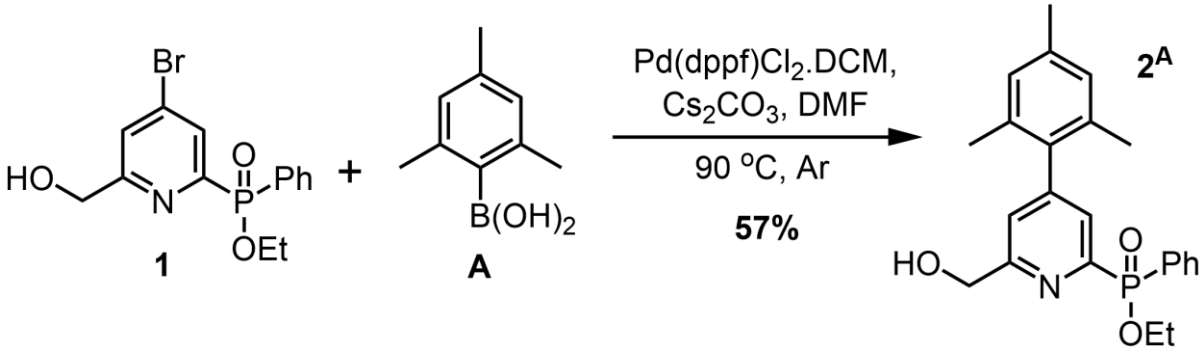

Figure 2.49. Preparation of the biaryl antenna **2^{A}** from its precursors **1** and **A**.

Mesylation of **2^{A}** in quantitative yield with methylsulphonic anhydride and DIEA in anhydrous THF and following alkylation on TACN with potassium carbonate basic catalyst in anhydrous MeCN of the ligand **L^{A}**. The complex **[Tb.L^{A}]** was obtained via alkaline hydrolysis of the three phosphinate esters of **L^{A}** followed by acidic metallation with terbium(III) chloride hexahydrate. The crude complex was purified via reverse phase HPLC in MeOH/water to afford **[Tb.L^{A}]** as a white powder, with an overall 57% yield over two steps.

*2.3.3. Characterisation of the HOMO – LUMO system of **[Tb.L^{A}]***

The HOMO and LUMO energy levels of **[Tb.L^{A}]** were measured using a joint spectrophotometric and electrochemical investigation. Measuring the HOMO and LUMO is essential to find hosts that have energy levels suitable to transfer energy to the host **[Tb.L^{A}]**. Absorption, excitation, and emission spectra of **[Tb.L^{A}]** were acquired in chloroform, (Figure 2.50). Lifetime was measured to be (1.88 ± 0.02) ms.

The band gap is the energy threshold for photons to be absorbed by a material. In the case of **[Tb.L^{A}]**, as shown in Figure 2.50, the band gap is equal to 320 nm (= 3.9 eV). Although not identical, the band gap provides a good first approximation of the HOMO – LUMO gap.

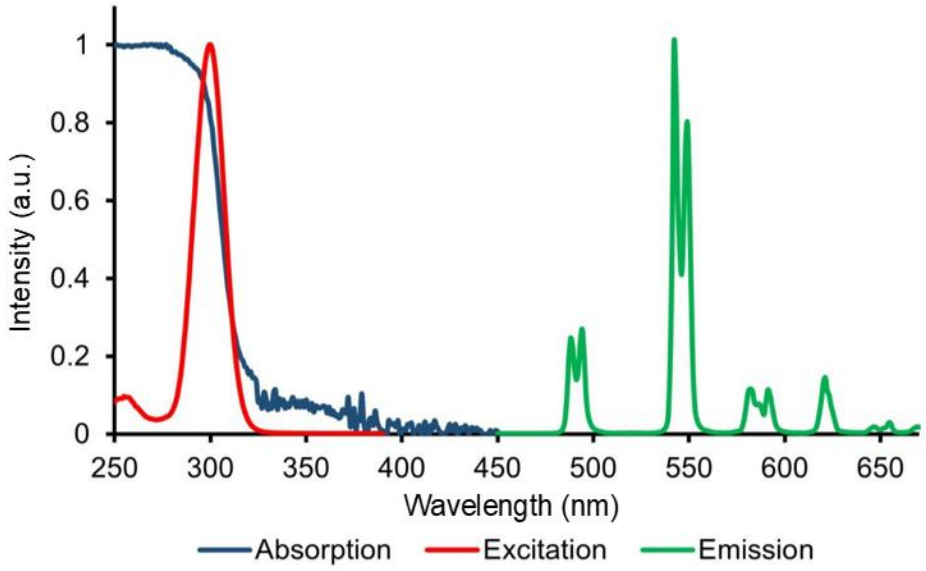

Figure 2.50. Absorption, excitation, and emission spectra of **[Tb.L^{A}]** in chloroform.

Cyclic voltammetry (CV) was performed according to a previously reported procedure[128] (*vide infra* - Experimental Methods Chapter) and is shown in Figure 2.51 and was measured in collaboration with Dr Francesco Furlan and Dr Martina Rimmele at Imperial College London. Cyclic voltammetry is an electrochemical measurement employed to measure redox properties using an electrochemical cell with a 3-electrode configuration: a working electrode, hosting the redox process of interest, a counter electrode, to complete the electrical circuit, and a reference electrode, with a well-defined potential to reference the potential of the other electrodes. All electrodes are immersed in an electrolyte solution and a potential sweep is applied over time, allowing redox reaction to occur at the working electrode. The collected current provides the current-voltage (I-V) characteristics, defined as a voltammogram. The sequence of three reversible reduction peaks corresponds to the sequential reduction of each biaryl antenna to afford the corresponding anionic radical. In the voltammogram shown in Figure 2.51, the first reduction process corresponds to the filling of the LUMO of **[Tb.L^{A}]**. The absolute reduction potential was determined by addition of ferrocene to the solution to reference the potential since its redox potential is known to be +0.4 eV. Combining this absolute measurement with the estimated HOMO – LUMO difference of 3.9 eV, the energies of the HOMO and LUMO of **[Tb.L^{A}]** were calculated to be -6.8 eV and -2.7 eV, respectively.

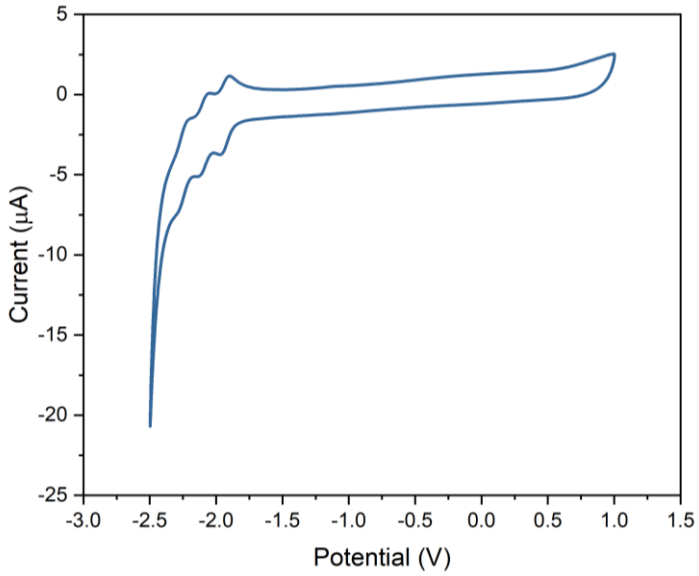

Figure 2.51. Voltammogram of **[Tb.L^{A}]**. 10^{-5} M **[Tb.L^{A}]** in a 0.1 M solution of tetrabutylammonium hexafluorophosphate in MeCN.

2.3.4. Investigation of hosts for OLEDs

Commercially available hosts that are solution processable usually range between a -2.3 eV LUMO and a -6.2 eV HOMO. Efficient charge injection and exciton trapping on the emissive material can occur if the HOMO and LUMO of the active material are contained between those of the host. The remarkably deep HOMO energy of -6.8 eV of **[Tb.L^{A}]** poses a great challenge, since most commonly used host materials have an insufficiently deep HOMO. Two commercially available compounds were identified as potential host material candidates: BSB (4,4'-di(triphenylsilyl)-biphenyl) and TSPO1 (diphenyl[4-(triphenylsilyl)phenyl]phosphine oxide), (Figure 2.52). These were benchmarked against the very commonly used host material PVK:OXD-7 (poly(9-vinylcarbazole : 1,3-bis[2-(4-*tert*-butylphenyl)-1,3,4-oxadiazo-5-yl]benzene), (Figure 2.53). Due to the expected difficulties, the OLED fabrication tests described in this chapter were carried out with racemic **[Tb.L^{A}]**, since its energetic properties are not affected.

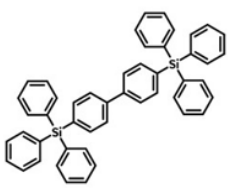

BSB

HOMO: -6.5 eV

LUMO: -2.3 eV

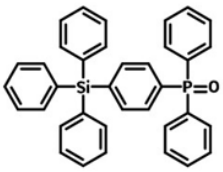

TSPO1

HOMO: -6.8 eV

LUMO: -2.4 eV

Figure 2.52. Structure and HOMO – LUMO energy levels of BSB and TSPO1.

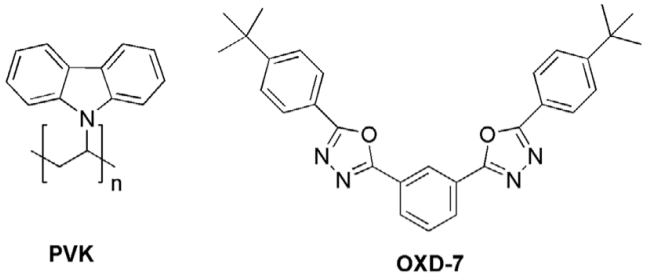

Figure 2.53. Structure of PVK:OXD-7. HOMO (PVK) = -5.6 eV, LUMO (OXD-7) = -2.7 eV.

Benchmark OLEDs were made using a 10% weight **[Tb.L^{A}]** guest in a PVK:OXD-7 host with the following structure: ITO/HTL/Active layer/TPBi/Ca/Al, where TPBi 2,2',2''-(1,3,5-Benzinetriyl)-*tris*(1-phenyl-1-H-benzimidazole) constitutes the electron transport layer. Three different types of device configuration with different HIL/HTL were tested: PEDOT:PSS; PEDOT:PSS/TFB and PEDOT:PSS/PVK, where TFB = Poly(9,9-dioctylfluorene-alt-*N*-(4-*sec*-butylphenyl)-diphenylamine). The *J-V-L* curve in the case of PEDOT:PSS/PVK is reported in Figure 2.54. Despite the low turn-on voltage (5.1 V), the light emission was white, meaning that there were no energy transfer or charge injection processes occurring from the host to the guest. The white emission was attributed to emission from the exciplex of PVK:OXD-7, as reported in the literature.[130]

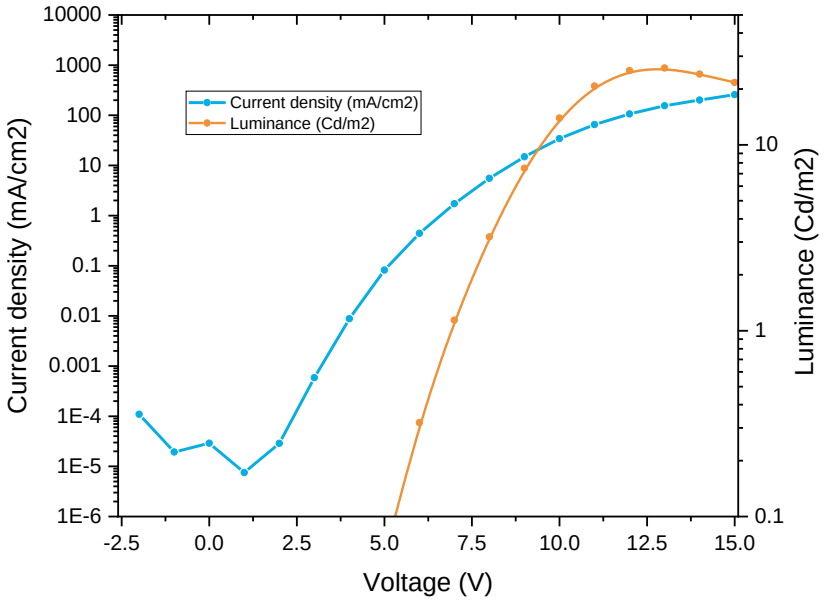

Figure 2.54. *J-V-L* curve of the ITO/PEDOT:PSS/PVK/PVK:OXD-7:**[Tb.L^{A}]**/TPBi/Ca/Al OLED.

An electroluminescence spectrum was recorded, (Figure 2.55). A small peak at 550 nm, corresponding to the strongest emission peak of Tb(III) is superimposed to the broad exciplex electroluminescence spectrum that accounts for the white emission. Evidence of emission arising from **[Tb.L^{A}]** suggests that it can work as an OLED emitter, provided that a more suitable host-guest system can be found.

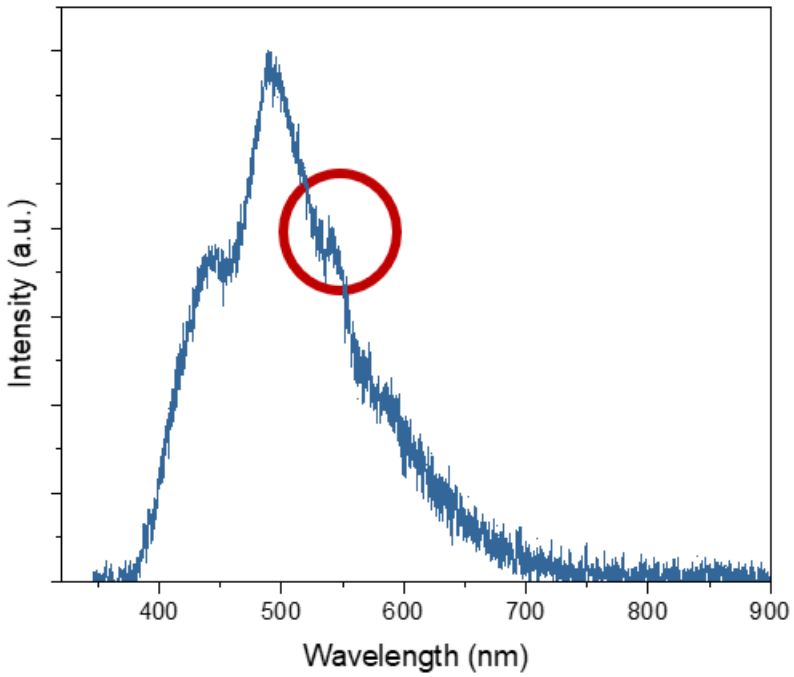

Figure 2.55. Electroluminescence spectrum of PVK:OXD-7. The 550 nm Tb(III) emission peak is highlighted in the red circle.

A similar ITO/PEDOT:PSS/PVK/Active layer/TPBi/Ca/Al architecture was tested, where the active layer consisted of a blend of BSB and **[Tb.L^{A}]** with different proportions, ranging from 2% to 20% weight of **[Tb.L^{A}]** in BSB. The best performances were obtained with a 10% weight ratio and the relative *J-V-L* curve is shown in Figure 2.56, *left*. The insert shows a picture of the pale green emission obtained at low luminance (< 1 cd/m^2). At higher luminance, white emission arising from TPBi electromer formation overcomes the green emission. Due to the low luminance, a 3 h accumulation was performed to record an electroluminescence spectrum with a good signal-to-noise ratio, (see Figure 2.56, *right*). Observation of the emission intensity at different times during this measurement proved the stability of the device when powered at 7.5 V. The first two emission manifolds of Tb(III) are highlighted in the red circles.

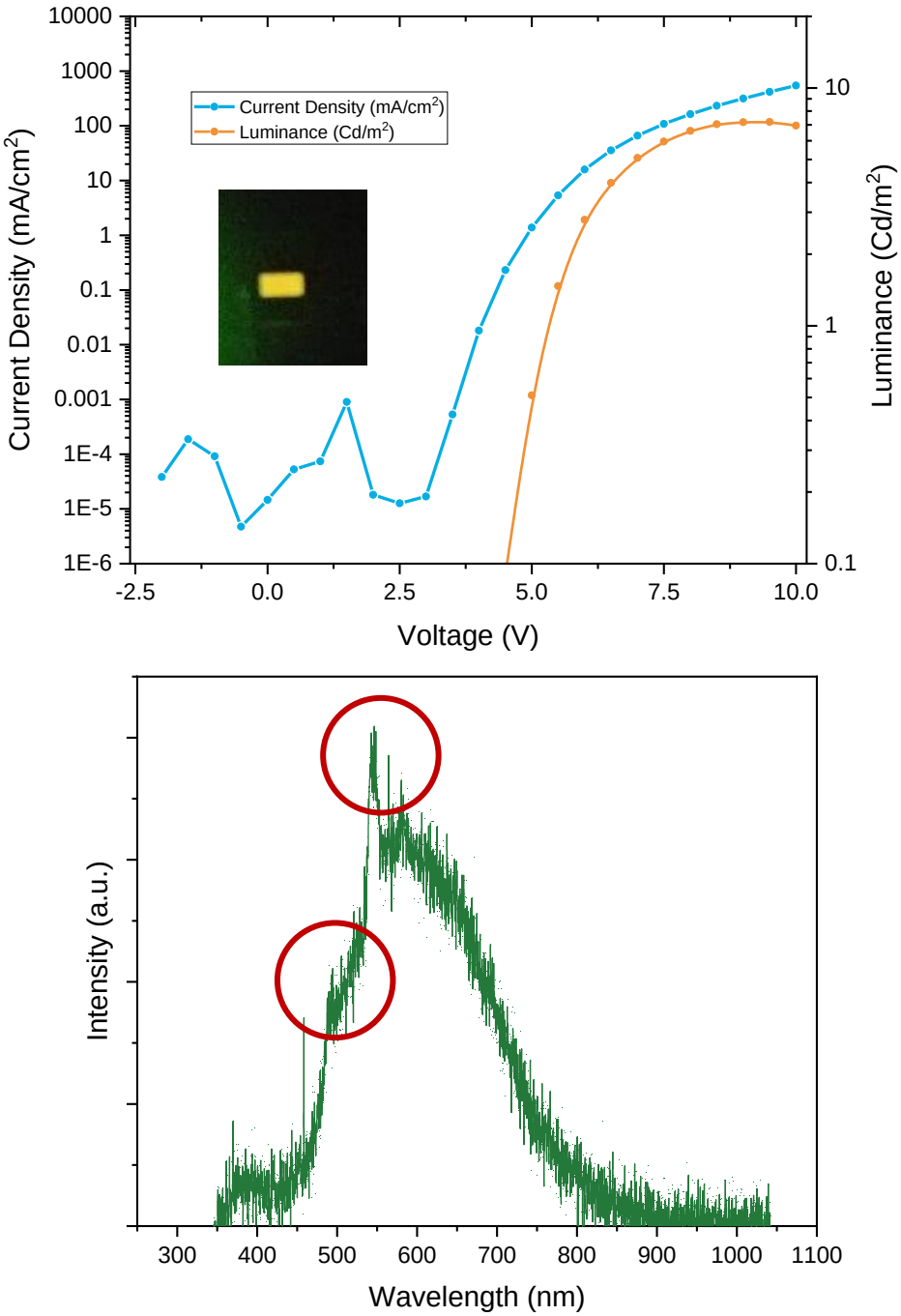

Figure 2.56. J-V-L curve (*top*) and electroluminescence spectrum (*bottom*) of the ITO/PEDOT:PSS/PVK/BSB:**[Tb.L^{A}]**/TPBi/Ca/Al OLED.

Finding a host that can match the very deep HOMO of **[Tb.L^{A}]** is a challenge that needs to be overcome to use it as a green emissive guest to fabricate OLEDs. However, the good optical properties of its emission, namely sharp emission peaks and excellent colour purity, were confirmed by electroluminescence spectra.

One further step ahead could be using TSPO1 as a host, with its remarkably low -6.8 eV HOMO. Pursuit of an ETL other than TPBi would also prevent the formation of the electromer responsible for the white background electroluminescence. More exotic hosts, including custom-made ones, may be explored and could provide better energy transfer and charge trapping properties, leading to higher efficiency and higher colour purity spectra.

2.4. Summary

The following aims were achieved:

1) Synthesis of a Eu(III) complex that displays mono-signate CPL transitions within a single emission manifold;
2) Design of a Eu(III) complex with linkers that enable late-stage functionalisation;
3) Synthesis of a Tb(III) complex with the potential to be used as the CPL-active green emitter to fabricate circularly polarised OLEDs;

1) The TACN-based complex **[Eu.L^{1}]** was identified as the target and synthesised. Chiral separation failed due to its negative charge. Conversion into its more apolar ethyl ester counterpart **[Eu.L^{1}]^{b}** allowed resolution of the two enantiomers. It was found that the two brightest emission manifolds (ΔJ = 1 and ΔJ = 2) of **[Eu.L^{1}]^{b}** are monosignate in NMP and EtOAc, effectively keeping opposite CPL sign cancellation low. NMP and EtOAc were chosen as solvents as they mimic the monomeric units constituting polyvinylpyrrolidone (PVP) and polymethylmethacrylate (PMMA), respectively. Embedding **[Eu.L^{1}]^{b}** in PMMA and PVP proved that the CPL spectrum sign features are retained when going from solution to films. This is particularly relevant when envisioning applications where bright, monosignate lanthanide-based films are used for calibration of CPL instrumentation. Strong CPL spectra of the *Λ* enantiomer of **[Eu.L^{1}]^{b}** in NMP were recorded using two-photon excitation (2PE).

2) A novel TACN-based Eu(III) complex, **[Eu.L^{5}]**, was synthesised, comprising three pyridyl-based carboxylate donor groups which saturate the coordination sphere of Eu(III). Two pyridylalkynylaryl antennae are grafted onto the macrocycle to enable efficient sensitisation of Eu(III) emission both in the UV region with single-photon excitation and in the NIR near-infrared *via* 2PE. A third macrocycle site is functionalised with a single pyridyl pendant arm, enabling linkage of the complex to various molecules via a *para*-nitro group that allows for facile late-stage functionalisation with a broad set of substituents. One of the aims of this work was to study how the total emission and CPL spectral profile of all-carboxylate complexes differ from those of all-phosphinate complexes. This objective was not pursued due to the failure of chiral resolution of the carboxylate-based **[Eu.L^{5}]**.

The shorter synthetic route of carboxylate donors compared to phosphinate ones afforded a larger amount of final product (50 mg, one order of magnitude larger than the usual mass obtained in the case of phosphinate donor-based complexes). The alkylation order necessary to install two different types of arms on the TACN scaffold was optimised to avoid the exposure of the alkynyl group to trifluoroacetic acid, which was shown to be the cause of the degradation of the triple bond of the antenna. Conjugation reactions, such as thiol-bearing polymer end-group modifications to obtain Eu(III)-tagged CPL emissive polymers. This is possible since conjugation reactions are mild and are expected to preserve the enantiopurity of the complex. A successful proof-of-concept conjugation test reacted racemate **[Eu.L^5]** with reduced L-glutathione under various conditions.

3) A novel Tb(III) chiral complex, **[Tb.L^A]**, characterised by the presence of three strongly sensitising biaryl arms was synthesised with the intention of preparing a green dopant for the fabrication of Circularly Polarised OLEDs. Combined photophysical and electrochemical characterisations *via* fluorescence spectroscopy and cyclic voltammetry were performed to estimate the energy of the HOMO and LUMO of **[Tb.L^A]**, calculated to be -6.8 eV and -2.7 eV, respectively. Commercially available hosts that are solution processable usually range between a -2.3 eV LUMO and a -6.2 eV HOMO. The remarkably deep HOMO energy of -6.8 eV of **[Tb.L^A]** poses a great challenge since a host with an insufficiently deep HOMO level does not ensure charge injection or exciton trapping on the emissive material. Preliminary attempts using commercially available hosts with similar, although not perfectly matching energy levels were performed. The presence of the signature green Tb(III) emission was proven *via* electroluminescence spectrometry, showing the potential of **[Tb.L^A]** as an emitter in OLEDs once better novel host materials with a large bandgap are found.

CHAPTER THREE

Solvent Dependence and Racemisation Kinetics

Chapter Three: Solvent Dependence and Racemisation Kinetics

The content presented in this chapter is based on the following publication:

Davide F. De Rosa, Matthieu Starck, David Parker, Robert Pal, *Unlocking same-sign CPL: solvent effects on spectral form and racemisation kinetics in nine-coordinate chiral europium(III) complexes*, Chemistry – A European Journal, Vol. 30, Issue 9, February 12, 2024, /doi.org/10.1002/chem.202303227

The main goal of the work presented in this Chapter is to study of the dependence of total and CPL emission of Eu(III) complexes on solvent polarity and investigation of solvent effects on racemisation kinetics.

3.1. Introduction

3.1.1. Motivation for the Study

Understanding the factors that shape the circularly polarised luminescence (CPL) emission profiles of Eu(III)-based CPL emitters to have specific sign properties, *e.g.* monosignate individual CPL transitions, is key to the design of novel chiral complexes for applications ranging from advanced security inks to bio-probes for live cell imaging.

Additionally, in terms of solvent polarity, solvent-specific effects influencing the kinetic stability of Eu(III) complexes with respect to enantiomer interconversion were investigated. The interactions between the chosen donor moieties that coordinate Eu(III) and the nature and polarity of the solvent determine the rate of racemisation and are crucial in the pursuit of chiral lanthanide emitters that are stable towards racemisation for applications at room temperature.

3.1.2. Properties of the Complexes

It is often assumed that lanthanide luminescence is fundamentally independent of the metal coordination environment, owing to the effective shielding experienced by the 4*f* orbitals. Recent findings highlight the striking effect of solvent polarity in determining emission spectra in coordinatively saturated complexes.[65] The present work extends the scope of the study performed by Fradgley *et al.* to *quasi-C*$_3$ symmetric complexes,

named **[Eu.L$^{7\text{-}9}$]**, (Figure 3.1), synthesised and chirally separated by Dr Matthieu Starck.[114,131] A photophysical and kinetic investigation has been conducted on this series of coordinatively saturated nine-coordinate Eu(III) systems based on 1,4,7-triazacyclononane to correlate structure and spectral features.

The lower symmetry removes the degeneracy of some transitions, leading to greater complexity in the spectral profile. The structurally related complexes **[Eu.L$^{7\text{-}9}$]**, possessing one, two, and three antennae, are used to probe the effect of small variations in the coordination environment.

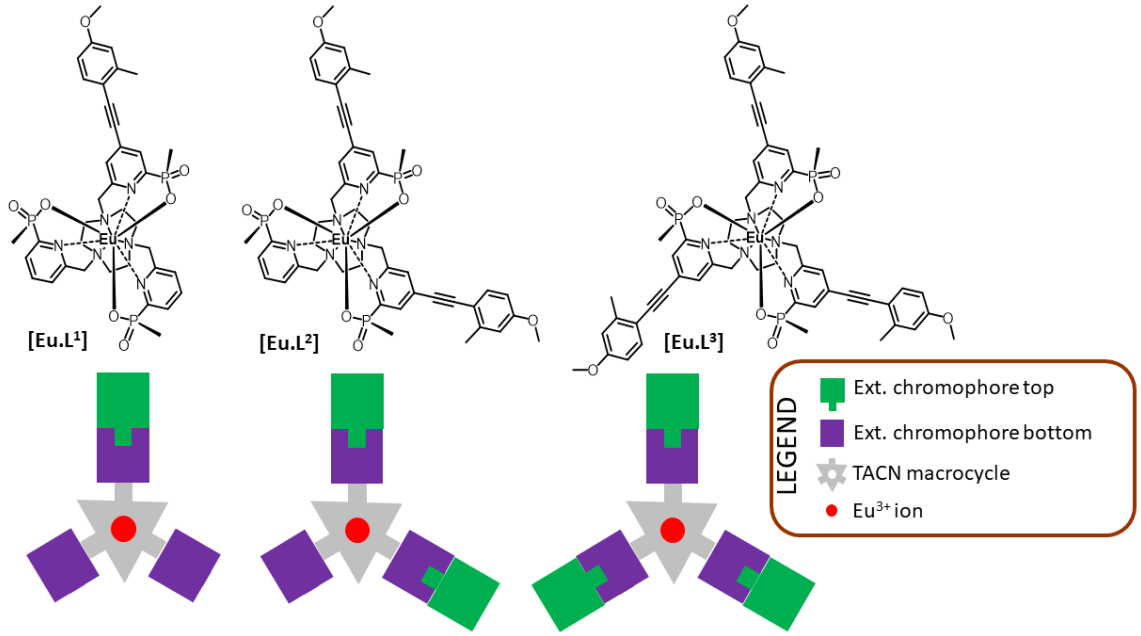

Figure 3.1. Structures and schematic representation of **[Eu.L$^{7\text{-}9}$]**.[30]

The ligand field and hence the spectral properties of Eu(III) complexes, are also affected by the nature and polarisability of the chromophores' donor groups. Since the polarisability of the chromophores is a function of solvent polarity, solvent dependent changes in luminescence are expected for such complexes. Understanding how solvent polarity shapes the CPL emission profile is a prerequisite in devising novel Eu(III) complexes with desirable chiroptical properties for applications such as *in vivo* sensing and security tagging. This issue is particularly relevant, as the rapid detection of CPL is facilitated by having relatively broad monosignate transitions within a given manifold in the CPL fingerprint spectrum.

Macrocyclic Eu(III) complexes of nonadentate ligands do not normally suffer from ligand dissociation in aqueous media and are not quenched by dissolved oxygen.[131,132] The presence of pyridylalkynylaryl chromophores in the ligand also allows efficient multiphoton excitation.[69,86] Controlling the sign and intensity of individual CPL transitions within a single emission manifold is key to tailor CPL spectra for specific purposes. Compared to total emission, CPL spectra may have increased resolution of individual transitions,[43] providing valuable insight into fine splitting states. In this case, the ideal highly resolved and informative CPL spectrum often consists of a sequence of opposing sign transitions within a single emission manifold. An interesting potential application of such a situation is in tailored CPL spectral fingerprint barcoding.[133] Conversely, a monosignate spectrum is ideal in circumstances where the goal is to maximise the number of photons having a defined CP handedness within a single emission manifold,. In this case, applications include CPL microscopy[69] and photography[134] using low-cost broad bandpass filters.

3.1.3. Theory of Solvatochromism

Solvatochromism refers to the reversible change in either absorption or emission spectral features of a fluorophore in different solvents. These changes are typically rationalised in terms of the differential effect that solvent polarity has in shifting the ground and first excited states of the emissive species, thereby affecting this energy difference. Fluorophores typically have a larger electric dipole moment in the excited state compared to the ground state. Emission wavelengths increase with increasing solvent polarity because while both the ground state and excited state of a fluorophore can be stabilised, the excited state is usually stabilised to a greater extent, resulting in a red shifted (bathochromic) emission in more polar solvents. In certain cases, *e.g.* for fluorophores which can access an internal charge transfer (ICT) state, solvent polarity effects are also observed in absorption spectra.[71] Being an excited state characterised by a strong charge separation and therefore a high electric dipole moment, the energy of the internal charge transfer state is altered by solvent polarity. As a consequence, variations in the spectral profile and shifts in absorption maxima can also be observed, in addition to the more commonly observed changes in emission spectra.[71] The Reichardt solvent polarity parameter E_T is commonly used to classify solvent polarity and is calculated using the longest wavelength absorptive transition of a pyridinium-

N-phenoxide betaine dye. More often, the normalised Reichardt solvent polarity parameter E_T^N is used, where the values of E_T^N of tetramethylsilane and water are normalised to 0 and 1, respectively.[135]

Recent work from Fradgley *et al.* has continued to challenge the dogma that lanthanide emission is insensitive towards changes in the ligand field, by showing that solvatochromism behaviour is not restricted to hypersensitive transitions.[65] The reference compounds examined were coordinatively saturated chiral Eu(III) complexes, in which solvent molecules cannot access the first coordination shell of the lanthanide ion due to preferential nonadentate binding of the ligand donor atoms. This situation excludes the possibility that the observed change is due to first-shell solvent-ion interactions. As anticipated, Eu(III) complexes that can access ICT excited states show marked solvatochromism in absorption. The small wavelength shifts in emission and variations of emission intensity were rationalised in terms of the changes of the ligand field experienced by the lanthanide centre in different solvents.

Solvent polarity exerts a complementary effect on total emission and CPL spectra. An increase in the magnitude of the electric dipole transition moment, usually favoured in polar solvents, leads to increased total emission intensity, since the oscillator strength of a transition is proportional to its square. Conversely, the dissymmetry factor, g_{em}, is inversely proportional to the magnitude of the electric dipole transition moment, usually leading to a decrease of CPL in more polar solvents, (eq. 3.1):

$$g_{\mathrm{em}}(\lambda) = 4\frac{\left|\mathbf{m}_{ij}\right|}{\left|\boldsymbol{\mu}_{ij}\right|}\cos\theta_{\boldsymbol{\mu},\mathbf{m}} \qquad (3.1)$$

Notwithstanding the contribution of the magnitude of the electric ($\boldsymbol{\mu}_{ij}$) and magnetic ($\boldsymbol{m}_{ij}$) dipole transition moments, the dissymmetry factor (g_{em}) is modulated by the angle between these two vectors and relates to the rotatory strength of the transition. The relative orientation of the two vectors is also expected to be affected by solvent polarity up to the point of being sufficient even to reverse the sign of g_{em}. A similar effect, where variation in the magnetic susceptibility tensor causes dramatic changes in NMR pseudocontact shifts, has been previously described.[136] The effect of solvent polarity on CPL spectra is examined here accordingly.

3.1.4. Theory and Modelling of Enantiomer Interconversion

The enantiomeric purity of enantioenriched samples decreases with time in the presence of an accessible pathway for enantiomer interconversion. This general phenomenon is termed racemisation. The energy barrier to the enantiomer interconversion process determines the time-dependence of the stability of a given compound towards racemisation. Enantiomers may be not isolable in the case of rapid interconversion or, conversely, can be virtually impossible to racemise. Fast racemisation of samples is undesirable for applications such as security inks,[137] CPL calibration standards, and CPL microscopy standards.[69] High stability towards racemisation is crucial for applications where the temperature can range from prolonged exposure to 37 °C (*e.g.* live cell imaging) to brief 150 °C incursions (*e.g.* bank note lamination which takes place at a speed of 1 cm s^{-1}).

TACN-based Eu(III) complexes possess a tricapped trigonal prismatic coordination geometry. Such complexes exists as a racemic mixture of two enantiomers (*RRR)-Λ(δδδ)* and (*SSS)-Δ(λλλ*), where *R* and *S* refer to the configuration of the phosphorus atom (since metal coordination renders the P centre stereogenic), *δ* and *λ* refer to the torsion angle in the NCCN chelate ring, and *Δ* and *Λ* to the propeller chirality imparted by the arms and defined by the $NCCN_{py}$ torsion angles, (see Figure 1.10). Although a larger number of diastereomeric combinations is possible in principle, interlinked steric requirements force the complex to exist as the two enantiomers (*RRR)-Λ(δδδ)* and (*SSS)-Δ(λλλ*) only. The high energy barrier to racemisation allows for enantiomer isolation by chiral HPLC.

In principle, the process of enantiomer interconversion could involve cooperative arm rotation or inversion of the nine-membered macrocycle ring. The energy barrier increases dramatically with the degree of steric hindrance. It is known that the three donor groups carboxylate, methylphosphinate, and phenylphosphinate display increasing stability towards racemisation.[138] In the present work, other factors impacting the racemisation kinetics of TACN-based Eu(III) complexes were investigated, including solvent polarity and the size and nature of the electric dipole moment of the chromophore.

The kinetic stability of the complexes towards enantiomer interconversion was quantified by monitoring the change in enantiomeric purity as a function of time. A solution of each complex was prepared in four solvents of different polarity, *i.e.* water, methanol, *N*-methyl pyrrolidone, ethyl acetate, held at 60 °C. Aliquots were sampled over time and examined by analytical chiral HPLC to measure the enantiomeric excess of each sample.

Mathematically, a kinetic relationship that correlates the concentration of each enantiomer with time can be derived based on the racemisation equilibrium, as previously reported,[64]

$$\Lambda \underset{k_{-1}}{\overset{k_1}{\rightleftharpoons}} \Delta$$

Assuming the rate constants for enantiomeric interconversion between the enantiomers are equal ($k_1 = k_{-1} = k$), the rate of interconversion can be written as follows.

$$-\frac{\mathrm{d}[\Lambda]}{\mathrm{d}t} = k[\Lambda] - k[\Delta] \tag{3.2}$$

Knowing that $[\Delta] = [\Lambda]_0 - [\Lambda]$, the differential equation can be integrated to give

$$\ln \frac{[\Lambda]_0}{2[\Lambda] - [\Lambda]_0} = 2kt \tag{3.3}$$

The left-hand term is calculated using the ratio of the integrals from analytical chiral HPLC traces for each enantiomer, and correlates linearly with time with a slope of 2*k*. The racemisation half-life can be defined as the time required for an enantiomeric excess of 50% to be reached, starting from an enantiomerically pure sample, *i.e.* the time to go from a ratio of 100:0 to a 75:25 scalemic mixture.

$$t_{1/2} = \frac{\ln 2}{2k} \tag{3.4}$$

The present work generalises this result to the case where the starting point of the experiment does not correspond to a perfectly enantiopure sample, but rather an enantioenriched sample at any concentration. Two linear first order differential

equations describe the racemisation kinetics. Due to the independence of the rate on absolute concentration, the linear system can be solved exclusively in terms of the ratio ρ defined at any time as:

$$\rho = \frac{[\Lambda]}{[\Delta]} \tag{3.5}$$

The initial condition is $[\Lambda] + [\Delta] = [\Lambda]_0 + [\Delta]_0$ and assuming that $[\Lambda]_0 > [\Delta]_0$ for simplicity, the differential equation can be solved as:

$$-\frac{\mathrm{d}}{\mathrm{d}t}\begin{bmatrix}\Lambda\\ \Delta\end{bmatrix} = k\begin{bmatrix}-1 & 1\\ 1 & -1\end{bmatrix}\begin{bmatrix}\Lambda\\ \Delta\end{bmatrix} \tag{3.6}$$

$$\begin{bmatrix}\Lambda\\ \Delta\end{bmatrix} = e^{k\begin{bmatrix}-1 & 1\\ 1 & -1\end{bmatrix}t}\begin{bmatrix}\Lambda_0\\ \Delta_0\end{bmatrix} \tag{3.7}$$

The matrix *M* can be diagonalised as $M = S\,J\,S^{-1}$ as

$$\begin{bmatrix}-1 & 1\\ 1 & -1\end{bmatrix} = \begin{bmatrix}-1 & 1\\ 1 & 1\end{bmatrix}\begin{bmatrix}-2 & 0\\ 0 & 0\end{bmatrix}\begin{bmatrix}-1/2 & 1/2\\ 1/2 & 1/2\end{bmatrix} \tag{3.8}$$

Substituting the diagonalised matrix in the solution gives

$$\begin{bmatrix}\Lambda\\ \Delta\end{bmatrix} = \frac{1}{2}\begin{bmatrix}-1 & 1\\ 1 & 1\end{bmatrix}\begin{bmatrix}e^{-2kt} & 0\\ 0 & 1\end{bmatrix}\begin{bmatrix}-1 & 1\\ 1 & 1\end{bmatrix}\begin{bmatrix}\Lambda_0\\ \Delta_0\end{bmatrix} \tag{3.9}$$

Expanding and dividing by $[\Delta]_0$

$$\begin{bmatrix}\Lambda/\Delta_0\\ \Delta/\Delta_0\end{bmatrix} = \frac{1}{2}\begin{bmatrix}e^{-2kt}+1 & -e^{-2kt}+1\\ -e^{-2kt}+1 & e^{-2kt}+1\end{bmatrix}\begin{bmatrix}\rho_0\\ 1\end{bmatrix} \tag{3.10}$$

Dividing the first equation by the second one

$$\rho = \frac{1+\frac{\rho_0-1}{\rho_0+1}e^{-2kt}}{1-\frac{\rho_0-1}{\rho_0+1}e^{-2kt}} \tag{3.11}$$

Solving for $2kt$ gives

$$2kt = -\ln\left(\frac{\rho-1}{\rho+1}\right) - \ln\left(\frac{\rho_0+1}{\rho_0-1}\right) \tag{3.12}$$

The second logarithmic term vanishes in the case of an initially enantiopure sample, as $\rho_0 = \infty$, recovering the limit case in the simplified equation used by Fradgley *et al.*[65] A plot of the right-hand side as a function of time gives a line passing through the origin, with a slope equal to 2*k*. Equation 3.12 will be referred to as the Corrected Racemisation Rate (CRR) hereafter.

3.2. Solvent Dependence

Investigation of the variation of spectral form in total emission and CPL as a function of solvent polarity was performed with **[Eu.L$^{7\text{-}9}$]**, *i.e.* the uncharged Eu(III) complexes bearing one, two, and three extended chromophore antennae, respectively. The spectral form of both total emission and CPL spectra was found to be solvent dependent, (Figures 3.2-3).

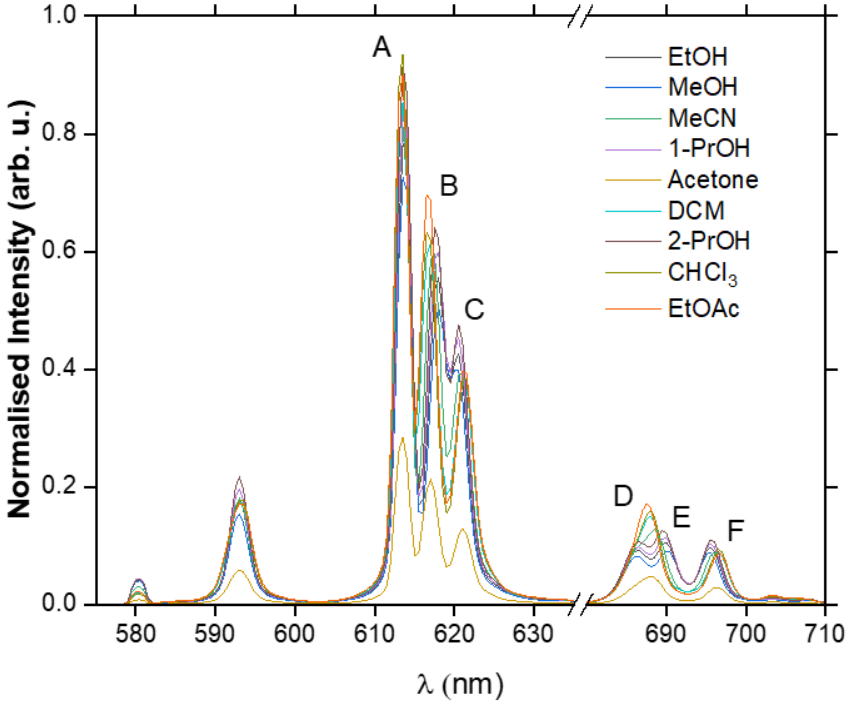

Figure 3.2. Total emission spectra of **[Eu.L^{7}]** in solvents of varying polarity with the six relevant transitions labelled. λ_{exc} = 336 nm, scanning step = 0.5 nm.

Previous studies have highlighted the sensitivity of the electric dipole allowed $\Delta J = 2$ and $\Delta J = 4$ manifolds in Eu(III) complexes to solvent effects.[65] The three bands within the $\Delta J = 2$ manifold are labelled ***A***, ***B***, and ***C***; the five transitions within the $\Delta J = 4$ manifold are labelled ***D-H***, where ***G*** and ***H*** are resolved only in CPL spectra. In the total emission spectra of **[Eu.L$^{7\text{-}9}$]**, the wavelength of the most intense transition ***A*** centred at 613.5 nm does not show any solvent dependence, whereas transition ***B***

exhibits a bathochromic (red-) shift ($\Delta\lambda$ = 1.5 nm going from EtOAc to MeOH), and transition ***C*** a $\Delta\lambda$ = 1.0 nm hypsochromic (blue-) shift, more pronounced in the C_3-symmetric complex **[Eu.L^9]**. In the ΔJ = 4 manifold, the two stronger transitions ***D*** and ***E*** are well resolved in polar media (686.5 *vs* 690.0 nm in MeOH across the series, $\Delta\lambda$ = 3.5 nm difference) but coalesce as solvent polarity decreases, merging into a single unresolved band centred at 688.0 nm. The transition ***F*** displays a $\Delta\lambda$ = 1.0 nm bathochromic shift. The solvatochromic shifts in total emission are highly consistent across the series. The intensity ratio of selected transitions exhibits a modest 10-20% change with polarity.

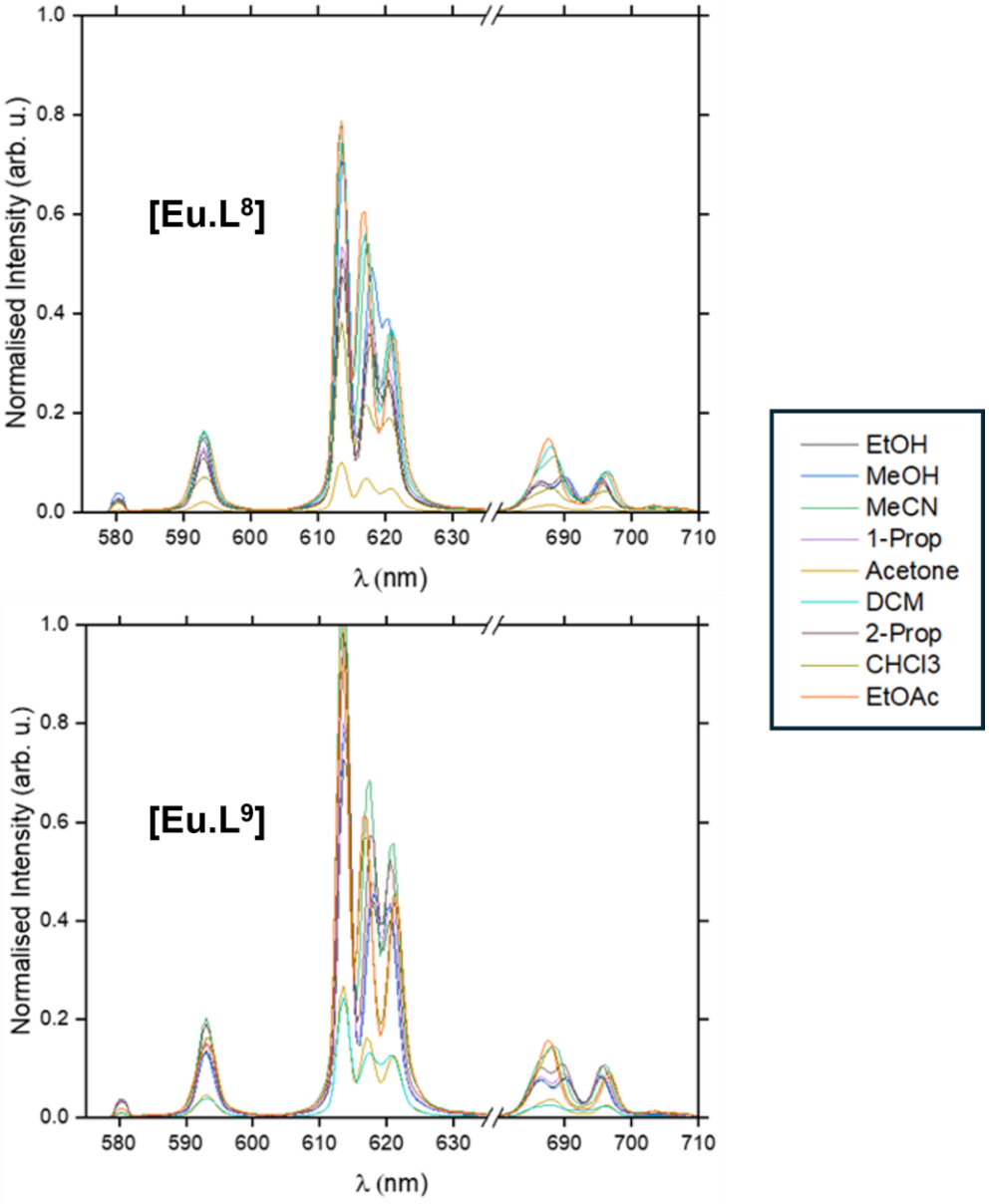

Figure 3.3. Total emission spectra of complex **[EuL^8]** (*top*) and **[EuL^9]** (*bottom*) in solvent with varying polarity. λ_{exc} = 336 nm, scanning step = 0.5 nm.

CPL spectra for **[Eu.L$^{7\text{-}8}$]** have transitions in the ΔJ = 2 manifold that undergo very small shifts of around 0.5 nm, (Figures 3.4-5). The intensity of transition ***A***, however, displays a tenfold increase with respect to the intensity of either ***B*** or ***C*** as polarity is decreased. This increase in CPL intensity is consistent with the decrease in the magnitude of the electric dipole moment in less polar solvents, since the dissymmetry factor is inversely proportional to the magnitude of the electric dipole moment, highlighting the potential of this system as a more sensitive polarity probe. In the ΔJ = 4 manifold, the ***D*** and ***E*** transitions are always resolved as they are of opposite sign in CPL. All the transitions display very small shifts (order of $\Delta\lambda$ = 0.5 nm) as the polarity of the medium is varied. Only transition ***E*** shows a more substantial 2.0 nm bathochromic shift, consistent with the trend observed in total emission spectra, where ***D*** and ***E*** coalesce as solvent polarity is decreased.

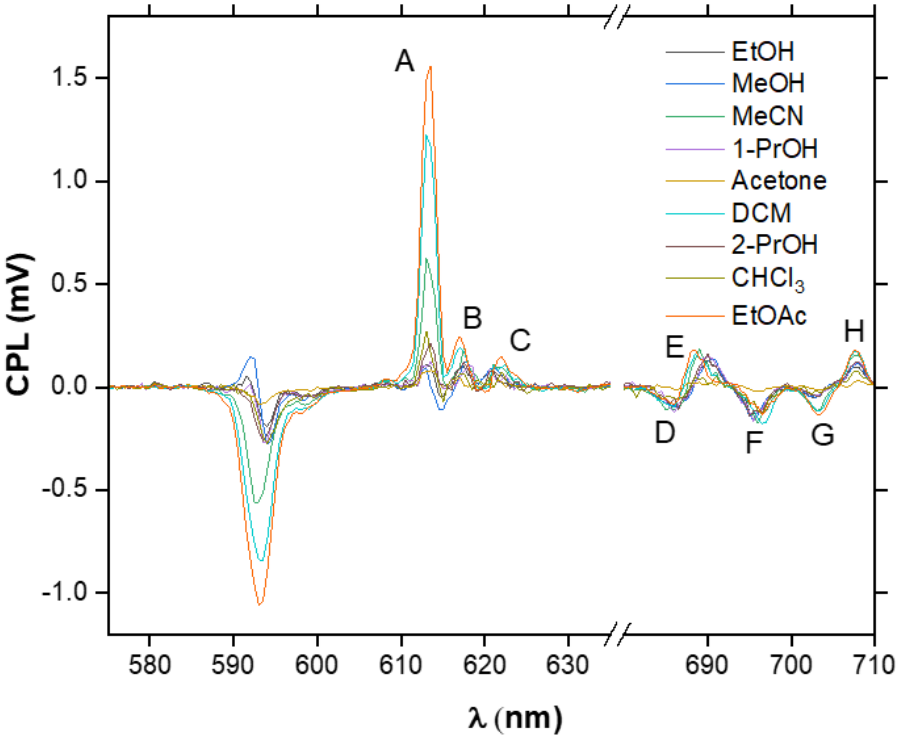

Figure 3.4. CPL spectra of Λ-[**Eu.L^{8}**] in solvents with varying polarity with the eight relevant transitions labelled. λ_{exc} = 336 nm, scanning step = 0.5 nm.

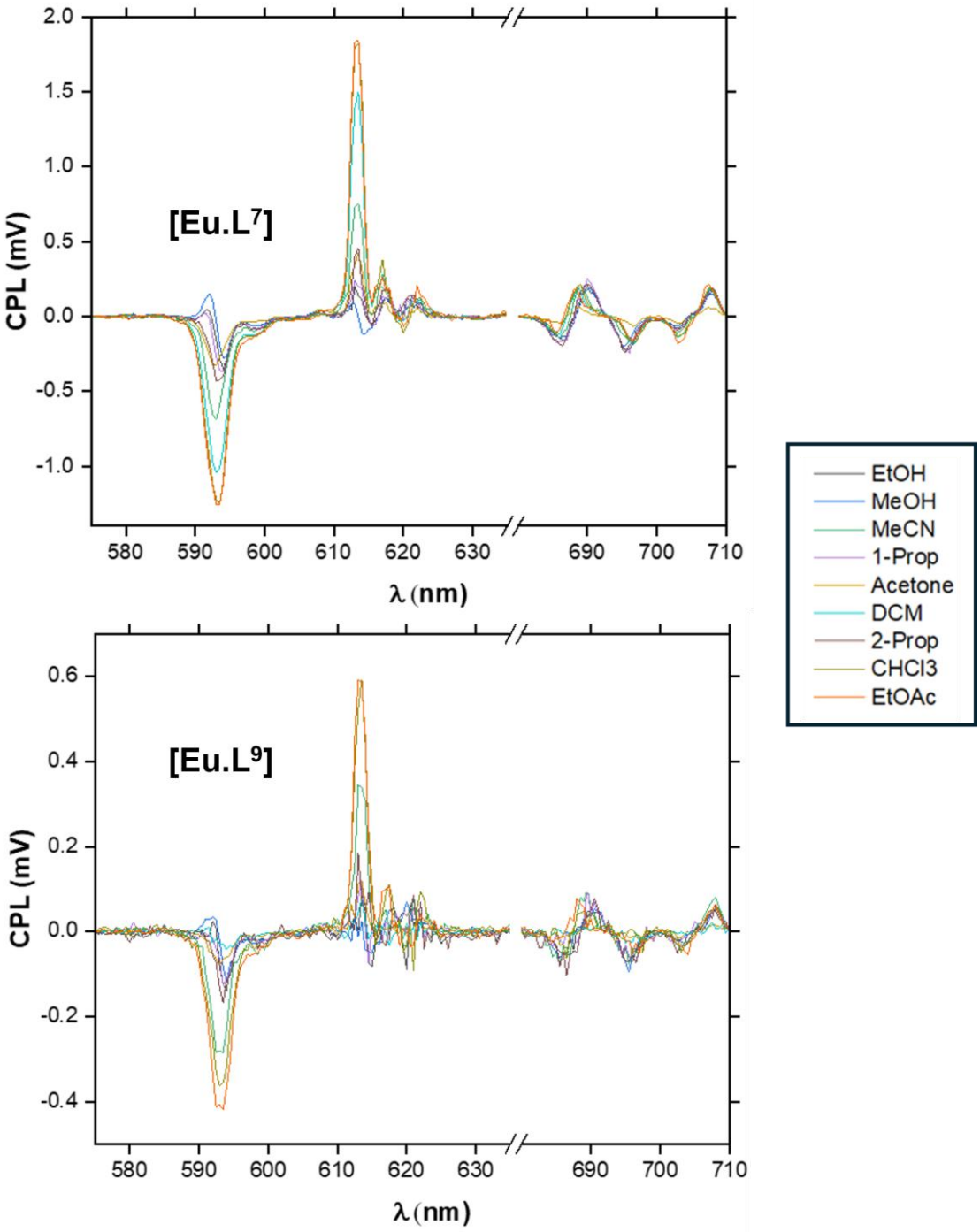

Figure 3.5. CPL spectra of complex **[EuL^7]** (*top*) and **[EuL^9]** (*bottom*) in solvent with varying polarity. λ_{exc} = 336 nm, scanning step = 0.5 nm.

The changes in intensity of transitions within the ΔJ = 4 manifold are much smaller than those observed in the ΔJ = 2 manifold. The stability of sign and intensity with respect to the nature of the solvent parallels the behaviour observed in previous studies, where it was shown that the sign sequence of transitions within the ΔJ = 4 manifold correlates with the propeller chirality of each enantiomer, *e.g.* the Λ enantiomer has a - / + / - / - / + sequence. The complex absolute configuration was independently determined via X-ray crystallography[22,56]. The simultaneous presence within the same emitting species of transitions that are highly sensitive towards solvent polarity (ΔJ = 2) and comparatively insensitive (ΔJ = 4) allows internally referenced ratiometric measurements of medium polarity to be undertaken, with greatly enhanced sensitivity. To exemplify this point, the intensity ratio between the CPL transitions ***A*** (belonging to the ΔJ = 2 manifold) and ***H*** (belonging to the ΔJ = 4 manifold) can be considered, (Figure 3.6). The intensity of transition ***A*** undergoes a 20-fold increase with respect to the intensity of transition ***H*** as solvent polarity decreases from MeOH to EtOAc.

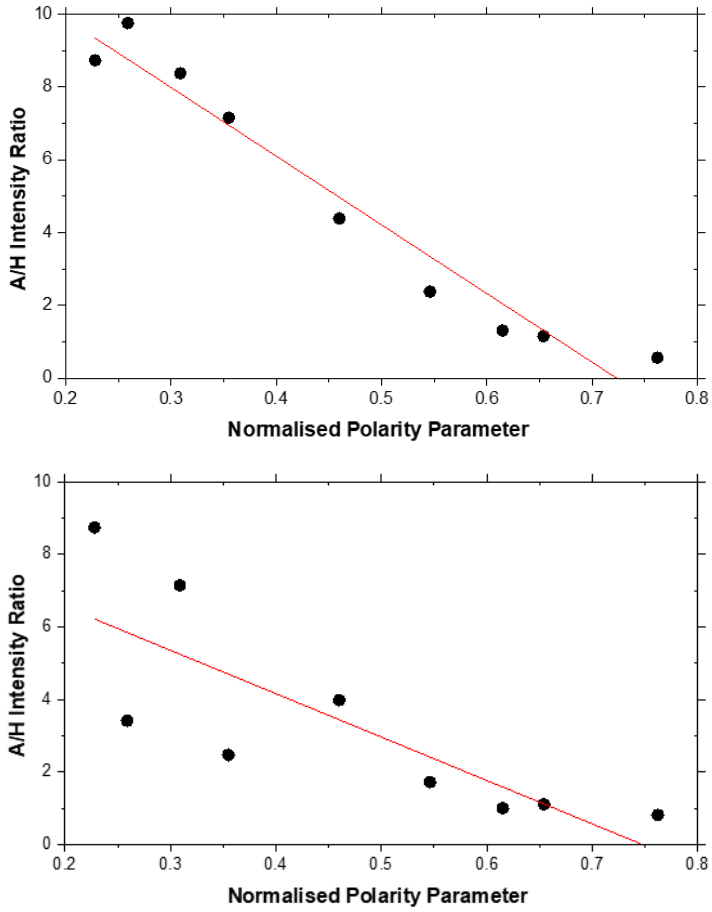

Figure 3.6. Intensity ratio for the CPL ***A*** and ***H*** transitions of **[Eu.L^7]** (*left*) and **[Eu.L^8]** (*right*) as a function of Reichardt's polarity parameter.

3.3. Racemisation Kinetics

3.3.1. Experimental Methodology

The complexes **[Eu.L$^{7\text{-}9}$]** were dissolved in the chosen solvent (water, MeOH, NMP, EtOAc; 0.5 mg of complex in 400 µL of solvent) in a closed LC/MS sample vial with a stirrer bar. The 12 sample vials were floated in a water bath held at 60 °C on a hotplate. Aliquots were taken (20 µL) at different times using a variable 2-20 µL pipette and stored at -18 °C in LC/MS sample vials to prevent any further undesired racemisation prior to the determination of the enantiomeric excess *via* analytical chiral HPLC.

The aliquots from the MeOH and NMP experiments were analysed on the chiral HPLC set up without any further preparation. The injection of samples in water and EtOAc resulted in noisy, unresolved HPLC traces. For this reason, aliquots in water and EtOAc were lyophilised and evaporated, and redissolved in 20 µL of MeOH each. A change in the carrier solvent does not affect enantiomeric excess, which was estimated as the ratio between the integrals of the peaks in the analytical HPLC traces corresponding to the two enantiomers of each complex, (Figure 3.7).

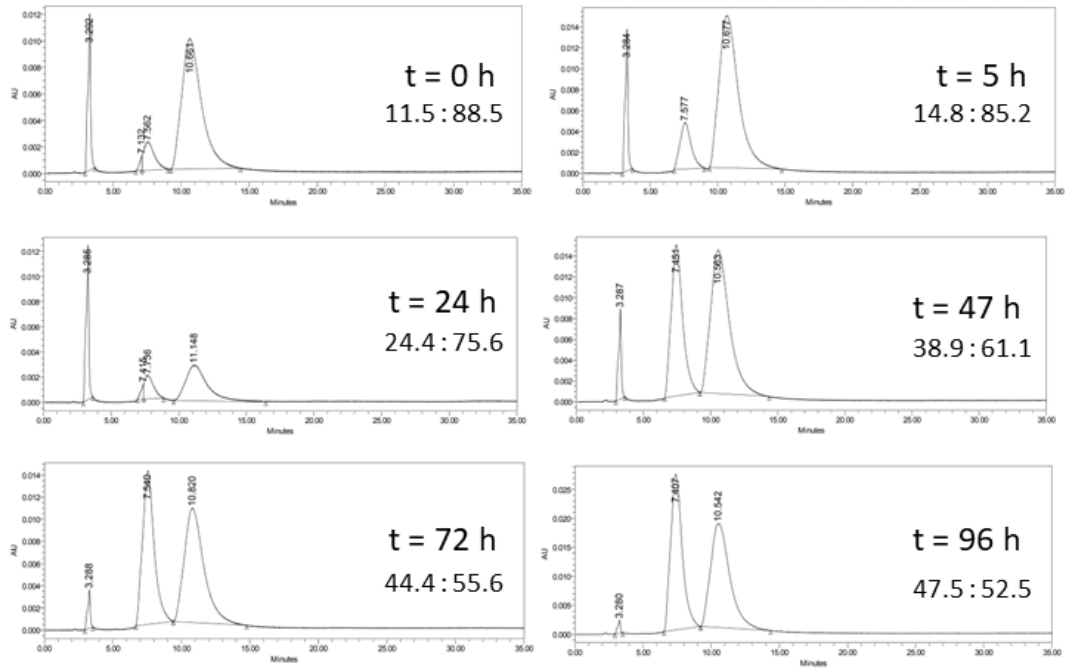

Figure 3.7. Analytical chiral HPLC traces of selected aliquots at different times of the complex **[EuL^7]** in H_2O at 60 °C. The first peak is an impurity; the second and third peaks are the *Δ* and *Λ* enantiomers of **[EuL^7]** respectively. The enantiomer excess is reported for each aliquot and was calculated as the ratio of the integrals of peaks corresponding to the enantiomers of **[EuL^7]**.

3.3.2. Racemisation Kinetics Studies

The kinetic plots for enantiomer interconversion of **[Eu.L^{7}]** at 60 °C in various solvents are shown in Figure 3.8. The slopes of the kinetic plots for **[Eu.L$^{7\text{-}9}$]** were used to calculate the racemisation half-lives at 60 °C according to the mathematical model, (Table 3.1). With the overarching goal of using such stable complexes for commercial security applications, half-lives at room temperature (25 °C) were estimated under the crude assumption that kinetic rates double upon a ten-degree temperature increase.

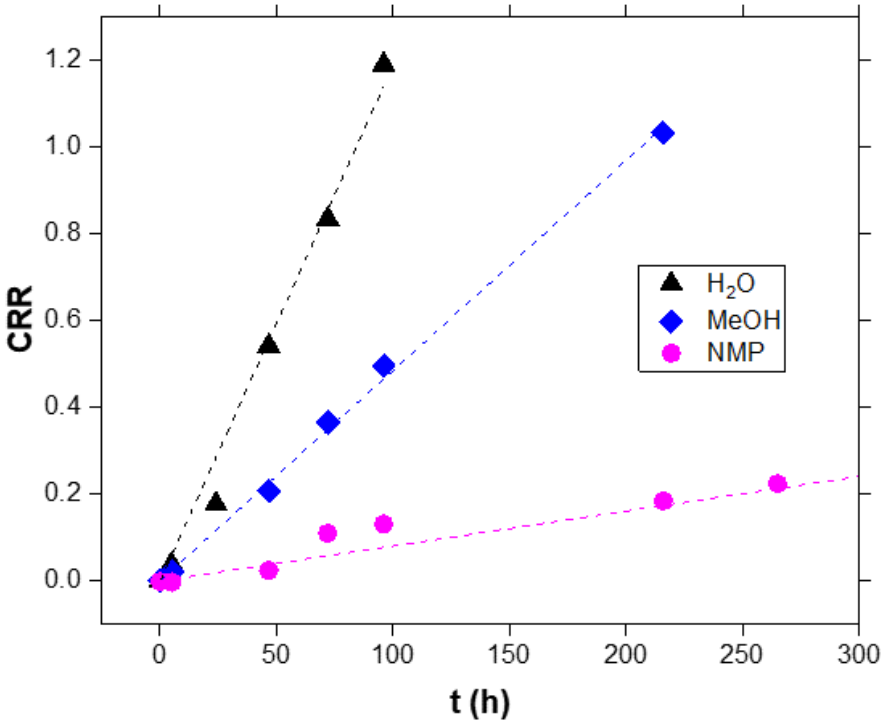

Figure 3.8. Kinetic plots for the corrected enantiomer interconversion rate (adjusted for a starting enantiomeric excess of 90:10, see eq. 12) for **[Eu.L^{7}]** at 60 °C in various solvents (*black triangle* = water; *blue square* = methanol; *magenta circle* = NMP). Ethyl acetate is not shown as no enantiomer interconversion was detected over a period of 300 h.

No evidence for racemisation was found for **[EuL^{8}]** and **[EuL^{9}]** within the limit of detection (1% enantiomeric excess, as measured by integrating the two peaks in the analytical chiral HPLC chromatogram) after two weeks in solution at 60 °C for both of the aprotic solvents NMP and EtOAc, (Figure 3.9). The complex **[EuL^{7}]** is the only one in the series showing slow, but unequivocable racemisation in NMP.

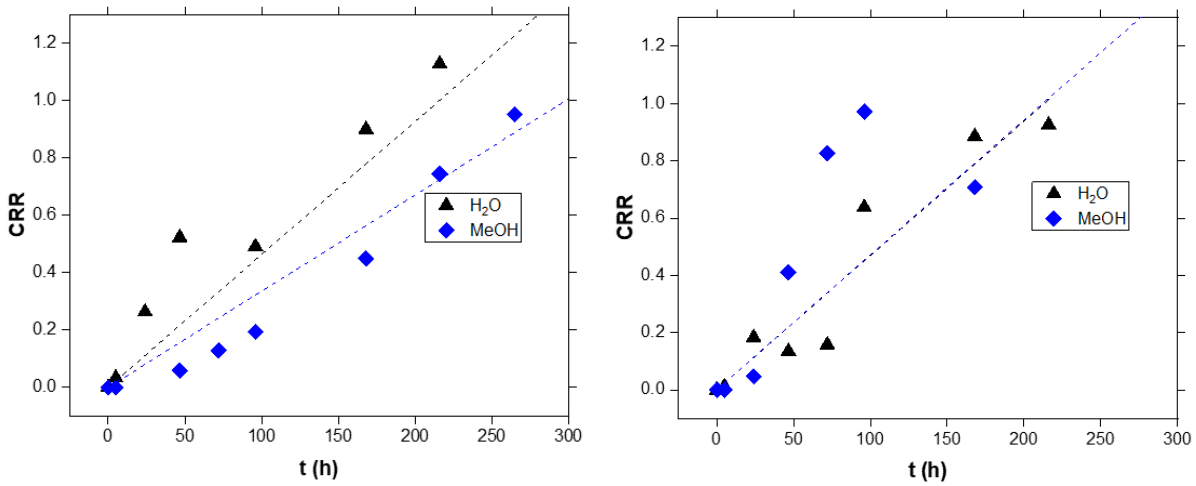

Figure 3.9. Kinetic plots for the corrected enantiomer interconversion rate for **[EuL^{8}]** (*left*) and **[EuL^{9}]** (*right*) at 60 °C (starting enantiomeric excess of 100 : 0 for both complexes) in various solvents (*black triangle* = water; *blue square* = methanol). Ethyl acetate is not shown as no enantiomer interconversion was detected over a period of 300 h. NMP is not shown as only an upper limit for enantiomer interconversion rate was estimated, (Table 3.1).

A lower limit to the racemisation half-life was estimated by assuming a racemisation rate equal to the instrumental error occurring between the first and last measured points in time. Half-lives in non-polar media at room temperature ranged therefore from centuries to millennia, highlighting the remarkable stability imparted by the phenyl phosphinate donor groups.

Table 3.1. Summary of half-lives for racemisation, $t_{1/2}$, for **[Eu.L$^{7\text{-}9}$]** in solvents of decreasing polarity (Reichardt's polarity parameters in parentheses). Half-lives measured at 60 °C are reported in days and estimated lifetimes at room temperature (25 °C) are expressed in years (in parentheses).

	Water (1.000)	**MeOH** (0.762)	**NMP** (0.355)	**EtOAc** (0.228)
[Eu.L^{7}]	2.4 d (22 y)	6.0 d (56 y)	36 d (340 y)	> 110 d (1000 y)[a]
[Eu.L^{8}]	5.3 d (50 y)	8.5 d (79 y)	> 400 d (3800 y)	> 1900 d (18,000 y)[a]
[Eu.L^{9}]	6.1 d (58 y)	4.5 d (42 y)	> 220 d (2000 y)	> 1900 d (18,000 y)[a]

(a) No evidence of racemisation within experiment error over a period of two weeks. The estimate given corresponds to the lower limit calculated for the racemisation half-time.

The enantiomer interconversion process requires sequential breaking of each bond between the phosphinate oxygen and the Eu(III) ion. The complex must pass through a short-lived charged intermediate, where the europium ion is bound to seven or less ligand donor atoms, with additional coordination sites taken up by the solvent. For

instance, water and MeOH are polar protic solvents capable of stabilising such a charged intermediate that arises from breaking a Eu-O and a Eu-N_{py} bond, facilitating the arm rotation step necessary for enantiomer interconversion.

Both NMP and EtOAc are aprotic solvents that are less effective at solvating the putative ionic intermediate (particularly local anionic charge centres), and hence are associated with a higher activation energy barrier and much longer racemisation half-lives. It is reasonable to assume that the cleavage of the ionic Eu-O bond is involved in the rate-limiting step, as it is thermodynamically stronger than the Eu-N_{py} bond. The complex with two extended chromophores (three in the case of water) exhibited the highest stability towards racemisation. These results are interesting for applications, as it allows the structure of the complex to be tailored more easily, *e.g.* by late-stage functionalisation of the simpler, single arm pyridyl donor moiety.[123]

In particular, low-polarity aprotic solvents such as NMP and ethyl acetate give rise to a more intense CPL signal in the ΔJ = 2 manifold and seem to have a tendency to promote same sign transitions.

3.4. Polymeric Films Preliminary Studies

The solvents NMP and EtOAc bear a strong resemblance to the monomers of polyvinylpyrrolidone (PVP) and polymethylmethacrylate (PMMA) respectively. For this reason, enantiopure lanthanide complexes are expected to be kinetically stable towards racemisation in such a polymeric matrix, as well as preserving the desirable CPL spectral feature shown in solution state. It is expected that in a more viscous medium, such as a polymer film, the racemisation half-lives with respect to the solution state would tend to increase, as the arm rotation motion required for enantiomer interconversion is likely to be disfavoured. Additionally, low-polarity aprotic solvents such as NMP and ethyl acetate were found to give more intense CPL signal in the ΔJ = 2 manifold and seem to promote same sign transitions. It is expected that a similar low polarity environment in a PMMA or PVP matrix may result in a similar CPL profile.

A proof-of-concept investigation of the spectral properties of Eu(III) complexes in such polymers was performed using two different complexes, (Figures 3.10.C and 3.11.C).

The complex **[Eu.L^{1b}]** was embedded in PMMA films and **[Eu.L^{10}]**, a structurally related Eu(III) complex previously prepared in the Parker group, was embedded in PVP by spin coating, (*vide infra* - Section 7.7).

Inhomogeneity at the edges of the deposited film caused internal reflections that resulted in phase-inversion and degradation of CPL signal. For this reason, only the bulk of these test-targets was considered suitable for the study. Solid state CPL was recorded adapting the existing custom-built PEM-CPL apparatus with a 3D printed custom-built 45° film holder inserted in the cuvette holder of the instrument. Complete CPL spectrum recovery when comparing lanthanide complexes in polymers to their corresponding solvent analogues was proven. Pairing our monosignate CPL emitters reported herein with our ambition to optimise the properties of CPL-active polymeric films, these parent systems will serve as a testbed for future generations of purposely engineered Eu(III) complexes for applications where broad monosignate CPL emission is needed, such as calibration of CPL instrumentation.

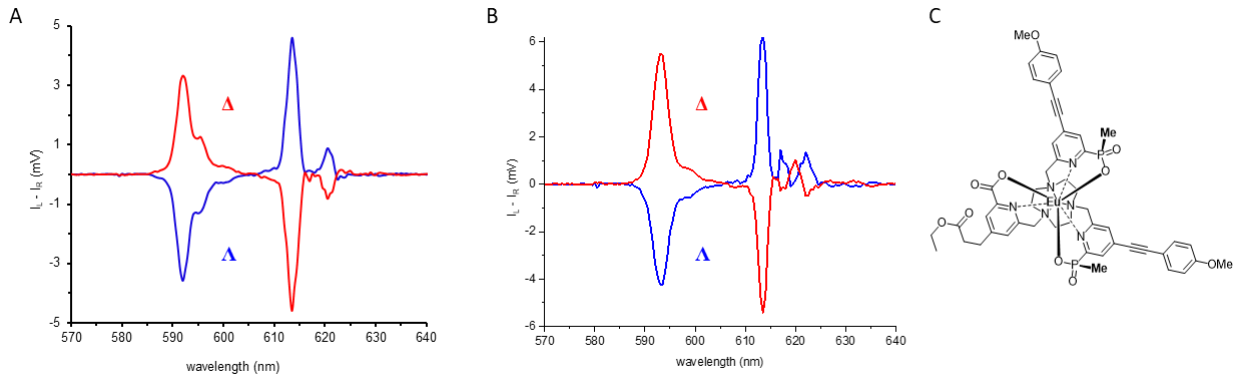

Figure 3.10. CPL spectra of the Λ and Δ enantiomers of a structurally related parent complex **[EuL^{1b}]** in (*A*) EtOH and in (*B*) drop cast PMMA matrix, 100 µm thickness, C = 5 × 10^{-5} M, (*C*) structure of **[EuL^{1b}]** for comparison.[134]

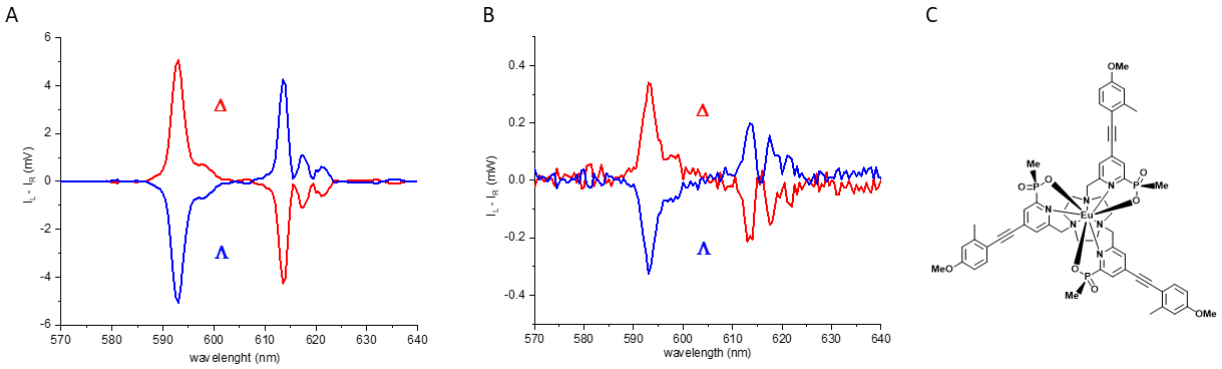

Figure 3.11. CPL spectra of the Λ and Δ enantiomers of a structurally related complex **[Eu:L^{10}]** in (*A*) NMP and in (*B*) spin coated PVP matrix, 15 µm thickness, C = 5 × 10^{-5} M, (*C*) structure of **[Eu:L^{10}]** for comparison.[69]

3.5. Discussion

This study draws attention to the crucial, albeit often neglected, relationship between the choice of solvent and the nature of the CPL active Eu(III) complex. The nature of the solvent can affect both the magnitude and sign of the emitted CPL signal, especially in the electric dipole allowed $\Delta J = 2$ and $\Delta J = 4$ transitions. For the sake of the above detailed specific CPL applications, the complex and the solvent should be considered as an inseparable pair. Although these conclusions are only qualitative, and not yet predictive, the present study represents a first step in the ambition to engineer bright, high g_{lum} and monosignate Eu(III) complexes by controlling their photophysical parameters. Further investigation with particular emphasis on varying

the nature and polarisability of the ligand donor atoms and the overall symmetry and stereochemistry at the Ln(III) centre is underway.

In particular, low-polarity aprotic solvents such as NMP and ethyl acetate give rise to a more intense CPL signal in the $\Delta J = 2$ manifold and seem to have a tendency to promote same sign transitions. Moreover, complete CPL spectrum recovery was shown in PVP and PMMA films, whose monomers are structurally similar to NMP and EtOAc, respectively. Pairing our monosignate CPL emitters reported herein with our ambition to optimise the properties of CPL-active polymeric films, these parent systems will serve as a prototype for future generations of purposely engineered Eu(III) complexes for applications where broad monosignate CPL emission is needed.

A deeper insight into racemisation kinetics and environmental factors has been gained. The comparatively lower racemisation half-lives in water and methanol, while still long enough for most applications, were interpreted in terms of assistance of the dissociative process by these small polar solvent molecules, via stabilisation of the transient ion pair in the transition state, through hydrogen bonding or specific solvation effects. The water molecule is especially efficient at coordinating to Eu(III) due to its high oxophilicity, completing its coordination sphere, and thereby lowering the energy of the transition state leading to its formation.[138,139] Indeed, the smallest racemisation half-life values were consistently obtained in water, followed by methanol. The abrupt increase in the racemisation half-life for low polarity solvents NMP and EtOAc can be ascribed to the absence of this stabilisation effect.

Extended chromophore antennae are expected to increase the structural stability of the complex by increasing the overall steric bulk of the system and the magnitude of the electric dipole moment. The enhanced polarisability of the pyridyl nitrogen atom and the pyridyl moiety itself can be associated with enhancement of the Eu-N_{py} bond strength and is expected to inhibit dissociation of the Eu-N_{py} bond, and hence increase the energy barrier to formation of a partly dissociated intermediate, thereby limiting the rate of enantiomer interconversion. The complexes with two extended chromophores showed the highest stability towards racemisation. Coincidentally, these systems have one pyridyl moiety available for applications such as functionalisation with a unique recognition motif that can be used as a recognition element for host-guest bio-

imaging.[18,123] The enhanced stability towards racemisation of this structure is a desirable property for the development of responsive chiral bio-probes.[66]

The unique photophysical phenomenon of circularly polarised emission can be utilised to monitor medium polarity. The solvation-induced changes in the shape of the CPL were found to be up to an order of magnitude larger and were more informative than those revealed by analysis of total emission variations.

This study highlights the importance of the solvent in both CPL fingerprint engineering of CPL-active Eu(III) complexes and their stability towards thermally assisted racemisation, to the point where complex design and solvent choice cannot be decoupled. Ultimately, by understanding the effect and influence of these vital external parameters a new generation of CPL active Eu(III) probes can be developed, that display either bright monosignate or well resolved opposing sign emission when paired with an adequate solvent. Additionally, examination of the effect of photo-irradiation on racemisation kinetics may be of interest. Previous work has shown the impact of photo-irradiation on the integrity of the coordinating bonds within Eu(III) complexes, *e.g.* in labilising the Eu-N_{py} bond.[140]

The present study has examined Eu(III) complexes but can be extended to other lanthanide complexes. For instance, Tb(III) complexes display more intricate CPL spectra owing to the multiplicity of the emissive and ground states.[132,141] For this reason, further work is necessary to verify if it is possible to exploit solvent effects to obtain monosignate CPL emission for chiral Tb(III) systems, for example over a narrow emission range.

CHAPTER FOUR

Temperature Responsiveness of Europium(III) Complexes

Chapter Four: Temperature Responsiveness of Europium(III) Complexes

The work presented in this Chapter aims at measuring and analysing properties of temperature sensitive Eu(III) complexes and the underlying mechanism of such behaviour

4.1. Luminescence thermometry

4.1.1. Introduction to luminescence thermometry

Temperature affects the emission properties of virtually all luminescent species,[71] as it is evident from the *T* dependence on the Boltzmann distribution regulating the population of the salient ground and excited state energy levels.[142] The *T* dependence of emission properties is usually small. Compounds exhibiting high temperature sensitivity find applications in luminescence thermometry[143] and temperature sensors make up 75-80% of the market for sensors.[144] Luminescence thermometry offers remarkable advantages over more established techniques, such as liquid-filled glass thermometers[145] and Seebeck effect thermocouples[146]. Optical sensors and more specifically molecular *T* probes possess the inherent advantage of embedded contactless measurements that allow monitoring of temperature. This form of luminescence thermometry can achieve spatial resolution of down to 10 μm, allowing measurements and imaging to be facilitated on small systems, such as microfluidic devices, integrated electric circuits or during live cell thermometry.[143]

Two relevant parameters that quantify the performance of *T* probes candidates are *sensitivity*, *i.e.* the slope of the chosen reporter signal change expressed as the percentage variation per degree Kelvin ([% K^{-1}]), and *resolution*, *i.e.* the temperature change corresponding to the minimum detectable signal change ([K]). Changes in luminescence caused by *T* are preferably detected by measurement of intensity ratios, in order to eliminate probe concentration dependence of the measurement and any potential fluorescence artifact. On the other hand, luminescence lifetime measurements may also be used and have the advantage of not requiring external referencing and are, to a wide extent, independent of concentration, optical thickness, geometry, and photobleaching.[71] In the case of lifetime measurements, long-lived emitters such as *d*-metal (order of μs) or *f*-metal complexes (ms regime) are preferred,

as less sophisticated excitation sources and detection methodologies are required to accurately measure small lifetime variations.

The mechanisms that account for a sensitive thermal response are diverse and numerous. Some fluorophores form exciplexes or excimers that display *T*-dependent properties; examples include perylene and *N*-allyl-*N*-methylalanine in a polystyrene matrix. Temperature driven dissociation of the excimer imparts thermal sensitivity.[147] Triarylboron-based fluorescent molecular thermometers have been described that are in thermal equilibrium between the local excited state emission (LE) and the twisted intramolecular charge transfer (TICT). As *T* increases, the TICT excited state is transferred into LE emission, inducing a thermochromic shift from green to blue emission. Molecules such as acridine yellow or fullerene exhibit highly *T*-dependent thermally activated delayed fluorescence (TADF).[148,149]

4.1.2. Lanthanide based luminescent thermometers

Metal-ligand complexes are good candidates for fluorescence thermometry as they possess orders of magnitude longer lifetimes, moderate brightness, and large pseudo-Stokes' shifts compared to purely organic emitters. The major disadvantages were traditionally considered to be their lability towards dissociation and quenching by oxygen, often obviated by encasing the probes in gas-impermeable polymers.[143] The long radiative lifetimes of *f*-metal ions make lanthanide complexes appealing candidates for luminescence thermometry. The europium thenoyltrifluoroacetonate chelate complex, $Eu(TTA)_3$, has been used in a PMMA matrix to image *T* via lifetime imaging on an integrated circuit.[150] The spatial resolution of this sensor was reported to be 0.7 mm. The probe was also injected into cells for thermal imaging of receptor-activated heat production in living cells.[151] Emission from this complex is not quenched by oxygen and the thin films responded to *T* change over the range of 47 – 97 °C with a sensitivity of 1.2% K^{-1}.

Lanthanide-based molecular thermometers described in the literature are suitable for applications in the physiological range, but often possess limited stability in aqueous solutions due to ligand dissociation.[17] An additional limitation of most lanthanide complexes is that they require excitation in the UVA range (315 – 400 nm) which can trigger notable bio-autofluorescence background and cellular damage under

prolonged irradiation. Therefore, longer wavelength excitation is preferable. Thermal imaging in cells is an emerging field of research, and intracellular heat mapping has been accomplished with a spatial resolution at the diffraction limit (200 nm) and a resolution of 0.18 – 0.58 K via the use of polymeric nanogels, establishing that the intracellular *T* map and its gradient are not uniform.[152]

4.2. Europium(III) pH responsive probes

4.2.1. Previous results

Recent studies by Fradgley *et al.*[114] attributed the pH sensitivity of some Eu(III) complexes to photo-induced electron transfer (PET) quenching of the Eu(III) excited state involving the lone pair of the peripheral amino nitrogen atom. This quenching pathway is only accessible when the lone pair is not engaged in a dative bond, and therefore only occurs for the unprotonated form of the complex. For this reason, the emission lifetime and intensity of the complex showed the typical sigmoidal shape of a titration curve as a function of pH, (Figure 4.1).

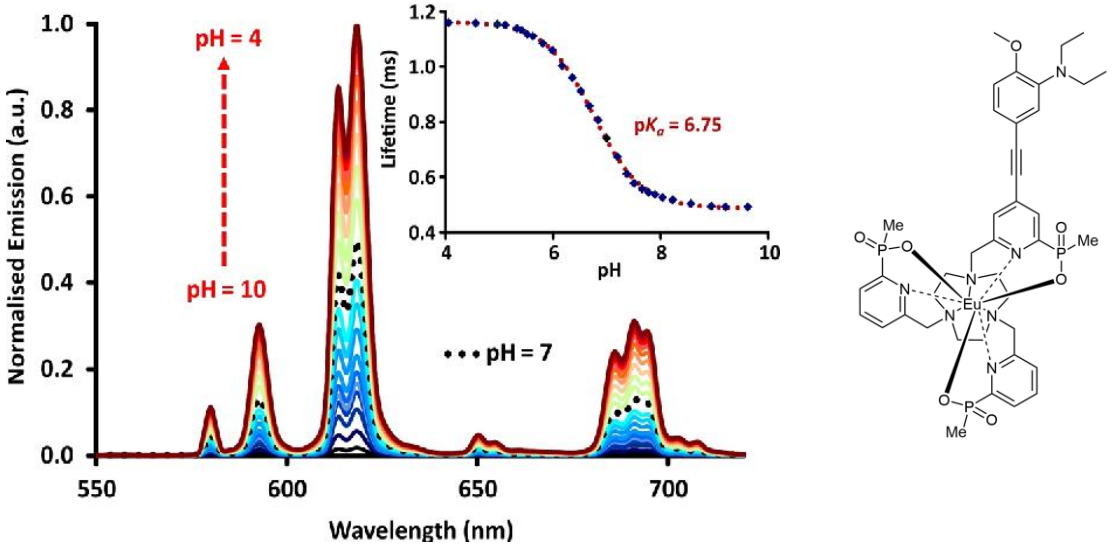

Figure 4.1. Variation of Eu(III) emission and lifetime with pH (*left*) of the Eu(III) complex, **[EuL^{11}]** (*right*), λ_{exc} = 331 nm. Image adapted from [114].

4.2.2. Remarkable temperature dependence of europium(III) pH probes

In the present study, the same pH sensitive Eu(III) probes are shown to exhibit remarkable temperature dependent quenching along with their pH dependence. An

investigation of the rationale of this temperature dependence and whether it is linked to pH sensitivity was carried out. C_3 Symmetric and *quasi*-C_3 symmetric Eu(III) complexes were examined, **[Eu.L$^{12\text{-}13}$]**, and the pH insensitive complexes[131] **[Eu.L^{8}]** and **[Eu.L^{14}]** were used as controls to test the photophysical properties and their dependence on temperature of two structurally related pH responsive complexes, **[Eu.L$^{12\text{-}13}$]**, (Figure 4.2).[55,114,131]

The temperature dependence of the emission properties of the pH probes **[Eu.L$^{12\text{-}13}$]** was studied over the range 25 - 50 °C in order to establish the impact of variable temperature on probe pH response. The origin of the pH responsive emissive properties of these complexes has been previously discussed and was initially attributed to a pH driven 'switch on/off' mechanism that arises from the PET quenching of the Eu(III) excited state by the lone pair of the peripheral amino group.[17]

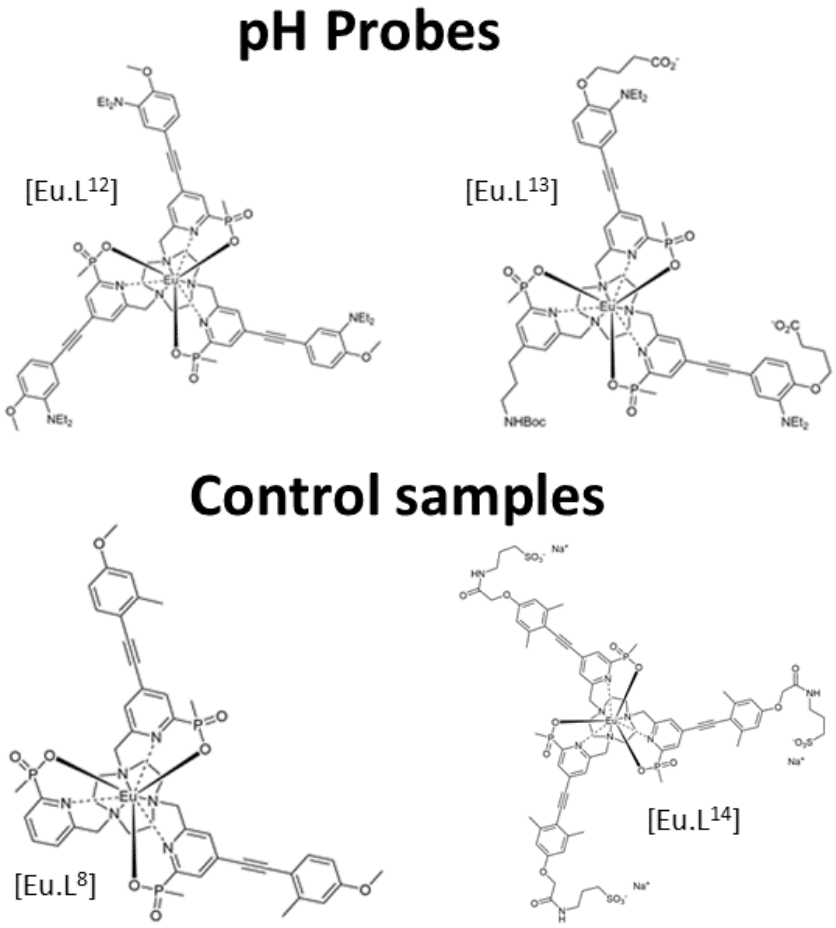

Figure 4.2. Structure of the pH probes **[Eu.L$^{12\text{-}13}$]** under investigation, along with the two reference complexes used as control samples, **[Eu.L$^{8\text{-}14}$]**.

Emission from the complex **[Eu.L^{12}]** was studied at pH 4 (over *99% protonated form* **[H$_3$Eu.L^{12}]$^{3+}$**, calculated from the pK_a value of 6.2 at room temperature)[114] and at pH 7 (*ca. 8% protonated*). Lifetimes and their percentage variation are presented in Figure 4.3.

Emission from **[Eu.L^{12}]** is quenched at pH 7 as the nitrogen lone pair on the peripheral aryl ring of the extended chromophore quenches the $^5D_0$ Eu(III) excited state via intramolecular PET, and is switched on in the triprotonated form accompanied by the lowering of the energy of the ICT excited state.

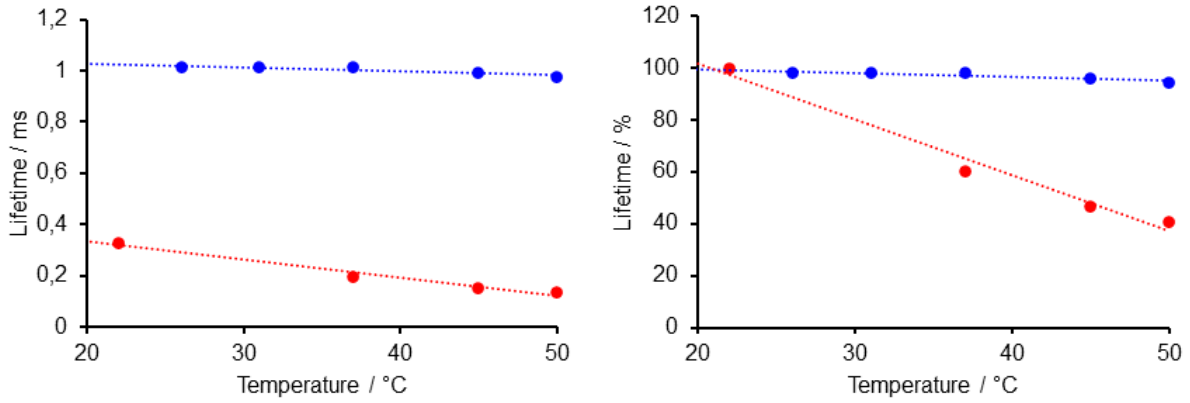

Figure 4.3. Lifetimes (*left*) and their percentage variation (*right*) of **[Eu.L^{12}]** at pH 4 (*blue dots*) and 7 (*red dots*).

To serve as a control, analogous experiments were carried out on the complexes **[Eu.L^8]** and **[Eu.L^{14}]**, whose emission are known to be pH-insensitive.[131] Interestingly, these experiments revealed a strong *T* dependence for each of the pH sensitive probes **[Eu.L$^{12\text{-}13}$]**, with significant thermal deactivation observed in the case of the quenched probes at pH 7. A maximum *T* relative sensitivity of 2.1% K^{-1} was found in the range 25 - 50 °C, a value higher than most other reported *T* probes in this range.[143] The calibration graph is linear over the *T* range investigated, thereby providing a constant sensitivity.

4.2.3. First hypothesis: T dependence of probes stems from their pH sensitivity

The pH-insensitive complex **[Eu.L^{14}]** has a temperature sensitivity of 0.25% K^{-1}, one order of magnitude smaller than **[Eu.L$^{12-13}$]**. The complex **[Eu.L^{8}]** shows a temperature sensitivity below 0.1% K^{-1}. Such behaviour is analogous to that exhibited by each of the pH probes in their protonated state, (Figure 4.4). This very small temperature dependence suggests that the *T* dependence observed for **[Eu.L$^{12-13}$]** may be correlated with its pH responsiveness. Figure 4.4 shows an overlay of the percentage lifetime variation of the control complex **[Eu.L^{8}]**, and the pH probe with the largest temperature dependence, **[Eu.L^{12}]**, at pH 4 and 7. The behaviour of **[H$_3$Eu.L^{12}]$^{3+}$** at pH 4 closely matches the trend observed for the control complex. At this pH, the complex is over 99% protonated and the PET quenching pathway is vigorously suppressed with the emission spectral properties being akin to those of a complex lacking the amino substituent. This observation supports the hypothesis that the observed temperature dependence is a consequence of a thermally activated process involving population of a low-lying charge transfer state.

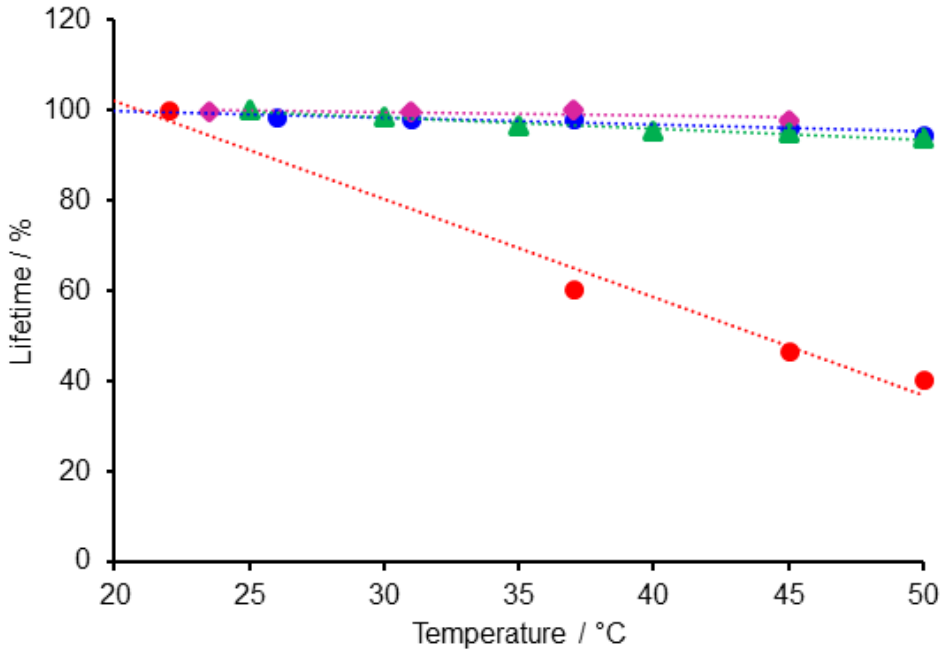

Figure 4.4. Percentage lifetime variation for the control complexes **[Eu.L^{8}]** (*purple squares*) and **[Eu.L^{14}]** (*green triangles*) compared to **[H$_3$Eu.L^{12}]$^{3+}$** at pH 4 (*blue dots*) and **[Eu.L^{12}]** at pH 7 (*red dots*). The behaviour of the protonated **[H$_3$Eu.L^{12}]$^{3+}$** complex matches that of the pH-insensitive controls.

The total emission intensity shows an analogous decrease with increasing temperature. This decrease has the same magnitude over the whole emission spectrum (there are no emission manifolds that are quenched preferentially) equal to a 2% K^{-1} decrease for the quenched probe, consistent with a common process for deactivation of the Eu(III)-centred excited state. The lifetime decrease can also be measured indirectly by integrating the total emission spectrum over a set integration time, as the recorded intensity decreases accordingly.

The *T* dependence of emission arising from the anionic pH probe **[Eu.L^{13}]$^{2-}$**, with analogous PET driven switch on/off properties, was studied at pH 7 (*switched off*). The results closely parallel those found for **[Eu.L^{12}]**, this time with a 1.1% K^{-1} decrease in total emission intensity and a lifetime decrease of 2.0% K^{-1}.

Further investigations were carried out to clarify the underlying mechanism and elucidate the origin of this strong thermal deactivation. The *T* sensitivity of the unprotonated probe **[Eu.L^{12}]** is 20 times higher than its conjugate acid **[H$_3$Eu.L^{12}]$^{3+}$**. This observation suggests a higher rate of PET quenching for **[Eu.L^{12}]** with respect to **[H$_3$Eu.L^{12}]$^{3+}$**. The processes involving the ground and excited states of each species are presented in Figure 4.5.

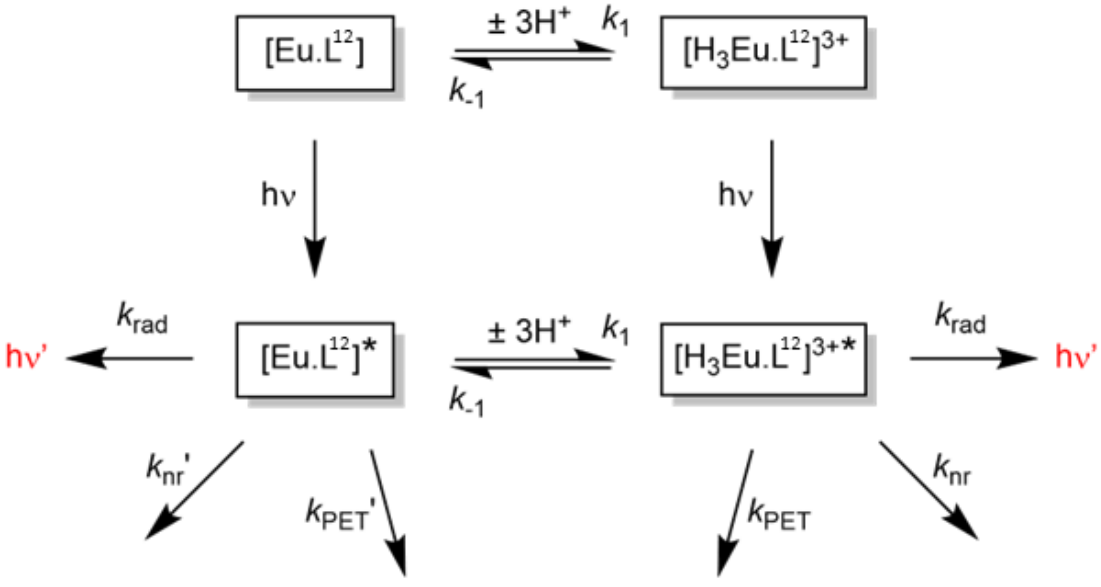

Figure 4.5. Processes and their rate constants for the ground and excited states of the protonated and unprotonated species of **[Eu.L^{12}]**. k_1 and k_{-1} = protonation and deprotonation rate constants (protonation at each site is considered independent on the others due to the large distances between the protonation sites); k_{PET} and $k_{PET'}$ = PET rate constants for the protonated and deprotonated complex; k_{rad} = radiative decay rate constant; k_{nr} and $k_{nr'}$ = non-radiative decay rate constants for the protonated and deprotonated complex.

In the absence of light, only the ground state of each species is populated. The position of the equilibrium is determined by the pH of the solution, and the rates of protonation and deprotonation are k_1 and k_{-1} respectively. Proton transfer to and from the aryl amino groups is fast, of the order of 10^{10} s^{-1}. *A priori*, four possible species could be present in solution, *i.e.* the unprotonated, mono-, di-, and tri-protonated complex. However, the pK_a of each peripheral amino group can be considered to be unaffected by protonation of the other amino groups as they are more than 10 Å apart. For this reason, the concentration of the mono- and di-protonated species can be neglected at pH values far from the pK_a, like those in this study carried out at pH 7 and 4. Absorption of a photon promotes either of the two major species to their excited state, labelled **$[H_3Eu.L^{12}]^{3+*}$** and **$[Eu.L^{12}]^*$**. These species also experience a fast proton transfer equilibrium. Radiative decay results in the emission of light with a rate constant k_{rad} of the order of 10^3 s^{-1}. The rates of PET quenching are k_{PET} and k_{PET}' for the protonated and unprotonated complex respectively, and are such that k_1, k_{-1} >> k_{PET}' > k_{PET} > k_{rad}. All the non-radiative decay pathways other than those of k_{PET} and k_{PET}' have been included in the k_{nr} term, which is smaller than k_{rad}. The available spectroscopic evidence presented suggests that the protonated and unprotonated species of the excited probe equilibrate quickly with respect to all the other processes. For this reason, the ratio of the two excited species is determined by the pH of the solution, in the same way as the ground state protonation equilibrium. The excited complex **$[Eu.L^{12}]^*$** has a comparatively larger k_{PET}' term that competes with k_{rad}, effectively quenching its luminescence.

The role of the potential energy barrier in determining the thermal activation of the quenching pathway was examined by comparing Arrhenius plots. The slope is proportional to the activation energy E_a for that process, based on the simple Arrhenius approximation, (eq. 4.1):

$$k = Ae^{-\frac{E_a}{RT}} \qquad (4.1)$$

where R is the universal gas constant, T is the absolute temperature, and A is a pre-exponential factor. The Arrhenius plots obtained for **$[Eu.L^{12\text{-}13}]$** are presented in Figure 4.6 and the inferred activation energies are reported in Table 4.1.

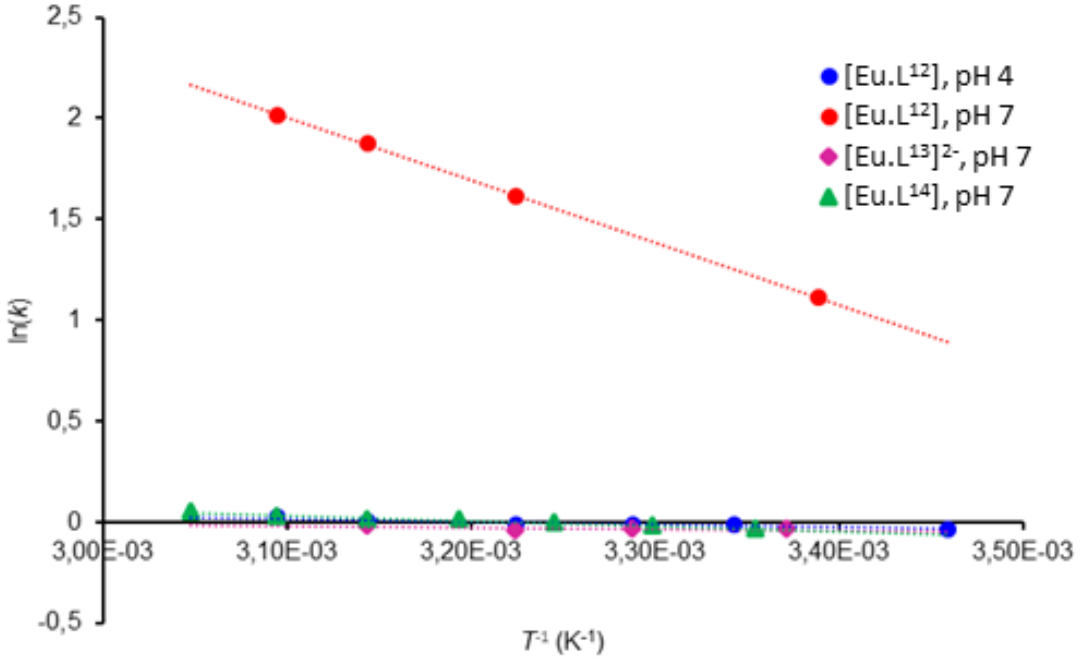

Figure 4.6. Arrhenius plots for **[Eu.L^{12}]** at pH 4 and 7 (*left*) and **[Eu.L^{13}]$^{2-}$** and **[Eu.L^{14}]** at pH 7 (*right*).

The data reported in Table 4.1 show that the two pH probes **[Eu.L$^{12\text{-}13}$]** display comparable lifetime percentage decreases at pH 7. The activation energy found for the PET quenching pathway is large enough when compared with the value of the thermal energy (*kT*) at room temperature to account for the remarkable temperature sensitivity in this range.

The sensitivity over the ambient and physiological temperature range is particularly interesting for the application of such complexes in luminescence thermometry. Conversely, the behaviour of the protonated pH probe **[H$_3$Eu.L^{12}]$^{3+}$** perfectly matches the trend observed in the control complex, **[Eu.L^{8}],** both in terms of percentage total emission and lifetime decrease, leading to the hypothesis that the availability of the nitrogen lone pair is key to explain the temperature dependence in this series of complexes.

Table 4.1. Summary of the data obtained from **[Eu.L$^{12\text{-}13}$]** and **[Eu.L^{8}]** in the range 25 – 50 °C.

Complex	% Emission [a] decrease / K	% Lifetime [a] decrease / K	E_a [b,c] (kJ mol^{-1})
[Eu.L^{13}]$^{2-}$, pH 7	1.1%	2.0%	12
[Eu.L^{12}], pH 7	2.0%	2.1%	13
[H$_3$Eu.L^{12}]$^{3+}$, pH 4	0.4%	0.1%	0.6
[Eu.L^{8}], pH insensitive	0.5%	<0.1%	N.D.
[Eu.L^{14}], pH insensitive	N.D.	0.25%	N.D.

[a] Errors in the percentage emission and lifetimes are 0.1%. [b] Errors on E_a values are 0.3 kJ mol^{-1}. [c] E_a values are to be compared to kT at 298 K equal to 2.5 kJmol^{-1}.

4.2.4. Second hypothesis: a more general quenching pathway

A remarkable sensitivity of luminescence on temperature variations has more recently been found on complexes that have no available *N* lone pairs, effectively disproving the generality of the first hypothesis involving a temperature-assisted quenching mechanism operated via lone pair electron donation. Parallel work is currently underway in Hong Kong Baptist University, identifying Eu(III) complexes whose photophysical properties display a strong temperature dependence despite the lack of lone pair donor atoms. New water-soluble Eu(III) complexes were synthesised by Tsz-Lam Cheung using a 1,4,7,11-tetraazacyclododecane (cyclen) scaffold. The structures of the two complexes are shown in Figure 4.7. The synthetic route, not described here, closely parallels the modular approach extensively detailed in Chapter Two regarding the synthesis of TACN-based lanthanide complexes.

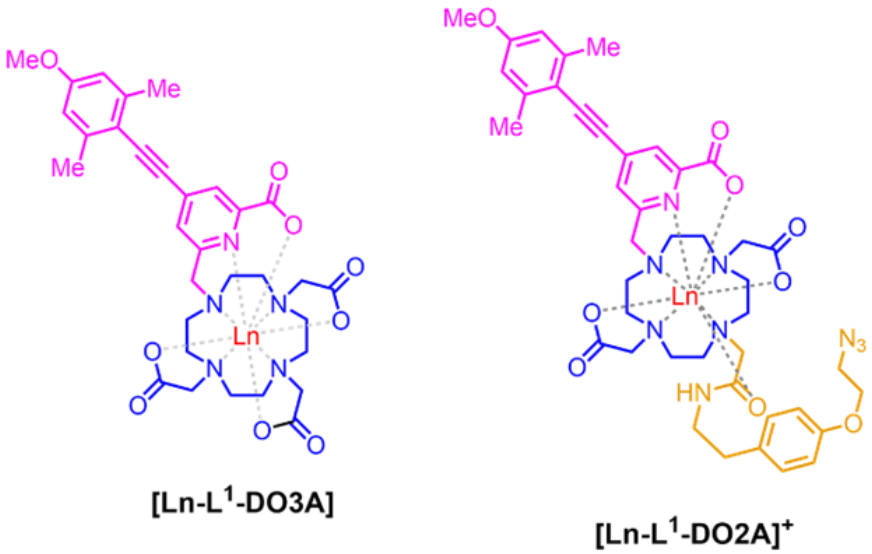

Figure 4.7. Structure of the complexes **[Eu-L^1-DO3A]** and **[Eu-L^1-DO2A]$^+$** that exhibit temperature dependent and pH independent luminescence. Image courtesy of Tsz-Lam Cheung.

A different decay pathway to account for the thermally activated non-radiative decay of the Eu(III) excited state can now be proposed, (Figure 4.8). This hypothesis is more general as it involves the crossing of the potential energy surface (PES) of the chromophore ICT excited state, rather than focusing on the properties of the nitrogen lone pair in isolation with respect to the highly conjugated chromophore that hosts it. The proposed decay pathway, (Figure 4.8), can be hypothesised to proceed as described by the following photophysical sequence:

- Excitation of the chromophore internal charge transfer (ICT) state follows the absorption of a UV photon; energy transfer from the ligand ICT state to the $^5D_1$ Eu(III) excited state occurring at the conical intersection between the ICT and $^5D_1$ potential energy surfaces; fast non-radiative relaxation to the radiatively long-lived $^5D_0$ Eu(III) excited state occurring as usual, (*vide supra* - Section 1.1.2);
- The $^5D_1$ Eu(III) excited state can either decay radiatively with a small rate constant k_{rad} to any of the ^7F_n states constituting the ground state manifold of Eu(III), or

- A back energy transfer (BET) process occurs characterised by a rate constant k_{BET} that competes with the radiative decay pathway. This transition is conditional on overcoming a thermal energy barrier E_a to populate the lower vibrational levels of the ICT PES, followed by fast relaxation until the conical intersection with the PES associated with the ^7F_n states provides a non-radiative decay pathway.

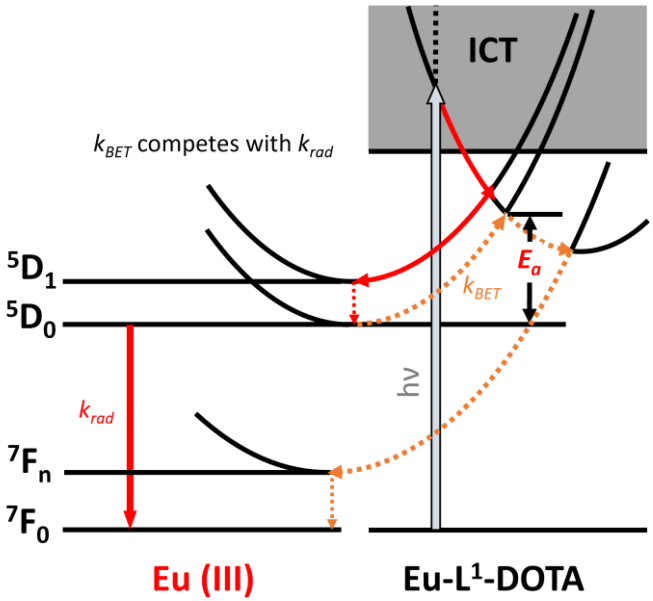

Figure 4.8. Schematic representation of the energy levels and potential energy surfaces of **[Eu-L^1-DO3A]**, with a particular focus on the position of conical intersections. Energy transfer pathways are indicated with arrows. Image courtesy of Tsz-Lam Cheung.

The magnitude of E_a determines the observed temperature dependence and is of the order of a few k_BT at room temperature. Due to Arrhenius law, a small variation in E_a/k_BT can result in a large variation of k_{BET} competing with k_{rad}. As k_{BET} increases, the emissive $^5D_0$ state gets depopulated and the Eu(III) emission is quenched. The same process may well occur with the shorter-lived Eu $^5D_1$ excited state. A rate equation can be written for the population of the ^5D state considering all the phenomena that depopulate it, namely radiative decay (k_{rad}), the suggested thermally activated back energy transfer quenching pathway (k_{BET}), and all other non-radiative decay pathways, summarised in the overall k_Q rate constant. Note the dependence of the BET term on the ICT excited state effective concentration [CT].

$$\frac{d[\,^5D]}{dt} = -k_{\mathrm{rad}}[\,^5D] - k_{\mathrm{Q}}[\,^5D] - k_{\mathrm{BET}}[\,^5D][CT] \qquad (4.2)$$

Assuming that the population of the ^5D state following absorption of a photon is equal to $[^5D]_0$ at $t = 0$, the rate equation can be integrated for $t > 0$ (positive terms on the right term of eq. 1 vanish for $t > 0$ as the ^5D state is no longer being populated) as:

$$[\,^5D] = [\,^5D]_0\, e^{-(k_{\mathrm{rad}} + k_{\mathrm{Q}} + k_{\mathrm{BET}}[CT])t} \qquad (4.3)$$

This implies an observed depopulation rate constant k_{obs} equal to:

$$k_{\mathrm{obs}} = k_{\mathrm{rad}} + k_{\mathrm{Q}} + A\, e^{-\frac{E_{\mathrm{a}}}{RT}} \qquad (4.4)$$

where the back energy transfer rate is expressed in term of the activation energy E_a according to Arrhenius law. A plot of ln(k_{obs}) with inverse temperature T^{-1} is expected to be approximately linear with a form correlated to the value of E_a; it shows some deviation from linearity due to the competing depopulation processes characterised by the k_{rad} and k_Q rate constants, (Figure 4.9.D).

Experimental results and data analysis are reported in Figure 4.9. The complex **[Eu-L^1-DO3A]** in water displays a marked lifetime reduction of 1.2 % K^{-1}, making it appealing for potential applications as a molecular thermometer, (Figure 4.9.C). The observed sensitivity is attributed to the thermal activation energy being estimated as E_a = (17 ± 2) kJ mol^{-1}, accessible around room temperature, (Figure 4.9.D).

Work is currently underway in Parker's group to find experimental evidence to support the energy crossover hypothesis. Furthermore, preliminary microscopy investigations have revealed the low cytotoxicity of the complex in live HeLa cells and demonstrated its ability to internalise into cells. The complex **[Eu-L^1-DO2A]$^+$** holds the potential to further this thanks to its versatile peripheral azide group that can be used for late-stage functionalisation, enabling the addition of lysosome- and mitochondria-targeting peptides to monitor temperature changes in specific organelles.

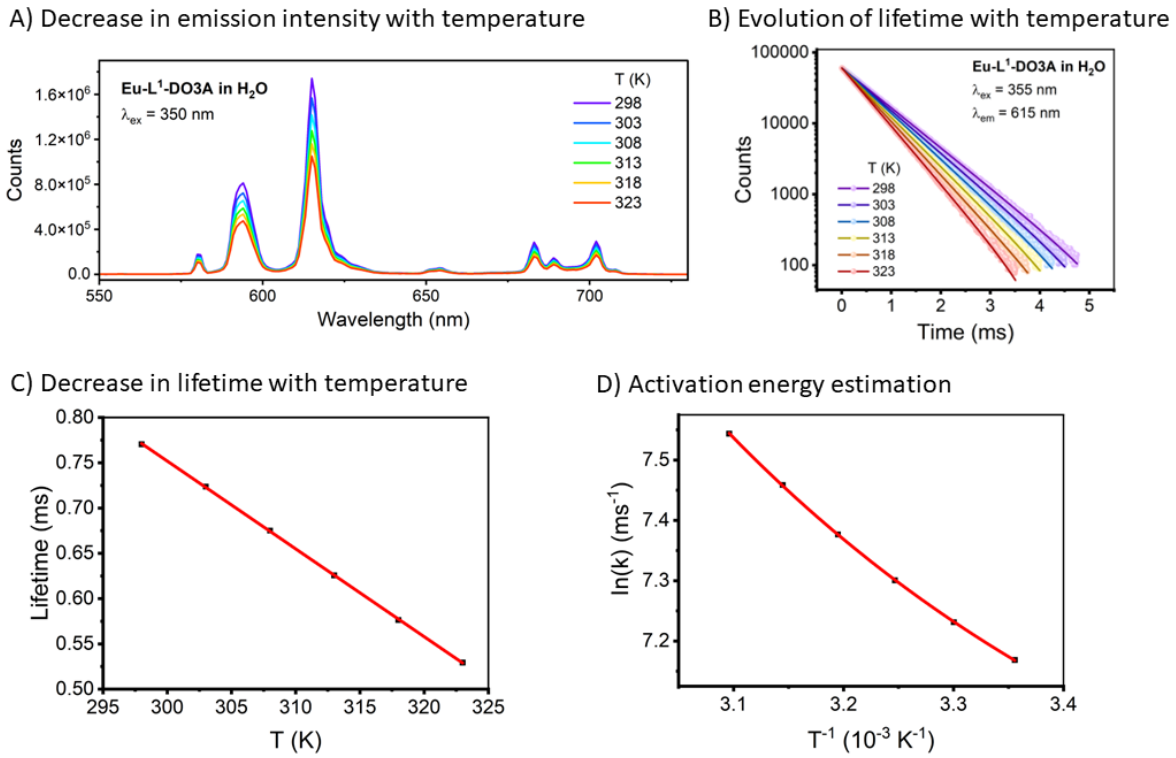

Figure 4.9. Experimental results and data analysis of the photophysical properties of **[Eu-L^1-DO3A]**. (*A*) Decrease in emission intensity with temperature. (*B*) Evolution of lifetime with temperature. (*C*) Decrease in lifetime with temperature. (*D*) Activation energy estimation. Images courtesy of Tsz-Lam Cheung.

4.3. Summary

Temperature measurements are ubiquitous in science and technology. New small molecules that display large temperature sensitivity are appealing in the field of molecular thermometry, as opposed to highly engineered nanomaterials that currently dominate the field.

In this chapter, the state-of-the-art in molecular thermometry was presented. A novel approach to the problem was proposed, exploiting the recently discovered large temperature sensitivity of certain luminescent Eu(III) complexes. These complexes display exceptionally large temperature sensitivities in lifetime and emission intensities, rivalling those of composite nanomaterials.

These complexes were previously synthesised as pH probes, their sensitivity arising from photo-induced electron transfer (PET) quenching operated by the peripheral nitrogen lone pair in the unprotonated complex. For this reason, an investigation to

check if the temperature dependence is correlated with the pH sensitivity, sharing a similar mechanism, was performed. As a first hypothesis, the temperature sensitivity was interpreted as a consequence of the small PET energy barrier: the quenching rate displays a strong *T* dependence as the quenching pathway is favoured at a larger temperature.

However, the empirical evidence of Eu(III) complexes that are pH insensitive and still display an equally large *T* dependence found at Hong Kong Baptist University urges an alternative explanation to this phenomenon. A more general decay pathway was proposed to account for the thermally activated non-radiative decay of the Eu(III) excited state, involving the potential energy surface crossing of the chromophore ICT excited state, rather than focusing on the properties of the N lone pair in isolation with respect to the highly conjugated chromophore that hosts it.

Preliminary investigations provide results that are compatible with the proposed model. Further investigations need to be carried out to fully validate the hypothesis. Fully understanding the mechanism that accounts for *T* sensitivity in Eu(III) complexes is key to the design of novel temperature probes. This discovery makes the design of molecular temperature probes easier because a pH sensitive temperature probe provides an ambiguous output in an environment with controlled, but unknown pH, such as in cells. On the other hand, a temperature probe that is intrinsically independent of pH would provide an absolute temperature measurement of its environment.

CHAPTER FIVE

CPL Photography

Chapter Five: CPL Photography

The content presented in this chapter is based on the following publication:

Davide F De Rosa, Patrycja Stachelek, Dominic J Black, Robert Pal, *Rapid handheld time-resolved circularly polarised luminescence photography camera for life and material sciences*, Nature Comm., 14, 1537 (2023)

The two main objectives of the work presented in this Chapter are the development of novel ink-based security tags that incorporate mono-signate CPL-active Eu(III) complexes as an additional layer of security; and the development of a novel compact, high-throughput CPL camera for facile scanning of CPL-based security tags.

5.1. Introduction

5.1.1. Critical analysis of state-of-the-art instrumentation

State of the art PEM-CPL spectrometers were thoroughly described earlier, (*vide supra* - Section 1.2.3). Previously published innovations at the frontier of CPL detection by Pal *et al.*, such as SS-CPL and CPL confocal microscopy,[153,154] were also presented earlier, (*vide supra* - Section 1.2.3). The present chapter focuses on building and benchmarking the first rapid handheld time-resolved CPL photography camera, a design that overcomes several limitations in instrumentation and has the potential of promoting well diversified commercial applications of CPL.[134]

PEM-CPL setups are bulky, relatively expensive (> £50k) instruments with slow spectral data acquisition rates (~1 h for a typical CPL spectrum, 100 nm spectral range, 5 averages with a 0.5 nm/s resolution).[155,156] More importantly, time-resolved detection of CPL is virtually inaccessible due to the fixed oscillating mechanically induced birefringence resonating nature of the PEM (@ 42 kHz). These issues explain why CPL is not currently used as a routine spectroscopic technique.

The more cost effective, smaller footprint SS-CPL circumvents part of the issues with the traditional PEM-CPL architecture, (Figure 5.1). The SS-CPL spectrometer replaces the PEM with a dual channel optical layout and two distinct rapid readout solid state linear CCD detectors, allowing the one-shot acquisition of individual left- and right-handed CPL spectra in as little as 10 ms. Signal-to-noise ratio can be substantially improved by averaging thousands of acquisitions, taking only a few

seconds in total. Furthermore, the SS-CPL spectrometer provides a simple way to enable time-gated CPL acquisition, a technique especially useful to distinguish long-lived lanthanide emitters from short-lived emission of other fluorescent species. The SS-CPL is also significantly cheaper than the standard PEM-CPL setup (£14,000 *vs* £57,800 at time of writing for in-house built setups). Although the SS-CPL was validated against the standard PEM-CPL setup for emitters with g_{lum} above 0.05, further studies need to be performed to assess potential sources of systematic error and how they affect the sensitivity of the SS-CPL for lower g_{lum} emitters. Despite this limitation, the SS-CPL spectrometer setup is particularly relevant to the present works as it represents the first high-throughput instrument in the literature.

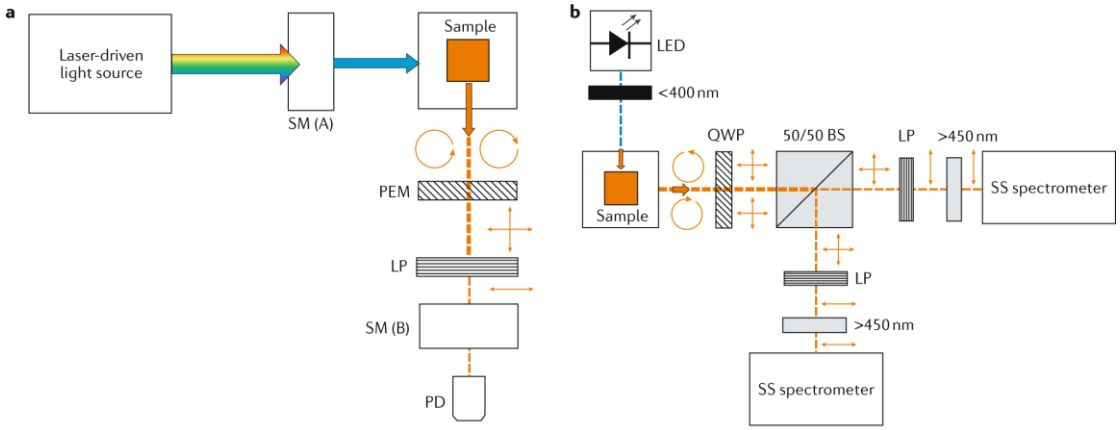

Figure 5.1. Schematic comparison between standard PEM-CPL spectrometers (*a*) and next-generation rapid SS-CPL spectrometer (*b*). Image adapted from [157].

In particular, the scheme of a SS-CPL spectrometer shown in Figure 5.1 can have two possible realisations, (Figure 5.2): the polarising beam splitter cube (*left*) can be replaced by a non-polarising beam splitter cube, provided that two orthogonal linear polarisers are placed in front of the CCDs (*right*).

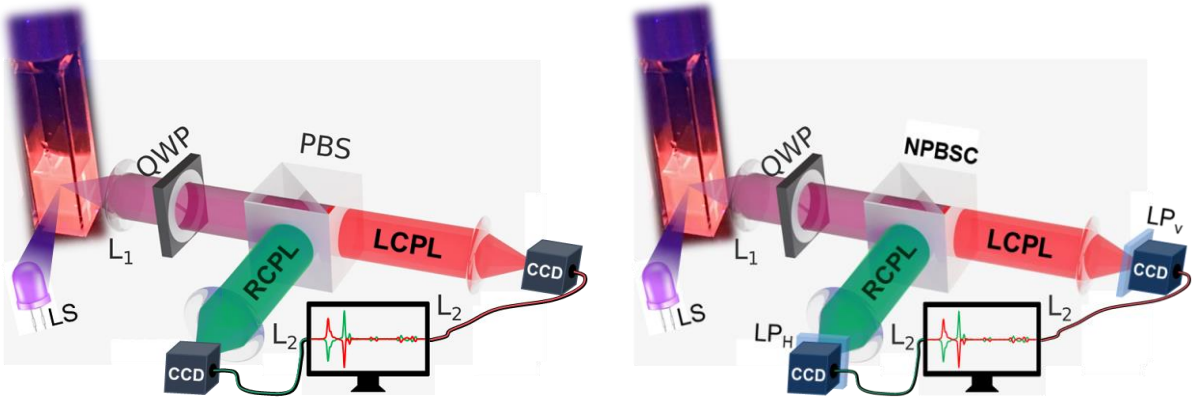

Figure 5.2. Comparison of SS-CPL spectrometers using a polarising beam splitter (*left*) and a non-polarising beam splitter with two linear polarisers (*right*).

The advantage of the latter rests on the easier calibration and alignment of the non-polarising beam splitter cube. These issues are particularly problematic in the case of emission arising from Eu(III) because the polarising beam splitter cube has a non-uniform retardation of the orthogonal S and P polarisation states in the red region of the visible spectrum, (Figure 5.3, left). The design shown on the right of Figure 5.2, *i.e.* with the non-polarising beam splitter cube, was preferred as it allows observation of the ΔJ = 4 emission manifold of Eu(III) without adding any spurious distortions, as the retardation of transmission is wavelength independent in this case, (Figure 5.3, right). The small difference in transmission between the two polarisation states can be effectively corrected in the 400 – 800 nm region using a standard calibration lamp.

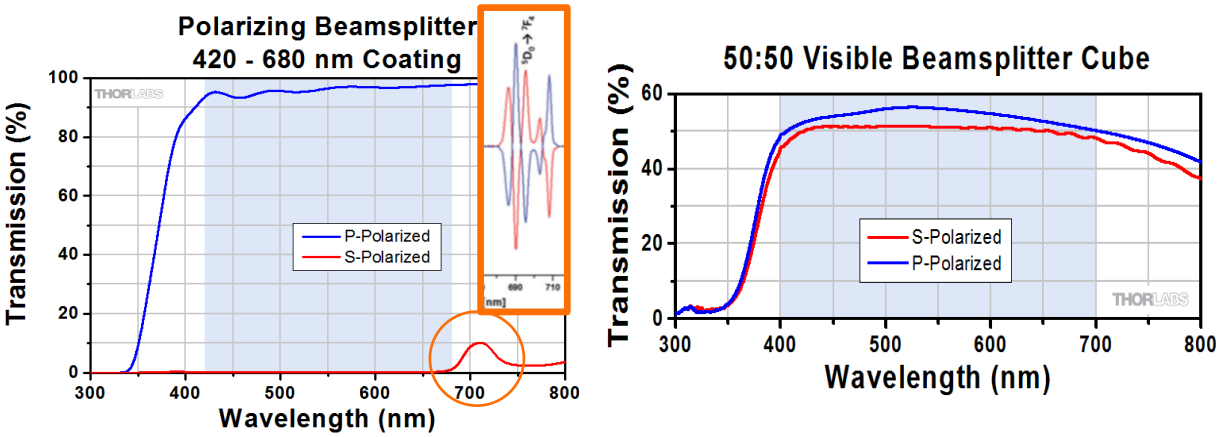

Figure 5.3. Transmission of the S and P polarisation states through the polarising beam splitter cube (*left*) and through the non-polarising one (*right*). The orange insert on the left highlights how the stray transmission of S-polarisation overlaps with the ΔJ = 4 emission manifold of Eu(III). Reference files can be found on the ThorLab website (https://www.thorlabs.com/newgrouppage9.cfm?objectgroup_id=13033).

5.1.2. Security inks

This research is fuelled by the ever-increasing need for authenticating products and documents with luminescent security inks that are vital to global commerce, health, and personal identity documents. Dyes incorporated into security inks should be invisible to the unaided eye and luminesce brightly upon UV-A irradiation, such as that of 365 nm LEDs commonly used in commercial optical document readers.[158] Suitable dyes are resistant towards photobleaching and retain their photophysical properties upon deposition, which often include lamination at temperatures often exceeding 150 °C.[159]

Lanthanide complexes are widely used in luminescent security inks due to their large pseudo-Stokes' shift, long-lived emission, reduced self-quenching, resistance to photobleaching, and narrow line-like emission profiles.[160–168] Multicomponent, multicolour inks presenting different colours under different time-gating regimes are employed on documents such as passports, (Figure 5.4).

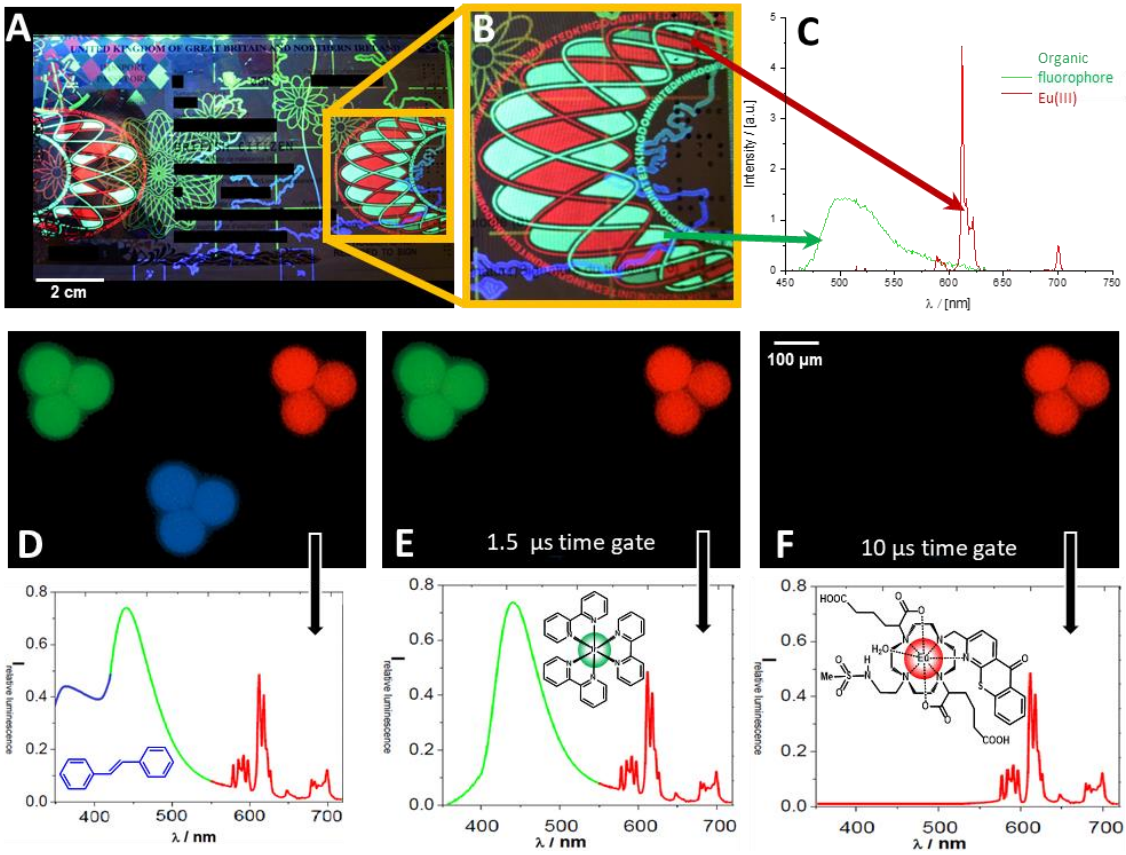

Figure 5.4. Multicomponent, multicolour inks presenting different colours under different time-gating regimes are employed on a contemporary UK passport. Short-lived blue emission from stilbene can be removed with a 1.5 µs time gate; longer-lived green emission from Ir(III) *tert*(bipyridyl) can be removed with a 10 µs time gate; long-lived (order of 1 ms) red emission from a Eu(III) complex. Image adapted from [157].

The superior CPL properties of lanthanide complexes, namely the high g_{lum} values and high CPB, have not been exploited as an added extra layer of security in advanced security inks. This is largely attributed to the limitations posed by current CPL instrumentation, where high throughput hand-held full frame/spectra detection and discrimination of L-CPL and R-CPL are not available. Embedding CPL features into security inks would prove particularly important in fighting counterfeiting as it is not

possible to make enantio-enriched dyes without advanced chiral chemistry expertise and expensive dedicated equipment, such as chiral HPLC.[169]

The solution hereby proposed to the instrumentation bottleneck that needs to be overcome to incorporate CPL features into security inks is to utilise a full frame/field of view (FOV) high sensitivity scientific camera aided by a chiroptical separator unit containing a rotating quarter waveplate (QWP) and precisely aligned stationary linear polariser (LP). The latter is important as, due to the unique birefringence of each CCD or CMOS camera chip, rotation of the LP as opposed to the QWP will result in light helicity mismatch and randomisation of CPL due to the induced light wave retardance by the detector chip itself. Subsequent spectral and chromatic (colour) selectivity can be achieved by employing an appropriate band pass filter (BPF) to match unique helicity transitions in the emitted light.

The best efforts to date on macroscale enantiomeric contrast imaging to demonstrate the potential of advanced CPL-active security inks belong to Frawley *et al.*[169] and Kitagawa *et al.*[170] The former provides a demonstration of chiral image contrast at selected wavelengths using enantiopure Eu(III) complexes blotted on brightener-free paper using a home-made detection setup based on a commercial camera; the latter concerns a luminescent glass containing an enantiopure Eu(III) complex using a similar imaging setup.

In Frawley's work, a Eu(III) complex, named **[Eu·L^1]** in the original work, was applied as a solution in methanol to non-optically brightened white paper and allowed to dry in air.[154] A time-resolved Zeiss Axiovert 200M epifluorescence microscope setup[171] was equipped with a variable pulse sequence generator, which allows both continuous and time-resolved operation. The microscope was fitted with a 365 nm pulsed UV LED (2W, 24V) and a 395 nm dichroic mirror to allow epifluorescence detection. A broad (400 – 800 nm) wavelength, 10 mm aperture achromatic quarter-wave plate, converts circularly polarised light into linearly polarised light, and is followed by a pair of high extinction (1:4000) linear polarisers that allow selection and differentiation of generated vertically and horizontally linearly polarised light. Enantioselective chiral contrast is demonstrated in Figure 5.5.

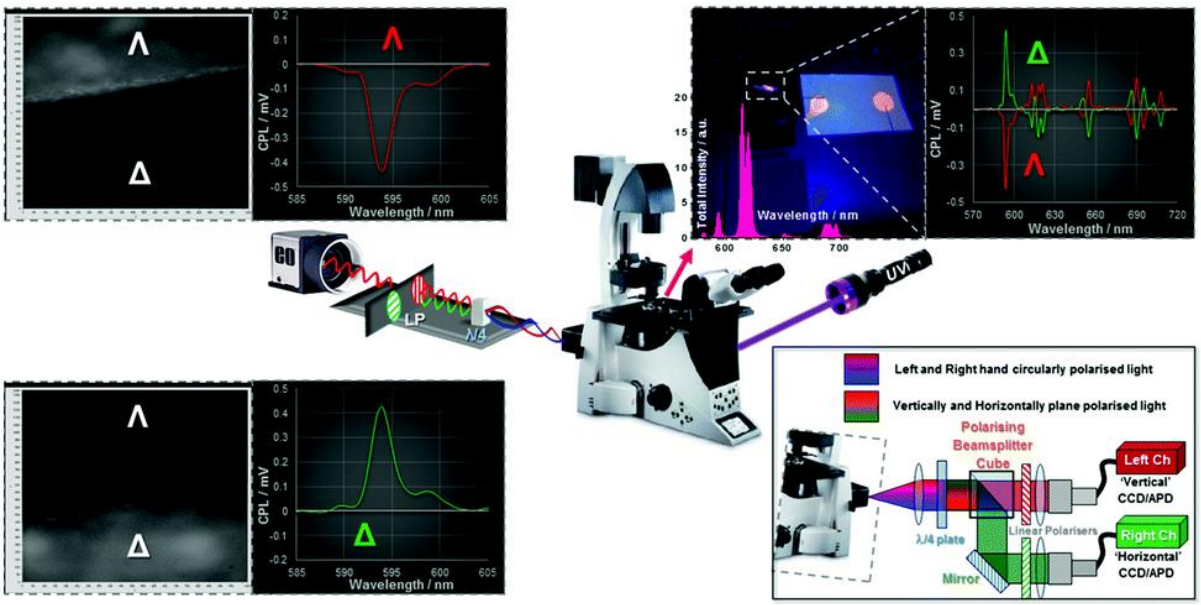

Figure 5.5. Proof-of-concept enantioselective chiral contrast on a CPL microscopy setup. Differential CPL images and relative CPL spectra (*left*), picture of the blotted paper under a 365 nm UV illumination (*top right*), and schematic layout of the dual channel chiroptical separator (*bottom right*).[154]

In Kitagawa's work, the well-characterised (±)-3-(trifluoroacetyl)camphor (±tfc) chiral ligand was used to form a complex with Eu(III) along with the achiral glass promoter tris(2,6-dimethoxyphenyl)phosphine (tmpo) ligand. Its glass formation properties arise from its multiple coordination sites provided by the phosphine oxide and methoxy moieties.[172,173] Additionally, the weakly coordinating tmpo ligand is expected to enhance CPL.[174] Solutions of $Eu(\pm tfc)_3(H_2O)_2$ and varying equivalents of tmpo in dichloromethane were drop cast onto glass substrates and allowed to evaporate at room temperature to afford a glassy homogeneous substrate, (Figure 5.6). Its amorphous structure was confirmed by X-ray diffraction spectroscopy.

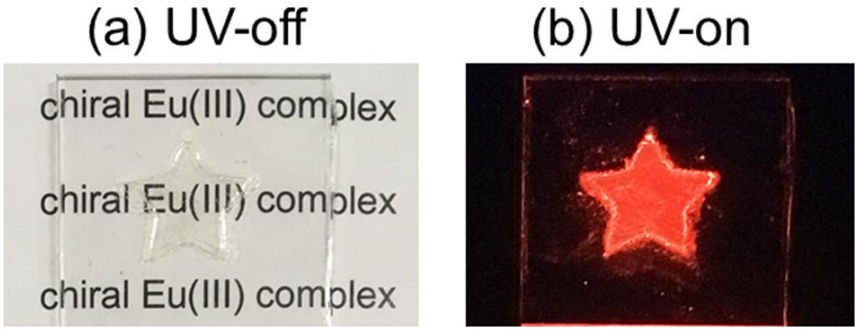

Figure 5.6. Photographs of Eu(III) lumino-glass without (*a*) and with UV light illumination (*b*, λ_{exc} = 365 nm). Image adapted from [170].

The Eu(III) lumino-glass is transparent to the naked eye and displays a very bright red emission upon UV light illumination. The brightness of the lumino-glass is 1000 times larger than that of other Eu(III) luminophores embedded in polymer films of similar thickness and concentration.[170] An interesting future development could be adapting Kitagawa's procedure to spin coating to obtain thinner films of reproducible thickness – a technique that is routinely used to cast polymer films.

A proof-of-concept demonstration of Eu(III) lumino-glass as a CPL paint was provided by Kitagawa *et al*.[170] Transparent glasses made with the two enantiomers were cast on a substrate in the shape of a sun and moon. CPL was visualised using a camera with a LP, a rotatable QWP, and a BPF, allowing the separate observation of the sun and moon shapes, (Figure 5.7). Most notably, the intensity and contrast were large enough to allow human detection of enantioselective contrast with the sole aid of the LP, QWP, and BPF. It is worth noting that the edges of the sun and moon shapes in the left- and right-CPL images have a noticeably different intensity when compared to the bulk, (Figure 7.d,e). This is due to helicity inversion of CP light upon reflection on the glass substrate or internal reflection in the material.

Lumino-glass has the disadvantage of not being flexible and that it cannot be laminated onto documents. For this reason, having in mind the goal of achieving CPL-active security inks, the present study will focus on lanthanide-doped solution-processed polymer matrices as a continuation of the previously discussed work by Frawley *et al.*[169] building on the recent advancements with CPL microscopy in the Pal group.[154]

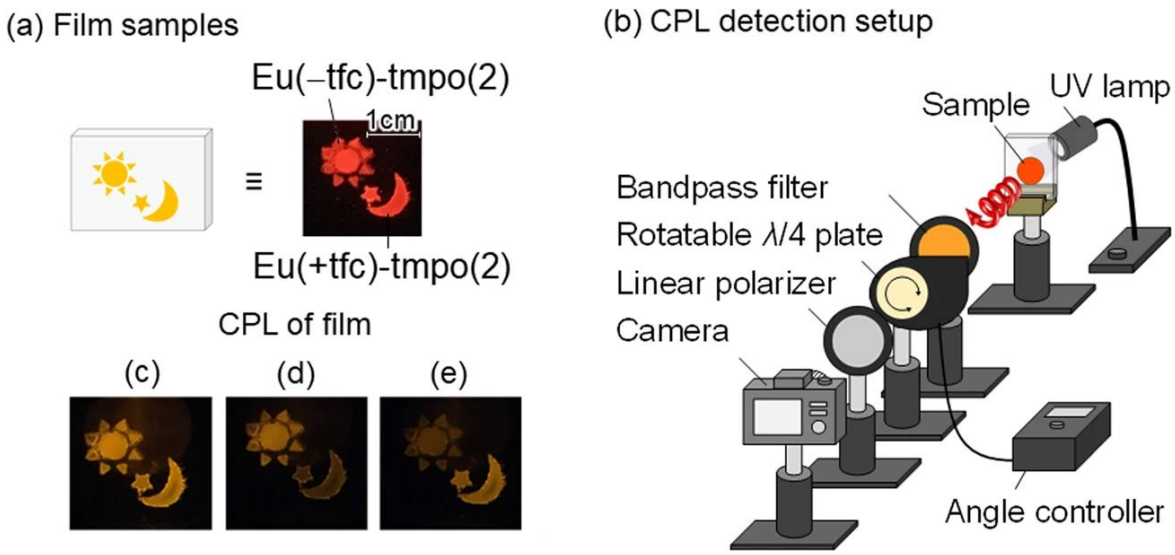

Figure 5.7. Photographs of Eu(III) lumino-glass under UV light illumination (*a*, λ_{exc} = 365 nm) and the simple CPL detection setup (b) used to acquire the enantiomeric chiral contrast pictures (*c*, total intensity; *d*, left-CPL, *e*, right-CPL). Image adapted from [170].

5.1.3. The necessity of tackling polarisation cancellation

The characteristic high dissymmetry factor and high brightness of lanthanide complexes alone are not sufficient to use a CPL-active lanthanide complex as a security ink. The difficulty with lanthanide complexes is that their emission manifolds, labelled by their *ΔJ* value, are narrow (order of 10 nm) and yet comprise of multiple transitions. The individual transitions within a single *ΔJ* manifold of lanthanide complexes often have discordant sign in CPL spectra, significantly lowering the overall CPB when integrated over the whole manifold. Unfortunately, any high throughput instrument cannot have a resolution sufficient to differentiate between the individual opposing-sign transitions (in other words, it has a large passing bandwidth). This polarisation cancellation effect manifests as a loss of signal even for emitters with a high dissymmetry factor and brightness. An example of this is shown in Figure 5.8. The absolute value of the integral of the negative and positive peaks of the CPL spectrum are comparable for either the Δ*J* = 1 and 2 manifolds. This complex would therefore be unsuitable for the purpose of this chapter due to extensive CPL sign cancellation effects.

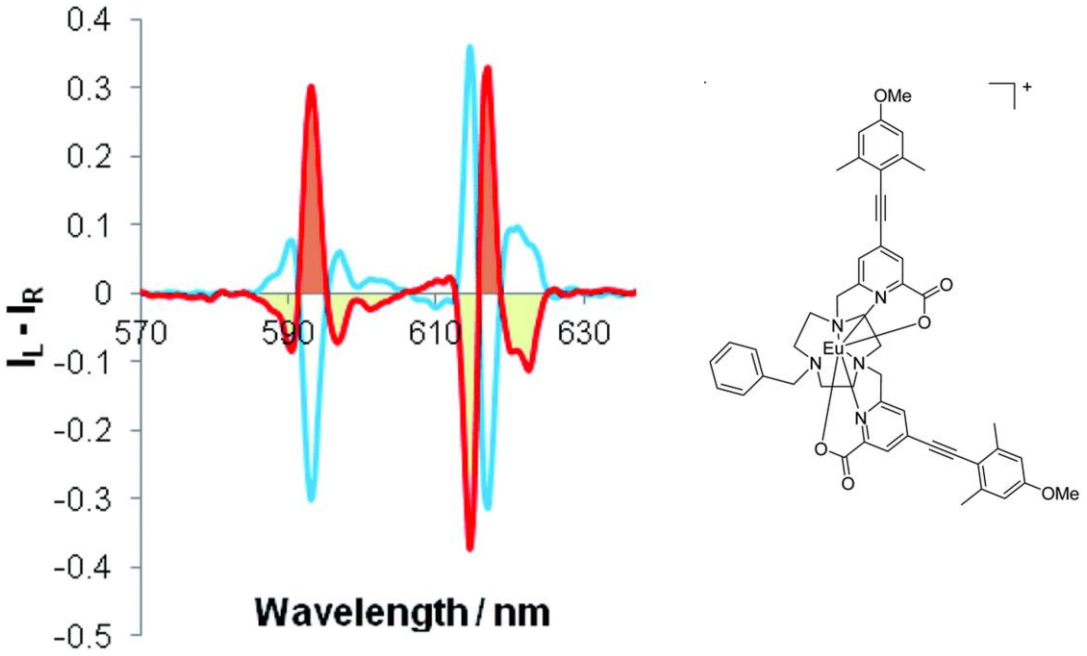

Figure 5.8. CPL spectrum of the Δ*J* = 1 and 2 manifolds (*left*) for the two enantiomers of a Eu(III) complex (*right*). Orange and yellow shadings mark the positive and negative transitions, respectively, of each shown manifold of the red CPL spectrum. Image adapted from ref.[37]

The lack of fine resolution from putative cheap, high throughput spectrometer puts constraints on the properties of the emitters used for CPL-active security inks: suitable lanthanide emitters need to have at least one monosignate CPL manifold, *i.e.* a manifold where all the individual transitions have the same sign. If this requirement is satisfied, the bandwidth does not hinder the apparent g_{lum} as CPL sign cancellation does not occur. By adopting this approach, part of the difficulty with instrumental design is transferred over to the synthetic design to achieve suitable photophysical properties of lanthanide complexes. Instrumentation and synthetic design go hand in hand and cannot be decoupled from each other, as observed in Chapter Three, where the crucial dependence of the CPL spectral profile on solvent polarity was proven.

5.2. Engineering lanthanide complexes as security dyes

Spurred on from our advancements in the field of CPL research,[153,154,157,169,175] we have coined the term Chameleon Security Inks (CSI) as a new class of intelligent security dyes. These blends of luminescent materials combine organic short-lived (ns) blue/green and red fluorophores and chiral CPL-active, high brilliance and circularly polarised brightness (CPB) red/green (europium/terbium) long-lived (ms) emitters

embedded into a transparent polymer matrix which are collectively invisible to the naked eye. The chiral molecular fingerprints encoded in the luminescence spectra of CPL active Ln(III) complexes, alongside the possibility of time-resolved colour separation, adds two extra layers of security to existing security inks. This allows for multi-layered unclonable QR or bar code generation. CSIs possess an unprecedented five-tiers of security comprised of multi-coloured, multi-spectral, opposing-helicity, combined with high spatial and temporal resolution. The increasing use of polymer-based banknotes, mainly made from biaxially oriented polypropylene (BOPP), allows the introduction of hidden in plain sight security features that can facilitate *ad hoc* verification greatly advancing security and authenticity checking when combined with the right high throughput read-out instrument.

Besides the restraint on their CPL properties, *i.e.* the aforementioned requirement to display monosignate CPL emission manifolds, there are several additional physical criteria that need to be mitigated in order to fully utilise luminescent lanthanide complexes as part of intelligent security inks.[176] A key characteristic of all security dyes is that they need to be readily soluble to be used as inks and retain required properties on deposition. They must be resistant toward fading caused by photobleaching and be thermally robust to survive conditions such as the relatively high temperatures (often excess of 150 °C for seconds – lamination speed 1 s cm^{-1}) necessary for document lamination or integration into modern plastic bank notes. Sufficient thermal stability is not trivial in the case of lanthanide emitters, as their CPL activity arises from the degree of enantiopurity which can in turn be decreased by heating due to thermally assisted enantiomer interconversion. For this reason, extra care needs to be put into the synthetic design of such emitters in order to increase the energy barrier to the enantiomer interconversion process. For a more detailed discussion on this aspect, refer to Chapter Four. Once all the above requirements have been met, the CSIs can easily be embedded into a suitable transparent polymer matrix via simple drop casting or spin coating techniques.

As highlighted above, a suitable Eu(III) complex for successful use in combination with a handheld high throughput CPL photographic (CPLP) camera needs to exhibit monosignate (single sign, either positive or negative), broad emission bands with high CPB. The sign of individual CPL bands within the $\Delta J = 1$ and 2 manifolds depends on the nature of the donor atoms used to chelate the central lanthanide ion and on the

polarity of the environment, as detailed in Chapter Three. Based on previous knowledge on the design and synthesis of luminescent lanthanide complexes,[162,176–179] a compound displaying the desired single sign properties in both Δ*J* = 1 and 2 transitions of the CPL emission in low polarity environments was designed and synthesised. The Eu(III) complex **[Eu.L^{1b}]** (Figure 5.9), bearing an ethyl ester functionality and mixed carboxylate and phosphinate donors, was synthesised and chirally resolved with complete photophysical characterisation as detailed in Section 2.1 and will be termed **[Eu.L^{1}]** in the present chapter for the sake of simplicity.

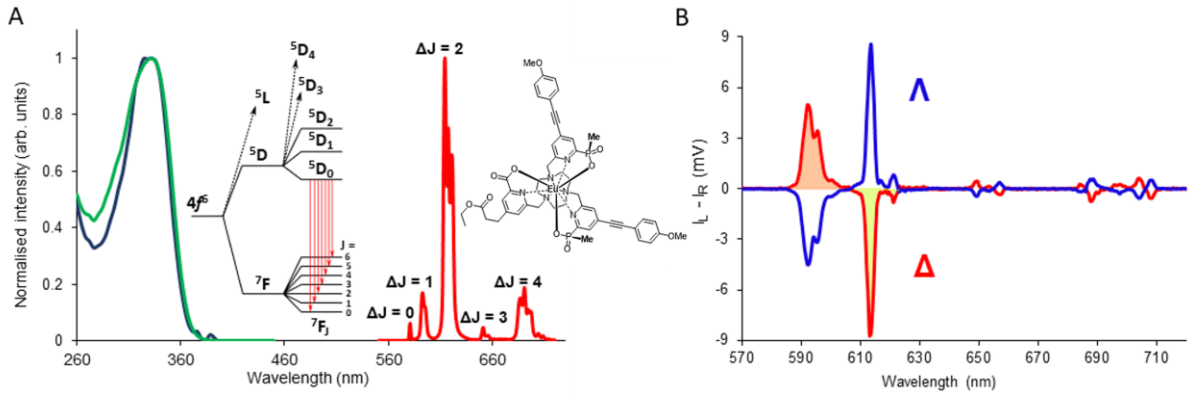

Figure 5.9. Photophysical characteristics of [Eu.L^{1}]. (A) Absorption (green), excitation (blue, λ_{em} = 614 nm) and total emission spectra (red, λ_{ex} = 355 nm) of **[Eu.L^{1}]** (c = 5.4 x 10^{-5} M) in EtOAc. (B) CPL emission spectra of Δ- (*red*) and Λ- (*blue*) enantiomers of Eu:L1. Single sign bands are highlighted with orange and yellow shading under and above the red curve. Both spectra were recorded in EtOAc, 295 K, 5 μM complex, λ_{exc} = 355 nm, 5 scans averaged with 0.5 nm resolution and 1 ms integration time.

The first CPL spectrum of lanthanide complexes obtained via multiphoton (MP) excitation was only recently achieved,[154] along with the determination of their two photon excitation (2PE) cross section.[180] One of the great advantages of arylalkynylpyridyl based complexes is that they may be efficiently sensitised via biologically favourable multiphoton – 2PE at λ_{exc} = 680 - 720 nm. The 2PE cross section of **[Eu.L^{1}]** measured according to established procedures[180,181] is σ^2 = 65 ± 3 GM (1 GM = 10^{-50} cm^4 s photon^{-1}) for both the Λ- and Δ-enantiomers, with complete CPL spectrum recovery recorded upon MP excitation at 680 nm, (*vide supra* - Section 2.1.10).

Preliminary solution-state multiphoton studies were performed both in EtOAc and NMP, (Figures 5.11-12, respectively). Total emission and CPL spectra are shown to be equivalent for one-photon and two-photon excitation of the complex **[Eu.L^1]**.

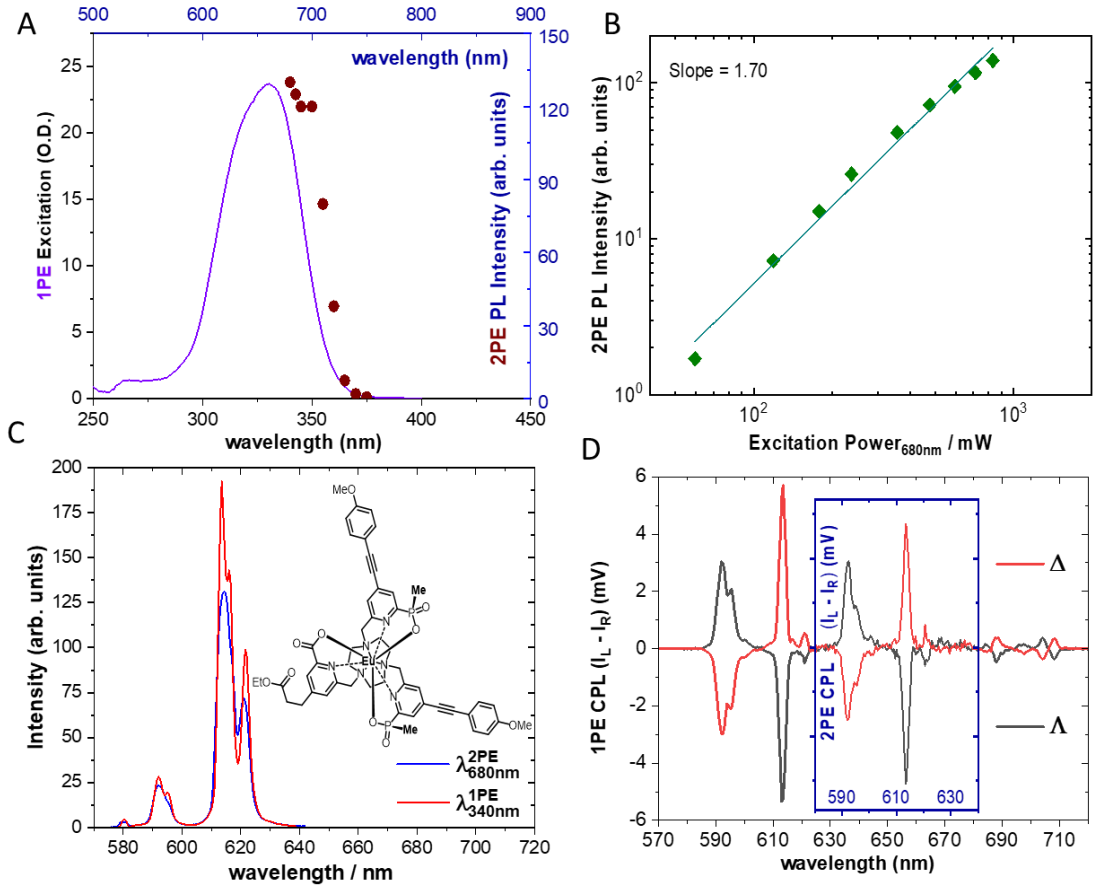

Figure 5.10. Key photophysical parameters and spectra of Λ- and Δ-**[Eu.L^1]** in EtOAc. (A) One photon excitation (solid purple line) and two photon excitation (maroon dots) spectra (λ_{em} = 614 nm) of **[Eu.L^1]**. (B) Excitation power dependency (green diamonds) of the 2PE induced photo luminescence (PL) intensity, slope 1.70 ± 0.1, σ^2 = 65 ± 3 GM (10 - 50 cm^{4}s/photon). (C) One (λ_{ex} = 340 nm, solid red line) and two photon (λ_{ex} = 680 nm, solid blue line) induced emission spectrum of the depicted (insert) Λ- and Δ-**[Eu.L^1]**. (D) One photon and (insert) two photon CPL spectra of Λ- and Δ-**[Eu.L^1]** (solid black and red line respectively). Spectra recorded in EtOAc (C = 5 × 10^{-5} M).

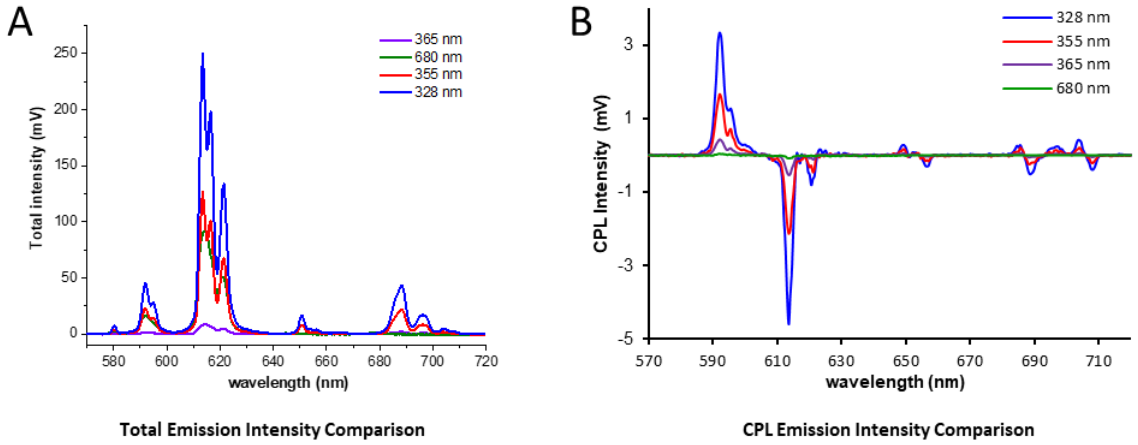

Figure 5.11. Comparison between total emission (*A*) and CPL spectra (*B*) of the *Λ* enantiomer of **[Eu.L^{1}]** in NMP at various excitation wavelengths (C = 5 × 10^{-5} M).

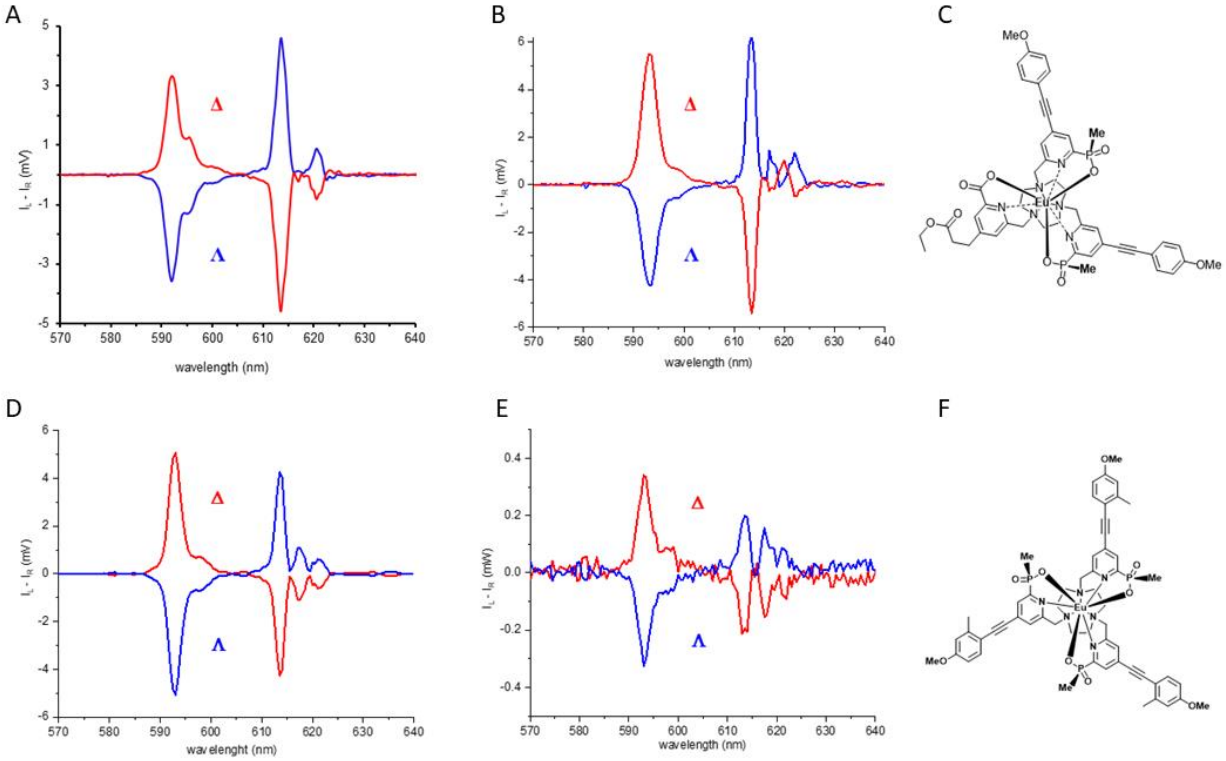

Figure 5.12. CPL spectra in EtOAc (*A*) and in PMMA (*B*) of Λ- and Δ-**[Eu.L^{1}]** (*C*) (C = 5 × 10^{-5} M), and in NMP (*D*) and in PVP (*E*) of **[Eu.L^{10}]** (*F*).[154] Note that the main spectral features of the solution-state CPL spectrum are preserved in polymeric films.

5.3. Circularly Polarised Luminescence Photography (CPLP)

5.3.1. Compact enantioselective CPL photography camera

As shown in the previous paragraph, the difficulty of finely resolving opposing-sign CPL transitions usually present in Eu(III) spectra was successfully shifted from the instrument to the synthetic design of a suitable Eu(III) complex displaying mono-signate CPL emission within a single emission manifold. This advancement allows for the use of cheaper instrumentation with a larger bandwidth and lower resolution, collecting all the radiation from a single monosignate manifold using a 10 nm wide bandpass filters without any CPL sign cancellation, (Table 5.1).

Table 5.1. Appropriate bandpass filters to select Eu(III) and Tb(III) CPL emission manifold that display strong CPB.

CPL Manifold	Bandpass filter
Eu(III) $\Delta J = 1$	BP594/10
Eu(III) $\Delta J = 2$	BP610/10
Tb(III) $\Delta J = 5$	BP546/10

The next challenge consists of exploiting the freedom to adapt optical components that are usually considered too coarse to detect lanthanide CPL to develop a solid state, small footprint single snapshot CPL photography camera. Portability is key to allow for the widespread use of CPL as an extra layer of security in the field of security inks. Systems that exploit a single detector equipped with a linear polariser (LP) and quarter waveplate (QWP), such as the setup used by Kitagawa *et al*., (Figure 5.7), or two independent detectors, such as the SS-CPL setup presented in Section 1.2.3, are prone to systematic error due to issues with calibration and alignment. Benchtop home built optical setups are sensitive to misalignment due to vibrations, touch, and just regular, correct use. This is particularly problematic if calibration files also depend on the configuration of the setup at any given time, especially the angle of the linear polariser. The ideal camera detector for such a setup should come as a single unit and, therefore, not suffer from the issue of misalignment over time. This is especially important as the CPLP setup is intended to be used for handheld detection, a situation more prone to impacts and vibration than a benchtop laboratory instrument. A robust,

all solid state, free of moving parts design is essential for the widespread commercial use of the CPLP setup.

Our proposed solution to the problem is to incorporate a scientific (CCD or CMOS array) camera where individual pixel alignment with respect to linear polarisation orientation is achieved resulting in a solid-state linear polarisation sensitive camera. Such a setup does not require beam splitting and measures CPL using a fixed QWP and a single detector, allowing for single-shot CPL image capture. The intrinsically simultaneous acquisition of the two channels required to compute the CPL image provides more reliable results compared to calculating enantioselective chiral contrast based on two images, one for each channel, taken at successive times. The latter relies on the hypothesis that the total and CPL emission are constant in time. This is not true in general, as is the case of OLEDs, which are prone to degradation via different mechanisms.[182] For instance, the difference between two successive shots to compute the enantioselective contrast image where the second one is dimmer due to degradation would provide a larger apparent dissymmetry in CPL emission.

The QWP needs to be carefully aligned at the time of construction of the instrument to match the intrinsic unique birefringence properties of the detector but have the advantage of being fixed at the time of measurement. This ensures reproducibility and portability from instrument to instrument.

The detector consists of a commercial linear polarisation sensitive camera (Kiralux® CS505MUP1, ThorLabs, Figure 5.13) which has never previously been used in the field of CPL imaging. Polarisation sensitive cameras were marketed in response to an increasing industrial interest in using linearly polarised light to probe stress in reflected or transmitted light in materials that exhibit stress-induced linear birefringence. The intended commercial applications of prime importance for polarisation sensitive cameras include stress detection for quality checks of car front shields and large double-glazed window panels for skyscrapers. Niche scientific applications of this camera are also on the rise. For example, this camera has been recently used in the field of life sciences for a high throughput analysis of differences in gene structures using polarisation coding, and validated on the spike protein gene sequences for three different model variants of the SARS-CoV-2 virus[183], and to characterise natural fibres

such as spider silk using chromaticity plots.[184] However, the present work constitutes the first adaptation of a polarisation-sensitive camera to CPL.

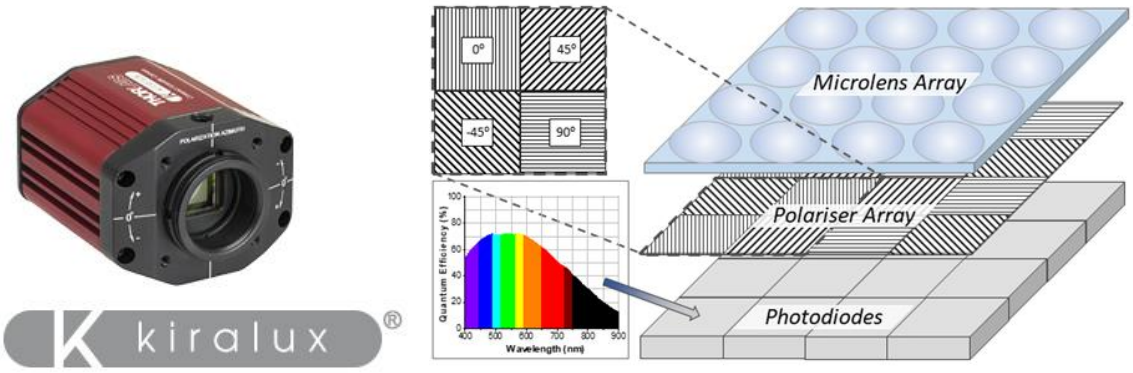

Figure 5.13. Picture of the Kiralux® CS505MUP1 polarisation sensitive camera from ThorLabs (*left*) and detailed schematics of its pixel layout and polarisation selector wire-grid alignment, displaying its wavelength-dependent quantum efficiency.

When light hits the Kiralux® CS505MUP1 camera, an array of microlenses focuses it on each pixel of the detector. Polarisation sensitivity is imparted by a linear polariser array embedded between the microlens array and the photodiodes. This way, the light reaching each pixel is filtered via a polariser at 0°, +45°, -45°, or 90°, (Figure 5.13). The design of the Kiralux® CS505MUP1 camera naturally lends itself to readaptation for CPL detection applications: the key idea is to convert left- and right-CPL emission coming from the sample into two orthogonal linear polarisations to be detected by the camera with a QWP, (Figure 5.14). This requires careful alignment of the QWP so that the directions of the linearly polarised light arising from it matches the direction of the polariser array in the camera to maximise the signal.

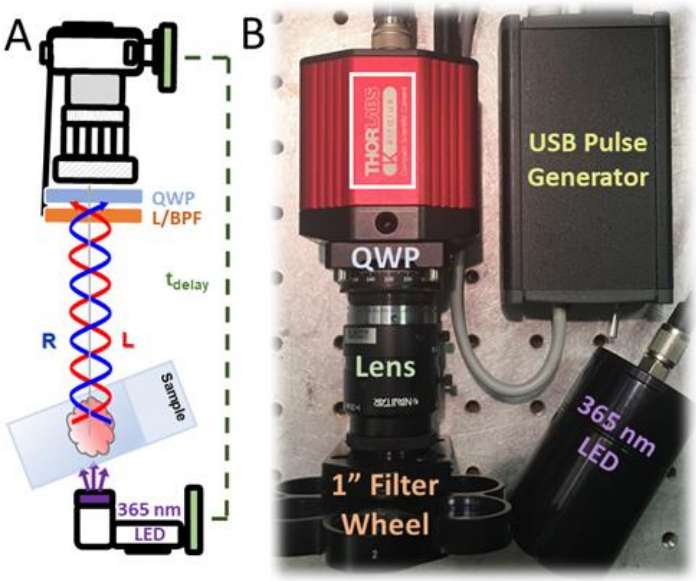

Figure 5.14. Schematic diagram of the CPLP camera layout (*A*) and the real apparatus (*B*) with its synchronised 365 nm LED (5.2 V, 500 mW) flash illuminator. The handheld USB powered apparatus comprises of a linear polarisation sensitive externally triggered camera (Kiralux®), a precisely aligned broad wavelength quarter waveplate (QWP, λ_{ex} = 400 –800 nm), a machine vision objective lens (f = 25 mm/F1.4) and a selectable filter wheel containing long-pass or narrow band-pass filters (L/BPF, d = 1") to achieve chromatic discrimination.

This setup not only allows instant pixel position decoded discrimination of L-CPL and R-CPL of photons emitted from a preselected spectral range, facilitated by precise fast axis orientation of the QWP to a pre-aligned polarisation angle (0°), but is also capable of simultaneous light detection regardless of circular polarisation state. In essence, all components required to calculate an EDCC image are encoded in one captured full field of view (FOV) frame. Total emission mapping of the frame is captured extracting pixel intensity values attributed to the sum of -45° and +45° wire grid alignment, with individual L-CPL and R-CPL captured using pixels with 0° and 90° polarisation orientation respectively. In practice, this is facilitated by recording an image with the camera in quad-view mode, where each of the four wire grid alignment attributed individual 8-bit images is presented as an array of 2 x 2 images in one frame. A post image acquisition protocol using a custom macro written in ImageJ (v.1.49r) crops the individual images and subsequently calculates the total emission and both (L-R and R-L) EDCC final images. The resultant three images are then saved as separate 8 bit greyscale images.

This setup can acquire CPL images in a single shot (as quickly as 27 µs per frame), allowing for time-gated acquisition. To do that, the CPLP camera system was synchronised to a pulsed 365 nm LED. This is facilitated by the camera's native PDX/bulb exposure trigger mode linked to the camera's global shutter operation circuit. The time gating sequence has been established and miniaturised in a USB (5.2 V) or battery powered custom built signal generator.[171,185] Due to the documented rise and fall time of the LED, 11 and 6 µs respectively, the time delay (t_d) has been set to 20 µs (incorporating the camera's inherent 13.72 µs post-exposure (t_{acq}) integration period) to allow gating of any short-lived organic fluorescence out from long-lived Ln(III) emission in the spectral window of interest. To provide maximum customisation and to harness the variable triggered total accumulated acquisition time of 27 µs to 14 s, the signal generator has been designed with variable illumination (up to 1 s) sequences operating at 0.1, 1, and 10 Hz overall frequency.

Besides the astounding technical benefits, the components required to build the CPL photography setup are cheaper than a home-built PEM-CPL by a factor of 7 and even than a new-generation SS-CPL by a factor of 2, (Table 5.2). The most significant price reduction when moving from a traditional PEM- to a SS-CPL spectrometer is due to the elimination of the PEM and the laser driven light source (LDLS). The major contributors to the price of the SS-CPL are the two CCDs (£ 2,000), which are not required for the CPLP setup. This allows a further, significant cost reduction when moving to the Kiralux® camera as it eliminates the need for two channels with two distinct detectors.

Table 5.2. Comparison of the total cost at time of writing of the component required to build a standard PEM-CPL spectrometer, a new-generation SS-CPL, and the CPL-P Camera setup described.

PEM-CPL		**SS-CPL**		**CPL-P Camera**	
Item	**Cost (£)**	**Item**	**Cost (£)**	**Item**	**Cost (£)**
LDLS	14,500	LED + Pow	50 + 300	LED	100
PEM	23,800	QWP	700	Kiralux®	2,200
APD	3,500	LP + Mount	1,300 × 2	Signal gen.	2,000
PD	900	CCDs	6,000 × 2	QWP	700

LIA	2,700	LPF	200 × 2	LPF/BPF	200 × 6
Monoch's	6,900 × 2	Diffuser	25	Mounts	500
	£ 59,200		**£ 16,075**		**£ 6,700**

LDLS = laser driven light source, PEM = photo-elastic modulator, APD = avalanche photo diode, PD = photo diode, LIA = lock-in amplifier, CCD = coupled charge detector, QWP = quarter wave plate, LP = linear polariser, LPF = long pass filter, BPF = band pass filter.

5.3.2. Enantioselective CPL photography

The solid-state CPLP camera system has been extensively tested using our library of legacy samples (called **[Eu.L$^{2\text{-}5}$]** in the present chapter, Figure 5.15.B) previously used for validating both the CPL-LSCM (Laser Scanning Confocal Microscope) and CPL-epifluorescence microscope,[154,169] as well as a newly constructed complex proof-of-concept (POC) CSI test targets using the newly synthesised (**[Eu.L^{1}]**, Figure 5.15.A) and commercial organic fluorophores anthracene, fluorescein, and rhodamine B. This section focuses on presenting the validation experiments in order of increasing complexity to describe the potential and limitations of the new CPLP camera.

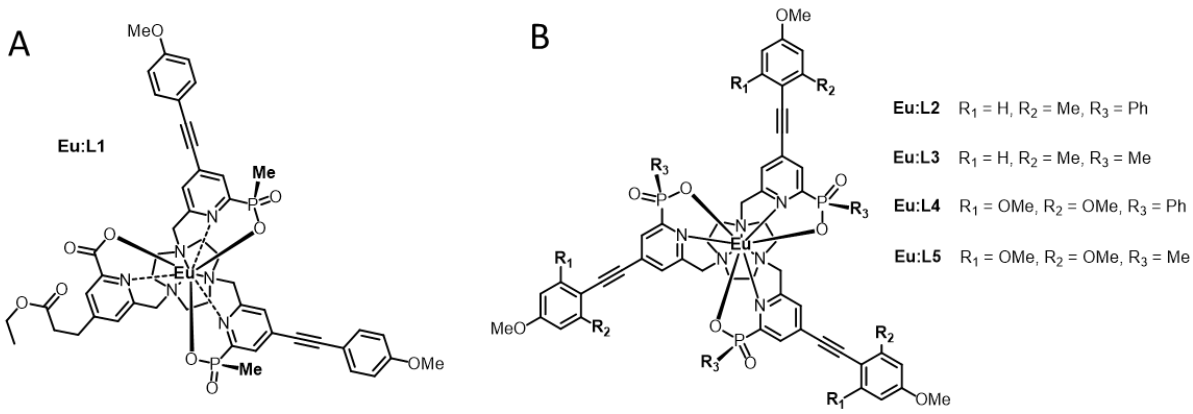

Figure 5.15. Chiral lanthanide complexes discussed as candidates for CPL-active security inks. (A) **[Eu.L^{1}]**, a newly synthesised complex that exhibits desirable strong single sign (exclusively left or right helicity) ΔJ = 1 and ΔJ = 2 transitions. (B) **[Eu.L$^{2\text{-}5}$]**, legacy complexes demonstrating suitable CPL spectra to be used for time-resolved CPLP (TR-CPLP).

Previous studies involved embedding bright, high CPB enantiopure europium complexes within a uniform polymer matrix (PVP-40).[154] Herein, the possibility of embedding **[Eu.L^{1}]** in the more widely used poly(methyl methacrylate) (PMMA, M_W = 15,000 g mol^{-1}) is shown. Two different techniques were tested: spin coating and drop

casting onto a glass surface. The solutions were prepared by blending PMMA with enantiopure solutions of *Δ*- and *Λ*-**[Eu.L^1]** (5 × 10^{-5} M, MeOH) as previously reported.[154] Complete CPL spectrum recovery has been achieved for luminescent PMMA films prepared with both enantiomers, (Figures 5.16-19; see Figures 3.10 and 3.11 for a comparison of the CPL spectra in solution *vs* film).

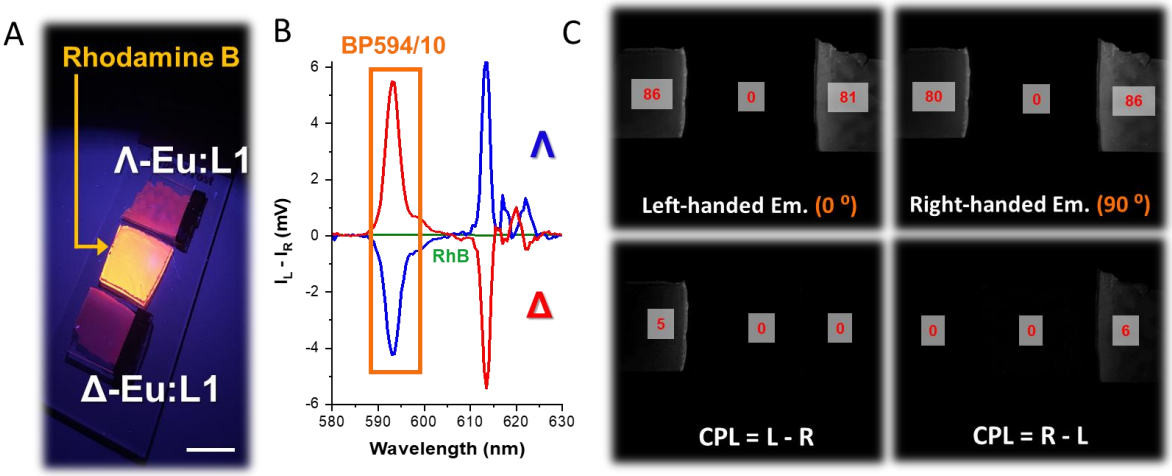

Figure 5.16. Solid state time-resolved EDCC photography of an organic emitter and a CPL active Eu(III) complex. (*A*) Conventional photo of Rhodamine B and Λ- and Δ-**[Eu.L^1]** in embedded into a PMMA matrix (C = 3 × 10^{-6} M) using 365 nm UV illumination. Scale bar = 1 cm. (*B*) CPL emission spectra of (green, RhB) rhodamine B, Δ- (red) and Λ- (blue) enantiomers of **[Eu.L^1]** in PMMA (λ_{exc} = 365 nm) highlighting the spectral window selected for photography using an BP594/10 (OD4.0) filter. (*C*) Time-resolved (t_d = 20 µs) images extracted from the quad polarisation view camera highlighting the recorded total emission, right- and left-handed emission with respect to the built-in polariser orientation to the fixed QWP fast axis. Numbers in red are avg. 8-bit pixel intensity values for each image region, $t_{acq.}$ = 400 ms, 10 avg. image, 100 total image accumulation.

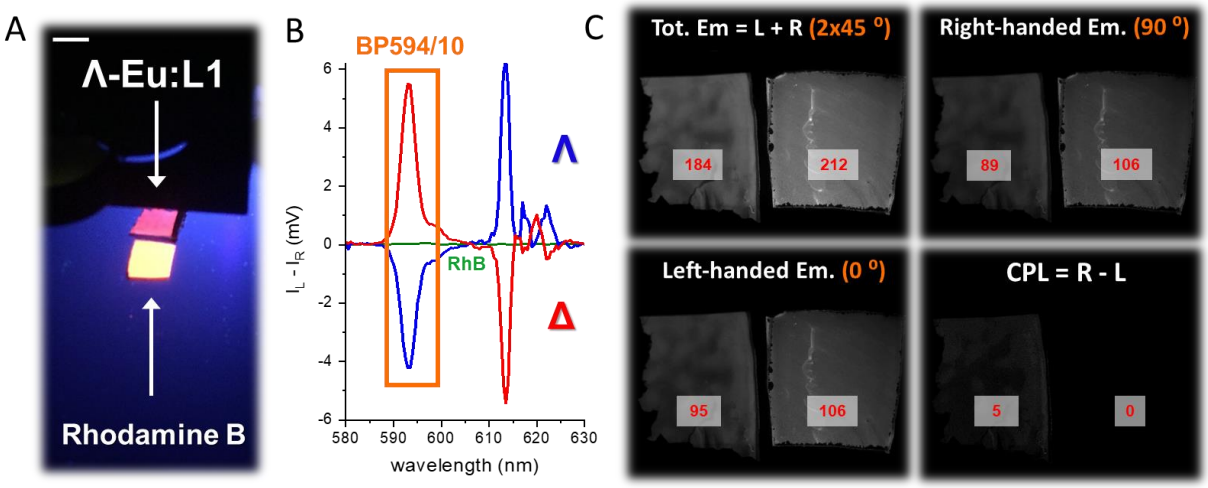

Figure 5.17. Solid state enantioselective differential chiral contrast (EDCC) photography of an organic emitter and a CPL active Eu(III) complex. (A) Conventional photo of Rhodamine B and Λ-**[Eu.L^1]** in embedded into a PMMA matrix (C = 3 × 10^{-6} M respectively) using 365 nm UV illumination. Scale bar = 1cm. (B) CPL emission spectra of (green, Rh B) rhodamine B, Δ- (red) and Λ- (blue) enantiomers of **[Eu.L^1]** in PMMA film (λ_{exc} = 365 nm) highlighting the spectral window selected for photography using an BP594/10 (OD4.0) filter. (C) Images extracted from the quad polarisation view camera highlighting the recorded total emission, right- and left-handed emission with respect to the built-in polariser orientation to the fixed QWP fast axis. The calculated EDCC image (R-L) shows clear CPL based emission only for Λ-**[Eu.L^1]**. Numbers in red are avg. 8-bit pixel intensity values for each image region, t_{acq} = 300 ms, 10 avg. image, 100 total image accumulation.

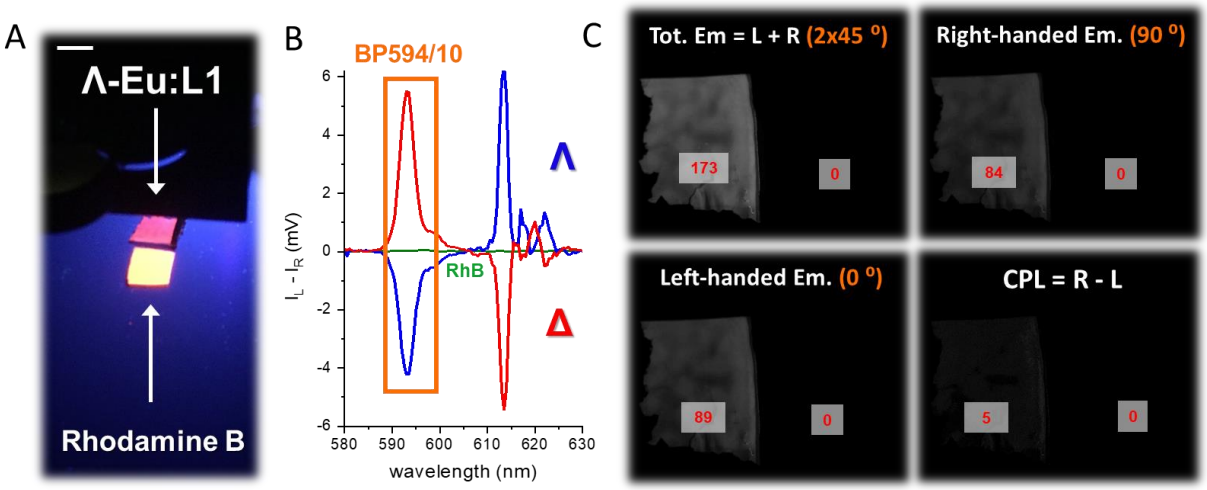

Figure 5.18. Solid state time resolved EDCC photography of an organic emitter and a CPL active Eu(III) complex. (A) Conventional photo of Rhodamine B and Λ-**[Eu.L^1]** in embedded into a PMMA matrix (C = 3 × 10^{-6} M respectively) using 365 nm UV illumination. Scale bar = 1cm. (B) CPL emission spectra of (green, RhB) rhodamine B, Δ- (red) and Λ- (blue) enantiomers of **[Eu.L^1]** PMMA film (λ_{exc} = 365 nm) highlighting the spectral window selected for photography using an BP594/10 (OD4.0) filter. (C) Time resolved (t_d = 20 µs) Images extracted from the quad polarisation view camera highlighting the recorded total emission, right- and left-handed emission with respect to the built-in polariser orientation to the fixed QWP fast axis. Under time-resolved conditions no emission from the organic fluorophore is detected, whilst the calculated EDCC image (R-L) shows clear CPL based emission only for Λ-**[Eu.L^1]**. Numbers in red are avg. 8-bit pixel intensity values for each image region, t_{acq} = 400 ms, 10 avg. image, 100 total image accumulation.

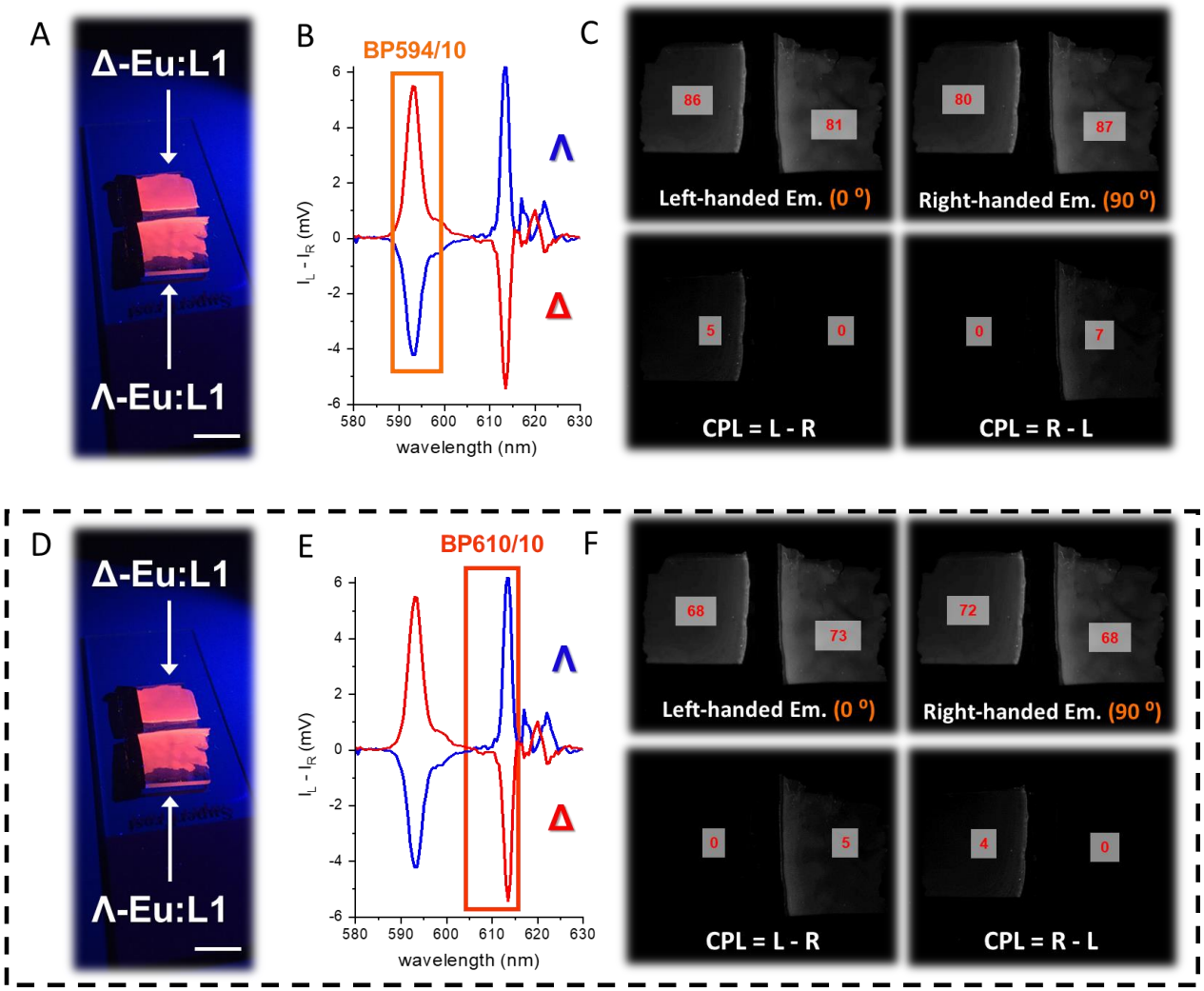

Figure 5.19. Solid state time resolved EDCC photography of an organic emitter and a CPL active Eu(III) complex. (A) Conventional photo of Rhodamine B and Λ-**[Eu.L^1]** in embedded into a PMMA matrix (C = 3 × 10^{-6} M respectively) using 365 nm UV illumination. Scale bar = 1 cm. (B) CPL emission spectra of Δ- (red) and Λ- (blue) enantiomers of **[Eu.L^1]** in PMMA film (λ_{exc} = 365 nm) highlighting the spectral window selected for photography using an BP594/10 (OD4.0) filter. (C) Time resolved (t_d = 20 μs) Images extracted from the quad polarisation view camera highlighting the recorded total emission, right- and left-handed emission with respect to the built-in polariser orientation to the fixed QWP fast axis. Under time-resolved conditions no emission from the organic fluorophore is detected, whilst the calculated EDCC image (L-R) shows clear CPL based emission only for Δ-**[Eu.L^1]** whilst R-L shows clear CPL based emission only for Λ-**[Eu.L^1]**. Numbers in red are avg. 8-bit pixel intensity values for each image region, t_{acq} = 400 ms, 10 avg. image. Opposite sign observations were made using BP610/10 (OD4.0), t_{acq} = 500 ms, 10 avg. image, 100 total image accumulation (Figure D, E and F in dashed black box).

First experiment: solution of Rhodamine B *vs* Λ-[Eu.L^1]

The very first attempt at CPLP was performed using the *Λ* enantiomer of the custom synthesised monosignate **[Eu.L^1]** complex in ethyl acetate solution. **[Eu.L^1]** in ethyl acetate displays bright, monosignate CPL emission from the Δ*J* = 1 and 2 manifolds as opposed to more polar solvents, (see Chapter Three). Solution conditions were preferred over films for the first experiment with CPLP as solution CPL is better characterised and reproducible. An ethyl acetate solution of achiral rhodamine B, a species that is bright in the 594/10 nm range, was used as a reference to be compared to *Λ*-**[Eu.L^1]**. The calculated EDCC image (R-L) shows clear CPL based emission only for Λ-**[Eu.L^1]**.

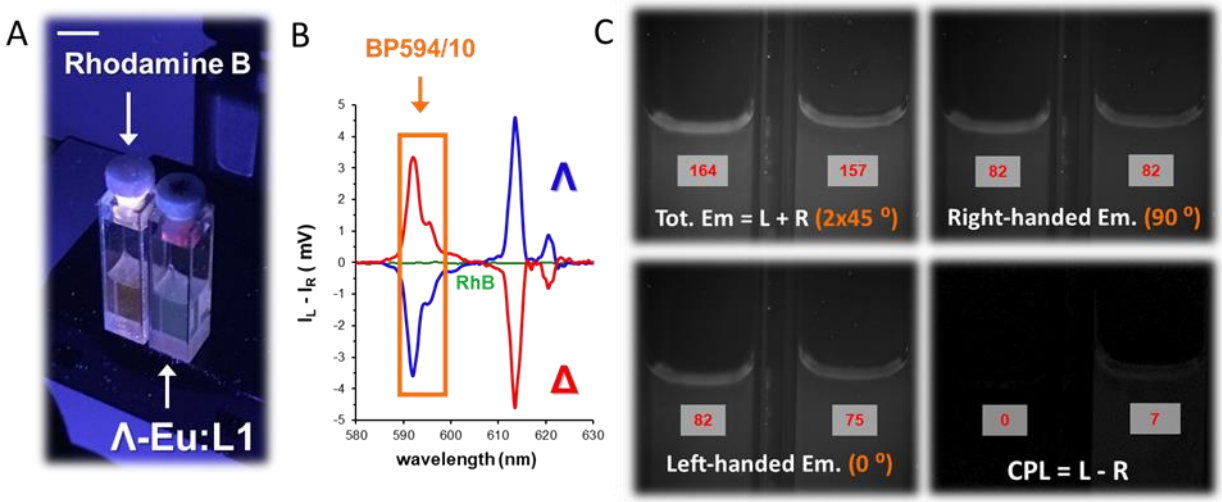

Figure 5.20. Solution state EDCC photography of an organic emitter and a CPL active Eu(III) complex. (A) Conventional photo of Rhodamine B and Λ-**[Eu.L^1]** in EtOAc using 365 nm UV illumination (C = 3 × 10^{-6} M respectively). Scale bar = 1 cm. (B) CPL emission spectra of (*green*) rhodamine B, Δ- (*red*) and Λ- (*blue*) enantiomers of **[Eu.L^1]** in EtOAc (λ_{exc} = 365 nm) highlighting the spectral window selected for photography using an BP594/10 (OD4.0) filter. (C) Images extracted from the quad polarisation view camera highlighting the recorded total emission, right- and left-handed emission with respect to the built-in polariser orientation to the fixed QWP fast axis. The calculated EDCC image (R-L) shows clear CPL based emission only for Λ-**[Eu.L^1]**. Numbers in red are avg. 8-bit pixel intensity values for each image region, $t_{acq.}$ = 250 ms, 10 avg. image, 100 total image accumulation.

Second experiment: [Eu.L^3] blotted paper and PVP film

Recording EDCC on an embedded system, not in the solution state, was first attempted on available, previously studied samples consisting of paper blotted with the two enantiomers of **[Eu.L^3]** as well as **[Eu.L^3]** doped spin coated PVP-40 films, (Figure 5.21), prepared and tested for homogeneity using a laser scanning confocal microscope as described in reference.[154] The sequence of steps used to process the raw data from the polarisation sensitive camera to extract L- and R-CPL images is shown in Figure 5.21.

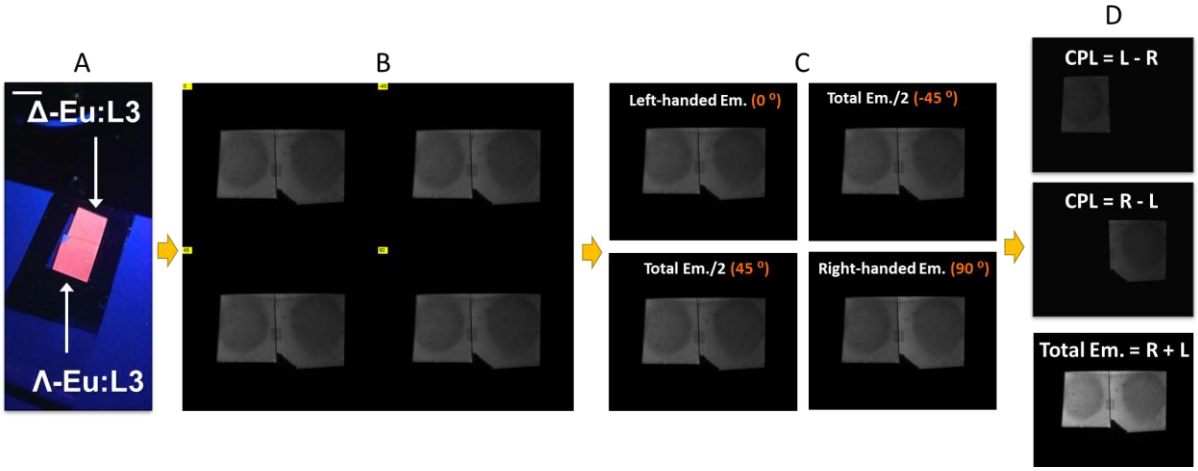

Figure 5.21. Example of data processing to extract EDCC images from raw images. (*A*) Conventional photography image. Scale bar = 1 cm, 365 nm LED illumination. (*B*) Quad-view one shot image of the FOV using ThorCam™ software, 16-bit. (*C*) Individual 8-bit image generation with respect to built-in wire grid polariser array to extract L-CPL, R-CPL and two half intensity total emission image using a custom written macro in ImageJ (v1.49j). (*D*) EDCC and calculated final image contrast bearing images using ImageJ's built-in calculator plus feature.

Previous findings using the same sample of paper blotted enantiopure Λ and Δ **[Eu.L^4]** used to demonstrate EDCC for the first time in 2016 were successfully replicated, (Figure 5.22).[175] Using the calculated EDCC images: L-R shows clear CPL based emission only for Δ-**[Eu.L^4]** whilst R-L shows clear CPL based emission only for Λ-**[Eu.L^4]** demonstrating the ability of this CPLP system to be used as a facile rapid methodology for enantioselective CPL readout.

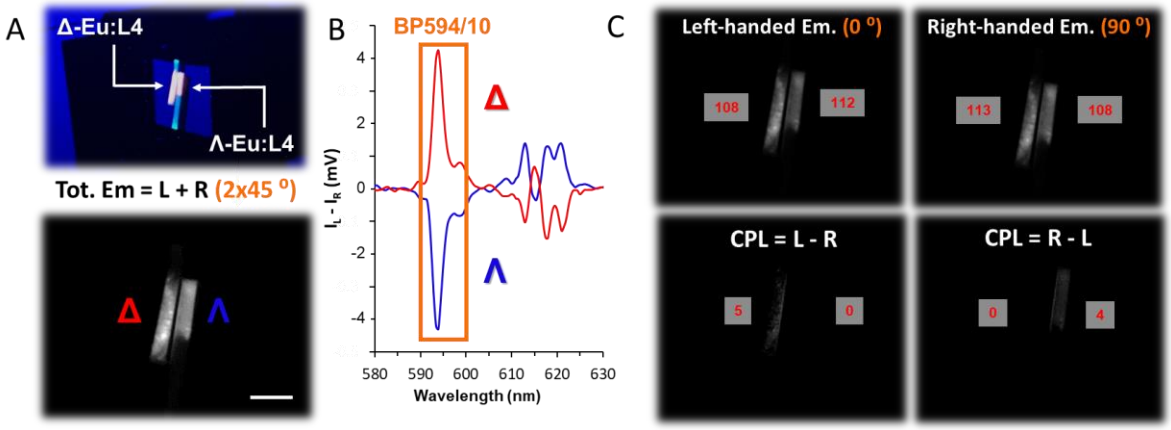

Figure 5.22. Solid state time-resolved EDCC photography of a CPL active Eu(III) complex on paper substrate. (A) (top) Conventional photo and (bottom) time-resolved CPLP of Λ and Δ-**[Eu.L^4]** in embedded into optical brightener free paper (c = 5 × 10^{-6} M) using 365 nm UV illumination from the smooth side of the paper. Scale bar = 0.5 cm. (B) CPL emission spectra of Δ- (*red*) and Λ- (*blue*) enantiomers of **[Eu.L^4]** in MeOH (λ_{exc} 365 nm) highlighting the spectral window selected for photography using an BP594/10 (OD4.0) filter. (C) Time-resolved (t_d = 20 µs) Images extracted from the quad polarisation view camera highlighting the recorded right- and left-handed emission with respect to the built-in polariser orientation to the fixed QWP fast axis. Numbers in red are avg. 8-bit pixel intensity values for each image region, t_{acq} = 300 ms, 10 avg. image, 100 total image accumulation.

It is worth noting that, similarly to the measurements performed using the CPL-LSCM, films deposited on glass showed partial randomisation of CPL due to reflection from jagged or smooth reflective surfaces. This is because, unlike linearly polarised light, which reflects by preserving its polarisation, the handedness of CPL is reversed upon reflection.

Third experiment: polymeric film [Eu.L^1] vs Rhodamine B

CPLP images of Λ- and Δ-**[Eu.L^1]** embedded into a PMMA matrix with an analogous film prepared using the short lived, organic, CPL inactive fluorophore rhodamine B were recorded. CPL emissive polymeric blends constitute an additional step forward to prototyping Chameleon Security Inks (CSIs) containing enantiopure CPL emitters. Multiple conditions were trialled, including the selection of either of the monosignate Δ*J* = 1 or 2 emission manifolds with a suitable 10 nm bandpass filter and ungated or time-gated acquisition mode, (Figure 5.23). Remarkable enantioselective contrast was achieved in all cases for the two enantiomers of **[Eu.L^1]**, whereas the emission of

rhodamine B vanishes in the two CPL channels. The calculated L-R EDCC images show clear CPL emission arising from the Δ enantiomer of **[Eu.L^1]** only, whilst R-L shows CPL emission only from the Λ enantiomer of **[Eu.L^1]**, demonstrating the capability of CPLP. Under time-resolved conditions no organic emission is detected even in the total emission channel. CPL active lanthanide emitters can be distinguished from achiral organic fluorophores by solely using the ungated EDCC mode described above, without time-gating. However, time-gated EDCC mode allows full discrimination among the four categories of emitters arising from the combinations of long- and short-lived chiral and achiral emitters, further increasing the level of embedded security.

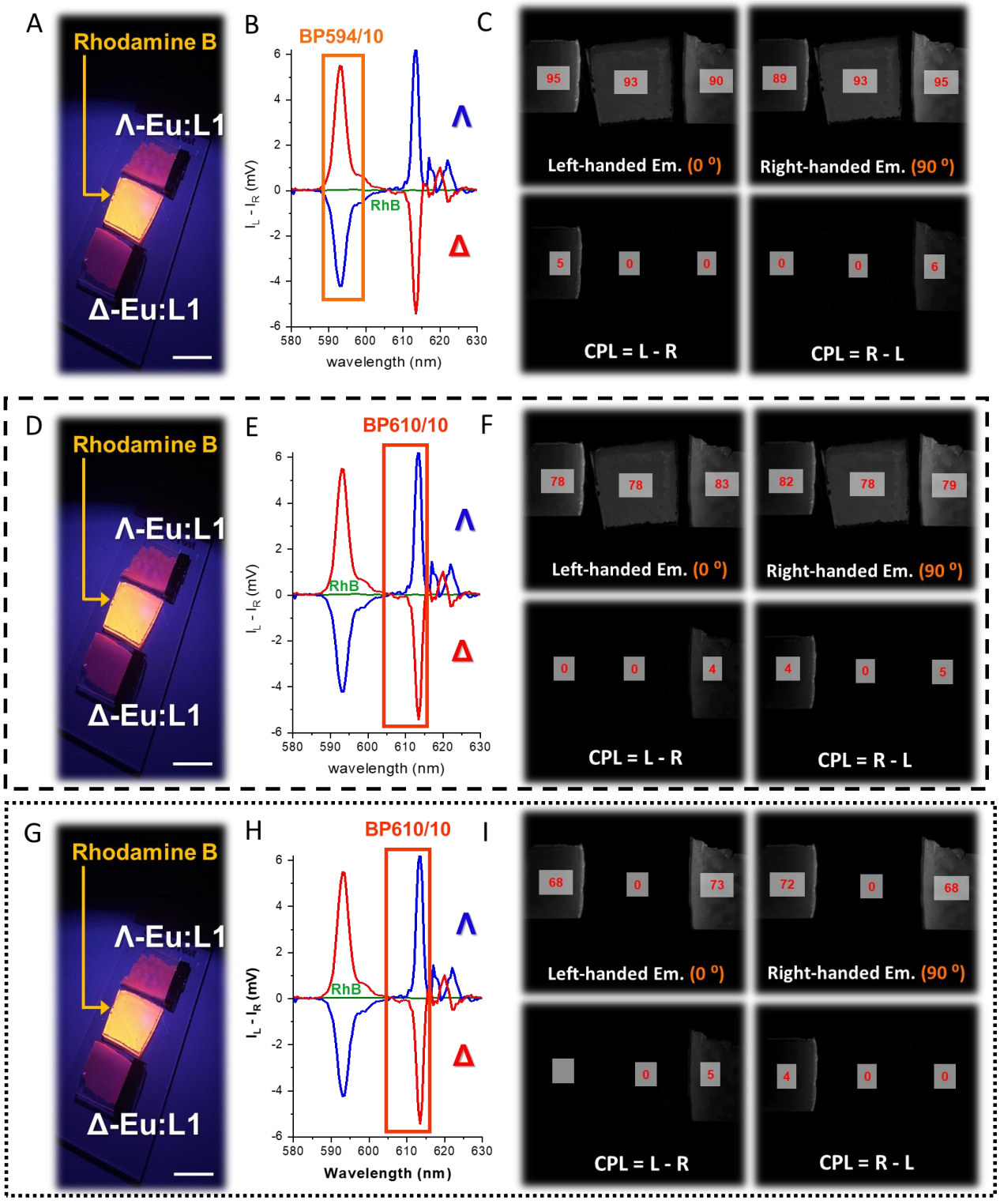

Figure 5.23. Solid state EDCC photography of an organic emitter and a CPL active Eu(III) complex. (A) Conventional photo of Rhodamine B and Λ- and Δ-**[Eu.L^1]** embedded into a PMMA matrix (C = 3 × 10^{-6} M) using 365 nm UV illumination. Scale bar = 1 cm. (B) CPL emission spectra of (green, Rh B) rhodamine B, Δ- (red) and Λ- (blue) enantiomers of **[Eu.L^1]** in PMMA (λ_{exc} = 365 nm) highlighting the spectral window selected for photography using an BP594/10 (OD4.0) filter. (C) Images extracted from the quad polarisation view camera

highlighting the recorded total emission, right- and left-handed emission with respect to the built-in polariser orientation to the fixed QWP fast axis. Using calculated EDCC images: L-R shows clear CPL based emission only for Δ-**[Eu.L^1]** whilst R-L shows clear CPL based emission only for Λ-**[Eu.L^3]**. Numbers in red are avg. 8-bit pixel intensity values for each image region, t_{acq} = 400 ms, 10 avg. image, 100 total image accumulation. Opposite sign observations were made using BP610/10 (OD4.0) in both steady state (Figure D, E and F in dashed black box) and time-resolved mode (Figure G, H and I in dotted black box), t_{acq} = 700 ms respectively, 10 avg. image, 100 total image accumulation.

Fourth experiment: solution of [Tb.L^6] vs fluorescein

The next step consisted of testing the CPLP camera setup in a different visible wavelength range. To access the green region of the spectrum a solution of the Δ enantiomer of a previously synthesised chiral Tb(III) complex, **[Tb.L^6]**, was prepared in water, (Figure 5.24).[141] A solution of fluorescein was used as an achiral organic emitter in a similar wavelength range.

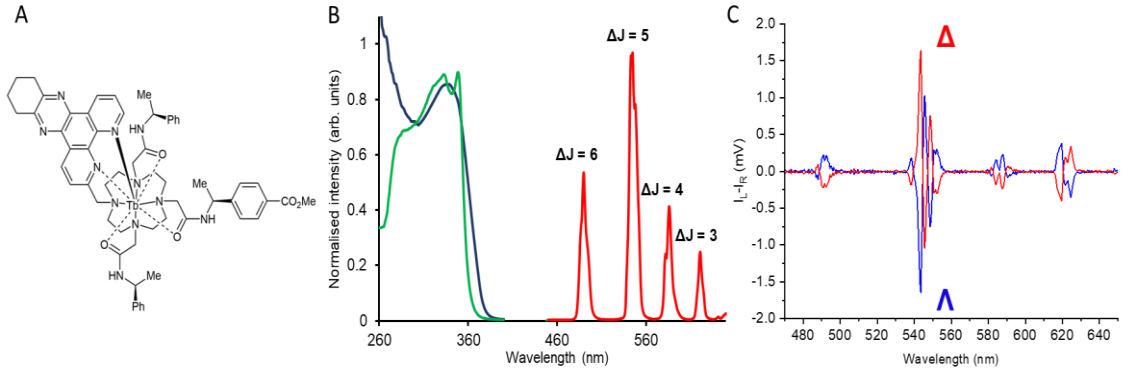

Figure 5.24. Photophysical characteristics of **[Tb.L^6]**.[141] (*A*) Chemical structure (*B*) Absorption (*green*), excitation (*blue*, λ_{em} = 544 nm) and total emission spectra (*red*, λ_{exc} = 344 nm) of **[Tb.L^6]** complexes (c = 5.4 x 10^{-5} M) in water. (*C*) CPL emission spectra of Δ- (red) and Λ- (blue) enantiomers of **[Tb.L^6]**. Both spectra were recorded in water, 295 K, 5 μM complex, λ_{exc} = 344 nm, 5 scans averaged with 0.5 nm resolution and 1 ms integration time.

The high CPB magnetic dipole-allowed Δ*J* = 5 emission manifold was selected using a 10 nm bandpass filter centred at 546 nm. CPL spectra of Tb(III) are often complex and characterised by several opposing-sign transition within a single manifold. As extensively discussed earlier, these conditions are not ideal to detect CPL with fast, large bandwidth instrument such as the CPLP camera due to CPL sign cancellation

occurring. However, the integral on the CPL spectrum of the $\Delta J = 5$ manifold within the BP546/10 region is a positive non-zero number, *i.e.* the sign cancellation is present but not complete. The CPLP camera setup proved to be sensitive enough to provide good contrast EDCC images despite the apparent g_{lum} being smaller due to CPL sign cancellation, (Figure 5.25).

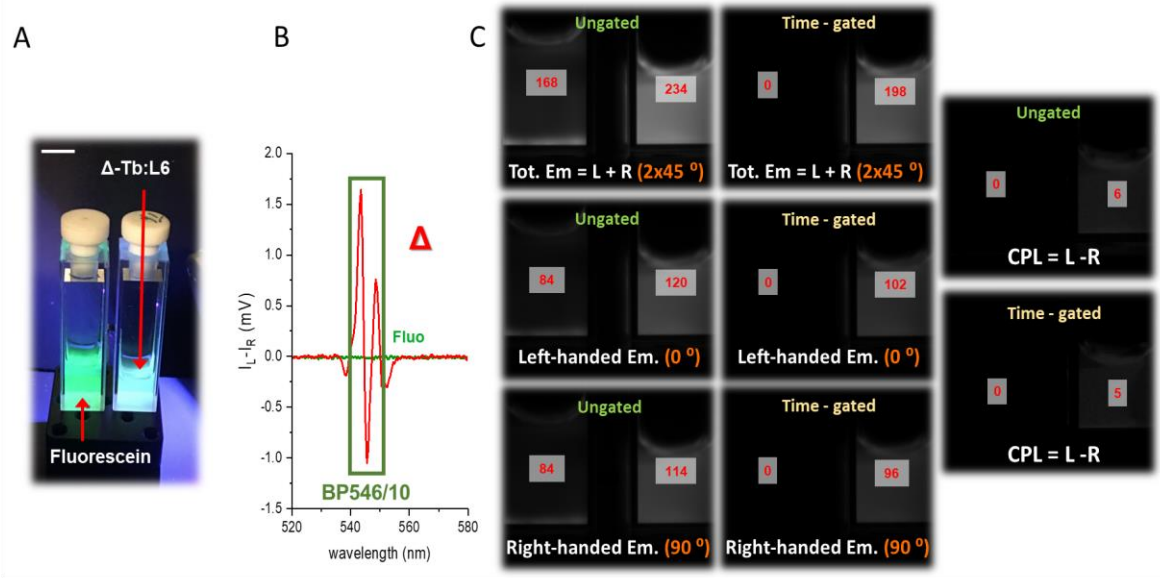

Figure 5.25. Solution state enantioselective differential chiral contrast (EDCC) photography of an organic emitter and a CPL active Tb(III) complex. (A) Conventional photo of fluorescein and Δ-**[Tb.L^6]** in water using 365 nm UV illumination (C = 3 × 10^{-6} M respectively). Scale bar = 1cm. (B) CPL emission spectra of (light green, Fluo) fluorescein, (green) Δ-enantiomers of **[Tb.L^6]** in water (λ_{exc} = 365 nm) highlighting the spectral window selected for photography using an BP546/10 (OD4.0) filter. (C) Images extracted from the quad polarisation view camera highlighting the recorded total emission, right and left-handed emission with respect to the built-in polariser orientation to the fixed QWP fast axis. Time-resolved (t_d = 20 µs) images show no detectable fluorescein emission throughout. The calculated EDCC images (L – R) shows clear CPL based emission only for Δ-**[Tb.L^6]** in both ungated and time-gated images. Numbers in red are avg. 8-bit pixel intensity values for each image region, $t_{acq.}$ = 2 s, 10 avg. image, 200 total image accumulation

Fifth experiment: proof-of-concept of CSIs

A proof-of-concept (POC) invisible hidden in plain sight CSI security tag was constructed to comprehensively demonstrate the validity of the claim that the all-solid state one-shot CPLP camera system developed herein is capable of five layers of security readout comprising of multi-coloured, multi-spectral, opposing-helicity, combined with high spatial and temporal resolution. This CSI tag (Figure 5.26) was

constructed using three different coloured - anthracene (blue), fluorescein (green), and rhodamine B (red) - commercially available short-lived organic fluorophores and enantiopure and racemic (50:50) mixtures of Λ- and Δ-**[Eu.L^1]**. The individual components (C = 2.8 × 10^{-6} M) of this CSI dye mixture were embedded onto an optical brightener free paper substrate under a standard UV document reader (365 nm lamp), with each layer homogeneously overdrawn multiple times to ensure that all tag features appear to be of comparable brightness to the naked eye. To add an extra layer of complexity, the paper had been pre-printed with black text prior to security tag construction using a commercial laser printer and the final POC CSI tag was laminated using a standard PET/EVA (polyethylene terephthalate/ethylene-vinyl acetate) laminating sheet and a laminator at 150 ºC (1 cm/s), and left in the dark for three days prior to CPLP imaging.

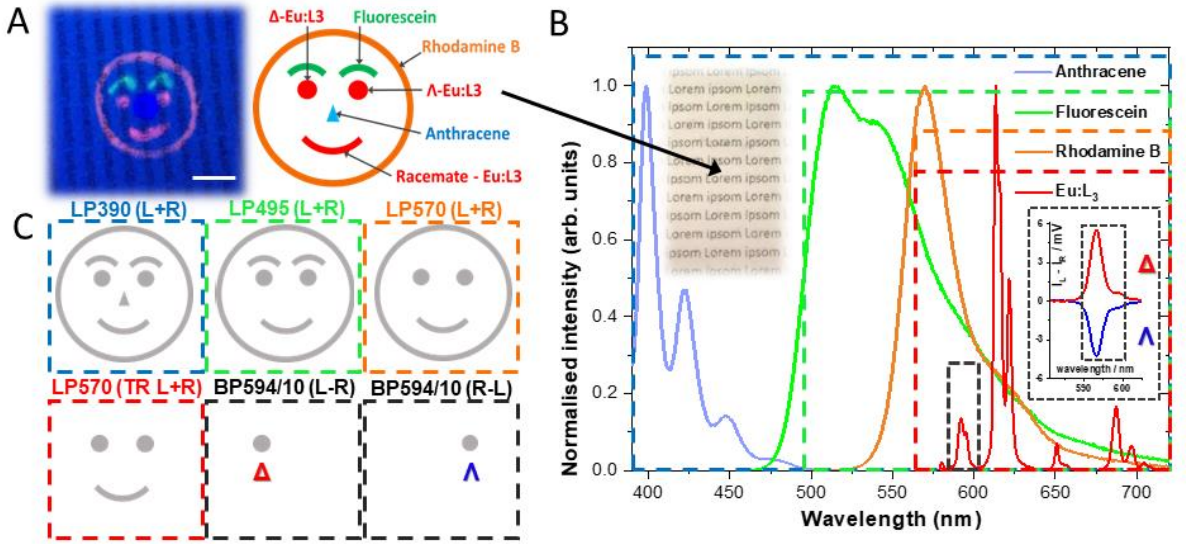

Figure 5.26. Design and composition of the proof-of-concept CSI security tag. (A) Schematics of the fluorophore composition and UV (365 nm, standard document reader) illuminated actual image of the concept invisible rudimentary Chameleon (CSI) security tag, scale bar 1 cm. (B) Individual emission spectra of the CSI's luminophores, highlighting the colour coded emission filters used for revealing five tiers of embedded security features. (C) Detection methodology and proposed CPLP imaging sequence of the POC CSI security tag. One image encodes six different images that can be individually revealed. Chromatic separation can be facilitated using a combination of appropriate bandpass filters and time-resolved (TR) detection as depicted using CPLP, whilst opposing helicity information can be read out using individual CPL channel detection.

A sequence of five one-shot CPLP images was recorded to highlight the POC CSI tag's invisible five tiers of security features. Three ungated images were recorded

(Figure 5.27.A-C) using chromatic RGB (red-green-blue) separation, facilitated by appropriate long pass filters - LP390 nm for RGB, LP495 nm for RG and LP570 nm for R. A time-resolved image collection mode was employed using the same red LP570 filter to gate out the short-lived red (rhodamine B) feature of the tag, revealing embedded additional 'secondary red' features due to long-lived **[Eu.L^3]** emission, (Figure 5.27.D).

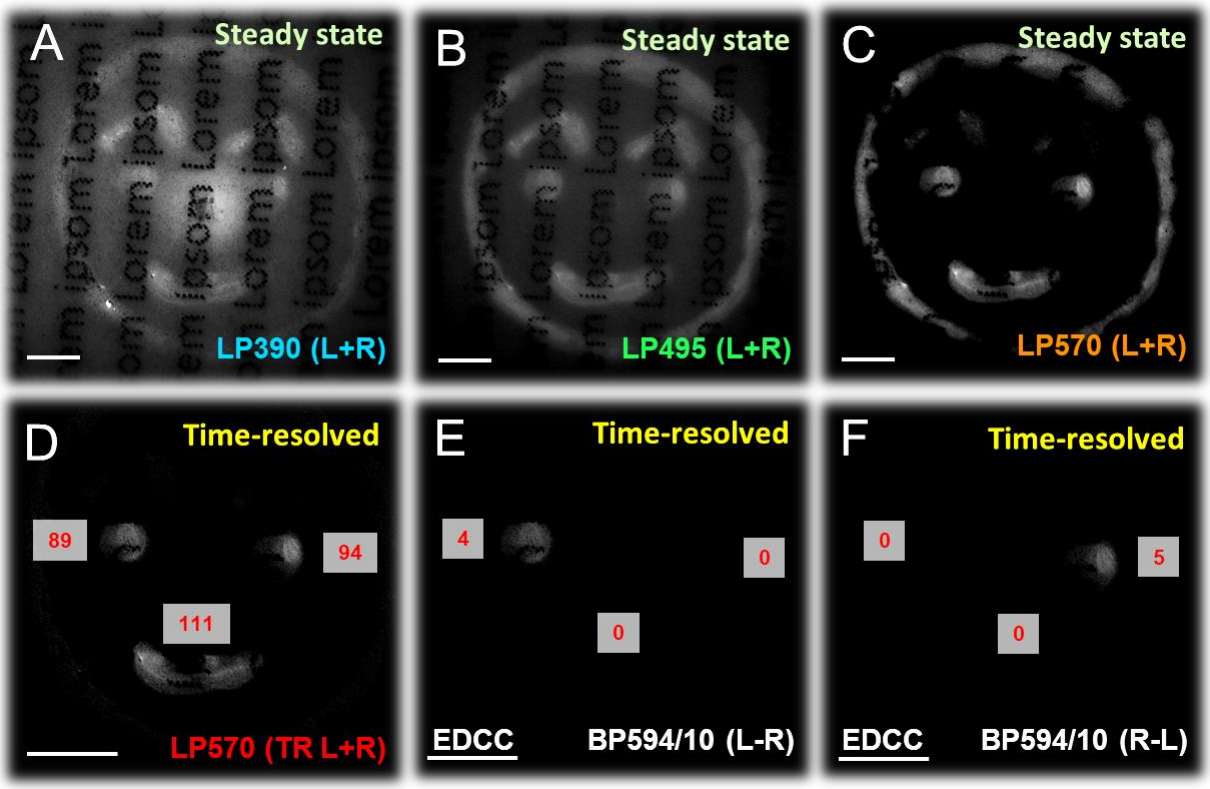

Figure 5.27. Decoding the RGB EDCC layering of the laminated POC CSI security tag. Images of the POC CSI security tag (λ_{exc} = 365 nm) using various colour and time resolution filtered CPLP. (A-C) Total emission under steady state illumination using a (A) LP390 nm (B) LP495 nm and (C) LP570 nm filter. (D) Time-resolved image (t_d = 20 µs) using a LP570 nm. (E) L-R EDCC image using a BP594/10 nm filter demonstrating clear CPL based emission for Δ-**[Eu.L^1]** whilst (F) R-L shows clear CPL based emission for Λ-**[Eu.L^1]**. Numbers in red are avg. 8 bit pixel intensity values for each image region, t_{acq} = 70-700 ms, 10 avg. image, 1-100 total image accumulation. Scale bar = 2 mm.

Finally, a time-resolved image was recorded (Figure 5.27.E,F) to reveal the left- or right-handed emitted CPL dominance of the employed enantiopure Eu(III)-complex features using a BP594/10 nm filter. The calculated EDCC L-R image shows clear

CPL emission arising exclusively from the Δ enantiomer, whilst the R-L image shows CPL emission only from the Λ enantiomer of **[Eu.L^1]**.

This rudimentary POC CSI invisible tag demonstrated the capability and simplicity of CPLP. Firstly, the imaging sequence and chromatic separation element can be further simplified by omitting the red channel (LP570 nm filter) element and only recording the steady state or time resolved red CPL spectral region of interest (BP594/10 nm) directly. EDCC images can still be calculated with high accuracy as the differential chiral contrast of a bright CPB luminophore is independent of the applied time domain (steady state *vs* time-resolved) mode of collection of CPLP. Secondly, the POC CSI tag has been constructed using stencils and calligraphy pens. However, this could have been made using inkjet printing adaptations for large scale commercial purposes. Furthermore, an extra dye and subsequent additional image feature could be introduced in the form of a second time-resolved green ink containing **[Tb.L^6]** using an additional BP546/10 nm filter. This extra layer of security was deliberately omitted to ensure simplicity when presenting monochromatic EDCC POC images.

5.4. Summary

This work constitutes a breakthrough in the intertwined disciplines of CPL detection, chiral luminescence imaging, and enhanced security applications. First and foremost, a handheld non-moving part CPLP system capable of rapid and simultaneous differentiation of left- and right-handed CPL was developed. It allows one-shot full field of view enantioselective differential chiral contrast imaging and photography. This is accompanied with the inherent advancement of differentiation between short-lived organic and long-lived lanthanide emission via time-resolved detection. Secondly, a simple protocol was defined to generate mixed chemical entities to act as rudimentary proof-of-concept chameleon security inks, encompassing five tiers of security, where both time-resolved colour separation and pattern recognition can be facilitated with the added possibility of further patterning using EDCC. These test targets consist of enantiopure high CPB europium complexes specifically designed to have exclusively positive or negative sign CPL within an emission manifold embedded into a PMMA matrix. Deposition of thick films was achieved by calligraphy or drop casting and spin coating. A rudimentary POC CSI security tag was constructed to evidence the

adaptability of CPLP. This invisible to the unaided eye tag demonstrates the capability and simplicity of CPLP and its of five layers of chromo-spatio-temporal-spectral-chiral discrimination. Importantly, these simple test target generation protocols can serve to compare and validate future CPLP devices capable of EDCC that may subsequently be developed by the multidisciplinary imaging community.

These developments may ignite research avenues especially in the field of lanthanide chemistry and luminescent security ink development for enhanced security applications. CPLP will play a vital role in the new era of layered information photography enabling the development of physically unclonable stochastically micro-patterned CPL-active chameleon security inks[157,176,186] and will promote EDCC to be adopted and utilised by a wider research community. Ultimately the work presented here could promote sufficiently high CPB luminescent chiral molecules to be used in many aspects of materials and life science. The development of such a compact multifunctional camera system and image differentiation methodology can also take centre stage and dictate the development and applications of chiral molecular emitters.

Future work in the area will build on the findings about solvent dependence detailed in Chapter Three. The main features of CPL spectra, especially the monosignate nature of the $\Delta J = 1$ and 2 manifolds, were shown to be preserved when going from solution to polymer matrices with similar chemical structures and polarity. Further steps include the fabrication of reliable polymer-based films for calibration of CPL instrumentation and appropriate functionalisation of Eu(III) complexes to make them soluble in water-based inks without affecting their chiroptical properties. This reinforces the idea that synthetic design of suitable emitters and instrumentation development go hand in hand and provide the best results when considered together.

Conclusions

Conclusions

The aim of the present work was to devise TACN-based Ln(III) complexes that are versatile, bright, linkable, and display desirable CPL behaviour. Ideal CPL tags should be chemically robust, display same sign CPL transitions within a single emission manifold, bear a functionalised alkyl chain to be exploited for late-stage conjugation of the complex with different species, and be suitable for cell uptake studies. Having a broad, intense, unique sign CPL emission manifold should greatly aid spectroscopic detection, as it would be possible to use low-cost broad band pass filters, allowing a larger number of photons reaching the detector without opposite sign CPL bands cancelling each other out. The hypothesis that replacing one or more phosphinate donors with carboxylates results in the coherence of the sign of CPL emission within one or more manifolds was verified. Great insight into the factors shaping spectral profiles as well as synthetic design rules was gained.

The aims of this thesis were broken down into the following seven objectives that will be reviewed, in turn, in the subsequent paragraphs:

4) Synthesis of Eu(III) complexes that display mono-signate CPL transitions within a single emission manifold;
5) Design of Eu(III) complexes with mixed donors and endowed with linkers that enable late-stage functionalisation;
6) Synthesis of a Tb(III) complex to be used as the CPL-active green emitter to fabricate circularly polarised OLEDs;
7) Study of the dependence of total and CPL emission of Eu(III) complexes on solvent polarity and investigation of solvent effects on racemisation kinetics;
8) Study of the properties of temperature sensitive Eu(III) complexes and the underlying mechanism of such behaviour;
9) Development of novel ink-based security tags that incorporate mono-signate CPL-active Eu(III) complexes as an additional layer of security;
10) Development of a novel compact, high-throughput CPL camera for facile scanning of CPL-based security tags.

1) The TACN-based complex **[Eu.L^{1}]** was identified as the target and synthesised. Chiral separation failed due to its negative charge. Conversion into its more apolar ethyl ester counterpart **[Eu.L^{1}]^{b}** allowed resolution of the two enantiomers. It was found that the two brightest emission manifolds (ΔJ = 1 and ΔJ = 2) of **[Eu.L^{1}]^{b}** are monosignate in NMP and EtOAc, effectively keeping opposite CPL sign cancellation low. NMP and EtOAc were chosen as solvents as they mimic the monomeric units constituting polyvinylpyrrolidone (PVP) and polymethylmethacrylate (PMMA), respectively. Embedding **[Eu.L^{1}]^{b}** in PMMA and PVP proved that the CPL spectrum sign features are retained when going from solution to films. This is particularly relevant when envisioning applications where bright, monosignate lanthanide-based polymeric films are used for calibration of CPL instrumentation. Strong CPL spectra of the *Λ* enantiomer of **[Eu.L^{1}]^{b}** in NMP were recorded using two-photon excitation (2PE).

2) A novel TACN-based Eu(III) complex, **[Eu.L^{5}]**, was synthesised, comprising three pyridyl-based carboxylate donor groups which saturate the coordination sphere of Eu(III). Two pyridylalkynylaryl antennae were grafted onto the macrocycle to enable efficient sensitisation of Eu(III) emission both in the UV region with single-photon excitation and in the NIR near-infrared *via* 2PE. A third macrocycle site was functionalised with a single pyridyl pendant arm, enabling linkage of the complex to various molecules via a *para*-nitro group that allows for facile late-stage functionalisation with a broad set of substituents. One of the aims of this work was to study how the total emission and CPL spectral profile of all-carboxylate complexes differ from those of all-phosphinate complexes. This was not pursued due to the failure of chiral resolution of the carboxylate-based **[Eu.L^{5}]**.

The shorter synthetic route of carboxylate donors compared to phosphinate ones afforded a larger amount of final product (50 mg, one order of magnitude larger than the usual mass obtained in the case of phosphinate donor-based complexes). The alkylation order necessary to install two different types of arms on the TACN scaffold was optimised to avoid the exposure of the alkynyl group to trifluoroacetic acid, which was shown to cause the degradation of the triple bond of the antenna. Conjugation reactions, such as thiol-bearing polymer end-group modifications to obtain Eu(III)-tagged CPL emissive polymers. This is possible since conjugation reactions are mild and are expected to preserve the enantiopurity of the complex. A successful proof-of-concept conjugation test reacted racemate **[Eu.L^5]** with reduced L-glutathione under various conditions.

3) A novel Tb(III) chiral complex, **[Tb.L^A]**, characterised by the presence of three strongly sensitising biaryl arms was synthesised with the intention of preparing a green dopant for the fabrication of Circularly Polarised OLEDs. Combined photophysical and electrochemical characterisation *via* fluorescence spectroscopy and cyclic voltammetry was performed to estimate the energy of the HOMO and LUMO of **[Tb.L^A]**, calculated to be -6.8 eV and -2.7 eV, respectively. Commercially available hosts that are solution processable usually range between a -2.3 eV LUMO and a -6.2 eV HOMO. The remarkably deep HOMO energy of -6.8 eV of **[Tb.L^A]** poses a great challenge since a host with an insufficiently deep HOMO level does not ensure charge injection or exciton trapping on the emissive material. Preliminary attempts using commercially available hosts with similar, although not perfectly matching energy levels were performed. The presence of the signature green Tb(III) emission was proven *via* electroluminescence spectrometry, showing the potential of **[Tb.L^A]** as an emitter in OLEDs once better novel host materials with a large bandgap are found.

4) Photophysical characterisation of racemic **[Eu.L^5]** evidenced a strong increase in λ_{abs} as the relative polarity of the solvent increases due to preferential stabilisation of the excited state with respect to the ground state. The solvatochromic properties of the complex suggest potential applications as a probe for local environment polarity. Photophysical studies in deuterated solvents proved that the solvent sensitivity of **[Eu.L^5]** cannot be attributed to first-shell solvent-lanthanide interaction. The strong solvent effect is due to the coupling of the solvent dipoles to the chromophore arm dipole, especially in the internal charge transfer state.

CPL emission of structurally related complexes **[Eu.L$^{7-9}$]** was found to increase as polarity decreases, consistently with the decrease in the magnitude of the electric dipole moment in less polar solvents. The simultaneous presence within the same emitting species of transitions that are highly sensitive towards solvent polarity variations ($\Delta J = 2$) and comparatively insensitive ($\Delta J = 4$) allows internally referenced ratiometric measurements of medium polarity to be undertaken, with greatly enhanced sensitivity. This ratiometric index undergoes an increase of up to a factor of 20 as solvent polarity decreases from MeOH to EtOAc, an order of magnitude larger than the same parameter when calculated using total emission.

Additionally, solvent-specific effects influencing the kinetic stability of Eu(III) complexes with respect to enantiomer interconversion were investigated in the pursuit of chiral lanthanide emitters that are stable towards racemisation for applications at room temperature. A generalised model of enantiomer interconversion was derived and used to measure racemisation half-lives, resulting in half-lives in non-polar media at room temperature ranging from weeks to millennia, highlighting the remarkable stability imparted by the phenyl phosphinate donor groups. The lower half-lives in water and MeOH can be rationalised in terms of the stabilisation of the charged intermediate that arises from breaking a Eu-O and a Eu-N_{py} bond, facilitating the arm rotation step necessary for enantiomer interconversion. Both NMP and EtOAc are aprotic solvents that are less effective at solvating the putative ionic intermediate (particularly local anionic charge centres), and hence are associated with a higher activation energy barrier and much longer racemisation half-lives. More interestingly, low-polarity aprotic solvents such as NMP and EtOAc give rise to a more intense CPL signal in the $\Delta J = 2$ manifold and seem to promote same sign transitions.

Due to the strong resemblance of the solvents NMP and EtOAc to the monomers of polyvinylpyrrolidone (PVP) and polymethylmethacrylate (PMMA) respectively, enantiopure lanthanide complexes are expected to be kinetically stable towards racemisation in such a polymeric matrix. Polymeric films doped with Eu(III) complexes were prepared and were shown to preserve the same monosignate CPL spectral feature shown in solution state.

5) In this study, pH sensitive Eu(III) probes were shown to also exhibit remarkable temperature dependent quenching. An investigation of the rationale of this temperature dependence and whether it is linked to pH sensitivity was carried out. A

maximum *T* sensitivity in luminescence intensity and lifetime of 2.1% K^{-1} was found in the range 25 - 50 °C, a value higher than most other highly engineered *T* probes in this range. The calibration curve was linear over the *T* range investigated, thereby providing a constant sensitivity. The sensitivity over the ambient and physiological temperature range is particularly interesting for applications in luminescence thermometry. Small molecule *T* probes are very appealing in the field of molecular thermometry, as opposed to highly engineered nanomaterials that currently dominate the field.

The behaviour of the protonated pH probes perfectly matches the trend observed in a *T*-insensitive control complex, both in terms of percentage total emission and lifetime decrease, leading to the hypothesis that the availability of the nitrogen lone pair is key for this series of complexes in the temperature dependence. A remarkable sensitivity of luminescence on temperature variations has more recently been found on complexes that have no available N lone pairs, disproving the formulated hypothesis. A more general mechanism involves the potential energy surface crossing of the chromophore ICT excited state to account for the thermally activated non-radiative decay of the Eu(III) excited state, rather than focusing on the properties of the N lone pair in isolation with respect to the highly conjugated chromophore that hosts it. Preliminary investigations provide results that are compatible with the proposed model. This discovery makes the design of molecular temperature probes easier because a pH sensitive temperature probe provides an ambiguous output in media with controlled, but unknown pH, such as in cells.

6) The superior CPL properties of lanthanide complexes, namely the high g_{lum} values and high CPB, have not been exploited as an added extra layer of security in advanced security inks. This is largely attributed to the limitations posed by current CPL instrumentation, where high throughput detection of L-CPL and R-CPL is not available. The difficulty with lanthanide complexes is that their emission manifolds are narrow and comprise of multiple transitions that often have discordant sign in CPL spectra. Unfortunately, any high throughput instrument cannot at the same time have an acquisition method capable of differentiating between the individual opposing-sign transitions and this polarisation cancellation effect manifests as a loss of signal even for emitters with a high dissymmetry factor and brightness.

This instrumental requirement puts a restraint on the properties of the emitters used for CPL-active security inks: suitable lanthanide emitters need to have at least one monosignate CPL manifold, *i.e.* a manifold where all the individual transitions have the same sign. If this requirement is satisfied, the lack of resolution does not hinder the apparent g_{lum} as CPL sign cancellation does not occur. By adopting this approach, part of the difficulty with instrumental design is transferred over to the synthetic design to achieve suitable photophysical properties of lanthanide complexes.

Chameleon Security Inks (CSI) are defined as a new class of intelligent security dyes. These blends of luminescent materials combine organic short-lived (ns) blue/green and red fluorophores and chiral CPL-active, high brilliance and circularly polarised brightness (CPB) red/green (europium/terbium) long-lived (ms) emitters embedded into a transparent polymer matrix and are collectively invisible to the naked eye. The chiral molecular fingerprints encoded in the luminescence spectra of CPL active Ln(III) complexes, alongside the possibility of time-resolved colour separation, adds two extra layers of security to existing security inks. This allows for multi-layered unclonable QR or bar code generation.

Sufficient thermal stability is not trivial in the case of lanthanide emitters, as their CPL activity arises from the degree of enantiopurity which can in turn be decreased by heating due to thermally assisted enantiomer interconversion. For this reason, extra care needs to be put in the synthetic design of such emitters to increase the energy barrier to the enantiomer interconversion process.

7) A breakthrough CPL imaging technique was developed to exploit the features of monosignate CPL emitters and was called Circularly Polarised Luminescence Photography (CPLP). This handheld non-moving parts setup can acquire a CPL image in a single shot (as quickly as 27 µs per frame), allowing for time-gated acquisition. At its core, the CPLP camera consists of a commercial polarisation-sensitive camera having a built-in linear polariser array and lens array coupled with a precisely aligned quarter-wave plate to convert circular polarisation into linear polarisation. Besides the astounding technical benefits, the components required to build the CPL photography setup are cheaper than a home-built PEM-CPL by a factor of 7 and even than a new-generation SS-CPL by a factor of 2. The CPLP apparatus was validated with a series of tests employing racemic organic emitters as well as racemic and enantiopure red-

emitting Eu(III) and green-emitting Tb(III) complexes. To comprehensively demonstrate the validity of our claim that the all-solid state one-shot CPLP camera system developed herein is capable of five layers of security readout comprising of multi-coloured, multi-spectral, opposing-helicity, combined with high spatial and temporal resolution we have constructed a proof-of-concept (POC) invisible hidden in plain sight CSI security tag. This CSI tag was constructed using three different coloured - anthracene (blue), fluorescein (green), and rhodamine B (red) - commercially available short-lived organic fluorophores and enantiopure and racemic (50:50) mixture of *Λ*- and *Δ*-**[Eu.L^1]**.

This innovation will likely ignite new research avenues especially in the field of lanthanide chemistry and luminescent security ink development for enhanced security applications. CPLP will play a vital role in the new era of layered information photography enabling the development of physically unclonable stochastically micro-patterned CPL-active chameleon security inks. Further steps include the fabrication of reliable polymer-based films for calibration of CPL instrumentation and appropriate functionalisation of Eu(III) complexes to make them soluble in water-based inks without affecting their chiroptical properties. This reinforces the idea that synthetic design of suitable emitters and instrumentation development go hand in hand and provide the best results when considered together.

Experimental Methods

Experimental Methods

7.1. General Procedures

Commercially available reagents were used as received. Solvents were laboratory grade and were dried over appropriate drying agents when required. Where appropriate, solvents were degassed using freeze-pump-thaw cycles.

Thin layer chromatography (TLC) was carried out on aluminium-backed silica gel plates with 0.2 mm thick silica gel 60 F254 (Merck), and visualised by UV irradiation at 254 nm or 366 nm. Preparative flash column chromatography was performed using flash silica gel 60 (230-400 mesh) from Merck or Fluorochem.

^{1}H, ^{13}C, and ^{31}P NMR spectra were recorded in commercially available deuterated solvents on a Bruker Avance-400 (^{1}H at 400.06 MHz, ^{13}C at 100.61 MHz, and ^{31}P at 161.95 MHz), a Mercury 400 (^{1}H at 399.95 MHz), a Varian VNMRS-600 (^{1}H at 599.67 MHz, ^{13}C at 150.79 MHz and ^{31}P at 242.75 MHz), or a Varian VNMRS-700 (^{1}H at 699.73 MHz, ^{13}C at 175.95 MHz and ^{31}P at 283.26 MHz). All chemical shifts are in ppm and coupling constants are in Hz.

Electrospray mass spectra were obtained on a TQD mass spectrometer equipped with an Acquity UPLC system, an electrospray ion source, and an Acquity photodiode array detector (Waters Ltd., UK). Accurate masses were recorded on an LCT Premier XE mass spectrometer or a QToF Premier Mass spectrometer, both equipped with an Acquity UPLC, a lock-mass electrospray ion source and an Acquity photodiode array detector (Waters Ltd., UK). MeOH or MeCN were used as the carrier solvents.

7.2. HPLC Analysis

Reverse-phase HPLC was performed at 295 K using a Shimadzu system comprising of a Degassing Unit (DGU-20A5R), a Prominence Preparative Liquid Chromatography pump (LC-20AP), a Prominence UV-Vis Detector (SPD-20A), and a Communications Bus Module (CBM-20A). A preparative XBridge C_{18} OBD column was used (19 × 100 mm, 5 µm) with a flow rate of 17 mL min^{-1}. Fraction collection was performed manually. The solvent system used to achieve purification is specified in the text. In general, a solvent system of water / MeCN (with or without 0.1% formic acid) was used with gradient elution as follows:

Step	Time / min	% H_2O	% MeCN/MeOH
0	0	90	10
1	4	90	10
2	14	0	100
3	19	0	100
4	22	90	10

Chiral HPLC analysis was carried out on a Perkin Elmer Series 200 system comprising of a Perkin Elmer Series 200 pump, autosampler, and UV-Vis detector, using a Daicel CHIRALPAK-IC or ID column (4.6 × 250 mm for analytical with a flow rate of 1.0 mL min^{-1}, 10 × 250 mm for preparative with a flow rate of 4.4 mL min^{-1}, all 5 µm particle size). Isocratic methanol, ethanol, and acetonitrile were used as the mobile phase. Fraction collection was automated.

7.3. Optical Measurements

All solution state optical analyses were carried out in quartz cuvettes with a path length of 1 cm. UV-Vis absorbance spectra were measured on an ATI Unicam UV-Vis spectrometer (Model UV2) using Vision software (version 3.33). Emission spectra were recorded using either an ISA Jobin-Yvon Spex Fluorolog-3 luminescence spectrometer using DataMax software (version 2.2.10) or a HORIBA Jobin-Yvon Fluorolog-3 luminescence spectrometer equipped with an iHR320 module, which selects either a HORIBA FL-1073 (Hammatsu R928P) photomultiplier tube or a HORIBA Synapse BIDD CCD for detection of emitted light, using FluorEssence software (based on Origin® software). Quantum yields were recorded using against the reference standard $[Ru(bipy)_3]Cl_2$, as described elsewhere.[115] Lifetime measurements were carried out using a Perkin Elmer LS55 spectrometer using FL Winlab software.

CPL spectra were recorded on a custom-built spectrometer consisting of a laser driven light source (Energetiq EQ-99 LDLS, spectral range 170 – 2100 nm) coupled to an Acton SP2150 monochromator (600 g nm^{-1}, 300 nm blaze) that allows excitation wavelengths to be selected with a 6 nm FWHM band-pass. The collection of the emitted light was facilitated (90° angle setup) by a Lock-In Amplifier (Hinds Instruments Signaloc 2100) and Photoelastic Modulator (Hinds Instruments Series II/FS2AA). The

differentiated light was focused onto an Acton SP2150 monochromator (1200 g nm^{-1}, 500 nm Blaze) equipped with a high sensitivity cooled Photo Multiplier Tube (Hamamatsu H10723-20 PhotoSensor). Red correction is embedded in the detection algorithm and was constructed using a calibrated Ocean Optics lamp. Spectra were recorded with 0.5 nm spectral intervals and 500 µs integration time, using a 5 spectral average sequence for Eu(III) complexes. The monochromators, PEM control unit and lock-in amplifier were interfaced with a desktop PC and controlled by LabView code.

7.4. PEM-CPL[132]

CPL was measured with a home-built (modular) spectrometer. The excitation source was a broad band (200 – 1000 nm) laser-driven light source EQ 99 (Elliot Scientific). The excitation wavelength was selected by feeding the broadband light into an Acton SP-2155 monochromator (Princeton Instruments); the collimated light was focused into the sample cell (1 cm quartz cuvette). Sample PL emission was collected perpendicular to the excitation direction with a lens (f = 150 mm). The emission was fed through a photoelastic modulator (PEM) (Hinds Series II/FS42AA) and through a linear sheet polariser (Comar). The light was then focused into a second scanning monochromator (Acton SP-2155) and subsequently on to a photomultiplier tube (PMT) (Hamamatsu H10723 series). The detection of the CPL signal was achieved using the field modulation lock-in technique. The electronic signal from the PMT was fed into a lock-in amplifier (Hinds Instruments Signaloc Model 2100). The reference signal for the lock-in detection was provided by the PEM control unit. The monochromators, PEM control unit, and lock-in amplifier were interfaced to a desktop PC and controlled by a Labview code. The lock-in amplifier provided two signals, an AC signal corresponding to (I_L- I_R) and a DC signal corresponding to (I_L + I_R) after background subtraction. The emission dissymmetry factor was therefore readily obtained from the experimental data, as 2 AC/DC.

Spectral calibration of the scanning monochromator was performed using a Hg-Ar calibration lamp (Ocean Optics). A correction factor for the wavelength dependence of the detection system was constructed using a calibrated lamp (Ocean Optics). The measured raw data was subsequently corrected using this correction factor. The validation of the CPL detection systems was achieved using light emitting diodes (LEDs) at various emission wavelengths. The LED was mounted in the sample holder and the light from the LED was fed through a broad band polarising filter and $\lambda/4$ plate

(Ocean Optics) to generate circularly polarised light. Prior to all measurements, the $\lambda/4$ plate and a LED were used to set the phase of the lock-in amplifier correctly. The emission spectra were recorded with 0.5 nm step size and the slits of the detection monochromator were set to a slit width corresponding to a spectral resolution of 0.25 nm. CPL spectra (as well as total emission spectra) were obtained through an averaging procedure of several scans. The CPL spectra have been smoothed using Savitzky-Golay smoothing (polynomial order 5, window size 9 with reflection at the boundaries) to enhance visual appearance; all calculations were carried out using raw spectral data. Analysis of smoothed *vs* raw data was used to help to estimate the uncertainty in the stated g_{em} factors, which was typically ±10%.

7.5. Multi-photon spectroscopy[154]

Two photon CPL spectroscopy has been achieved by coupling (beam routing using mirrors, Thor Labs BB1-E03) a tunable femtosecond pulsed laser (680 – 1300 nm, Coherent Discovery TPC, 100 fs, 80 MHz) to the pre-existing PEM-CPL spectrometer detailed above. Initial proof of concept two photon spectroscopy has been achieved by perpendicularly mounting an Ocean Optics HR2000Pro (2048-pixel linear CCD Sony ILX5 chip, 200 µm slit, H3 grating, 350 – 850 nm spectral region) spectrometer as a 'third arm' to the Discovery TPC laser. The laser beam was focused onto the centre of the 1 cm path sample holder (Thor labs CVH100) by a dedicated ultrafast laser lens (Edmund Optics 11711, 50 mm focal length). The spectrometer has also been equipped with a perpendicularly mounted 365 nm LED (nichia, 1W) and been operated using a custom time resolved detection and accumulation algorithm written in Labview2013 program. In order to eliminate unwanted artefacts associated with MP excitation each spectrometer have been equipped with a rotating filter wheel (Thor Labs, CFW6) housing an LP420 (Comar Optics, for 365 nm UVLED excitation) and SP650 and SP700 (Edmund Optics, 8472 and 8474 for MP excitation) filters.

7.6. Cyclic Voltammetry

CV measurements are collected with an Autolab PGSTAT101 potentiostat in a 3-electrod configuration electrochemical cell comprising of a glassy-carbon electrode, a Pt counter electrode, and an Ag^{+}/Ag reference electrode. The investigated material was also present in solution with a concentration of 10^{-5} M. All electrodes were immersed in a 0.1 M solution of tetrabutylammonium hexafluorophosphate electrolyte in acetonitrile and measured with a scan speed of 0.1 V/s.

7.7. Film Preparation

Films of **[Eu.L^{1b}]** in PMMA were prepared by drop casting a 2% solution of the lanthanide complex in poly(methylmethacrylate) (PMMA) (M_w ~ 15,000 g/mol, Sigma-Aldrich) matrix as follows. The polymer was stirred in dichloromethane (DCM) (40 mg/mL) and refluxed at 40 ^{o}C for 15 minutes. The lanthanide complex was dissolved in DCM and added to the polymer solution and refluxed at 40 ^{o}C for 5 minutes. A layer of the solution of the above mixture was deposited on a glass substrate using a glass Pasteur pipette. The carrier solvent was allowed to evaporate at room temperature to afford a film.

Films of **[Eu.L^{10}]** were prepared in PVP by spin coating a 2% solution of the lanthanide complex in a PVP (M_w ~ 40,000 $gmol^{-1}$, Sigma-Aldrich) matrix as follows. The polymer was dissolved in methanol (MeOH) (55 mg/ml) and left stirring overnight at room temperature. The lanthanide complex was dissolved in MeOH. 500 µL of the PVP solution was subsequently mixed with 100 µL of the lanthanide complex solution. The above mixture was deposited on a glass substrate at 1,500 RPM for 1 minute. The resulting film was annealed on a hot plate for 5 – 10 minutes at 35 ^{o}C after each layer was deposited to ensure the absence of cracks on the surface of the film.

The thickness of all films was verified using Phase Modulation Nanoscopy (PhMoNa) enhanced Laser Scanning Confocal Microscopy capable of achieving 380 nm axial resolution using a x63 NA objective and a 355 nm (Nd:YAG laser, 3rd harmonic) excitation wavelength.[187] Thickness of the films was determined to be 15 ± 3 micron (µm) via fluorescence emission tracking using diffraction-limited z-stack images.

7.8. OLED Fabrication and Characterisation

Pre-patterned indium tin oxide (ITO) was cleaned in a succession of ultrasonic baths using de-ionised water, acetone, and isopropanol, followed by O_2 plasma treatment for 7 min. A 40-50 nm layer of PEDOT:PSS (Heraeus Al 4083) was deposited via spin coating at 2500 rpm for 60 s and annealed at 135 °C for 15 min. The hole transport layer, PVK, was spin-coated from a 1,2-dichlorobenzene solution (5 mg/mL) and annealed at 150°C for 15 min under nitrogen. The active layer was then processed, followed by thermal evaporation of top contacts with of 30nm of TPBi (30 nm), Ca (10 nm) and Al (100 nm), defining a pixel area of 0.045 cm^2.

J-V-L curves of fabricated OLEDs were characterised with a Keithley 2400 source meter and a luminance meter (LS-160), assuming a Lambertian emission profile. Electroluminescence spectra were characterised with a CCD detector (Ocean Optics fl-400).

7.9. Variable Temperature Setup

Variable temperature experiments were performed using a Temperature-37 microscope objective lens collar temperature control unit and a Zeiss objective lens (range 20 – 60 °C) heating element, in conjunction with a small contact thermometer capable of 1 °C resolution (–20 – +70 °C, Thorlabs, TSP01). This setup was used to maintain the temperature of the all-aluminium cuvette holder of a Perkin Elmer LS 55 spectrometer while recording emission spectra and measuring radiative lifetimes.

7.10. Synthetic procedures

Diethyl 4-bromopyridine-2,6-dicarboxylate, 1

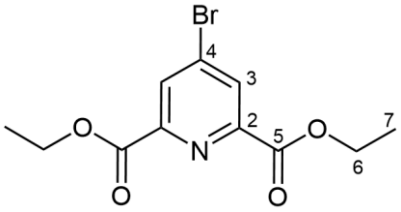

Compound **1** was prepared following a literature method.[105] Chelidamic acid (1.70 g, 9.30 mmol) and phosphorus pentabromide (12.0 g, 27.9 mmol) were stirred at 95 °C for 3 h. Anhydrous chloroform (25 mL) was added to the melted mixture and filtered while hot. Anhydrous EtOH (35 mL) was added at 0 °C under argon and stirred for 20'. Solvents were evaporated under reduced pressure to afford a brown oil. Ice-cold water (150 mL) was added to form a brown precipitate that was vacuum filtered. The precipitate was washed with ice-cold water (3 × 10 mL) and desiccated under high vacuum. The solid was recrystallised in hexane and the crystals washed with cold hexane to afford the product as a white powder (2.24 g, 80%); **^{1}H-NMR** (400 MHz, $CDCl_3$) δ 8.40 (2H, s, H^3), 4.47 (4H, q, $^{3}J_{H\text{-}H}$ 7, H^6), 1.43 (6H, t, $^{3}J_{H\text{-}H}$ 7, H^7); **^{13}C-NMR** (101 MHz, $CDCl_3$) δ 163.6 (C^5), 149.5 (C^2), 135.0 (C^4), 131.2 (C^3), 62.8 (C^6), 14.3 (C^7); **ESI-LRMS** (+) *m/z* 302 $[M+H]^+$; **ESI-HRMS** (+) calc. for $[C_{12}H_{13}NO_4Br]^+$ 302.0028, found 302.0038.

Ethyl 4-bromopyridine-2-carboxylate, 2

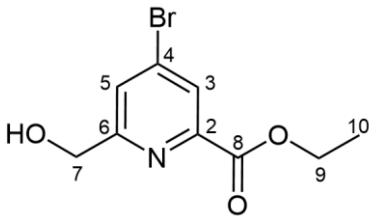

Compound **1** (960 mg, 3.18 mmol) was dissolved in anhydrous DCM (9 mL) and anhydrous EtOH (6 mL). The solution was stirred at 0 °C under argon and sodium borohydride (175 mg, 4.62 mmol) was added slowly. The solution was stirred for 90 min with monitoring by TLC every 15 min (3% MeOH in DCM; $\mathbf{R_f}$ 0.3). After 90 min, further sodium borohydride (61 mg, 1.6 mmol) was added to ensure reaction completion. After 3.5 h, the reaction was quenched by slow addition of hydrochloric acid (1 M HCl, 2 mL). The solution was stirred for 10 min before addition of DCM (20

mL) and water (25 mL). The aqueous phase was extracted with DCM (3 × 10 mL), and the combined organic extracts were washed with water (2 × 10 mL), dried over Na_2SO_4 and the solvent evaporated under reduced pressure to yield a yellow oil. The residue was purified by silica column chromatography (0 to 2.5% MeOH in DCM in 0.5% increments) to afford a white solid (489 mg, 59%); **^{1}H-NMR** (600 MHz, $CDCl_3$) δ 7.57 (1H, d, $^4J_{H\text{-}H}$ 2, H^3), 7.26 (1H, d, $^4J_{H\text{-}H}$ 2, H^5), 4.32 (2H, s, H^7), 3.91 (2H, q, $^3J_{H\text{-}H}$ 7, H^9), 3.70 (1H, br s, OH), 0.87 (3H, t, $^3J_{H\text{-}H}$ 7, H^{10}); **^{13}C-NMR** (151 MHz, $CDCl_3$) δ 163.9 (C^8), 162.6 (C^6), 134.5 (C^4), 127.1 (C^5), 126.9 (C^3), 64.4 (C^7), 62.4 (C^9), 14.2 (C^{10}); **ESI-LRMS** (+) *m/z* 260 $[M+H]^+$; **ESI-HRMS** (+) calc. for $[C_9H_{11}NO_3Br]^+$ 259.9922, found 259.9932; **MP** 63.1 - 66.0 °C.

Ethyl 6-(hydroxymethyl)-4-[3-methoxy-3-oxoprop-1-en-1-yl]pyridine-2-carboxylate, 3

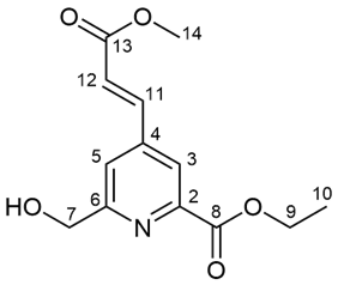

Compound **2** (101 mg, 0.390 mmol) was dissolved in anhydrous acetonitrile (2 mL). Allylpalladium(II) chloride dimer (19 mg, 0.052 mmol), piperidine (0.15 mL, 1.5 mmol), methyl acrylate (0.20 mL, 1.3 mmol), and tri-*tert*-butylphosphine (0.10 mL, 0.42 mmol) were added under argon. The solution was heated at 75 °C for 18 h. The solvents were removed and the residue dissolved in DCM (40 mL) and washed with water (4 × 50 mL). The combined aqueous phases were extracted with DCM (3 × 40 mL). The organic phases were combined, dried over Na_2SO_4, and the solvent evaporated under reduced pressure to afford a dark red oil. The crude residue was purified by reverse-phase HPLC (10 to 100% MeCN in H_2O over 10 min, t_R = 9.0 min) to yield the *E* stereoisomer as a yellow residue (88 mg, 85%); **^{1}H-NMR** (600 MHz, $CDCl_3$) δ 8.09 (1H, s, H^1), 7.65 (1H, d, $^3J_{H\text{-}H}$ 16, H^{11}), 7.60 (1H, s, H^5), 6.69 (1H, d, $^3J_{H\text{-}H}$ 16, H^{12}), 4.88 (2H, s, H^7), 4.47 (2H, q, $^3J_{H\text{-}H}$ 7, H^9), 3.83 (3H, s, H^{14}), 1.43 (3H, t, $^3J_{H\text{-}H}$ 7, H^{10}); **^{13}C-NMR** (151 MHz, $CDCl_3$) δ 166.2 (C^{13}), 164.6 (C^8), 161.4 (C^6), 148.2 (C^2), 143.6 (C^4), 140.9 (C^{11}), 123.7 (C^{12}), 121.9 (C^5), 121.7 (C^3), 64.5 (C^7), 62.2 (C^9), 52.1 (C^{14}), 14.3

(C^{10}); **ESI-LRMS** (+) *m/z* 266 $[M+H]^+$; **ESI-HRMS** (+) calc. for $[C_{13}H_{16}NO_5]^+$ 266.1028, found 266.1051.

Ethyl 6-(hydroxymethyl)-4-[3-methoxy-3-oxopropyl]pyridine-2-carboxylate, 4

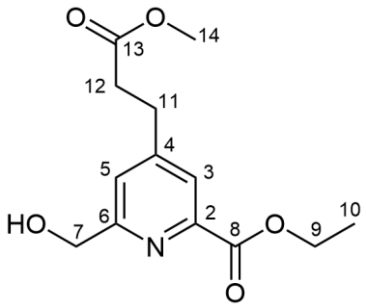

Compound **3** (99 mg, 0.37 mmol) was dissolved in ethanol (20 mL). Palladium on carbon (Pd content 10%, 15 mg) was added and the vessel was loaded onto a Parr hydrogenator (pressure 40 psi H_2) and the reaction mixture was agitated for 4 h. The completion of the hydrogenation reaction was confirmed via LC/MS. The catalyst was removed by filtration and the solvent removed under reduced pressure to yield a white solid (99 mg, quant.); **^{1}H-NMR** (600 MHz, $CDCl_3$) δ 7.83 (1H, s, H^3), 7.38 (1H, s, H^5), 4.81 (2H, s, H^7), 4.43 (2H, q, $^3J_{H\text{-}H}$ 7, H^9), 3.65 (3H, s, H^{14}), 3.01 (2H, t, $^3J_{H\text{-}H}$ 8, H^{11}), 2.67 (2H, t, $^3J_{H\text{-}H}$ 8, H^{12}), 1.40 (3H, t, $^3J_{H\text{-}H}$ 7, H^{10}); **^{13}C-NMR** (151 MHz, $CDCl_3$) δ 172.5 (C^{13}), 165.2 (C^8), 160.8 (C^6), 151.6 (C^4), 147.6 (C^2), 123.9 (C^3), 123.8 (C^5), 64.6 (C^7), 62.0 (C^9), 52.0 (C^{14}), 34.1 (C^{12}), 30.2 (C^{11}), 14.4 (C^{10}); **ESI-LRMS** (+) *m/z* 268 $[M+H]^+$; **ESI-HRMS** (+) calc. for $[C_{13}H_{18}NO_5]^+$ 268.1205, found 268.1185.

Ethyl 6-(hydroxymethyl)-4-{[3-(*tert*-butoxy)carbonyl]aminoprop-1-en-1-yl}pyridine-2-carboxylate, 5

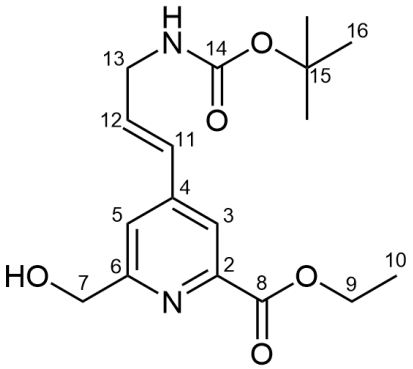

Compound **2** (49 mg: 0.19 mmol), *tert*-butyl *N*-allylcarbamate (130 mg: 0.827 mmol), and allylpalladium(II) chloride dimer (12 mg: 0.045 mmol) were dissolved in anhydrous MeCN (2 mL). Tri-*tert*-butylphosphine (0.10 mL, 0.42 mmol) and piperidine (0.10 mL, 1.0 mmol) were added under argon. The solution was heated at 70 °C for 18 h. The solvents were removed and the residue dissolved in DCM (40 mL) and washed with water (4 × 50 mL). The combined aqueous phases were extracted with DCM (3 × 40 mL). The organic phases were combined, dried over Na_2SO_4, and the solvent evaporated under reduced pressure to afford an amber oil. The crude residue was purified by reverse-phase HPLC (10 to 100% MeCN in H_2O over 10 min, t_R = 9.0 min) to yield the *E* stereoisomer as a yellow residue (30 mg, 47%); **^{1}H-NMR** (600 MHz, $CDCl_3$) δ 7.97 (1H, d, $^4J_{H\text{-}H}$ 1.4, H^3), 7.40 (1H, d, $^4J_{H\text{-}H}$ 1.4, H^5), 6.56 – 6.48 (2H, m, H^{11} + H^{12}), 4.82 (2H, s, H^7), 4.46 (2H, q, $^3J_{H\text{-}H}$ 7.2, H^9), 3.19 – 3.14 (2H, m, H^{13}), 1.47 (9H, s, H^{16}), 1.43 (3H, t, $^3J_{H\text{-}H}$ 7.2, H^{10}); **^{13}C-NMR** (151 MHz, $CDCl_3$) δ 165.3 (C^8), 160.7 (C^6), 155.8 (C^{14}), 147.9 (C^2), 146.3 (C^4), 121.2 (C^3), 120.9 (C^5), 79.8 (C^{15}), 64.5 (C^7), 62.1 (C^9), 40.2 (C^{13}), 32.6 (C^{11}), 30.7 (C^{12}), 28.5 (C^{16}), 14.1 (C^{10}); **ESI-LRMS** (+) *m/z* 337 $[M+H]^+$; **ESI-HRMS** (+) calc. for $[C_{17}H_{25}N_2O_5]^+$ 337.1763, found 337.1769.

Ethyl 6-(hydroxymethyl)-4-{[3-(*tert*-butoxy)carbonyl]aminopropyl}pyridine-2-carboxylate, 6

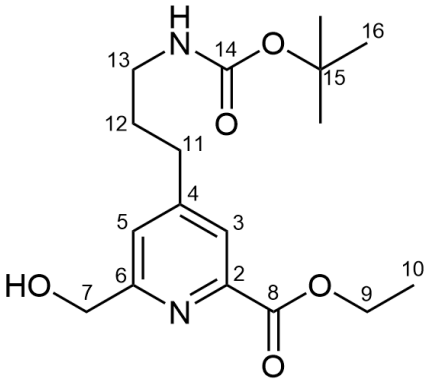

Compound **5** (26 mg, 0.077 mmol) was dissolved in ethanol (20 mL). Palladium on carbon (Pd content 10%, 10 mg) was added and the vessel was loaded onto a Parr hydrogenator (pressure 40 psi H_2) and the reaction mixture was agitated for 3 h. The completion of the hydrogenation reaction was confirmed via LC/MS. The catalyst was removed by filtration and the solvent removed under reduced pressure to yield a white solid (26 mg, quant.) that was used in the next step without further purification; **^{1}H-**

NMR (600 MHz, $CDCl_3$) δ 7.86 (1H, s, H^3), 7.35 (1H, s, H^5), 4.83 (2H, s, H^7), 4.61 (1H, br s, NH), 4.45 (2H, q, $^3J_{H\text{-}H}$ 7.1, H^9), 3.19 – 3.14 (2H, m, H^{13}), 2.75 – 2.70 (2H, m, H^{11}), 1.89 – 1.82 (2H, m, H^{12}), 1.44 (9H, s, H^{16}), 1.43 (3H, t, $^3J_{H\text{-}H}$ 7.1, H^{10}); **^{13}C-NMR** (151 MHz, $CDCl_3$) δ 165.2 (C^8), 160.3 (C^6), 156.1 (C^{14}), 153.2 (C^2), 147.3 (C^4), 124.2 (C^3), 124.1 (C^5), 79.6 (C^{15}), 64.5 (C^7), 62.2 (C^9), 40.1 (C^{13}), 32.6 (C^{11}), 30.8 (C^{12}), 28.5 (C^{16}), 14.1 (C^{10}); **ESI-LRMS** (+) *m/z* 339 $[M+H]^+$; **ESI-HRMS** (+) calc. for $[C_{17}H_{27}N_2O_5]^+$ 339.1920, found 339.1902.

Ethyl (4-nitro-6-methylpyridin-2-yl)methylphosphinate, 8

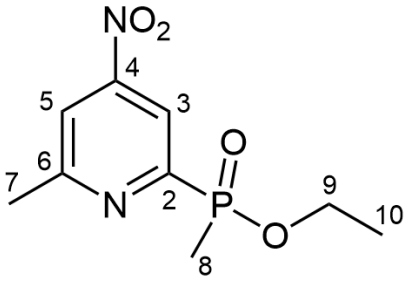

Compound **8** was prepared by adapting a literature method.[188] 2-Bromo-6-methyl-4-nitropyridine (2.70 g, 12.3 mmol), ethyl methyl phosphinate (1.60 g, 14.8 mmol) and NEt_3 (6.0 mL, 43 mmol) were added to anhydrous toluene (20 mL) before freeze-pump-thaw was carried out three times to degas the solution. [1,1'-Bis(diphenylphosphino)ferrocene]dichloropalladium (II) (0.56 g, 0.68 mmol) was added and freeze-pump-thaw was repeated. The red solution was stirred at 110 °C under argon for 18 h. Solvents were evaporated and the resulting black residue was dissolved in DCM (50 mL) and dispersed on silica. Purification was performed by dry-loaded column chromatography (0 to 75% EtOAc in hexane) to give the product as a yellow solid (1.82 g, 61%); **^{1}H NMR** (400 MHz, $CDCl_3$) δ 8.57 (1H, dd, $^3J_{H\text{-}P}$ 8, $^4J_{H\text{-}H}$ 2, H^3), 7.91 (1H, s, H^5), 4.20-4.13 (2H, m, H^9), 2.75 (3H, s, H^7), 1.73 (3H, d, $^2J_{H\text{-}P}$ 15, H^8), 1.40 (3H, t, $^3J_{H\text{-}H}$ 7, H^{10}); **ESI-LRMS** (+) *m/z* 245 $[M+H]^+$.

Ethyl (4-bromo-6-methylpyridin-2-yl)methylphosphinate, 9

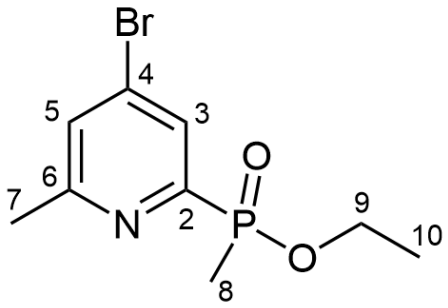

Compound **9** was prepared by adapting a literature method.[188] Compound **8** (1.81 g, 7.41 mmol) was dissolved in acetyl bromide (28.0 mL, 380 mmol) and stirred at 70 °C under argon for 18 h. The solution was cooled in an ice bath and ice-cold methanol (60 mL) was added and the solution stirred at 0 °C for 1 h. Solvents were removed under reduced pressure to afford a brown oil. Triethyl orthoformate (65 mL) was added and the solution was stirred at 140°C for 48 h. Solvents were evaporated to yield a brown solid that was purified by column chromatography (0 to 2% MeOH in DCM) to give yellow crystals (1.75 g, 85%); **^{1}H NMR** (400 MHz, $CDCl_3$) δ 8.08 (1H, dd, $^3J_{H\text{-}P}$ 7, $^4J_{H\text{-}H}$ 2, H^3), 7.41 (1H, s, H^5), 4.20-4.10 (2H, m, H^9), 2.56 (3H, s, H^7), 1.74 (3H, d, $^2J_{H\text{-}P}$ 15, H^8), 1.38 (3H, t, $^3J_{H\text{-}H}$ 7, H^{10}); **ESI-LRMS** (+) *m/z* 279 $[M+H]^+$.

Ethyl (4-bromo-6-methylpyridin-N-oxide-2-yl)methylphosphinate, 10

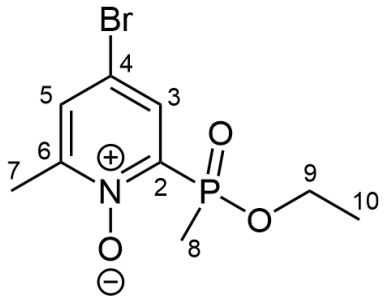

Compound **10** was prepared by adapting a literature method.[188] Compound **9** (1.70 g, 6.11 mmol) and *m*-chloroperbenzoic acid (3.75 g, 21.7 mmol) were dissolved in anhydrous chloroform (40 mL) and the solution was stirred at 65 °C for 24 h. Solvents were removed under reduced pressure and the resulting yellow solid was dissolved in DCM (50 mL). The solution was washed with 4% $NaHCO_3$ in water (3 x 50 mL) and the aqueous layer was extracted with DCM (3 x 30 mL). The organic layers were combined and dried over Na_2SO_4, filtered, and evaporated under reduced pressure to give a yellow oil used without further purification (1.65 g, 92%); **^{1}H NMR**

(400 MHz, $CDCl_3$) δ 8.08 (1H, dd, $^3J_{H\text{-}P}$ 8, $^4J_{H\text{-}H}$ 3, H^3), 7.45 (1H, d, $^4J_{H\text{-}H}$ 3, H^5), 4.19-4.09 (2H, m, H^9), 2.32 (3H, s, H^7), 1.74 (3H, d, $^2J_{H\text{-}P}$ 15, H^8), 1.37 (3H, t, $^3J_{H\text{-}H}$ 7, H^{10}); **ESI-LRMS** (+) *m/z* 294 $[M+H]^+$.

Ethyl (4-bromo-6-hydroxymethylpyridin-2-yl)methylphosphinate, 11

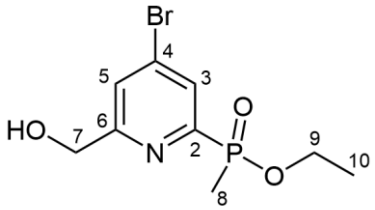

Compound **11** was prepared by adapting a literature method.[188] Compound **10** (1.65 g, 5.61 mmol) was dissolved in anhydrous chloroform (45 mL). Trifluoroacetic anhydride (17.0 mL , 25.7 mg, 122 mmol) was added and the solution was stirred at 60 °C for 5 hours. Solvents were removed under reduced pressure and the residue dissolved in a 1:1 EtOH:water mixture (10 mL) then stirred for at r.t. for 18 h. Organic solvent was removed under reduced pressure and the aqueous layer was extracted with DCM (3 x 70 mL). Combined organic layers were dried over Na_2SO_4, filtered and evaporated to give a viscous orange oil. The crude material was purified by column chromatography (30 to 100% EtOAc in hexane) to yield an orange oil (702 mg, 48 %);; **^{1}H-NMR** (400 MHz, $CDCl_3$) *δ* 8.05 (1H, d, $^3J_{H\text{-}P}$ 6, H^3), 7.71 (1H, s, H^5), 4.78 (2H, s, H^7), 4.33 (1H, br s, OH), 4.12-3.80 (2H, m, H^9), 1.73 (3H, d, $^2J_{H\text{-}P}$ 15, H^8), 1.24 (3H, d, $^3J_{H\text{-}H}$ 7, H^{10}); **^{13}C-NMR** (101 MHz, $CDCl_3$) *δ* 163.5 (d, $^3J_{C\text{-}P}$ 20, C^6), 154.7 (d, $^1J_{C\text{-}P}$ 156, C^2), 134.6 (d, $^3J_{C\text{-}P}$ 13, C^4), 129.4 (d, $^2J_{C\text{-}P}$ 22, C^3), 126.5 (d, $^4J_{C\text{-}P}$ 3, C^5), 64.3 (C^7), 61.8 (d, $^2J_{C\text{-}P}$ 6, C^9), 16.6 (d, $^3J_{C\text{-}P}$ 6, C^{10}), 13.8 (d, $^1J_{C\text{-}P}$ 104, C^8); **ESI-LRMS** (+) *m/z* 294 $[M+H]^+$.

1-Iodo-2,6-dimethyl-4-methoxybenzene, 12

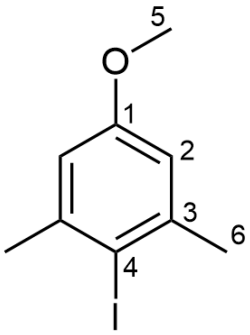

3,5-Dimethyl-4-iodophenol (735 mg, 2.96 mmol) and K_2CO_3 (830 mg, 6.01 mmol) were dissolved in MeCN (6 mL). Iodomethane (6.0 mL, 96 mmol) was added and the mixture refluxed at 40 °C under argon for 4 h. The reaction mixture was washed with water (3 × 20 mL) and extracted with DCM (3 × 20 mL). The combined organic layers were dried over Na_2SO_4, filtered, and evaporated to afford the crude intermediate **14[a]** as white crystals (731 mg, 94%) used in the next step without further purification; **^{1}H-NMR** (600 MHz, $CDCl_3$) δ 6.69 (2H, s, H^2), 3.80 (3H, s, H^5), 2.48 (6H, s, H^6); **ESI-LRMS** (+) *m/z* 263 $[M+H]^+$.

1-Trimethylsilylacetilene-2,6-Dimethyl-4-methoxybenzene, 13

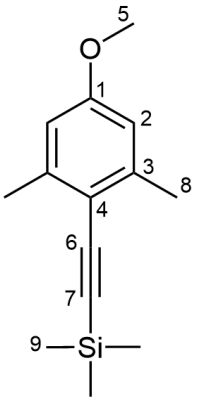

Compound **12** (731 mg, 2.79 mmol) and allylpalladium chloride dimer (101 mg, 2.79 mmol) were dissolved in anhydrous MeCN (10 mL). Ethynyl trimethyl silane (0.76 mL, 5.6 mmol), P(^{t}Bu)$_3$ (0.10 mL, 0.41 mmol), and piperidine (0.83 mL) were added and the mixture stirred at 35 °C under argon for 18 h. The solvents were removed under reduced pressure and the resulting residue dry loaded onto silica using DCM (50 mL). The crude was purified via column chromatography (0 to 10% EtOAc in hexane) to afford the product as a white solid (341 mg, 53%); **^{1}H NMR** (600 MHz, $CDCl_3$) δ 6.59

(2H, s, H^2), 3.76 (3H, s, H^5), 2.42 (6H, s, H^8), 0.25 (9H, s, H^9); **ESI-LRMS** (+) *m/z* 233 $[M+H]^+$.

2,6-Dimethyl-4-methoxyphenylacetylene, 14

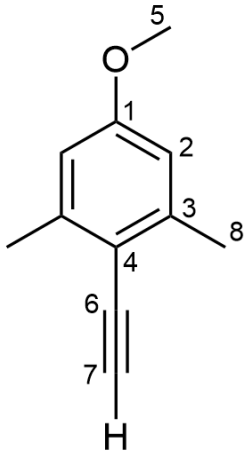

Compound **13** (210 mg, 0.904 mmol) was dissolved in anhydrous THF (2.8 mL). $Et_3N.3HF$ (2.8 mL, 17 mmol) was added and the solution stirred at 30 °C under argon for 24 h. Solvents were evaporated and the residue dissolved in DCM (40 mL), washed with water (3 × 40 mL). Combined aqueous layers were extracted with DCM (3 × 40 mL). Combined organic layers were dried over Na_2SO_4, filtered, and evaporated to afford the product as a brown oil (155 mg, 93%); **^{1}H NMR** (600 MHz, $CDCl_3$) δ 6.59 (2H, s, H^2), 3.79 (3H, s, H^5), 3.43 (1H, s, H^7), 2.45 (6H, s, H^8); **ESI-LRMS** (+) *m/z* 161 $[M+H]^+$.

3,5-Dimethyl-4-((2-(ethoxy(methyl)phosphoryl)-6-(hydroxymethyl)pyridine-4-yl)ethynyl)methoxybenzene, 15

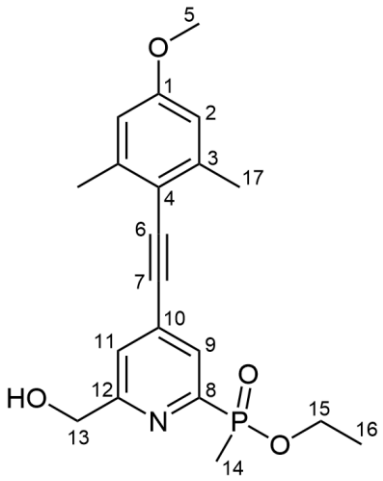

Compounds **14** (69 mg, 0.43 mmol) and **11** (115 mg, 0.391 mmol) were dissolved in anhydrous THF (3 mL) and the solution was degassed (3 × freeze-pump-thaw cycle). Anhydrous triethylamine (0.30 mL, 2.2 mmol) was added and the solution was further degassed (1 × freeze-pump-thaw cycle). [1,1'-Bis(diphenylphosphino)ferrocene]dichloropalladium(II) complex with DCM (42 mg, 0.052 mmol) and copper(I) iodide (7.6 mg, 0.040 mmol) were added and the solution was stirred at 65 °C under argon for 18 h. The solvents were removed under reduced pressure and the resulting residue dissolved in DCM (50 mL) and washed with water (4 × 30 mL). The combined aqueous phases were extracted with DCM (3 × 30 mL). The organic phases were combined, dried over Na_2SO_4, and evaporated under reduced pressure to afford a dark red oil. The crude residue was purified via reverse-phase HPLC (10 to 100% MeCN in H_2O over 10 min, t_R = 13.4 min) to yield a dark yellow solid (92 mg, 63%); **^{1}H-NMR** (600 MHz, $CDCl_3$) δ 8.03 (1H, d, $^3J_{H\text{-}P}$ 6, H^9), 7.48 (1H, s, H^{11}), 6.63 (2H, s, H^2), 4.84 (2H, s, H^{13}), 4.16-4.09 (1H, m, H^{15}), 3.96-3.85 (1H + 1H, m, OH + H^{15}), 3.81 (3H, s, H^5), 2.49 (6H, s, H^{17}), 1.80 (3H, d, $^2J_{H\text{-}P}$ 16, H^{14}), 1.29 (3H, t, $^3J_{H\text{-}H}$ 7, H^{16}); **^{13}C-NMR** (101 MHz, $CDCl_3$) δ 13.6 (d, $^1J_{C\text{-}P}$ 105, C^{14}), 16.5 (d, $^3J_{C\text{-}P}$ 6, C^{16}), 21.5 (C^{17}), 55.3 (C^5), 61.3 (d, $^2J_{C\text{-}P}$ 6, C^{15}), 64.2 (C^{13}), 93.4 (d, $^4J_{C\text{-}P}$ 2, C^7), 94.3 (C^6), 112.8 (C^2), 113.9 (C^4), 124.0 (C^{11}), 128.0 (C^9), 133.6 (d, $^3J_{C\text{-}P}$ 10, C^{10}), 143.1 (C^3), 153.2 (d, $^1J_{C\text{-}P}$ 153, C^8), 160.3 (C^1), 160.7 (d, $^3J_{C\text{-}P}$ 19, C^{12}); **^{31}P-NMR** (162 MHz, $CDCl_3$) δ +39.7; **ESI-LRMS** (+) *m/z* 374 $[M+H]^+$; **ESI-HRMS** (+) calc. for $[C_{20}H_{25}NO_5P]^+$ 374.1521, found 374.1508.

2-(2,2-Dibromovinyl)-1,3,5-trimethoxybenzene, 18

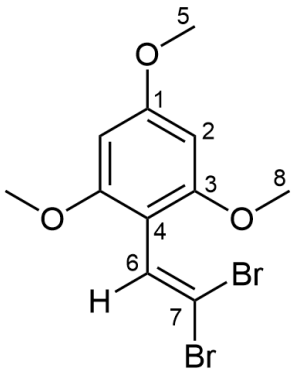

2,4,6-Trimethoxybenzaldehyde (0.50 g, 2.5 mmol) and triphenylphosphine (1.46 g, 5.57 mmol) were dissolved in anhydrous DCM (2 mL) and stirred at 0 °C. A solution of CBr_4 (1.71 g, 4.28 mmol) in anhydrous DCM (3 mL) was added dropwise under argon. The reaction was allowed to warm to room temperature and was stirred for 24 h. Solvents were removed under reduced pressure and the dark red slurry was washed with water (50 mL) and extracted with DCM (4 × 50 mL). Combined organic layers were dried over Na_2SO_4, and evaporated under reduced pressure to afford a red solid, further purified by silica gel column chromatography (0 to 70% EtOAc in hexane) to give a white solid (318 mg, 36%); **^{1}H NMR** (600 MHz, $CDCl_3$) δ 7.20 (1H, s, H^6), 6.10 (2H, s, H^2), 3.83 (3H, s, H^5), 3.81 (6H, s, H^8); **ESI-LRMS** (+) *m/z* 353 $[M+H]^+$.

(2,4,6-Trimethoxyphenyl)acetylene, 17

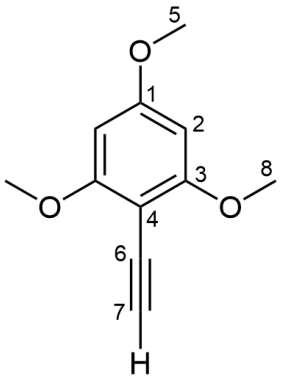

Compound **18** (310 mg, 0.88 mmol) was dissolved in anhydrous THF (10 mL) and the solution was cooled to -78 °C. *n*-Butyllithium (1.06 mL of a 2.5 M solution in hexane) was added dropwise and the yellow solution was stirred for 1 h. Water (20 mL) was added slowly and the solution was stirred for 1 h. The organic solvents were removed

under reduced pressure and the remaining aqueous solution extracted with EtOAc (4 x 20 mL). Combined organic layers were washed with brine (40 mL), dried over Na_2SO_4, filtered, and concentrated under reduced pressure to yield a white solid (173 mg, quant; **^{1}H NMR** (600 MHz, $CDCl_3$) δ 6.10 (2H, s, H^2), 3.88 (6H, s, H^8), 3.84 (3H, s, H^5), 3.50 (1H, s, H^7); **ESI-LRMS** (+) *m/z* 192 $[M+H]^+$.

3,5-Dimethoxy-4-((2-(ethoxy(methyl)phosphoryl)-6-(hydroxymethyl)pyridine-4-yl)ethynyl)methoxybenzene, 19

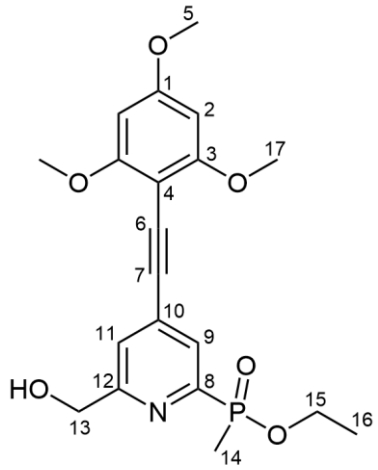

Compound **17** (165 mg, 0.863 mmol), compound **11** (235 mg, 0.799 mmol), and allylpalladium(II) chloride dimer (31 mg, 0.086 mmol) were combined in anhydrous acetonitrile (4 mL). Tri-*tert*-butylphosphine (0.05 mL, 0.2 mmol) and piperidine (0.30 mL, 3.0 mmol) were added and the solution stirred under argon at 40 °C for 2 d. The solvent was evaporated under reduced pressure and the dark red residue dissolved in DCM (30 mL) and washed with water (3 × 30 mL). The combined aqueous phases were extracted with DCM (3 × 30 mL). The organic phases were combined, dried over Na_2SO_4, and evaporated under reduced pressure to afford a dark red oil. The residue was purified via reverse-phase HPLC (10 to 100% MeCN in H_2O over 10 min, t_R = 9.5 min) to afford a yellow solid (140 mg, 43%); **^{1}H-NMR** (600 MHz, $CDCl_3$) *δ* 8.02 (1H, d, $^3J_{H\text{-}P}$ 6, H^9), 7.52 (1H, s, H^{11}), 6.06 (2H, s, H^2), 4.77 (2H, s, H^{13}), 4.17 (1H, br s, OH), 4.10-4.03 (1H, m, H^{15}), 3.78-3.86 (1H, m, H^{15}), 3.85 (6H, s, H^{17}), 3.80 (3H, s, H^5), 1.74 (3H, d, $^2J_{H\text{-}P}$ 15, H^{14}), 1.22 (3H, t, $^3J_{H\text{-}H}$ 7, H^{16}); **^{13}C-NMR** (101 MHz, $CDCl_3$) *δ* 162.9 (C^1), 162.8 (C^3), 160.7 (d, $^3J_{C\text{-}P}$ 19, C^{12}), 152.8 (d, $^1J_{C\text{-}P}$ 156, C^8), 133.8 (d, $^3J_{C\text{-}P}$ 11, C^{10}), 128.1 (d, $^2J_{C\text{-}P}$ 22, C^9), 124.1 (d, $^4J_{C\text{-}P}$ 3, C^{11}), 93.5 (d, $^4J_{C\text{-}P}$ 2, C^7), 93.2 (C^6), 90.5 (C^2), 89.8 (C^4), 64.2 (C^{13}), 61.2 (d, $^2J_{C\text{-}P}$ 6, C^{15}), 56.1 (C^{17}), 55.5 (C^5), 16.5 (d,

$^{3}J_{C\text{-}P}$ 6, C^{16}), 13.6 (d, $^{1}J_{C\text{-}P}$ 104, C^{14}); **^{31}P-NMR** (162 MHz, $CDCl_3$) δ +39.6; **ESI-LRMS** (+) *m/z* 406 $[M+H]^+$; **ESI-HRMS** (+) calc. for $[C_{20}H_{25}NO_6P]^+$ 406.1420, found 406.1415.

3-Methyl-4-((2-(ethoxy(methyl)phosphoryl)-6-(hydroxymethyl)pyridine-4-yl)ethynyl)methoxybenzene, 20

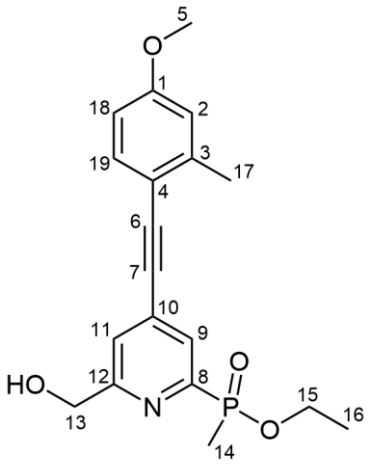

The compound was prepared according to a literature method by Dr M. Starck.[22] **^{1}H-NMR** (600 MHz, $CDCl_3$) δ 8.02 (1H, d, $^{3}J_{H\text{-}P}$ 6, H^9), 7.51 (1H, s, H^{11}), 7.43 (1H, d, $^{3}J_{H\text{-}H}$ 9, H^{19}), 6.78 (1H, d, $^{4}J_{H\text{-}H}$ 2, H^2), 6.74 (1H, dd, $^{4}J_{H\text{-}H}$ 2, $^{3}J_{H\text{-}H}$ 9, H^{18}), 4.83 (2H, s, H^{13}), 4.16-4.09 (1H, m, H^{15}), 3.97 (1H, br s, OH), 3.92-3.84 (1H, m, H^{15}), 3.82 (3H, s, H^5), 2.49 (3H, s, H^{17}), 1.79 (3H, d, $^{2}J_{H\text{-}P}$ 15, H^{14}), 1.29 (3H, t, $^{3}J_{H\text{-}H}$ 7, H^{16}); **^{13}C-NMR** (101 MHz, $CDCl_3$) δ 160.9 (d, $^{3}J_{C\text{-}P}$ 19, C^{12}), 160.7 (C^1), 153.2 (d, $^{1}J_{C\text{-}P}$ 155, C^8), 143.0 (C^3), 134.1 (C^{19}), 133.4 (d, $^{3}J_{C\text{-}P}$ 11, C^{10}), 128.1 (d, $^{2}J_{C\text{-}P}$ 22, C^9), 124.1 (d, $^{4}J_{C\text{-}P}$ 3, C^{11}), 115.4 (C^2), 113.8 (C^4), 111.7 (C^{18}), 95.3 (C^6), 89.1 (d, $^{4}J_{C\text{-}P}$ 2, C^7), 64.2 (C^{13}), 61.3 (d, $^{2}J_{C\text{-}P}$ 6, C^{15}), 55.4 (C^5), 21.1 (C^{17}), 16.5 (d, $^{3}J_{C\text{-}P}$ 6, C^{16}), 13.5 (d, $^{1}J_{C\text{-}P}$ 104, C^{14}); **^{31}P-NMR** (240 MHz, $CDCl_3$) δ +39.6; **ESI-LRMS** (+) *m/z* 438 $[M+H]^+$.

Compound 21

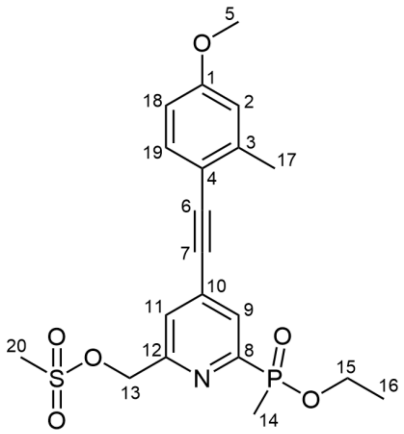

Compound **20** (200 mg, 0.557 mmol) and methanesulfonic anhydride (230 mg, 1.32 mmol) were dissolved in anhydrous THF (3 mL) under argon. DIEA (0.25 mL, 1.4 mmol) was added and the solution stirred for 1 h. The solvents were removed under reduced pressure and the resulting residue was dissolved in DCM (30 mL) and washed with water (3 × 30 mL). The combined aqueous phases were extracted with DCM (3 × 30 mL) and the combined organic phases were dried over Na_2SO_4 and evaporated under reduced pressure to afford a dark yellow oil (243 mg, quant.); **^{1}H-NMR** (400 MHz, $CDCl_3$) δ 8.06 (1H, d, $^3J_{H\text{-}P}$ 6, H^9), 7.60 (1H, s, H^{11}), 7.43 (1H, d, $^3J_{H\text{-}H}$ 8, H^{19}), 6.76 (1H, d, $^4J_{H\text{-}H}$ 2, H^2), 6.72 (1H, dd, $^3J_{H\text{-}H}$ 8, $^4J_{H\text{-}H}$ 2, H^{18}), 5.35 (2H, s, H^{13}), 4.10 (1H, m, H^{15}), 3.91-3.82 (1H, m, H^{15}), 3.80 (3H, s, H^5), 3.13 (3H, s, H^{20}), 2.47 (3H, s, H^{17}), 1.76 (3H, d, $^2J_{H\text{-}P}$ 15, H^{14}), 1.26 (3H, t, $^3J_{H\text{-}H}$ 7, H^{16}); **^{31}P-NMR** (162 MHz, $CDCl_3$) δ +39.4; **ESI-LRMS** (+) *m/z* 438 $[M+H]^+$; **ESI-HRMS** (+) calc. for $[C_{20}H_{25}NO_6SP]^+$ 438.1140, found 438.1135.

Compound 22

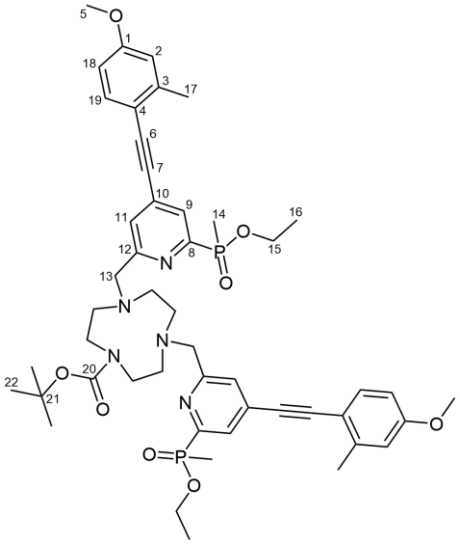

Compound **21** (240 mg, 0.549 mmol) and Boc-protected TACN (70 mg, 0.23 mmol) were dissolved in anhydrous acetonitrile (3 mL) under argon. Potassium carbonate (317 mg, 2.29 mmol) was added and the mixture stirred at 60 °C for 18 h. The reaction solution was separated from the inorganic salts by centrifugation to yield the crude ligand as a yellow residue. The residue was purified via reverse-phase HPLC (10 to 100% MeCN in H_2O over 10 min, t_R = 15.0 min) to yield a dark yellow solid (170 mg, 80%); **^{1}H-NMR** (600 MHz, $CDCl_3$) δ 7.96 (2H, app t, H^9 + $H^{9'}$), 7.65 (1H, s, H^{11}), 7.58 (1H, s, $H^{11'}$), 7.40 (2H, d, $^3J_{H\text{-}H}$ 8, H^{19} + $H^{19'}$), 6.74 (2H, d, $^4J_{H\text{-}H}$ 2, H^2 + $H^{2'}$), 6.71-6.68 (2H, m, H^{18} + $H^{18'}$), 4.11-3.04 (2H, m, H^{15}), 3.95 (2H, s, H^{13}), 3.93 (2H, s, $H^{13'}$), 3.88-3.81 (2H, m, $H^{15'}$), 3.79 (6H, s, H^5), 3.40-3.34 (4H, m, 9-N_3 ring), 3.12-3.04 (4H, m, 9-N_3 ring), 2.74-2.66 (4H, m, 9-N_3 ring), 2.45 (6H, s, H^{17} + $H^{17'}$), 1.75 (3H, d, $^2J_{H\text{-}P}$ 15, C^{14}), 1.74 (3H, d, $^2J_{H\text{-}P}$ 15, C^{14}), 1.45 (9H, s, H^{22}), 1.23 (6H, 2 × t, $^3J_{H\text{-}H}$ 7, H^{16} + $H^{16'}$); **^{13}C-NMR** (101 MHz, $CDCl_3$) δ 161.6 (d, $^3J_{C\text{-}P}$ 20, C^{12}), 161.4 (d, $^3J_{C\text{-}P}$ 20, $C^{12'}$), 160.6 (C^1), 160.5 ($C^{1'}$), 155.6 (C^{20}), 153.8 (2 × d, $^1J_{C\text{-}P}$ 157, C^8 + $C^{8'}$), 142.8 (2 × s, C^3 + $C^{3'}$), 133.9 (2 × s, C^{19} + $C^{19'}$), 132.8 (app t, C^{10} + $C^{10'}$), 127.6 (d, $^2J_{C\text{-}P}$ 22, C^9), 127.5 (d, $^2J_{C\text{-}P}$ 22, $C^{9'}$), 126.5 (C^{11}), 126.3 ($C^{11'}$), 115.3 (2 × s, C^2 + $C^{2'}$), 114.0 (C^4), 113.9 ($C^{4'}$), 111.6 (2 × s, C^{18} + $C^{18'}$), 94.8 (C^6), 94.5 ($C^{6'}$), 89.4 (d, $^4J_{C\text{-}P}$ 2, C^7), 89.3 (d, $^4J_{C\text{-}P}$ 2, $C^{7'}$), 79.5 (C^{21}), 63.0 (C^{13}), 62.6 ($C^{13'}$), 61.0 (2 × d, $^2J_{C\text{-}P}$ 6, C^{15} + $C^{15'}$), 55.9 (9-N_3 ring), 55.3 (C^5 + $C^{5'}$), 55.2 (9-N_3 ring), 54.6 (9-N_3 ring), 54.1 (9-N_3 ring), 50.0 (9-N_3 ring), 49.8 (9-N_3 ring), 28.7 (C^{22}), 21.1 (2 × s, C^{17} + $C^{17'}$), 16.5 (d, $^3J_{C\text{-}P}$ 6, C^{16} + $C^{16'}$), 13.3 (2 × d, $^1J_{C\text{-}P}$ 104, C^{14} + $C^{14'}$); **^{31}P-NMR** (162 MHz, $CDCl_3$) δ +40.1 (s, P), +40.0 (s, P'); **ESI-**

LRMS (+) *m/z* 912 $[M+H]^+$; **ESI-HRMS** (+) calc. for $[C_{49}H_{64}N_5O_8P_2]^+$ 912.4230, found 912.4223.

Compound 23

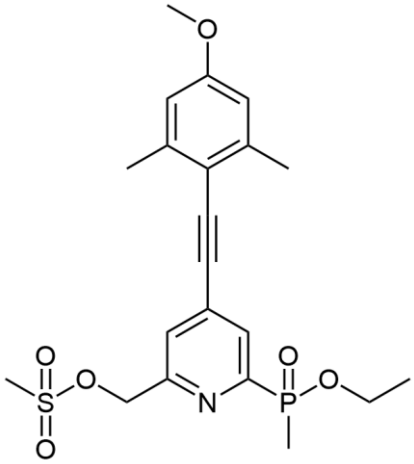

Compound **15** (90 mg, 0.24 mmol) and methanesulfonic anhydride (89 mg, 0.51 mmol) were dissolved in anhydrous THF (3.5 mL) under argon. DIEA (0.10 mL, 0.57 mmol) was added and the solution stirred for 1 h. The solvents were removed and the dark yellow residue was dissolved in DCM (50 mL) and washed with water (3 × 30 mL). The combined aqueous phases were extracted with DCM (3 × 30 mL). The organic phases were combined, dried over Na_2SO_4, and evaporated under reduced pressure to give a dark yellow oil (108 mg, quant.); **ESI-LRMS** (+) *m/z* 452 $[M+H]^+$; **ESI-HRMS** (+) calc. for $[C_{21}H_{27}NO_6SP]^+$ 452.1297, found 452.1285.

Compound 24

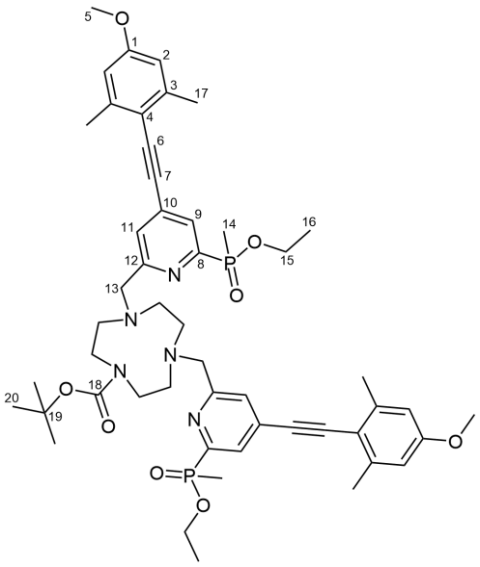

Compound **23** (108 mg, 0.241 mmol) and Boc-protected TACN (28 mg, 0.093 mmol) were dissolved in anhydrous acetonitrile (3 mL) under argon. Potassium carbonate (58 mg, 0.051 mmol) was added, and the mixture stirred at 60 °C for 18 h. The reaction solution was separated from the inorganic salts by centrifugation and concentrated to yield a yellow residue. The residue was purified via reverse-phase HPLC (10 to 100% MeCN in H_2O over 10 min, t_R = 15.3 min) to afford a dark yellow solid (68 mg, 78%); **^{1}H-NMR** (600 MHz, $CDCl_3$) δ 8.01-7.98 (2H, m, H^9 + $H^{9'}$), 7.66 (1H, s, H^{11}), 7.64 (1H, s, $H^{11'}$), 6.62 (4H, s, H^2 + $H^{2'}$), 4.16-4.07 (2H, m, H^{15} + $H^{15'}$), 3.97 (4H, 2 × s, H^{13} + $H^{13'}$), 3.90-3.84 (2H, m, H^{15} + $H^{15'}$), 3.81 (6H, s, H^5 + $H^{5'}$), 3.45-3.37 (4H, m, 9-N_3 ring), 3.15-3.07 (4H, m, 9-N_3 ring), 2.78-2.70 (4H, m, 9-N_3 ring), 2.47 (12H, s, H^{17} + $H^{17'}$), 1.79 (6H, 2 × d, $^2J_{H\text{-}P}$ 15, H^{14} + $H^{14'}$), 1.47 (9H, s, H^{20} + $H^{20'}$), 1.27 (6H, 2 × t, $^3J_{H\text{-}H}$ 7, H^{16} + $H^{16'}$); **^{13}C-NMR** (101 MHz, $CDCl_3$) δ 161.6 (d, $^3J_{C\text{-}P}$ 20, $C^{12'}$), 161.5 (d, $^3J_{C\text{-}P}$ 20, C^{12}), 160.1 (2 × s, C^1 + $C^{1'}$), 155.6 (C^{18} + $C^{18'}$), 153.9 (d, $^1J_{C\text{-}P}$ 157, $C^{8'}$), 153.8 (d, $^1J_{C\text{-}P}$ 157, C^8), 143.0 (C^3 + $C^{3'}$), 133.1 (app t, C^{10} + $C^{10'}$), 127.5 (d, $^2J_{C\text{-}P}$ 23, $C^{9'}$), 127.4 (d, $^2J_{C\text{-}P}$ 23, C^9), 126.5 (d, $^4J_{C\text{-}P}$ 2, $C^{11'}$), 126.3 (d, $^4J_{C\text{-}P}$ 2, C^{11}), 114.1 (2 × s, C^4 + $C^{4'}$), 112.8 (2 × s, C^2 + $C^{2'}$), 93.8 ($C^{6'}$), 93.7 (d, $^4J_{C\text{-}P}$ 2, $C^{7'}$), 93.6 (d, $^4J_{C\text{-}P}$ 2, C^7), 93.5 (C^6), 79.5 (C^{19} + $C^{19'}$), 63.2 ($C^{13'}$), 62.8 (C^{13}), 61.1 (C^{15} + $C^{15'}$), 55.8 (9-N_3 ring), 55.4 (9-N_3 ring), 55.3 (C^5 + $C^{5'}$), 54.6 (9-N_3 ring), 54.1 (9-N_3 ring), 50.0 (9-N_3 ring), 28.7 (C^{20} + $C^{20'}$), 21.5 (2 × s, C^{17} + $C^{17'}$), 16.6 (2 × s, C^{16} + $C^{16'}$), 13.4 (2 × d, $^1J_{C\text{-}P}$ 104, C^{14} + $C^{14'}$); **^{31}P-NMR** (162 MHz, $CDCl_3$) δ +40.2; **ESI-LRMS** (+) *m/z* 912 $[M+H]^+$; **ESI-HRMS** (+) calc. for $[C_{49}H_{64}N_5O_8P_2]^+$ 912.4230, found 912.4223.

Compound 25

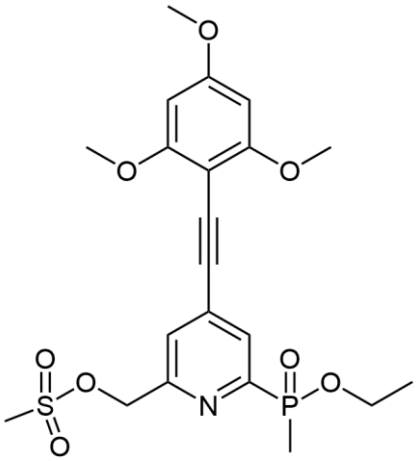

Compound **19** (95 mg, 0.23 mmol) and methanesulfonic anhydride (87 mg, 0.50 mmol) were dissolved in anhydrous THF (2.5 mL) under argon. DIEA (0.11 mL, 0.63 mmol) was added and the solution stirred for 1 h. The solvent was evaporated under reduced pressure and the residue dissolved in DCM (40 mL) and washed with water (4 × 40 mL). The combined aqueous layers were extracted with DCM (3 × 40 mL). The organic extracts were combined, dried over Na_2SO_4, and evaporated under reduced pressure to give a dark yellow oil (112 mg, quant.). The crude product was used for the next step without further purification.

Compound 26

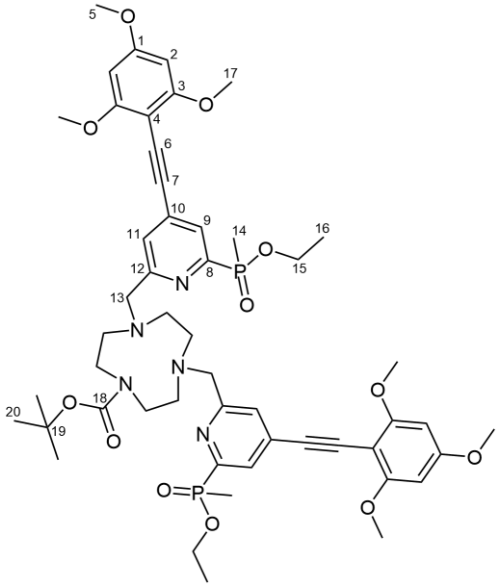

Compound **25** (119 mg, 0.247 mmol) and Boc-protected TACN (32 mg, 0.11 mmol) were dissolved in anhydrous acetonitrile (1.5 mL) under argon. Potassium carbonate

(56 mg, 0.41 mmol) was added, and the mixture stirred at 60 °C for 18 h. The reaction solution was separated from the inorganic salts by centrifugation and concentrated to yield a yellow residue. The residue was purified via reverse-phase HPLC (10 to 100% MeCN in H_2O over 10 min, t_R = 12.5 min) to afford a yellow solid (63 mg, 59%); **^{1}H-NMR** (600 MHz, $CDCl_3$) δ 8.02 (2H, 2 × m, H^9 + $H^{9'}$), 7.61 (2H, 2 × s, H^{11} + $H^{11'}$), 6.07 (4H, s, H^2 + $H^{2'}$), 3.95-3.91 (4H, 2 × m, H^{13} + $H^{13'}$), 4.08-4.00 (2H, 2 × m, H^{15} + $H^{11'}$), 3.86-3.79 (2H, 2 × m, H^{15} + $H^{15'}$), 3.84 (12H, s, H^{17} + $H^{17'}$), 3.81 (6H, s, H^5 + $H^{5'}$), 3.40-3.30 (4H, m, 9-N_3 ring), 3.11-3.04 (4H, m, 9-N_3 ring), 2.73-2.65 (4H, m, 9-N_3 ring), 1.74 (6H, 2 × d, $^2J_{H\text{-}P}$ 15, H^{14} + $H^{14'}$), 1.44 (9H, s, H^{20}), 1.21 (6H, 2 × t, $^3J_{H\text{-}H}$ 7, H^{16} + $H^{16'}$); **^{13}C-NMR** (101 MHz, $CDCl_3$) δ 162.9 (2 × s, C^1 + $C^{1'}$ + C^{18}), 162.8 (C^3 + $C^{3'}$), 161.2 (app t, C^{12} + $C^{12'}$), 153.0 (d, $^1J_{C\text{-}P}$ 157, C^8), 152.9 (d, $^1J_{C\text{-}P}$ 157, $C^{8'}$), 133.4 (app t, C^{10} + $C^{10'}$), 127.7 (d, $^2J_{C\text{-}P}$ 22, C^9), 127.6 (d, $^2J_{C\text{-}P}$ 22, $C^{9'}$), 126.4 (2 × s, C^{11} + $C^{11'}$), 93.7 (m, C^7 + $C^{7'}$), 93.4 (C^6), 93.3 ($C^{6'}$), 90.5 (C^2 + $C^{2'}$), 89.1 (C^4), 89.0 $C^{4'}$), 79.5 (C^{19}), 62.8 C^{13}), 62.5 ($C^{13'}$), 61.0 (2 × d, $^2J_{C\text{-}P}$ 6, C^{15} + $C^{15'}$), 56.1 (2 × s, C^{17} + $C^{17'}$), 55.5 (C^5 + $C^{5'}$), 55.2 (9-N_3 ring), 54.3 (9-N_3 ring), 53.7 (9-N_3 ring), 53.5 (9-N_3 ring), 49.9 (9-N_3 ring), 28.7 (C^{20}), 16.5 (2 × s, C^{16} + $C^{16'}$), 13.3 (2 × d, $^1J_{C\text{-}P}$ 104, C^{14} + $C^{14'}$); **^{31}P-NMR** (162 MHz, $CDCl_3$) δ +40.4; **ESI-LRMS** (+) *m/z* 1004 $[M+H]^+$; **ESI-HRMS** (+) calc. for $[C_{51}H_{68}N_5O_{12}P_2]^+$ 1004.434, found 1004.434.

Ethyl 6-[(methanesulfonyloxy)methyl]-4-(3-methoxy-3-oxopropyl)pyridine-2-carboxylate, 29

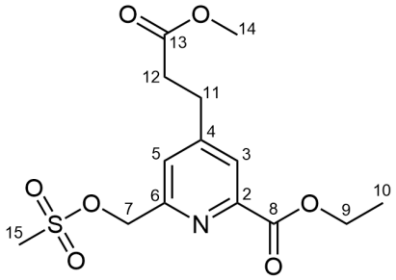

Compound **4** (66 mg, 0.25 mmol) and methanesulfonic anhydride (85 mg, 0.49 mmol) were combined in anhydrous THF (2 mL) under argon. DIEA (0.11 mL, 0.063 mmol) was added and the solution stirred for 1 h. The solvent was evaporated under reduced pressure and the resulting residue dissolved in DCM (20 mL). The organic phase was

washed with water (2 × 20 mL) and dried over Na_2SO_4 to yield a dark yellow solid (84 mg, quant.); **^{1}H-NMR** (400 MHz, $CDCl_3$) δ 7.93 (1H, s, H^3), 7.48 (1H, s, H^5), 5.38 (2H, s, H^7), 4.43 (2H, q, $^3J_{H\text{-}H}$ 7, H^9), 3.65 (3H, s, H^{14}), 3.15 (3H, s, H^{15}), 3.03 (2H, t, $^3J_{H\text{-}H}$ 8, H^{11}), 2.69 (2H, t, $^3J_{H\text{-}H}$ 8, H^{12}), 1.39 (3H, t, $^3J_{H\text{-}H}$ 7, H^{10}); **ESI-LRMS** (+) *m/z* 346 $[M+H]^+$; **ESI-HRMS** (+) calc. for $[C_{14}H_{20}NO_7S]^+$ 346.0960, found 346.0964.

L^1

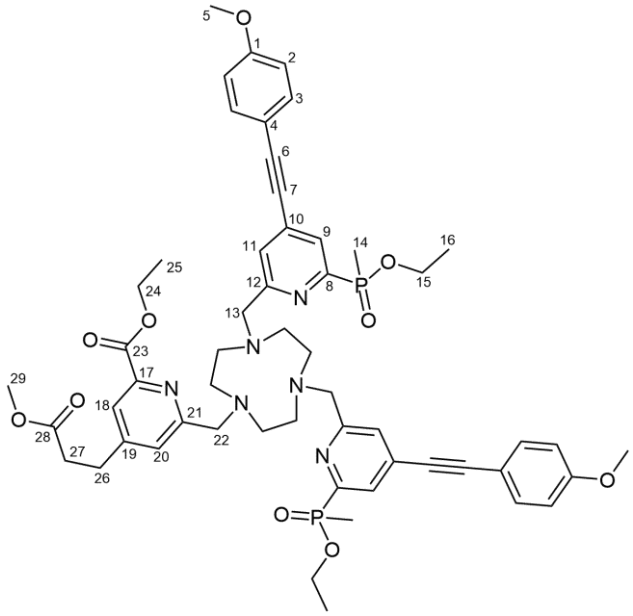

Compound **28** (77 mg, 0.098 mmol), compound **29** (85 mg, 0.25 mmol), and potassium carbonate (40 mg, 0.29 mmol) were combined in anhydrous MeCN (3 mL) under argon. The mixture was stirred at 60 °C for 18 h. The reaction solution was separated from the inorganic salts by centrifugation and concentrated to afford the crude ligand as a yellow residue (58 mg, 57%); **^{1}H-NMR** (400 MHz, $CDCl_3$) δ 7.94 (2H, d, $^5J_{H\text{-}P}$ 6, H^{11}), 7.83 (1H, s, H^{18}), 7.81 (2H, d, $^3J_{H\text{-}P}$ 11, H^9), 7.44 (4H, d, $^3J_{H}$-H 9, H^3), 7.39 (1H, s, H^{20}), 6.87 (4H, d, $^3J_{H\text{-}H}$ 9, H^2), 5.27 (1H, s, H^{22}), 4.81 (4H, s, H^{13}), 4.42 (2H, q, $^3J_{H\text{-}H}$ 7, H^{24}), 4.13-4.02 (2H, m, H^{15}), 3.95-3.83 (8H, m, H^{15} + 9-N_3 ring), 3.81 (3H, s, H^5), 3.65 (3H, s, H^{29}), 3.00 (2H, t, $^3J_{H\text{-}H}$ 8, H^{26}), 2.67 (2H, t, $^3J_{H\text{-}H}$ 8, H^{27}), 1.73 (3H, d, $^2J_{H\text{-}P}$ 16, H^{14}), 1.39 (3H, t, $^3J_{H\text{-}H}$ 7, H^{25}), 1.22 (6H, t, $^3J_{H\text{-}H}$ 7, H^{16}), 2.85 (6H, br s, 9-N_3 ring); **ESI-LRMS** (+) *m/z* 1033 $[M+H]^+$; **ESI-HRMS** (+) calc. for $[C_{55}H_{67}N_6O_{10}P_2]^+$ 1033.440, found 1033.444.

[Eu.L^1]

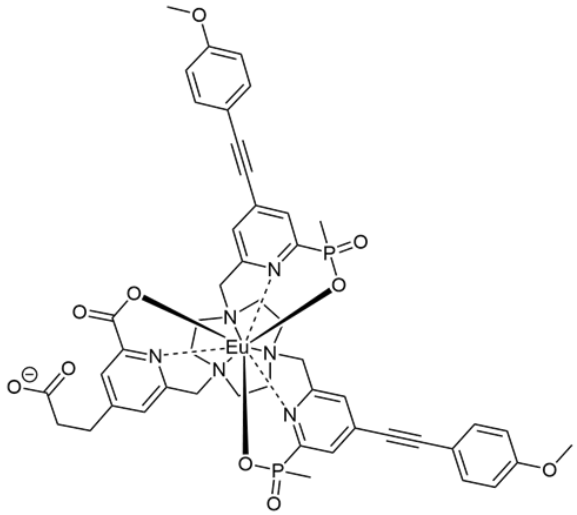

The crude ligand (58 mg) from the previous step, **L^1**, was dissolved in a mixture of MeOH/water (4:1, 3 mL total) and the pH was adjusted to 12 using aqueous NaOH solution. The solution was heated at 60 °C for 8 h. The complete hydrolysis of the phosphinate and carboxylic acid ester groups was confirmed by LC/MS analysis. After cooling and adjustment of the pH to 6.5 using aqueous HCl, $EuCl_3 \cdot 6H_2O$ (23 mg, 0.063 mmol) was added. The reaction mixture was heated to 60 °C for 18 h. The solvent was evaporated under reduced pressure to afford a white solid residue. The crude residue was purified by reverse-phase HPLC (10 to 100% MeCN in H_2O over 10 min, t_r = 9.6 min) to yield a white solid (17.5 mg, 29%); **ESI-LRMS** (+) *m/z* 1083 $[M+H]^+$; **ESI-HRMS** (+) calc. for $[C_{48}H_{49}{}^{151}EuN_6O_{10}P_2]^+$ 1083.226, found 1083.229; $\boldsymbol{\tau_{MeOH}}$ (ms) = 1.20, $\boldsymbol{\tau_{H2O}}$ (ms) = 1.00, $\boldsymbol{\tau_{D2O}}$ (ms) = 1.24, $\boldsymbol{\Phi_{MeOH}}$ = 34%, $\boldsymbol{\Phi_{D2O}}$ = 21%. NMR spectra not assigned due to the paramagnetic shift induced by the lanthanide ion.

[Eu.L^1]^a

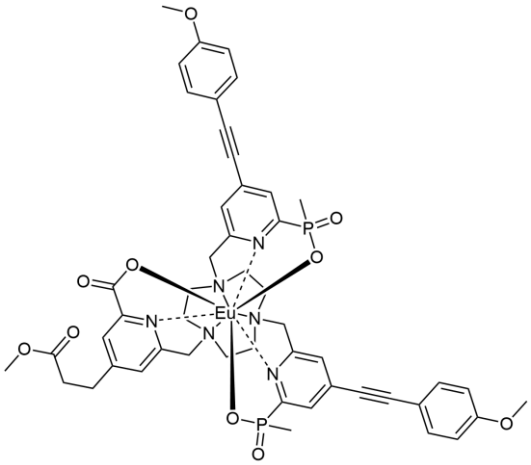

[Eu.L^1] (5.0 mg, 4.6 µmol) was dissolved in anhydrous MeOH (1 mL). A drop of acetyl chloride was added and the mixture stirred under argon at room temperature for 18 h. The solvent was removed under reduced pressure to afford a white solid (1.7 mg, 34%); **ESI-LRMS** (+) *m/z* 550 $[M+2H]^{2+}$. NMR spectra not assigned due to the paramagnetic shift induced by the lanthanide ion.

[Eu.L^1]^b

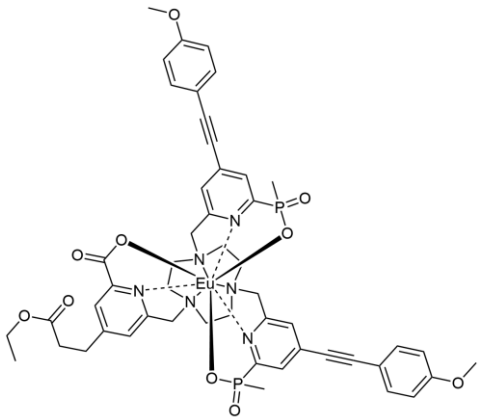

[Eu.L^1] (3.0 mg, 2.8 µmol) was dissolved in anhydrous EtOH (1 mL). A drop of acetyl chloride was added and the mixture stirred under argon at room temperature for 18 h. The solvent was evaporated under reduced pressure to afford a white solid (quant.); **ESI-LRMS** (+) *m/z* 1113 $[M+H]^+$; **ESI-HRMS** (+) calc. for $[C_{50}H_{54}{}^{151}EuN_6O_{10}P_2]^+$ 1113.260, found 1113.255. NMR spectra not assigned due to the paramagnetic shift induced by the lanthanide ion.

6-Methylpyridine-N-oxide-2-carboxylic acid, 33

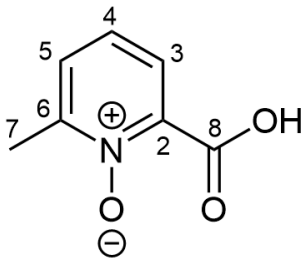

Compound **33** was prepared using a reported procedure.[121] 6-Methylpyridine-2-carboxylic acid (3.76 g, 27.4 mmol) was dissolved in anhydrous MeCN (6 mL). *m*-CPBA (9.16 g, 53.1 mmol) was added and the solution was stirred at 65 °C for 18 h under argon. Solvents were removed to afford pale-yellow crystals purified by flash column chromatography (50 to 100% EtOAc in) to yield a white solid (983 mg, 24%); **^{1}H NMR** (400 MHz, $CDCl_3$) δ 8.38 – 8.32 (1H, m, H^3), 7.63 – 7.65 (2H, m, H^4 + H^5), 2.66 (3H, s, H^7); **^{13}C NMR** (100 MHz, $CDCl_3$) δ 161.8, 149.4, 137.2, 130.1, 129.9, 127.4, 17.8; **ESI-LRMS** (+) *m/z* 154 $[M+H]^+$.

6-Methyl-4-nitropyridine-N-oxide-2-carboxylic acid, 34

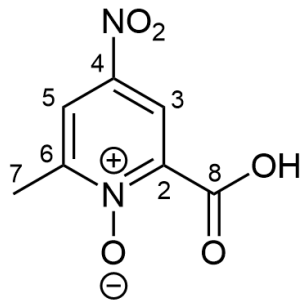

Compound **34** was prepared using a reported procedure.[121] Compound **33** (983 mg, 6.42 mmol) was dissolved in concentrated H_2SO_4 (53 mL) at 0 °C, to which concentrated HNO_3 (48 mL) was added slowly. The mixture was refluxed at 100 °C for 66 h after which ice (250 g) was added and the mixture was stirred for a further 2 h at 0 °C. The mixture was extracted with DCM (5 x 70 mL). Combined organic layers were dried on Na_2SO_4, filtered, and evaporated to afford a green solid, used in the next step without further purification (925 mg, 73%); **^{1}H NMR** (400 MHz, $CDCl_3$) δ 9.07 (1H, d, $^4J_{H\text{-}H}$ 3.0, H^3), 8.36 (1H, d, $^4J_{H\text{-}H}$ 3.0, H^5), 2.74 (3H, s, H^7); **^{13}C NMR** (100 MHz, $CDCl_3$) δ 159.5, 152.4, 144.5, 138.7, 123.1, 121.7, 18.4; **ESI-LRMS** (+) *m/z* 199 $[M+H]^+$.

2-Ethoxycarbonyl-6-methyl-4-nitropyridine-N-oxide, 35

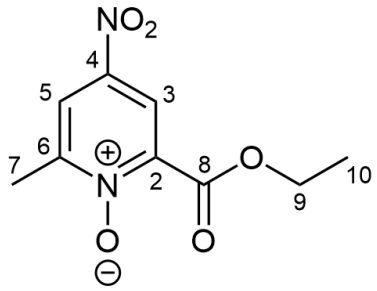

Compound **35** was prepared using a reported procedure.[121] Compound **6** (251 mg, 1.27 mmol) was dissolved in anhydrous EtOH (100 mL) with a catalytic amount of concentrated H_2SO_4 (0.5 mL). The solution was stirred under argon at 65 °C for 72 h. Solvents were removed under reduced pressure and the residue was dissolved in EtOAc (70 mL). The organic layer was washed with 4% aqueous $NaHCO_3$ (2 x 70 mL) and with brine (1 x 70 mL). The organic layer was dried over Na_2SO_4, filtered, and the solvent was removed under reduced pressure to give a yellow solid, used in the next step without further purification (181 mg, 63%); **^{1}H NMR** (400 MHz, $CDCl_3$) δ 8.31 (1H, d, $^4J_{H\text{-}H}$ 3.0, H^3), 8.18 (1H, d, $^4J_{H\text{-}H}$ 3.0, H^5), 4.50 (2H, q, $^3J_{H\text{-}H}$ 7.1, H^9), 2.58 (3H, s. H^7), 1.44 (3H, t, $^4J_{H\text{-}H}$ 7.1, H^{10}); **^{13}C NMR** (100 MHz, $CDCl_3$) δ 160.3, 152.6, 142.5, 140.5, 121.2, 119.0, 63.4, 18.3, 14.2; **ESI-LRMS** (+) *m/z* 227 $[M+H]^+$.

Ethyl 6-(hydroxymethyl)-4-nitropicolinate, 36

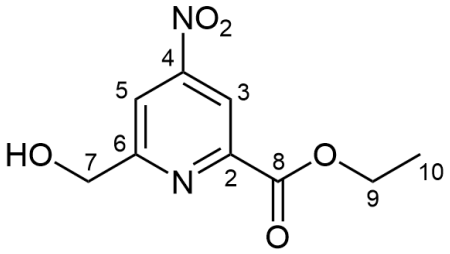

Compound **36** was prepared using a reported procedure.[121] Compound **7** (291 mg, 1.29 mmol) was dissolved in anhydrous chloroform (9 mL) under argon. Trifluoroacetic anhydride (4.5 mL, 32 mmol) was added and the solution was stirred at 60 °C for 4 h. The solvent was evaporated, and the residue was dissolved in 1:1 EtOH/water (30 mL), and stirred at room temperature for 18 h. Solvents were removed under reduced pressure, and the residue was dissolved in water (20 mL) and extracted with DCM (3 x 20 mL). The organic layers were combined, dried over Na_2SO_4, filtered, and the solvent was removed under reduced pressure to yield the product as an orange

crystalline solid (189 mg, 65%); **^{1}H NMR** (600 MHz, $CDCl_3$) δ 8.64 (1H, d, $^{4}J_{H\text{-}H}$ 2.0, H^{3}), 8.34 (1H, d, $^{4}J_{H\text{-}H}$ 2.0, H^{5}), 5.02 (2H, s, H^{7}), 4.51 (2H, q, $^{3}J_{H\text{-}H}$ 7.1, H^{9}), 3.60-3.10 (1H, br, OH), 1.45 (3H, t, $^{3}J_{H\text{-}H}$ 7.1, H^{10}); **^{13}C NMR** (150 MHz, $CDCl_3$) δ 164.8 (C^{4}), 163.4 (C^{8}), 155.5 (C^{2}), 150.3 (C^{6}), 116.5 (C^{3}), 116.4 (C^{5}), 64.8 (C^{7}), 63.0 (C^{9}), 14.4 (C^{10}); **ESI-LRMS** (+) *m/z* 227 $[M+H]^{+}$.

Ethyl 6-(((methylsulfonyl)oxy)methyl)-4-nitropicolinate, 37

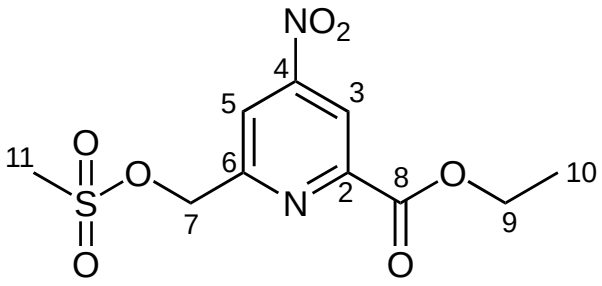

Compound **37** was prepared by adapting a reported procedure.[121] Compound **36** (61.5 mg, 0.272 mmol) was dissolved in anhydrous THF (3 mL) and DIEA (0.15 mL, 0.86 mmol) was added under argon at r.t. Methanesulfonic anhydride (94.6 mg, 0.543 mmol) was added, and the reaction was stirred at r.t. for 50 min, monitored by TLC (2% MeOH in DCM, $\mathbf{R_f}$ = 0.6). The solvent was removed under reduced pressure and the resulting orange crystals were dissolved in DCM (50 mL) and washed with water (3 x 50 mL). The aqueous layers were combined and extracted with DCM (2 x 50 mL). The organic layers were combined, dried over Na_2SO_4, and the solvent was removed under reduced pressure. The residue was dried *in vacuo* to yield an orange oil used in the next step without further purification (74.2 mg, 90%); **^{1}H NMR** (400 MHz, $CDCl_3$) δ 8.75 (1H, d, $^{4}J_{H\text{-}H}$ 2.0, H^{3}), 8.38 (1H, d, $^{4}J_{H\text{-}H}$ 2.0, H^{5}), 5.55 (2H, s, H^{7}), 4.54 (2H, q, $^{3}J_{H\text{-}H}$ 7.0, H^{9}), 3.24 (3H, s, H^{11}), 1.47 (3H, t, $^{3}J_{H\text{-}H}$ 7.0, H^{10}); **^{13}C NMR** (101 MHz, $CDCl_3$) δ 162.9 (C^{4}), 158.3 (C^{8}), 155.7 (C^{2}), 151.1 (C^{6}), 116.5 (C^{3}), 116.4 (C^{5}), 64.8 (C^{7}), 63.0 (C^{9}), 38.4 (C^{11}), 14.4 (C^{10}); **ESI-LRMS** (+) *m/z* 305 $[M+H]^{+}$.

Di-*tert*-butyl 7-((6-(ethoxycarbonyl)-4-nitropyridin-2-yl)methyl)-1,4,7-triazacyclononane-1,4-dicarboxylate, 39

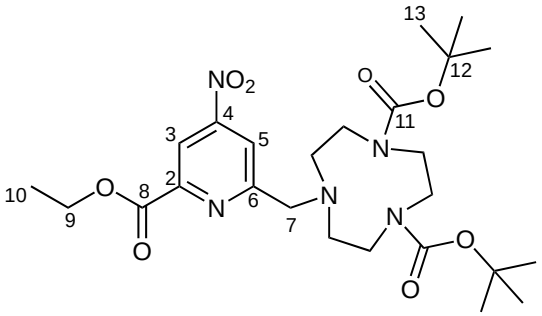

Compound **39** was synthesised as reported.[18] Compound **37** (74.3 mg, 0.244 mmol) and compound **38** (69.0 mg, 0.188 mmol) were dissolved in anhydrous MeCN (3 mL) and K_2CO_3 (69 mg, 0.50 mmol) was added under argon. The reaction was stirred under argon at r.t. for 18 h. The inorganic salts were removed by centrifugation and the solvent was removed under reduced pressure. The residue was dried *in vacuo* to yield an orange oil (67.4 mg, 67%, mixture of conformers). **^{1}H NMR** (600 MHz, $CDCl_3$) δ 8.60 (0.6H, d, $^4J_{H\text{-}H}$ 2.0, H^3, isomer A), 8.59 (0.4H, d, $^4J_{H\text{-}H}$ 2.0, H^3, isomer B), 8.48 (0.6H, d, $^4J_{H\text{-}H}$ 2.0, H^5, isomer A), 8.46 (0.4H, d, $^4J_{H\text{-}H}$ 2.0, H^5, isomer B) 4.51 (2H, 2 × q,$^3J_{H\text{-}H}$ 7.0, H^9, isomers A and B), 4.08 (2H, s, H^7), 1.49 – 1.40 (m, 21H, H^{10} + H^{13}, isomers A and B); **ESI-LRMS** (+) *m/z* 539 $[M+H]^+$; **ESI-HRMS** (+) calc. for $[C_{25}H_{40}N_5O_8]^+$ 538.2877, found 538.2866.

Ethyl 6-((1,4,7-Triazacyclononan-1-yl)methyl)-4-nitropicolinate *Bis*-trifluoroacetate salt, 40

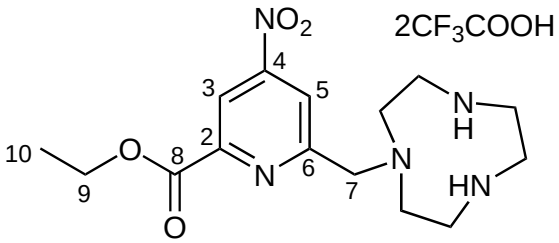

Compound **39** (67.4 mg, 0.125 mmol) was dissolved in TFA and DCM (20% V/V, 5 mL total) and the solution was stirred at r.t. under argon for 75 min. The solvent was removed under reduced pressure and the remaining TFA co-evaporated with DCM (4 × 15 mL) to afford compound **40** as its trifluoroacetate salt as an orange oil (70.0 mg, quant.); **ESI-LRMS** (+) *m/z* 338 $[M+H]^+$; **ESI-HRMS** (+) calc. for $[C_{15}H_{24}N_5O_4]^+$ 338.1828, found 338.1843.

Ethyl 6-(hydroxymethyl)-4-[4-(1-methoxy-3-methylphenyl)ethynyl]pyridine-2-carboxylate, 31

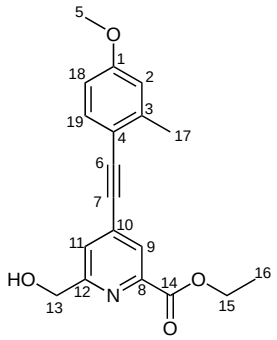

Compound **2** (421 mg, 1.62 mmol) and 1-ethynyl-4-methoxy-2-methylbenzene (269 mg, 1.84 mmol) were dissolved in anhydrous THF (8 mL). The solution was degassed using 3 × freeze-pump-thaw cycles. NEt_3 (1.2 mL, 8.6 mmol) was added and the solution was degassed again using a further freeze-pump-thaw cycle. $Pd(dppf)Cl_2$.DCM (136mg, 0.166 mmol) and copper(I) iodide (80.1 mg, 0.421 mmol) were added under argon at r.t. to form a brown solution that was stirred at 65 °C for 21 h. The solvent was removed under reduced pressure before the residue was dissolved in DCM (50 mL) and washed with H_2O (4 × 50 mL). The aqueous layers were combined and extracted with DCM (3 x 30 mL) before the organic layers were all combined and dried over Mg_2SO_4. The solution was filtered, and DCM was removed under reduced pressure to afford the crude product as a brown residue. The residue was purified by reverse-phase HPLC (10 to 100% MeCN in H_2O over 10 min, t_R = 11.8 min) to yield a brown oil (196 mg, 37%); **^{1}H NMR** (600 MHz, $CDCl_3$) δ 8.03 (1H, s, H^9), 7.57 (1H, s, H^{11}), 7.44 (1H, d, $^3J_{H\text{-}H}$ 8.4, H^{19}), 6.78 (1H, s, H^2), 6.73, (1H, d, $^3J_{H\text{-}H}$ 8.4, H^{18}), 4.85 (2H, s, H^{13}), 4.46 (2H, q, $^3J_{H\text{-}H}$ 7.0, H^{15}), 3.81 (3H, s, H^5), 3.78 – 3.63 (1H, br s, OH), 2.49 (3H, s, H^{17}), 1.43 (3H, t, $^3J_{H\text{-}H}$ 7.0, H^{16}); **^{13}C NMR** (150 MHz, $CDCl_3$) δ 164.9 (C^{14}), 160.7 (C^{12}), 160.6 (C^1), 147.5 (C^8), 142.9 (C^3), 134.1 (C^{19}), 134.0 (C^{10}), 125.5 (C^9), 125.2 (C^{11}), 115.4 (C^2), 113.8 (C^4), 111.7 (C^{18}), 94.9 (C^6), 89.1 (C^7), 64.6 (C^{13}), 62.2 (C^{15}), 55.4 (C^5), 21.1 (C^{17}), 14.4 (C^{16}); **ESI-LRMS** (+) *m/z* 326 $[M+H]^+$; **ESI-HRMS**[a] (+) calc. for $[C_{19}H_{20}NO_4]^+$ 326.1392, found 326.1400.

Ethyl 6-[(methanesulfonyloxy)methyl]-4-[4-(1-methoxy-3-methylphenyl)ethynyl]pyridine-2-carboxylate, 32

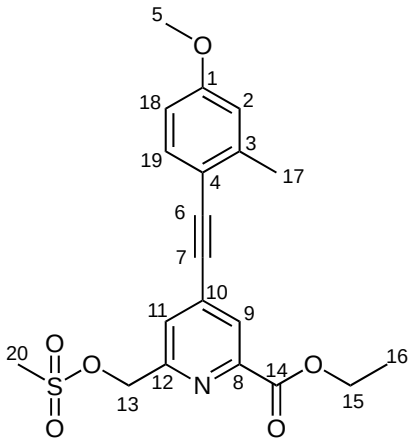

Compound **31** (153 mg, 0.470 mmol) was dissolved in anhydrous THF (3 mL) and DIEA (0.21 mL, 1.2 mmol) was added under argon. Methanesulfonic anhydride (165 mg, 0.947 mmol) was added, and the reaction was stirred at r.t. under argon for 1 h, monitored by TLC (3% MeOH in DCM, $\mathbf{R_f}$ = 0.8). The solvent was removed under reduced pressure and the residue was dissolved in DCM (50 mL) and washed with water (3 x 50 mL), before the aqueous layers were combined and extracted with DCM (2 x 50 mL). The organic layers were combined, dried over Na_2SO_4, and the DCM was removed under reduced pressure. The residue was dried *in vacuo* to yield a brown oil (166 mg, 88%,); **^{1}H NMR** (400 MHz, $CDCl_3$) δ 8.12 (1H, s, H^9), 7.68 (1H, s, H^{11}), 7.47 (1H, d, $^3J_{H\text{-}H}$ 8.4, H^{19}), 6.79 (1H, s, H^2), 6.75, (1H, d, $^3J_{H\text{-}H}$ 8.4, H^{18}), 5.42 (2H, s, H^{13}), 4.49 (2H, q, $^3J_{H\text{-}H}$ 7.1, H^{15}), 3.83 (3H, s, H^5), 3.19 (3H, s, H^{20}), 2.51 (3H, s, H^{17}), 1.44 (3H, t, $^3J_{H\text{-}H}$ 7.1, H^{16}); **ESI-LRMS** (+) *m/z* 404 $[M+H]^+$.

Ethyl 6-((4,7-*Bis*((6-(ethoxycarbonyl)-4-((4-methoxy-2-methylphenyl)ethynyl)pyridin-2-yl)methyl)-1,4,7-triazacyclononan-1-yl)methyl)-4-nitropicolinate, *pro*-L^{5}

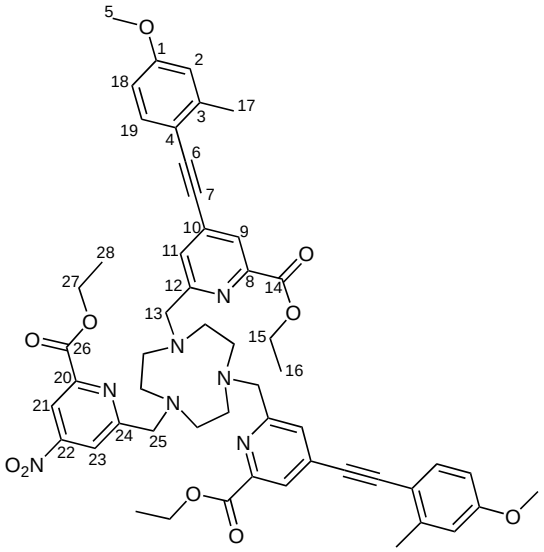

Compound **32** (128 mg, 0.317 mmol) and compound **40** (70.0 mg, 0.124 mmol) were dissolved in anhydrous MeCN (3 mL) and K_2CO_3 (69 mg, 0.50 mmol) was added under Ar. The reaction was stirred under argon at r.t. for 18 h. The inorganic salts were removed by centrifugation and the solvent was removed to yield a dark orange residue (85.0 mg 72%); **^{1}H NMR** (600 MHz, $CDCl_3$) δ 8.11 (2H, s, H^{9}), 8.04 (1H, s, H^{21}), 7.67 (2H, s, H^{11}), 7.56 (1H, s, H^{23}), 7.46 (2H, d, $^{3}J_{H\text{-}H}$ 8.3, H^{19}), 6.79 (2H, d, $^{4}J_{H\text{-}H}$ 2.3, H^{2}), 6.74 (2H, dd, $^{3}J_{H\text{-}H}$ 8.3, $^{4}J_{H\text{-}H}$ 2.3, H^{18}), 5.41 (3H, s, H^{25}), 5.29 (6H, s, H^{13}), 4.47 (4H + 2H, q, $^{3}J_{H\text{-}H}$ 7.0, H^{15} + H^{27}), 3.82 (6H, s, H^{5}), 3.18 (6H, s, H^{17}) 2.53 – 2.40 (12H, m, TACN ring), 1.43 (6H + 3H, t, $^{3}J_{H\text{-}H}$ 7.0, H^{16} + H^{28}); **^{13}C NMR** (150 MHz, $CDCl_3$) δ 164.9 (C^{22}), 164.5 (C^{14} + C^{26}), 160.9 (C^{1}), 160.7 (C^{12}), 154.6 (C^{20}), 148.3 (C^{8}), 147.6 (C^{24}), 143.0 (C^{3}), 134.8 (C^{10}), 134.1 (C^{19}), 126.6 (C^{9}), 126.3 (C^{11}), 125.5 (C^{21}), 125.1 (C^{23}), 115.5 (C^{2}), 113.6 (C^{4}), 111.8 (C^{18}), 96.0 (C^{6}), 88.7 (C^{7}), 71.0 (C^{25}), 63.6 (C^{13}), 62.4 (C^{15} + C^{27}), 55.4 (C^{5}), 38.3 (C^{17}), 21.1 (3 x s, TACN ring), 14.4 (C^{16} + C^{28}); **ESI-LRMS** (+) *m/z* 953 $[M+H]^+$; **ESI-HRMS** (+) calc. for $[C_{53}H_{58}N_7O_{10}]^+$ 952.4245, found 952.4230.

Ethyl 6-((4,7-*Bis*((6-(carboxylic acid)-4-((4- methoxy-2-methylphenyl)ethynyl)pyridin-2-yl)methyl)- 1,4,7-triazacyclononan-1-yl)methyl)-4-nitropicolinate, 41

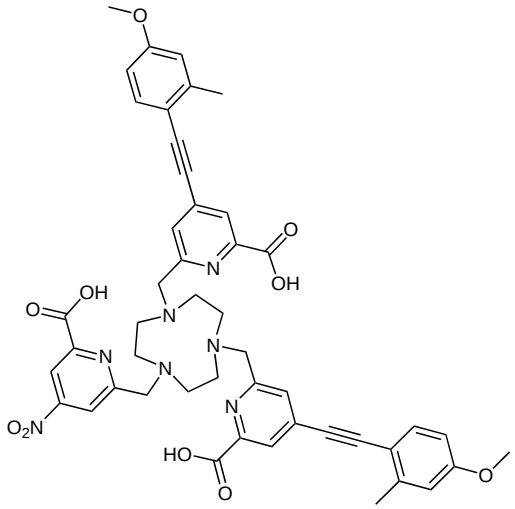

Compound ***pro*-L^{1}** (85.0 mg, 0.0893 mmol) was dissolved in MeCN and H_2O (50% V/V). The pH was adjusted to 12 with NaOH solution and stirred at r.t. for 60 h. Monitoring by LCMS showed the formation of compound **41**, which was used in a same-pot reaction during the next step; **ESI-LRMS** (+) *m/z* 869 $[M+H]^+$.

[Eu.L^{5}]

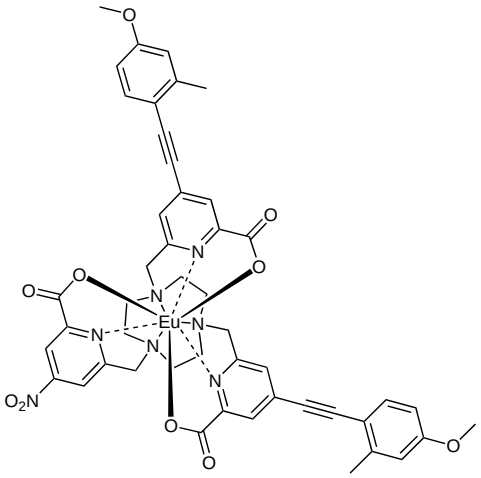

The MeCN/H_2O solution containing compound **41** was adjusted to pH 6 using HCl solution and europium chloride hexahydrate (100 mg, 0.274 mmol) was added. The solution was stirred at r.t. for 48 h, after which the solvent was removed under reduced pressure to yield the crude product as a pale-yellow solid. The residue was purified by HPLC (10 to 100% MeCN in H_2O over 10 min, t_R = 10.8 min) to yield **[Eu.L^{5}]** as a white solid (46.7 mg, 51% over two steps); **ESI-LRMS** (+) *m/z* 1018 $[M+H]^+$; **ESI-HRMS** (+)

calc. for $[C_{47}H_{43}EuN_7O_{10}]^+$ 1018.229, found 1018.229. NMR spectra not assigned due to the paramagnetic shift induced by the lanthanide ion.

[Eu.L^{5b}]

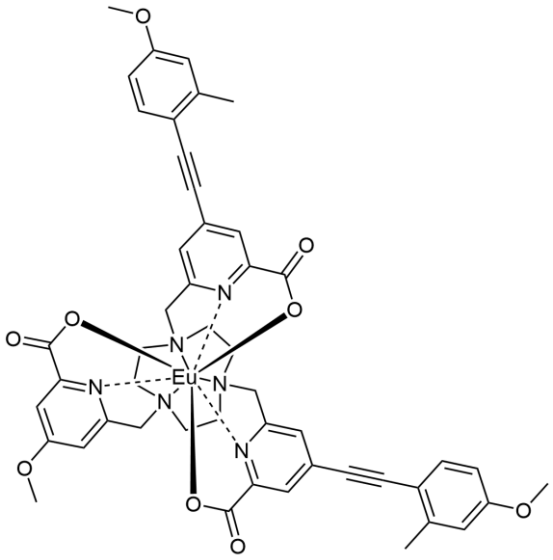

Freshly cut Na metal (50 mg, 2.2 mmol) was dissolved under argon in anhydrous MeOH (1 mL). The resulting sodium methoxide solution in MeOH was transferred to a suspension of **[Eu.L^5]** (2.7 mg, 0.003 mmol) in MeOH (2 mL) under argon. The cloudy suspension of the complex becomes clear upon addition of the sodium methoxide solution. LC/MS analysis revealed complete conversion after 15 minutes; **ESI-LRMS** (+) *m/z* 1001 $[M+H]^+$; **ESI-HRMS** (+) calc. for $[C_{48}H_{46}{}^{151}EuN_6O_9]^+$ 1001.255, found 1001.254. NMR spectra not assigned due to the paramagnetic shift induced by the lanthanide ion.

2^{A}

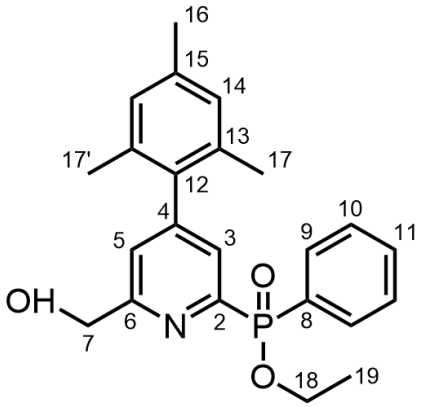

Compound **1** (234 mg, 0.656 mmol), trimethyl phenylboronic acid (304 mg, 1.85 mmol), and Cs_2CO_3 (556 mg, 1.71 mmol) were dissolved in anhydrous DMF (3 mL) and degassed with Ar for 15 minutes. $Pd(dppf)Cl_2 \cdot DCM$ (101 mg, 0.123 mmol) was added and the solution stirred at 90 °C. LC/MS analysis revealed complete conversion after 48 h. The reaction mixture was diluted in EtOAc (150 mL) and washed with 10% LiCl w/w in water (5 × 40 mL). The organic layer was dried over Na_2SO_4, filtered, and evaporated to afford a black residue that was purified via reverse phase HPLC in MeCN/water to afford the product (151 mg, 58%); **^{1}H NMR** (600 MHz, $CDCl_3$) δ 7.98 (2H, dd, $^{3}J_{P\text{-}H}$ 12, $^{3}J_{H\text{-}H}$ 8, H^{9}), 7.82 (1H, d, $^{3}J_{P\text{-}H}$ 6, H^{3}), 7.56 (1H, t, $^{3}J_{H\text{-}H}$ 8, H^{11}), 7.49 (2H, td, $^{3}J_{H\text{-}H}$ 4, $^{3}J_{H\text{-}H}$ 8, H^{10}), 7.13 (1H, s, H^{5}), 6.94 (2H, d, $^{4}J_{H\text{-}H}$ 6, H^{14}), 4.80 (2H, s, H^{7}), 4.17 (2H, app. qui, $^{3}J_{H\text{-}H}$ 7, H^{18}), 2.32 (3H, s, H^{16}), 1.98-1.93 (3H + 3H, s, H^{17} + $H^{17'}$), 1.37 (3H, t, $^{3}J_{H\text{-}H}$ 7, H^{19}); **ESI-LRMS** (+) *m/z* 396 $[M+H]^{+}$; **ESI-HRMS** (+) calc. for $[C_{23}H_{27}NO_3P]^{+}$ 396.1729, found 396.1726.

3^{A}

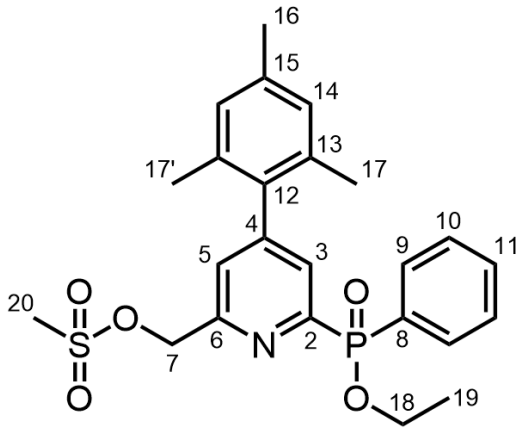

Compound **2^{A}** (150 mg, 0.38 mmol) was dissolved in anhydrous THF (1.2 mL). Anhydrous DIEA (0.18 mL, 0.95 mmol) followed by Ms_2O (130 mg, 0.76 mmol) were added. The reaction was monitored via TLC (3% MeOH in DCM) and stopped after 1 h. Solvents were evaporated under reduced pressure, the residue dissolved in DCM and washed with water (3×). The combined aqueous layer was re-extracted with DCM (2×) and the combined organic layer was dried over Na_2SO_4, filtered, evaporated, and used in the next step without further purification; **^{1}H NMR** (400 MHz, $CDCl_3$) *δ* 7.98 (dd), 7.89 (d), 7.59 (t), 7.51 (m), 7.37 (s), 6.97 (s), 5.40 (s), 5.31 (s), 4.19 (m), 3.02 (s), 2.34 (s), 1.98 (d), 1.39 (t), 1.27 (s), 1.09 (m); **ESI-LRMS** (+) *m/z* 474 $[M+H]^+$; **ESI-HRMS** (+) calc. for $[C_{24}H_{29}NO_5PS]^+$ 474.1504, found 474.1501.

L^{A}

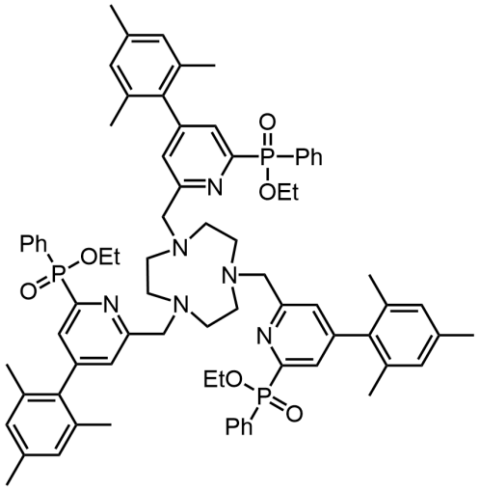

Compound **3^{A}**, TACN·3HCl (25.8 mg, 0.108 mmol), and K_2CO_3 (105 mg, 0.758 mmol) were added to anhydrous MeCN (2 mL) under Ar and stirred at 60 °C for 18 h. The reaction mixture was centrifuged, and the solid residue washed several times with fresh MeCN. The solvent was evaporated to afford a brown residue that was used in the next step without further purification; **^{1}H NMR** (600 MHz, $CDCl_3$) *δ* 7.93 (6H, dd), 7.70 (3H, d), 7.41 (3H, t), 7.34 (6H, m), 7.24 (3H, s), 6.87 (6H, d), 4.10 (6H, m), 3.76 (6H, s), 2.62 (9H, s), 2.29 (9H, s), 1.96 (3H, s), 1.89 (9H, t), 1.84 (9H, t), 1.28 (9H, t); **ESI-LRMS** (+) *m/z* 1262 $[M+H]^+$; **ESI-HRMS** (+) calc. 1261.598, found 1261.600.

[Tb.L^{A}]

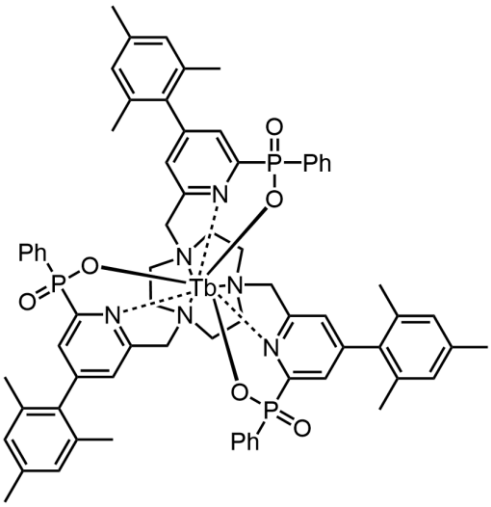

The crude ligand (150 mg) from the previous step, **L^{A}**, was dissolved in a mixture of MeOH/water (4:1, 3 mL total) and the pH was adjusted to 12 using aqueous NaOH solution. The solution was heated at 60 °C for 8 h. The complete hydrolysis of the phosphinate and carboxylic acid ester groups was confirmed by LC/MS analysis. After cooling and adjustment of the pH to 6.5 using aqueous HCl, $TbCl_3 \cdot 6H_2O$ (41 mg, 0.11 mmol) was added. The reaction mixture was heated to 60 °C for 18 h. The solvent was evaporated under reduced pressure to afford a solid residue. The crude residue was purified by reverse-phase HPLC in MeOH/water to yield a white solid (78 mg, 57%); **ESI-LRMS** (+) *m/z* 1333 $[M+H]^+$; **ESI-HRMS** (+) calc. 1333.411, found 1333.406. NMR spectra not assigned due to the paramagnetic shift induced by the lanthanide ion.

References

(1) Kasha, M. Characterization of Electronic Transitions in Complex Molecules. *Discuss. Faraday Soc.* **1950**, *9* (0), 14–19. https://doi.org/10.1039/DF9500900014.

(2) Mitschke, U.; Bäuerle, P. The Electroluminescence of Organic Materials. *J. Mater. Chem.* **2000**, *10* (7), 1471–1507. https://doi.org/10.1039/a908713c.

(3) Ono, Y. A. *Electroluminescence in Encyclopedia of Applied Physics*; G. L. Trigg, VCH, Weinheim, 1993.

(4) Sano, M.; Pope, M.; Kallmann, H. Electroluminescence and Band Gap in Anthracene. *J. Chem. Phys.* **1965**, *43* (8), 2920–2921. https://doi.org/10.1063/1.1697243.

(5) Baldo, M. A.; Thompson, M. E.; Forrest, S. R. *Phosphorescent Materials for Application to Organic Light Emitting Devices, vol 71, n 11, pp 2095-2106, 1999, doi.org/10.1351/pac199971112095*

(6) Kunić, S.; Šego, Z. OLED Technology and Displays. In *Proceedings ELMAR-2012*; 2012; pp 31–35.

(7) Bünzli, J.-C. G. Lanthanide Luminescence for Biomedical Analyses and Imaging. *Chem. Rev.* **2010**, *110* (5), 2729–2755. https://doi.org/10.1021/cr900362e.

(8) Monteiro, J. H. S. K. Recent Advances in Luminescence Imaging of Biological Systems Using Lanthanide(III) Luminescent Complexes. *Molecules* **2020**, *25* (9), 2089. https://doi.org/10.3390/molecules25092089.

(9) Carnall, W. T. Chapter 24 The Absorption and Fluorescence Spectra of Rare Earth Ions in Solution. In *Handbook on the Physics and Chemistry of Rare Earths*; Non-metallic Compounds - I; Elsevier, 1979; Vol. 3, pp 171–208. https://doi.org/10.1016/S0168-1273(79)03007-5.

(10) Tanner, P. A.; Zhou, L.; Duan, C.; Wong, K.-L. Misconceptions in Electronic Energy Transfer: Bridging the Gap between Chemistry and Physics. *Chem. Soc. Rev.* **2018**, *47* (14), 5234–5265. https://doi.org/10.1039/C8CS00002F.

(11) Jha, A.; Richards, B.; Jose, G.; Teddy-Fernandez, T.; Joshi, P.; Jiang, X.; Lousteau, J. Rare-Earth Ion Doped TeO2 and GeO2 Glasses as Laser Materials. *Prog. Mater. Sci.* **2012**, *57* (8), 1426–1491. https://doi.org/10.1016/j.pmatsci.2012.04.003.

(12) Yanagida, T. Study of Rare-Earth-Doped Scintillators. *Opt. Mater.* **2013**, *35* (11), 1987–1992. https://doi.org/10.1016/j.optmat.2012.11.002.

(13) Poole, S.; Payne, D.; Mears, R.; Fermann, M.; Laming, R. Fabrication and Characterization of Low-Loss Optical Fibers Containing Rare-Earth Ions. *J. Light. Technol.* **1986**, *4* (7), 870–876. https://doi.org/10.1109/JLT.1986.1074811.

(14) New, E. J.; Parker, D.; Smith, D. G.; Walton, J. W. Development of Responsive Lanthanide Probes for Cellular Applications. *Curr. Opin. Chem. Biol.* **2010**, *14* (2), 238–246. https://doi.org/10.1016/j.cbpa.2009.10.003.

(15) Starck, M.; Fradgley, J. D.; Di Vita, S.; Mosely, J. A.; Pal, R.; Parker, D. Targeted Luminescent Europium Peptide Conjugates: Comparative Analysis Using Maleimide and *Para*- Nitropyridyl Linkages for Organelle Staining. *Bioconjug. Chem.* **2020**, *31* (2), 229–240. https://doi.org/10.1021/acs.bioconjchem.9b00735.

(16) Heffern, M. C.; Matosziuk, L. M.; Meade, T. J. Lanthanide Probes for Bioresponsive Imaging. *Chem. Rev.* **2014**, *114* (8), 4496–4539. https://doi.org/10.1021/cr400477t.

(17) Parker, D.; Fradgley, J. D.; Wong, K.-L. The Design of Responsive Luminescent Lanthanide Probes and Sensors. *Chem. Soc. Rev.* **2021**, https://doi.org/10.1039/D1CS00310K.

(18) Starck, M.; Fradgley, J. D.; Vita, S. D.; Mosely, J. A.; Pal, R.; Parker, D. Targeted Luminescent Europium Peptide Conjugates: Comparative Analysis Using Maleimide and Para-Nitropyridyl Linkages for Organelle Staining. *Bioconjug. Chem.* **2020,** 31, 2, 229-240. https://doi.org/10.1021/acs.bioconjchem.9b00735.

(19) Főrster, Th. 10th Spiers Memorial Lecture. Transfer Mechanisms of Electronic Excitation. *Discuss Faraday Soc* **1959**, *27* (0), 7–17. https://doi.org/10.1039/DF9592700007.

(20) Dexter, D. L. A Theory of Sensitized Luminescence in Solids. *J. Chem. Phys.* **1953**, *21* (5), 836–850. https://doi.org/10.1063/1.1699044.
(21) D'Aléo, A., Pointillart, F., Ouahab, L., Andraud, C., Maury, O., *Charge transfer excited states sensitization of lanthanide emitting from the visible to the near-infra-red, Coordination Chemistry Reviews, 256, 15–16,2012,pp 1604-1620,* https://doi.org/10.1016/j.ccr.2012.03.023.
(22) Soulié, M.; Latzko, F.; Bourrier, E.; Placide, V.; Butler, S. J.; Pal, R.; Walton, J. W.; Baldeck, P. L.; Le Guennic, B.; Andraud, C.; Zwier, J. M.; Lamarque, L.; Parker, D.; Maury, O. Comparative Analysis of Conjugated Alkynyl Chromophore–Triazacyclononane Ligands for Sensitized Emission of Europium and Terbium. *Chem. – Eur. J.* **2014**, *20* (28), 8636–8646. https://doi.org/10.1002/chem.201402415.
(23) Szabo, A.; Ostlund, N. S. *Modern Quantum Chemistry: Introduction to Advanced Electronic Structure Theory*; Courier Corporation, 2012.
(24) Richardson, F. S. Selection Rules for Lanthanide Optical Activity. *Inorg. Chem.* **1980**, *19* (9), 2806–2812. https://doi.org/10.1021/ic50211a063.
(25) Bünzli, J.-C. G. On the Design of Highly Luminescent Lanthanide Complexes. *Coord. Chem. Rev.* **2015**, *293–294*, 19–47. https://doi.org/10.1016/j.ccr.2014.10.013.
(26) Cotton, S. *Lanthanide and Actinide Chemistry*; John Wiley & Sons, 2024.
(27) Seitz, M.; Moore, E. G.; Ingram, A. J.; Muller, G.; Raymond, K. N. Enantiopure, Octadentate Ligands as Sensitizers for Europium and Terbium Circularly Polarized Luminescence in Aqueous Solution. *J. Am. Chem. Soc.* **2007**, *129* (50), 15468–15470. https://doi.org/10.1021/ja076005e.
(28) Petoud, S.; Muller, G.; Moore, E. G.; Xu, J.; Sokolnicki, J.; Riehl, J. P.; Le, U. N.; Cohen, S. M.; Raymond, K. N. Brilliant Sm, Eu, Tb, and Dy Chiral Lanthanide Complexes with Strong Circularly Polarized Luminescence. *J. Am. Chem. Soc.* **2007**, *129* (1), 77–83. https://doi.org/10.1021/ja064902x.
(29) Alpha, B.; Ballardini, R.; Balzani, V.; Lehn, J.-M.; Perathoner, S.; Sabbatini, N. Antenna Effect in Luminescent Lanthanide Cryptates: A Photophysical Study. *Photochem. Photobiol.* **1990**, *52* (2), 299–306. https://doi.org/10.1111/j.1751-1097.1990.tb04185.x.
(30) De Rosa, D. F.; Starck, M.; Parker, D.; Pal, R. Unlocking Same-Sign CPL: Solvent Effects on Spectral Form and Racemisation Kinetics in Nine-Coordinate Chiral Europium(III) Complexes. *Chem. – Eur. J. n/a* (n/a), e202303227. https://doi.org/10.1002/chem.202303227.
(31) Pescitelli, G.; Di Bari, L.; Berova, N. Application of Electronic Circular Dichroism in the Study of Supramolecular Systems. *Chem Soc Rev* **2014**, *43* (15), 5211–5233. https://doi.org/10.1039/C4CS00104D.
(32) Pfeiffer, P.; Quehl, K. Über Einen Neuen Effekt in Lösungen Optisch-Aktiver Substanzen (I. Mitteil.). *Berichte Dtsch. Chem. Ges. B Ser.* **1931**, *64* (10), 2667–2671. https://doi.org/10.1002/cber.19310641015.
(33) Kirschner, S.; Bakkar, I. Utilization of the Pfeiffer Effect and Outer-Sphere Complexation for the Prediction of Absolute Configurations of Optically Active Metal Complexes. *Coord. Chem. Rev.* **1982**, *43*, 325–335. https://doi.org/10.1016/S0010-8545(00)82103-7.
(34) Muller, G.; Riehl, J. P. Use of Induced Circularly Polarized Luminescence (CPL) from Racemic D3 Lanthanide Complexes to Determine the Absolute Configuration of Amino Acids. *J. Fluoresc.* **2005**, *15* (4), 553–558. https://doi.org/10.1007/s10895-005-2828-4.
(35) Moussa, A.; Pham, C.; Bommireddy, S.; Muller, G. Importance of Hydrogen-Bonding Sites in the Chiral Recognition Mechanism between Racemic D3 Terbium(III) Complexes and Amino Acids. *Chirality* **2009**, *21* (5), 497–506. https://doi.org/10.1002/chir.20628.
(36) Brittain, H. G. Studies of the Pfeiffer Effect Induced in Tris(Pyridine-2,6-Dicarboxylato)Terbate(III) by Monosaccharide Aldose Sugars. *J. Chem. Soc. Dalton Trans.* **1984**, No. 7, 1367. https://doi.org/10.1039/dt9840001367.
(37) Neil, E. R.; Fox, M. A.; Pal, R.; Pålsson, L.-O.; O'Sullivan, B. A.; Parker, D. Chiral Probe Development for Circularly Polarised Luminescence: Comparative Study of Structural Factors

Determining the Degree of Induced CPL with Four Heptacoordinate Europium(III) Complexes. *Dalton Trans.* **2015**, *44* (33), 14937–14951. https://doi.org/10.1039/C5DT02358K.

(38) Freund, C.; Porzio, W.; Giovanella, U.; Vignali, F.; Pasini, M.; Destri, S.; Mech, A.; Di Pietro, S.; Di Bari, L.; Mineo, P. Thiophene Based Europium β-Diketonate Complexes: Effect of the Ligand Structure on the Emission Quantum Yield. *Inorg. Chem.* **2011**, *50* (12), 5417–5429. https://doi.org/10.1021/ic1021164.

(39) Malta, O. L.; Brito, H. F.; Menezes, J. F. S.; Gonçalves e Silva, F. R.; de Mello Donegá, C.; Alves, S. Experimental and Theoretical Emission Quantum Yield in the Compound Eu(Thenoyltrifluoroacetonate)3.2(Dibenzyl Sulfoxide). *Chem. Phys. Lett.* **1998**, *282* (3), 233–238. https://doi.org/10.1016/S0009-2614(97)01283-9.

(40) Lunkley, J. L.; Shirotani, D.; Yamanari, K.; Kaizaki, S.; Muller, G. Chiroptical Spectra of a Series of Tetrakis((+)-3-Heptafluorobutylyrylcamphorato)Lanthanide(III) with an Encapsulated Alkali Metal Ion: Circularly Polarized Luminescence and Absolute Chiral Structures for the Eu(III) and Sm(III) Complexes. *Inorg. Chem.* **2011**, *50* (24), 12724–12732. https://doi.org/10.1021/ic201851r.

(41) Lunkley, J. L.; Shirotani, D.; Yamanari, K.; Kaizaki, S.; Muller, G. Extraordinary Circularly Polarized Luminescence Activity Exhibited by Cesium Tetrakis(3-Heptafluoro-Butylryl-(+)-Camphorato) Eu(III) Complexes in EtOH and $CHCl_3$ Solutions. *J. Am. Chem. Soc.* **2008**, *130* (42), 13814–13815. https://doi.org/10.1021/ja805681w.

(42) Riehl, J. P.; Richardson, F. S. Circularly Polarized Luminescence Spectroscopy., Chem. Rev. 1977.

(43) Zinna, F.; Bari, L. D. Lanthanide Circularly Polarized Luminescence: Bases and Applications. *Chirality* **2015**, *27* (1), 1–13. https://doi.org/10.1002/chir.22382.

(44) Idée, J.-M.; Port, M.; Robic, C.; Medina, C.; Sabatou, M.; Corot, C. Role of Thermodynamic and Kinetic Parameters in Gadolinium Chelate Stability. *J. Magn. Reson. Imaging* **2009**, *30* (6), 1249–1258. https://doi.org/10.1002/jmri.21967.

(45) Bui, A. T.; Roux, A.; Grichine, A.; Duperray, A.; Andraud, C.; Maury, O. Twisted Charge-Transfer Antennae for Ultra-Bright Terbium(III) and Dysprosium(III) Bioprobes. *Chem. – Eur. J.* **2018**, *24* (14), 3408–3412. https://doi.org/10.1002/chem.201705933.

(46) Quici, S.; Marzanni, G.; Cavazzini, M.; Anelli, P. L.; Botta, M.; Gianolio, E.; Accorsi, G.; Armaroli, N.; Barigelletti, F. Highly Luminescent Eu^{3+} and Tb^{3+} Macrocyclic Complexes Bearing an Appended Phenanthroline Chromophore. *Inorg. Chem.* **2002**, *41* (10), 2777–2784. https://doi.org/10.1021/ic025543j.

(47) Williams, J. A. G.; Maffeo, D. Intramolecular Sensitisation of Europium(III) Luminescence by 8-Benzyloxyquinoline in Aqueous Solution. *Intramolecular sensitisation of europium(III) luminescence by 8-benzyloxyquinoline in aqueous solution*. Inorganica Chimica Acta, 2003, pp 127–136.

(48) Murray, B. S.; New, E. J.; Pal, R.; Parker, D. Critical Evaluation of Five Emissive Europium(Iii) Complexes as Optical Probes: Correlation of Cytotoxicity, Anion and Protein Affinity with Complex Structure, Stability and Intracellular Localisation Profile. *Org. Biomol. Chem.* **2008**, *6* (12), 2085. https://doi.org/10.1039/b803895c.

(49) Atkinson, P.; Findlay, K. S.; Kielar, F.; Pal, R.; Parker, D.; Poole, R. A.; Puschmann, H.; Richardson, S. L.; Stenson, P. A.; Thompson, A. L.; Yu, J. Azaxanthones and Azathioxanthones Are Effective Sensitisers for Europium and Terbium Luminescence. *Org. Biomol. Chem.* **2006**, *4* (9), 1707. https://doi.org/10.1039/b601357k.

(50) E. Bodman, S.; Breen, C.; Plasser, F.; J. Butler, S. Impact of Varying the Phenylboronic Acid Position in Macrocyclic Eu(Iii) Complexes on the Recognition of Adenosine Monophosphate. *Org. Chem. Front.* **2022**, *9* (20), 5494–5504. https://doi.org/10.1039/D2QO01067D.

(51) Cole, E.; Copley, R. C. B.; Howard, J. A. K.; Parker, D.; Ferguson, G.; Gallagher, J. F.; Kaitner, B.; Harrison, A.; Royle, L. Additions and Corrections. *J. Chem. Soc. Dalton Trans.* **1994**, No. 14, 2221–2221. https://doi.org/10.1039/DT9940002221.

(52) Frawley, A. T., Highly Emissive Chiral Lanthanide(III) Complexes for Labelling and Imaging, PhD Thesis, Durham University, 2017.
(53) Seveus, L.; Väisälä, M.; Syrjänen, S.; Sandberg, M.; Kuusisto, A.; Harju, R.; Salo, J.; Hemmilä, I.; Kojola, H.; Soini, E. Time-Resolved Fluorescence Imaging of Europium Chelate Label in Immunohistochemistry and in Situ Hybridization. *Cytometry* **1992**, *13* (4), 329–338. https://doi.org/10.1002/cyto.990130402.
(54) Latva, M.; Takalo, H.; Mukkala, V.-M.; Matachescu, C.; Rodríguez-Ubis, J. C.; Kankare, J. Correlation between the Lowest Triplet State Energy Level of the Ligand and Lanthanide(III) Luminescence Quantum Yield. *J. Lumin.* **1997**, *75* (2), 149–169. https://doi.org/10.1016/S0022-2313(97)00113-0.
(55) Fradgley, J. D.; Starck, M.; Laget, M.; Bourrier, E.; Dupuis, E.; Lamarque, L.; Trinquet, E.; Zwier, J. M.; Parker, D. Targeted pH Switched Europium Complexes Monitoring Receptor Internalisation in Living Cells. *Chem. Commun.* **2021**, *57* (47), 5814–5817. https://doi.org/10.1039/D1CC01029H.
(56) Walton, J. W.; Bourdolle, A.; Butler, S. J.; Soulie, M.; Delbianco, M.; McMahon, B. K.; Pal, R.; Puschmann, H.; Zwier, J. M.; Lamarque, L.; Maury, O.; Andraud, C.; Parker, D. Very Bright Europium Complexes That Stain Cellular Mitochondria. *Chem. Commun.* **2013**, *49* (16), 1600. https://doi.org/10.1039/c2cc35247h.
(57) Wheeler, S.; Butler, S. J. Exploiting the Unique Properties of Lanthanide Complexes as FRET Probes: From Quantitation to Protein Dynamics. *Anal. Sens.* **2023**, *3* (1), https://doi.org/10.1002/anse.202200036.
(58) Shuvaev, S.; Pal, R.; Parker, D. Selectively Switching on Europium Emission in Drug Site One of Human Serum Albumin. *Chem. Commun.* **2017**, *53* (50), 6724–6727. https://doi.org/10.1039/C7CC03071A.
(59) Pal, R.; Parker, D.; Costello, L. C. A Europium Luminescence Assay of Lactate and Citrate in Biological Fluids. *Org. Biomol. Chem.* **2009**, *7* (8), 1525. https://doi.org/10.1039/b901251f.
(60) Jennings, L. B.; Shuvaev, S.; Fox, M. A.; Pal, R.; Parker, D. Selective Signalling of Glyphosate in Water Using Europium Luminescence. *Dalton Trans.* **2018**, *47* (45), 16145–16154. https://doi.org/10.1039/C8DT03823F.
(61) Shuvaev, S.; Fox, M. A.; Parker, D. Monitoring of the ADP/ATP Ratio by Induced Circularly Polarised Europium Luminescence. *Angew. Chem.* **2018**, *130* (25), 7610–7614. https://doi.org/10.1002/ange.201801248.
(62) Walter, E. R. H.; Williams, J. A. G.; Parker, D. APTRA-Based Luminescent Lanthanide Complexes Displaying Enhanced Selectivity for Mg^{2+}. *Chem. - Eur. J.* **2018**, *24* (30), 7724–7733. https://doi.org/10.1002/chem.201800745.
(63) Delbianco, M.; Sadovnikova, V.; Bourrier, E.; Mathis, G.; Lamarque, L.; Zwier, J. M.; Parker, D. Bright, Highly Water-Soluble Triazacyclononane Europium Complexes To Detect Ligand Binding with Time-Resolved FRET Microscopy. *Angew. Chem. Int. Ed.* **2014**, *53* (40), 10718–10722. https://doi.org/10.1002/anie.201406632.
(64) Fradgley, J. D. *pH Responsive Chiral Europium Complexes*; PhD Thesis, Durham University, 2021.
(65) Fradgley, J. D.; Frawley, A. T.; Pal, R.; Parker, D. Striking Solvent Dependence of Total Emission and Circularly Polarised Luminescence in Coordinatively Saturated Chiral Europium Complexes: Solvation Significantly Perturbs the Ligand Field. *Phys. Chem. Chem. Phys.* **2021**, *23* (19), 11479–11487. https://doi.org/10.1039/D1CP01686E.
(66) Frawley, A. T.; Linford, H. V.; Starck, M.; Pal, R.; Parker, D. Enantioselective Cellular Localisation of Europium(III) Coordination Complexes. *Chem. Sci.* **2018**, *9* (4), 1042–1049. https://doi.org/10.1039/C7SC04422D.
(67) Ning, Y.; Tang, J.; Liu, Y.-W.; Jing, J.; Sun, Y.; Zhang, J.-L. Highly Luminescent, Biocompatible Ytterbium(Iii) Complexes as near-Infrared Fluorophores for Living Cell Imaging. *Chem. Sci.* **2018**, *9* (15), 3742–3753. https://doi.org/10.1039/C8SC00259B.

(68) Picot, A.; D'Aléo, A.; Baldeck, P. L.; Grichine, A.; Duperray, A.; Andraud, C.; Maury, O. Long-Lived Two-Photon Excited Luminescence of Water-Soluble Europium Complex: Applications in Biological Imaging Using Two-Photon Scanning Microscopy. *J. Am. Chem. Soc.* **2008**, *130* (5), 1532–1533. https://doi.org/10.1021/ja076837c.
(69) Stachelek, P.; MacKenzie, L.; Parker, D.; Pal, R. Circularly Polarised Luminescence Laser Scanning Confocal Microscopy to Study Live Cell Chiral Molecular Interactions. *Nat. Commun.* **2022**, *13* (1), 553. https://doi.org/10.1038/s41467-022-28220-z.
(70) Haas, Y.; Stein, G. Quenching of the Fluorescence of Rare Earth Ions by High Energy Vibrations of Solvent Molecules: Calculations of Franck-Condon Factors from Spectral Data. *Chem. Phys. Lett.* **1972**, *15* (1), 12–16. https://doi.org/10.1016/0009-2614(72)87003-9.
(71) Lakowicz, J. R. *Principles of Fluorescence Spectroscopy*; Kluwer Academic/Plenum Publishers, New York, London, Moscow, 2006.
(72) Makarov, N. S.; Drobizhev, M.; Rebane, A. Two-Photon Absorption Standards in the 550-1600 Nm Excitation Wavelength Range. *Opt. Express* **2008**, *16* (6), 4029. https://doi.org/10.1364/OE.16.004029.
(73) Parker, D.; Suturina, E. A.; Kuprov, I.; Chilton, N. F. How the Ligand Field in Lanthanide Coordination Complexes Determines Magnetic Susceptibility Anisotropy, Paramagnetic NMR Shift, and Relaxation Behavior. *Acc. Chem. Res.* **2020**, *53* (8), 1520–1534. https://doi.org/10.1021/acs.accounts.0c00275.
(74) Dickins, R. S.; Parker, D.; Bruce, J. I.; Tozer, D. J., Correlation of Optical and NMR Spectral Information with Coordination Variation for Axially Symmetric Macrocyclic Eu(Iii) and Yb(Iii) Complexes: Axial Donor Polarisability Determines Ligand Field and Cation Donor Preference. *Dalton Trans.* **2003**, No. 7, 1264–1271. https://doi.org/10.1039/b211939k.
(75) D'Aléo, A.; Picot, A.; Beeby, A.; Williams, J. A. G.; Le Guennic, B.; Andraud, C.; Maury, O. Efficient Sensitization of Europium, Ytterbium, and Neodymium Functionalized Tris-Dipicolinate Lanthanide Complexes through Tunable Charge-Transfer Excited States. *Inorg. Chem.* **2008**, *47* (22), 10258–10268. https://doi.org/10.1021/ic8012969.
(76) Emeis, C. A.; Oosterhoff, L. J. The N-π* Absorption and Emission of Optically Active *Trans-β* -Hydrindanone and *Trans-β* -Thiohydrindanone. *J. Chem. Phys.* **1971**, *54* (11), 4809–4819. https://doi.org/10.1063/1.1674756.
(77) Carr, R.; Evans, N. H.; Parker, D. Lanthanide Complexes as Chiral Probes Exploiting Circularly Polarized Luminescence. *Chem. Soc. Rev.* **2012**, *41* (23), 7673. https://doi.org/10.1039/c2cs35242g.
(78) Arrico, L.; Bari, L. D.; Zinna, F. Quantifying the Overall Efficiency of Circularly Polarized Emitters. *Chem. – Eur. J.* **2021**, *27* (9), 2920–2934. https://doi.org/10.1002/chem.202002791.
(79) Gendron, F.; Moore II, B.; Cador, O.; Pointillart, F.; Autschbach, J.; Le Guennic, B. Ab Initio Study of Circular Dichroism and Circularly Polarized Luminescence of Spin-Allowed and Spin-Forbidden Transitions: From Organic Ketones to Lanthanide Complexes. *J. Chem. Theory Comput.* **2019**, *15* (7), 4140–4155. https://doi.org/10.1021/acs.jctc.9b00286.
(80) Elshafie, H. S.; Camele, I. An Overview of Metabolic Activity, Beneficial and Pathogenic Aspects of Burkholderia Spp. *Metabolites* **2021**, *11* (5), 321. https://doi.org/10.3390/metabo11050321.
(81) MacKenzie, L. E.; Pålsson, L.-O.; Parker, D.; Beeby, A.; Pal, R. Rapid Time-Resolved Circular Polarization Luminescence (CPL) Emission Spectroscopy. *Nat. Commun.* **2020**, *11* (1), 1676. https://doi.org/10.1038/s41467-020-15469-5.
(82) Steinberg, I. Z.; Gafni, A. Sensitive Instrument for the Study of Circular Polarization of Luminescence. *Rev. Sci. Instrum.* **1972**, *43* (3), 409–413. https://doi.org/10.1063/1.1685648.
(83) Zhang, S.; Wang, Y.; Meng, F.; Dai, C.; Cheng, Y.; Zhu, C. Circularly Polarized Luminescence of AIE-Active Chiral O-BODIPYs Induced via Intramolecular Energy Transfer. *Chem. Commun.* **2015**, *51* (43), 9014–9017. https://doi.org/10.1039/C5CC01994J.
(84) *Polarization-selective and wavelength-selective luminescence spectroscopy of lanthanide (III) complexes - ProQuest*.

https://www.proquest.com/openview/77176144b65ccdd564d500c2efa3d5b2/1?cbl=18750&diss=y&pq-origsite=gscholar (accessed 2021-06-13).

(85) Hua, K. T.; Xu, J.; Quiroz, E. E.; Lopez, S.; Ingram, A. J.; Johnson, V. A.; Tisch, A. R.; de Bettencourt-Dias, A.; Straus, D. A.; Muller, G. Structural and Photophysical Properties of Visible- and Near-IR-Emitting Tris Lanthanide(III) Complexes Formed with the Enantiomers of *N* , *N* ′-Bis(1-Phenylethyl)-2,6-Pyridinedicarboxamide. *Inorg. Chem.* **2012**, *51* (1), 647–660. https://doi.org/10.1021/ic202094p.

(86) Starck, M.; MacKenzie, L. E.; Batsanov, A. S.; Parker, D.; Pal, R. Excitation Modulation of Eu:BPEPC Based Complexes as Low-Energy Reference Standards for Circularly Polarised Luminescence (CPL). *Chem. Commun.* **2019**, *55* (94), 14115–14118. https://doi.org/10.1039/C9CC07290J.

(87) Arjona-Esteban, A.; Volz, D. Status and Next Steps of TADF Technology: An Industrial Perspective. In *Highly Efficient OLEDs*; John Wiley & Sons, Ltd, 2018; pp 543–572. https://doi.org/10.1002/9783527691722.ch15.

(88) Takahashi, Y.; Furuki, Y.; Yoshida, S.; Otani, T.; Muto, M.; Suga, Y.; Ito, Y. 29.1: A New Achromatic Quarter-Wave Film Using Liquid-Crystal Materials for Anti-Reflection of OLEDs. *SID Symp. Dig. Tech. Pap.* **2014**, *45* (1), 381–384. https://doi.org/10.1002/j.2168-0159.2014.tb00103.x.

(89) Wong, M. Y.; Zysman-Colman, E. Purely Organic Thermally Activated Delayed Fluorescence Materials for Organic Light-Emitting Diodes. *Adv. Mater.* **2017**, *29* (22). https://doi.org/10.1002/adma.201605444.

(90) Tang, C. W.; VanSlyke, S. A. Organic Electroluminescent Diodes. *Appl. Phys. Lett.* **1987**, *51* (12), 913–915. https://doi.org/10.1063/1.98799.

(91) Hong, G.; Gan, X.; Leonhardt, C.; Zhang, Z.; Seibert, J.; Busch, J. M.; Bräse, S. A Brief History of OLEDs—Emitter Development and Industry Milestones. *Adv. Mater.* **2021**, *33* (9). https://doi.org/10.1002/adma.202005630.

(92) *Novel materials for fabrication and encapsulation of OLEDs - ScienceDirect*. https://www.sciencedirect.com/science/article/pii/S1364032114010090?casa_token=PhE3NHrJkSMAAAAA:Updb_QtZahXLt6q7qeSzV1_ggL5vUlq7YJQBdzDYo4VEdgnOJOcKT288SHyz3OS4Kb0LTymH (accessed 2024-01-27).

(93) Uoyama, H.; Goushi, K.; Shizu, K.; Nomura, H.; Adachi, C. Highly Efficient Organic Light-Emitting Diodes from Delayed Fluorescence. *Nature* **2012**, *492* (7428), 234–238. https://doi.org/10.1038/nature11687.

(94) Wang, L.; Zhao, Z.; Wei, C.; Wei, H.; Liu, Z.; Bian, Z.; Huang, C. Review on the Electroluminescence Study of Lanthanide Complexes. *Adv. Opt. Mater.* **2019**, *7* (11), 1801256. https://doi.org/10.1002/adom.201801256.

(95) Wang, S.; Zhang, H.; Zhang, B.; Xie, Z.; Wong, W.-Y. Towards High-Power-Efficiency Solution-Processed OLEDs: Material and Device Perspectives. *Mater. Sci. Eng. R Rep.* **2020**, *140*, 100547. https://doi.org/10.1016/j.mser.2020.100547.

(96) Lu, N.; Li, L.; Banerjee, W.; Sun, P.; Gao, N.; Liu, M. Charge Carrier Hopping Transport Based on Marcus Theory and Variable-Range Hopping Theory in Organic Semiconductors. *J. Appl. Phys.* **2015**, *118* (4), 045701. https://doi.org/10.1063/1.4927334.

(97) Han, T.-H.; Song, W.; Lee, T.-W. Elucidating the Crucial Role of Hole Injection Layer in Degradation of Organic Light-Emitting Diodes. *ACS Appl. Mater. Interfaces* **2015**, *7* (5), 3117–3125. https://doi.org/10.1021/am5072628.

(98) Choy, W. C. H.; Chan, W. K.; Yuan, Y. Recent Advances in Transition Metal Complexes and Light-Management Engineering in Organic Optoelectronic Devices. *Adv. Mater.* **2014**, *26* (31), 5368–5399. https://doi.org/10.1002/adma.201306133.

(99) Slinker, J. D.; Rivnay, J.; Moskowitz, J. S.; Parker, J. B.; Bernhard, S.; Abruña, H. D.; Malliaras, G. G. Electroluminescent Devices from Ionic Transition Metal Complexes. *J. Mater. Chem.* **2007**, *17* (29), 2976–2988. https://doi.org/10.1039/B704017B.

(100) Xie, M.; Sun, M.; Xue, S.; Yang, W. Recent Progress of Blue Fluorescent Organic Light-Emitting Diodes with Narrow Full Width at Half Maximum. *Dyes Pigments* **2023**, *208*, 110799. https://doi.org/10.1016/j.dyepig.2022.110799.
(101) Bettencourt-Dias, A. de. Lanthanide-Based Emitting Materials in Light-Emitting Diodes. *Dalton Trans.* **2007**, *0* (22), 2229–2241. https://doi.org/10.1039/B702341C.
(102) Canzler, T. W.; Kido, J. Exciton Quenching in Highly Efficient Europium-Complex Based Organic Light-Emitting Diodes. *Org. Electron.* **2006**, *7* (1), 29–37. https://doi.org/10.1016/j.orgel.2005.10.004.
(103) Zinna, F.; Giovanella, U.; Bari, L. D. Highly Circularly Polarized Electroluminescence from a Chiral Europium Complex. *Adv. Mater.* **2015**, *27* (10), 1791–1795. https://doi.org/10.1002/adma.201404891.
(104) Lamarque, L.; Delbianco, M. Nouveaux Agents Complexants Hydrosolubles et Complexes de Lanthanide Correspondants. WO201411166.
(105) Takalo, H.; Kankare, J.; Lund, H.; Makmur, L.; Norrestam, R. Synthesis of Dimethyl and Diethyl 4-(Phenylethynyl)-2,6-Pyridinedicarboxylate. *Acta Chem. Scand.,* **1987**, *41*, 219–221. https://doi.org/10.3891/acta.chem.scand.41b-0219.
(106) Starck, M.; Pal, R.; Parker, D. Structural Control of Cell Permeability with Highly Emissive Europium(III) Complexes Permits Different Microscopy Applications. *Chem. – Eur. J.* **2016**, *22* (2), 570–580. https://doi.org/10.1002/chem.201504103.
(107) Nadri, S., Rafiee E., Jamali S., Joshaghani M., *1,1'-Methylene-3,3'-Bis[(N-(Tert-Butyl)Imidazol-2-Ylidene] and Its Effect in Palladium-Catalyzed C–C Coupling*; Synlett 2015; 26(05), 619-624, 2015, 10.1055/s-0034-1379954.
(108) Soheili, A.; Albaneze-Walker, J.; Murry, J. A.; Dormer, P. G.; Hughes, D. L. Efficient and General Protocol for the Copper-Free Sonogashira Coupling of Aryl Bromides at Room Temperature. *Org. Lett.* **2003**, *5* (22), 4191–4194. https://doi.org/10.1021/ol035632f.
(109) Boekelheide, V.; Linn, W. J. Rearrangements of N-Oxides. A Novel Synthesis of Pyridyl Carbinols and Aldehydes. *J. Am. Chem. Soc.* **1954**, *76* (5), 1286–1291. https://doi.org/10.1021/ja01634a026.
(110) Chinchilla, R.; Nájera, C. The Sonogashira Reaction: A Booming Methodology in Synthetic Organic Chemistry. *Chem. Rev.* **2007**, *107* (3), 874–922. https://doi.org/10.1021/cr050992x.
(111) Liang, B.; Dai, M.; Chen, J.; Yang, Z. Copper-Free Sonogashira Coupling Reaction with $PdCl_2$ in Water under Aerobic Conditions. *J. Org. Chem.* **2005**, *70* (1), 391–393. https://doi.org/10.1021/jo048599z.
(112) Corey, E. J.; Fuchs, P. L. A Synthetic Method for Formyl→ethynyl Conversion (RCHO→RC□CH or RC□CR'). *Tetrahedron Lett.* **1972**, *13* (36), 3769–3772. https://doi.org/10.1016/S0040-4039(01)94157-7.
(113) Butler, S. J.; McMahon, B. K.; Pal, R.; Parker, D.; Walton, J. W. Bright Mono-Aqua Europium Complexes Based on Triazacyclononane That Bind Anions Reversibly and Permeate Cells Efficiently. *Chem. – Eur. J.* **2013**, *19* (29), 9511–9517. https://doi.org/10.1002/chem.201301273.
(114) Starck, M.; Fradgley, J. D.; Pal, R.; Zwier, J. M.; Lamarque, L.; Parker, D. Synthesis and Evaluation of Europium Complexes That Switch on Luminescence in Lysosomes of Living Cells. *Chem. Weinh. Bergstr. Ger.* **2021**, *27* (2), 766–777. https://doi.org/10.1002/chem.202003992.
(115) Nakamaru, K. Synthesis, Luminescence Quantum Yields, and Lifetimes of Trischelated Ruthenium(II) Mixed-Ligand Complexes Including 3,3'-Dimethyl-2,2'-Bipyridyl. *Bull. Chem. Soc. Jpn.* **1982**, *55* (9), 2697–2705. https://doi.org/10.1246/bcsj.55.2697.
(116) H. Evans, N.; Carr, R.; Delbianco, M.; Pal, R.; S. Yufit, D.; Parker, D. Complete Stereocontrol in the Synthesis of Macrocyclic Lanthanide Complexes: Direct Formation of Enantiopure Systems for Circularly Polarised Luminescence Applications. *Dalton Trans.* **2013**, *42* (44), 15610–15616. https://doi.org/10.1039/C3DT52425F.

(117) Walton, J. W.; Carr, R.; Evans, N. H.; Funk, A. M.; Kenwright, A. M.; Parker, D.; Yufit, D. S.; Botta, M.; De Pinto, S.; Wong, K.-L. Isostructural Series of Nine-Coordinate Chiral Lanthanide Complexes Based on Triazacyclononane. *Inorg. Chem.* **2012**, *51* (15), 8042–8056. https://doi.org/10.1021/ic300147p.
(118) Frawley, A. T.; Pal, R.; Parker, D. Very Bright, Enantiopure Europium(III) Complexes Allow Time-Gated Chiral Contrast Imaging. *Chem. Commun.* **2016**, *52* (91), 13349–13352. https://doi.org/10.1039/C6CC07313A.
(119) Fu, L.-M.; Wen, X.-F.; Ai, X.-C.; Sun, Y.; Wu, Y.-S.; Zhang, J.-P.; Wang, Y. Efficient Two-Photon-Sensitized Luminescence of a Europium(III) Complex. *Angew. Chem. Int. Ed.* **2005**, *44* (5), 747–750. https://doi.org/10.1002/anie.200462382.
(120) Pålsson, L.-O.; Pal, R.; S. Murray, B.; Parker, D.; Beeby, A. Two- Photon Absorption and Photoluminescence of Europium Based Emissive Probes for Bioactive Systems. *Dalton Trans.* **2007**, *0* (48), 5726–5734. https://doi.org/10.1039/B710717J.
(121) Shah, A.; Roux, A.; Starck, M.; Mosely, J. A.; Stevens, M.; Norman, D. G.; Hunter, R. I.; El Mkami, H.; Smith, G. M.; Parker, D.; Lovett, J. E. A Gadolinium Spin Label with Both a Narrow Central Transition and Short Tether for Use in Double Electron Electron Resonance Distance Measurements. *Inorg. Chem.* **2019**, *58* (5), 3015–3025. https://doi.org/10.1021/acs.inorgchem.8b02892.
(122) Clayden, J.; Greeves, N.; Warren, S. *Organic Chemistry*, 2nd edition.; 2012.
(123) Starck, M.; Fradgley, J. D.; De Rosa, D. F.; Batsanov, A. S.; Papa, M.; Taylor, M. J.; Lovett, J. E.; Lutter, J. C.; Allen, M. J.; Parker, D. Versatile Para-Substituted Pyridine Lanthanide Coordination Complexes Allow Late Stage Tailoring of Complex Function. *Chem. – Eur. J.* **2021**, *27* (71), 17921–17927. https://doi.org/10.1002/chem.202103243.
(124) (125) Sherwood, J.; Parker, H. L.; Moonen, K.; Farmer, T. J.; Hunt, A. J., Green Chemistry, 2016, Supplementary Information: N-Butylpyrrolidinone as a Dipolar Aprotic Solvent for Organic Synthesis.
(125) De-Bettencourt-Dias, A. Lumin. Lanthanide Ions Coord. Compd. Nanomater.; 2014; pp 1–48.
(126) Supkowski, R. M.; Horrocks, W. DeW. On the Determination of the Number of Water Molecules, q, Coordinated to Europium(III) Ions in Solution from Luminescence Decay Lifetimes. *Inorganica Chim. Acta* **2002**, *340*, 44–48. https://doi.org/10.1016/S0020-1693(02)01022-8.
(127) H. Walter, E. R.; Williams, J. A. G.; Parker, D. Solvent Polarity and Oxygen Sensitivity, Rather than Viscosity, Determine Lifetimes of Biaryl-Sensitised Terbium Luminescence. *Chem. Commun.* **2017**, *53* (100), 13344–13347. https://doi.org/10.1039/C7CC08361K.
(128) Zinna, F.; Arrico, L.; Funaioli, T.; Bari, L. D.; Pasini, M.; Botta, C.; Giovanella, U. Modular Chiral Eu(Iii) Complexes for Efficient Circularly Polarized OLEDs. *J. Mater. Chem. C* **2022**, *10* (2), 463–468. https://doi.org/10.1039/D1TC05023K.
(129) Shuvaev, S.; Suturina, E. A.; Mason, K.; Parker, D. Chiral Probes for α_1-AGP Reporting by Species-Specific Induced Circularly Polarised Luminescence. *Chem. Sci.* **2018**, *9* (11), 2996–3003. https://doi.org/10.1039/C8SC00482J.
(130) Kumar, M.; Chapran, M.; Wiosna-Salyga, G.; Sleczkowski, P.; Luszczynska, B.; Pereira, L. Insights into Charge Transport in High-Efficiency Green Solution-Processed Thermally Activated Delayed Fluorescence Organic Light-Emitting Diodes with a Single Emitting Layer. *J. Phys. Chem. C* **2020**, *124* (40), 21935–21947. https://doi.org/10.1021/acs.jpcc.0c04938.
(131) Butler, S. J.; Lamarque, L.; Pal, R.; Parker, D. EuroTracker Dyes: Highly Emissive Europium Complexes as Alternative Organelle Stains for Live Cell Imaging. *Chem. Sci.* **2014**, *5* (5), 1750. https://doi.org/10.1039/c3sc53056f.
(132) Carr, R.; Puckrin, R.; McMahon, B. K.; Pal, R.; Parker, D.; Pålsson, L.-O. Induced Circularly Polarized Luminescence Arising from Anion or Protein Binding to Racemic Emissive Lanthanide Complexes. *Methods Appl. Fluoresc.* **2014**, *2* (2), 024007. https://doi.org/10.1088/2050-6120/2/2/024007.

(133) Willis, O. G.; Zinna, F.; Pescitelli, G.; Micheletti, C.; Di Bari, L. Remarkable Near-Infrared Chiroptical Properties of Chiral Yb, Tm and Er Complexes. *Dalton Trans.* **2022**, *51* (2), 518–523. https://doi.org/10.1039/D1DT03843E.
(134) De Rosa, D. F.; Stachelek, P.; Black, D. J.; Pal, R. Rapid Handheld Time-Resolved Circularly Polarised Luminescence Photography Camera for Life and Material Sciences. *Nat. Commun.* **2023**, *14* (1), 1537. https://doi.org/10.1038/s41467-023-37329-8.
(135) Reichardt, T.; Welton, T. *Solvents and Solvent Effects in Organic Chemistry*, 4 ed.; 2010.
(136) Mason, K.; Harnden, A. C.; Patrick, C. W.; Poh, A. W. J.; Batsanov, A. S.; Suturina, E. A.; Vonci, M.; McInnes, E. J. L.; Chilton, N. F.; Parker, D. Exquisite Sensitivity of the Ligand Field to Solvation and Donor Polarisability in Coordinatively Saturated Lanthanide Complexes. *Chem. Commun.* **2018**, *54* (61), 8486–8489. https://doi.org/10.1039/C8CC04995E.
(137) MacKenzie, L. E.; Pal, R. Circularly Polarized Lanthanide Luminescence for Advanced Security Inks. *Nat. Rev. Chem.* **2021**, *5* (2), 109–124. https://doi.org/10.1038/s41570-020-00235-4.
(138) Frawley, A. T. HIGHLY EMISSIVE CHIRAL LANTHANIDE(III) COMPLEXES FOR LABELLING AND IMAGING. 290.
(139) Evans, N. H.; Carr, R.; Delbianco, M.; Pal, R.; Yufit, D. S.; Parker, D. Complete Stereocontrol in the Synthesis of Macrocyclic Lanthanide Complexes: Direct Formation of Enantiopure Systems for Circularly Polarised Luminescence Applications. *Dalton Trans.* **2013**, *42* (44), 15610. https://doi.org/10.1039/c3dt52425f.
(140) Li, H.; Lan, R.; Chan, C.-F.; Jiang, L.; Dai, L.; Kwong, D. W. J.; Lam, M. H.-W.; Wong, K.-L. Real-Time in Situ Monitoring via Europium Emission of the Photo-Release of Antitumor Cisplatin from a Eu–Pt Complex. *Chem. Commun.* **2015**, *51* (74), 14022–14025. https://doi.org/10.1039/C5CC05461C.
(141) Montgomery, C. P.; New, E. J.; Parker, D.; Peacock, R. D. Enantioselective Regulation of a Metal Complex in Reversible Binding to Serum Albumin: Dynamic Helicity Inversion Signalled by Circularly Polarised Luminescence. *Chem. Commun.* **2008**, No. 36, 4261. https://doi.org/10.1039/b810978h.
(142) Grattan, K.; Zhang, Z. Y. *Fiber Optic Fluorescence Thermometry*; Springer, 1995.
(143) Wang, X.; Wolfbeis, O. S.; Meier, R. J. Luminescent Probes and Sensors for Temperature. *Chem. Soc. Rev.* **2013**, *42* (19), 7834. https://doi.org/10.1039/c3cs60102a.
(144) Childs, P. R. N.; Greenwood, J. R.; Long, C. A. Review of Temperature Measurement. *Rev. Sci. Instrum.* **2000**, *71* (8), 2959–2978. https://doi.org/10.1063/1.1305516.
(145) Michalski, L.; Eckersdorf, K.; Kucharski, J.; McGhee, J. *Temperature Measurement*; Wiley: Chichester, UK, 2001.
(146) Ashcroft, N.; Mermin, N. *Solid State Physics*; Saunders College: Philadelphia, 1976.
(147) Chandrasekharan, N.; Kelly, L. A. A Dual Fluorescence Temperature Sensor Based on Perylene/Exciplex Interconversion. *J. Am. Chem. Soc.* **2001**, *123* (40), 9898–9899. https://doi.org/10.1021/ja016153j.
(148) Fister, J. C.; Rank, Diana.; Harris, J. M. Delayed Fluorescence Optical Thermometry. *Anal. Chem.* **1995**, *67* (23), 4269–4275. https://doi.org/10.1021/ac00119a011.
(149) Baleizão, C.; Nagl, S.; Borisov, S. M.; Schäferling, M.; Wolfbeis, O. S.; Berberan-Santos, M. N. An Optical Thermometer Based on the Delayed Fluorescence of C70. *Chem. – Eur. J.* **2007**, *13* (13), 3643–3651. https://doi.org/10.1002/chem.200601580.
(150) Kolodner, P.; Tyson, J. A. Remote Thermal Imaging with 0.7-μm Spatial Resolution Using Temperature-dependent Fluorescent Thin Flims. *Appl. Phys. Lett.* **1983**, *42* (1), 117–119. https://doi.org/10.1063/1.93766.
(151) Zohar, O.; Ikeda, M.; Shinagawa, H.; Inoue, H.; Nakamura, H.; Elbaum, D.; Alkon, D. L.; Yoshioka, T. Thermal Imaging of Receptor-Activated Heat Production in Single Cells. *Biophys. J.* **1998**, *74* (1), 82–89. https://doi.org/10.1016/S0006-3495(98)77769-0.

(152) Okabe, K.; Inada, N.; Gota, C.; Harada, Y.; Funatsu, T.; Uchiyama, S. Intracellular Temperature Mapping with a Fluorescent Polymeric Thermometer and Fluorescence Lifetime Imaging Microscopy. *Nat. Commun.* **2012**, *3* (1), 705. https://doi.org/10.1038/ncomms1714.
(153) MacKenzie, L. E.; Pålsson, L.-O.; Parker, D.; Beeby, A.; Pal, R. Rapid Time-Resolved Circular Polarization Luminescence (CPL) Emission Spectroscopy. *Nat. Commun.* **2020**, *11* (1), 1676. https://doi.org/10.1038/s41467-020-15469-5.
(154) Stachelek, P.; MacKenzie, L.; Parker, D.; Pal, R. Circularly Polarised Luminescence Laser Scanning Confocal Microscopy to Study Live Cell Chiral Molecular Interactions. *Nat. Commun.* **2022**, *13* (1), 1–8.
(155) Dai, L.; Zhang, J.; Chen, Y.; Mackenzie, L. E.; Pal, R.; Law, G.-L. Synthesis of Water-Soluble Chiral DOTA Lanthanide Complexes with Predominantly Twisted Square Antiprism Isomers and Circularly Polarized Luminescence. *Inorg. Chem.* **2019**, *58* (19), 12506–12510. https://doi.org/10.1021/acs.inorgchem.9b01799.
(156) Shiraki, T.; Tsuchiya, Y.; Noguchi, T.; Tamaru, S.; Suzuki, N.; Taguchi, M.; Fujiki, M.; Shinkai, S. Creation of Circularly Polarized Luminescence from an Achiral Polyfluorene Derivative through Complexation with Helix-Forming Polysaccharides: Importance of the Meta -Linkage Chain for Helix Formation. *Chem. - Asian J.* **2014**, *9* (1), 218–222. https://doi.org/10.1002/asia.201301216.
(157) MacKenzie, L. E.; Pal, R. Circularly Polarized Lanthanide Luminescence for Advanced Security Inks. *Nat. Rev. Chem.* **2021**, *5* (2), 109–124. https://doi.org/10.1038/s41570-020-00235-4.
(158) Valentín, K.; Wild, P.; Štolc, S.; Daubner, F.; Clabian, M. Optical Benchmarking of Security Document Readers for Automated Border Control. In *Optics and Photonics for Counterterrorism, Crime Fighting, and Defence XII*; SPIE, 2016; Vol. 9995, pp 20–30. https://doi.org/10.1117/12.2241169.
(159) Belair, S. D.; Maupin, C. L.; Logue, M. W.; Riehl, J. P. Analysis of the Temperature Dependence of the Racemization of Eu(III) Complexes through Measurement of Steady-State Circularly Polarized Luminescence. *J. Lumin.* **2000**, *86* (1), 61–66. https://doi.org/10.1016/S0022-2313(99)00175-1.
(160) Martin-Ramos, P., Martin-Ramos, S., Zinna, F., Di Bari, L., *Lanthanide-Based Multifunctional Materials From OLEDs to SIMs*, 1st Edition;, Ed.; Elsevier, 2018.
(161) Binnemans, K. Interpretation of Europium(III) Spectra. *Coord. Chem. Rev.* **2015**, *295*, 1–45. https://doi.org/10.1016/j.ccr.2015.02.015.
(162) Butler, S. J.; Lamarque, L.; Pal, R.; Parker, D. EuroTracker Dyes: Highly Emissive Europium Complexes as Alternative Organelle Stains for Live Cell Imaging. *Chem. Sci.* **2014**, *5* (5), 1750. https://doi.org/10.1039/c3sc53056f.
(163) Muller, G. Luminescent Chiral Lanthanide(III) Complexes as Potential Molecular Probes. *Dalton Trans.* **2009**, *44*, 9692–9707.
(164) Friedman, H. G.; Choppin, G. R.; Feuerbacher, D. G. The Shapes of the f Orbitals. *J. Chem. Educ.* **1964**, *41* (7), 354. https://doi.org/10.1021/ed041p354.
(165) Bünzli, J. G. Rising Stars in Science and Technology: Luminescent Lanthanide Materials. *Eur. J. Inorg. Chem.* **2017**, *2017* (44), 5058–5063. https://doi.org/10.1002/ejic.201701201.
(166) Bünzli, J. G.; Eliseeva, S. V. Intriguing Aspects of Lanthanide Luminescence. *Chem. Sci.* **2013**, *4* (5), 1939. https://doi.org/10.1039/c3sc22126a.
(167) Vleck, J. H. Van. The Puzzle of Rare-Earth Spectra in Solids. *J. Phys. Chem.* **1937**, *41* (1), 67–80. https://doi.org/10.1021/j150379a006.
(168) Parker, D.; Fradgley, J. D.; Wong, K.-L. The Design of Responsive Luminescent Lanthanide Probes and Sensors. *Chem. Soc. Rev.* **2021**, *50* (14), 8193–8213. https://doi.org/10.1039/D1CS00310K.
(169) Frawley, A. T.; Pal, R.; Parker, D. Very Bright, Enantiopure Europium(III) Complexes Allow Time-Gated Chiral Contrast Imaging. *Chem. Commun.* **2016**, *52* (91), 13349–13352. https://doi.org/10.1039/c6cc07313a.

(170) Kitagawa, Y.; Wada, S.; Islam, M. D. J.; Saita, K.; Gon, M.; Fushimi, K.; Tanaka, K.; Maeda, S.; Hasegawa, Y. Chiral Lanthanide Lumino-Glass for a Circularly Polarized Light Security Device. *Commun. Chem.* **2020**, *3* (1), 119. https://doi.org/10.1038/s42004-020-00366-1.
(171) Pal, R.; Beeby, A. Simple and Versatile Modifications Allowing Time Gated Spectral Acquisition, Imaging and Lifetime Profiling on Conventional Wide-Field Microscopes. *Methods Appl. Fluoresc.* **2014**, *2* (3). https://doi.org/10.1088/2050-6120/2/3/037001.
(172) Hasegawa, Y.; Miura, Y.; Kitagawa, Y.; Wada, S.; Nakanishi, T.; Fushimi, K.; Seki, T.; Ito, H.; Iwasa, T.; Taketsugu, T.; Gon, M.; Tanaka, K.; Chujo, Y.; Hattori, S.; Karasawa, M.; Ishii, K. Spiral Eu(III) Coordination Polymers with Circularly Polarized Luminescence. *Chem. Commun.* **2018**, *54* (76), 10695–10697. https://doi.org/10.1039/C8CC05147J.
(173) Zhang, W.-Y.; Zhang, Y.-Q.; Jiang, S.-D.; Sun, W.-B.; Li, H.-F.; Wang, B.-W.; Chen, P.; Yan, P.-F.; Gao, S. Dramatic Impact of the Lattice Solvent on the Dynamic Magnetic Relaxation of Dinuclear Dysprosium Single-Molecule Magnets. *Inorg. Chem. Front.* **2018**, *5* (7), 1575–1586. https://doi.org/10.1039/C8QI00266E.
(174) Wada, S.; Kitagawa, Y.; Nakanishi, T.; Gon, M.; Tanaka, K.; Fushimi, K.; Chujo, Y.; Hasegawa, Y. Electronic Chirality Inversion of Lanthanide Complex Induced by Achiral Molecules. *Sci. Rep.* **2018**, *8* (1), 16395. https://doi.org/10.1038/s41598-018-34790-0.
(175) Frawley, A. T.; Linford, H. V.; Starck, M.; Pal, R.; Parker, D. Enantioselective Cellular Localisation of Europium (III) Coordination Complexes. *Chem. Sci.* **2018**, *9* (4), 1042–1049. https://doi.org/10.1039/C7SC04422D.
(176) Arppe, R.; Sørensen, T. J. Physical Unclonable Functions Generated through Chemical Methods for Anti-Counterfeiting. *Nat. Rev. Chem.* **2017**, *1* (4), 31. https://doi.org/10.1038/s41570-017-0031.
(177) Butler, S. J.; Parker, D. Anion Binding in Water at Lanthanide Centres: From Structure and Selectivity to Signalling and Sensing. *Chem Soc Rev* **2013**, *42* (4), 1652–1666. https://doi.org/10.1039/C2CS35144G.
(178) Starck, M.; MacKenzie, L. E.; Batsanov, A. S.; Parker, D.; Pal, R. Excitation Modulation of Eu:BPEPC Based Complexes as Low-Energy Reference Standards for Circularly Polarised Luminescence (CPL). *Chem. Commun.* **2019**, *55* (94), 14115–14118. https://doi.org/10.1039/C9CC07290J.
(179) Barry, D. E.; Caffrey, D. F.; Gunnlaugsson, T. Lanthanide-Directed Synthesis of Luminescent Self-Assembly Supramolecular Structures and Mechanically Bonded Systems from Acyclic Coordinating Organic Ligands. *Chem. Soc. Rev.* **2016**, *45* (11), 3244–3274. https://doi.org/10.1039/C6CS00116E.
(180) Xu, C.; Webb, W. W. Measurement of Two-Photon Excitation Cross Sections of Molecular Fluorophores with Data from 690 to 1050 Nm. *J. Opt. Soc. Am. B* **1996**, *13* (3), 481. https://doi.org/10.1364/josab.13.000481.
(181) Pålsson, L.-O.; Pal, R.; Murray, B. S.; Parker, D.; Beeby, A. Two-Photon Absorption and Photoluminescence of Europium Based Emissive Probes for Bioactive Systems. *Dalton Trans.* **2007**, *48*, 5726.
(182) Sudheendran Swayamprabha, S.; Dubey, D. K.; Shahnawaz; Yadav, R. A. K.; Nagar, M. R.; Sharma, A.; Tung, F.-C.; Jou, J.-H. Approaches for Long Lifetime Organic Light Emitting Diodes. *Adv. Sci.* **2021**, *8* (1), 2002254. https://doi.org/10.1002/advs.202002254.
(183) Zimnyakov, D.; Alonova, M.; Skripal, A.; Dobdin, S.; Feodorova, V. Quantification of the Diversity in Gene Structures Using the Principles of Polarization Mapping. *Curr. Issues Mol. Biol.* **2023**, *45* (2), 1720–1740. https://doi.org/10.3390/cimb45020111.
(184) Linklater, D.; Vailionis, A.; Ryu, M.; Kamegaki, S.; Morikawa, J.; Mu, H.; Smith, D.; Maasoumi, P.; Ford, R.; Katkus, T.; Blamires, S.; Kondo, T.; Nishijima, Y.; Moraru, D.; Shribak, M.; O'Connor, A.; Ivanova, E. P.; Ng, S. H.; Masuda, H.; Juodkazis, S. Structure and Optical Anisotropy of Spider Scales and Silk: The Use of Chromaticity and Azimuth Colors to Optically Characterize Complex

Biological Structures. *Nanomaterials* **2023**, *13* (12), 1894. https://doi.org/10.3390/nano13121894.
(185) Pal, R.; Parker, D.; Costello, L. C. A Europium Luminescence Assay of Lactate and Citrate in Biological Fluids. *Org. Biomol. Chem.* **2009**, *7* (8), 1525. https://doi.org/10.1039/b901251f.
(186) Wan, L.; Wade, J.; Salerno, F.; Arteaga, O.; Laidlaw, B.; Wang, X.; Penfold, T.; Fuchter, M. J.; Campbell, A. J. Inverting the Handedness of Circularly Polarized Luminescence from Light-Emitting Polymers Using Film Thickness. *ACS Nano* **2019**, *13* (7), 8099–8105. https://doi.org/10.1021/acsnano.9b02940.
(187) Pal, R. Phase Modulation Nanoscopy: A Simple Approach to Enhanced Optical Resolution. *Faraday Discuss.* **2015**, *177* (0), 507–515. https://doi.org/10.1039/C4FD00158C.
(188) US Pat., US 20150361116 A1. 2015.

Appendices

Publications during period of study

1. **D.F. De Rosa**, M. Starck, D. Parker, R. Pal*, Unlocking same-sign CPL: assessing solvent polarity and racemisation kinetics in nine-coordinate europium complexes,* **Chem. Eur. J.***,* 2023, 30, 9

2. O. Willis, F. Petri, **D.F. De Rosa**, A. Mandoli, R. Pal, F. Zinna, L. Di Bari, *Two-photon circularly polarized luminescence of chiral Eu complexes,* **J. Am. Chem. Soc.**, 2023, 145, 46, 25170–25176

3. **D.F. De Rosa**, P. Stachelek, D.J. Black, R. Pal, *Rapid handheld time-resolved circularly polarised luminescence (CPL) photography camera for life and material sciences,* **Nature Comm.**, 2023,14, 1537

4. M. Starck, J.D. Fradgley, **D.F. De Rosa**, A.S. Batsanov, M. Papa, M.J. Taylor, J.E. Lovett, J.C. Lutter, M.J. Allen, D. Parker, *Versatile para-substituted pyridine lanthanide coordination complexes allow late stage tailoring of complex function,* **Chem. Eur. J.**, 2021, 27, 17921–17927